Ultrafast Terahertz Dynamics in Semiconductors and Nanomaterials

by

David N. Purschke

A thesis submitted in partial fulfillment of the requirements for the degree of

Doctor of Philosophy

Department of Physics

University of Alberta

Abstract

Ultrafast terahertz (THz) spectroscopy is presently the most powerful tool available to materials scientists for directly probing ultrafast conductivity dynamics. Its low center frequency and phase-resolved measurement, which yields sub-picosecond temporal resolution, make it ideally suited for studying properties such as carrier mobility and relaxation dynamics. In new materials and nanomaterials, with rapid carrier lifetimes and difficulties with electronic contacts, THz spectroscopy can sometimes be the only technique able to study the detailed carrier transport properties. Recent sources of intense THz pulses, enabled by the tilted-pulse front technique, have also facilitated new spectroscopic techniques to investigate phenomena such as ultrafast high-field transport and hot-carrier physics. Moreover, with the development of novel sources of THz radiation the future of this exciting field promises to yield new insight into the nature of light-matter interaction.

This thesis explores three areas of THz science and technology, beginning with THz pulse generation via optical rectification with tilted-pulse fronts. New perspectives are presented that highlight the role of higher-order angular dispersion (AD) in the spatiotemporal intensity of tilted-pulse fronts. A simple setup for controlling quadratic AD is proposed that could have impact in multiple areas of ultrafast science. Moreover, a novel tilted-pulse front THz source in gallium nitride (GaN) is proposed. Simulations are used to show that, due to the large GaN band gap and phonon frequency, this source could be capable of high-intensity THz pulse generation in the 5-12 THz gap where there is a current lack of ultrafast and high-spectral-intensity

table-top sources. The development of tilted-pulse front sources over several years in the Ultrafast Nanotools lab is also detailed, culminating in the generation of THz pulses with peak electric fields in excess of 600 kV/cm.

Second, the modulation of semiconductor photoluminescence (PL) with intense THz pulses, THz-ΔPL, is explored and shown to result from THz-control of hot-carriers. To validate this conclusion, a diffusion-based model is developed that simultaneously captures both PL quenching near the band gap and PL enhancement in the high-energy tail with a single tunable parameter: the initial hot-carrier temperature. With minimal assumptions as to the nature of the detailed hot-carrier physics, the model shows excellent qualitative and even semi-quantitative agreement with data. Moreover, the diffusion model is shown to accurately describe the THz-ΔPL in multiple direct-gap semiconductors and, in principle, should be broadly applicable to the study of hot-carrier dynamics in a variety of semiconductors. Further experimental results prove that the simple diffusion model captures the scaling of THz-ΔPL over range of injection levels, however, the model breaks down at high fluence due to optical nonlinearities. This suggests that even more information about the hot-carrier physics can be found from this simple experiment and several extensions to the model are proposed that could provide clarity.

Finally, time-resolved THz spectroscopy (TRTS) is applied to probe the transient photoconductivity of tin iodide phosphide (SnIP) nanowires for the first time. SnIP, an inorganic double-helix material, is a quasi-1D van der Waals semiconductor that shows promise in photocatalysis and flexible electronics. However, our understanding of the fundamental photophysics and charge transport dynamics of this new material is limited. New insight into the highly anisotropic electronic structure from quantum chemical calculations, along with measurements of the carrier scattering time from TRTS, reveals a carrier mobility as high as 280 $\mathrm{cm^2\,V^{-1}s^{-1}}$ along the double-helix axis and a hole mobility of 238 $\mathrm{cm^2\,V^{-1}s^{-1}}$ perpendicular to the double-helix axis.

This high mobility is supported by a detailed comparison between the commonly used Drude-Smith model, plasmon model, and Bruggeman model for the optical conductivity that shows a similarly high mobility for each model. Notably, our results indicate that Drude-Smith model most effectively describes transport in these SnIP nanowires. Additionally, measurements of the THz infrared (IR) active vibrational spectrum reveals two vibrational resonances, which show excellent agreement with first-principles calculations. Interestingly, an ultrafast photoexcitation-induced charge redistribution is observed that manifests as a reduction in amplitude of a twisting mode of the outer SnI helix on picosecond timescales. Finally, TRTS reveals that the carrier lifetime and mobility are limited by a trap density greater than $10^{18}\,\mathrm{cm}^{-3}$. Most importantly, these results demonstrate a remarkably high carrier mobility for such a soft and flexible material, suggesting that it could be ideally suited for future flexible electronics applications.

Preface

The results presented in this thesis were obtained under the supervision of professor Frank A. Hegmann (FH) in the Department of Physics at the University of Alberta (U of A) with co-supervision from professor Tom Nilges (TN) in the Department of Chemistry at the Technical University of Munich (TUM). The majority of my time was spent at U of A with several months of research exchange at TUM in fulfillment of the requirements for the joint PhD program through the ATUMS collaboration. All figures contained in this thesis were created by myself with the exception of Figure 4.2b-d. Much of the work was performed collaboratively, as detailed in the following.

The models for pulse propagation and THz generation presented in Chapter 2 were developed in part by C. Huang (CH) and D. Mildenberger as undergraduate research projects under my supervision. The theory and calculations in Chapter 3 were developed entirely by myself. To the best of my knowledge, the calculations involving higher-order angular dispersion and the prism-grating pair for spatiotemporal pulse-shaping have not been addressed in the literature and a modified version of this material will be submitted for publication at a later date. Moreover, the potential of tilted-pulse front THz generation in GaN and the calculations in this section have not been discussed in the literature, to the best of my knowledge. Additional work on this project towards the fabrication of a grating on GaN has been performed by Andreas Zeidler (AZ), Felix Eckmann (FE), and Theresa Hoffman.

The work in Chapter 4 on the development of THz sources in the Ultrafast Nanotools lab was highly collaborative. The Gen. 1 source was initially constructed by A. Ayesheshim. The Gen. 2 source was initially constructed with guidance from L. V. Titova (LT) and FH in my MSc and extensively modified in my doctoral work, which is detailed in this thesis. The purge box was constructed with the assistance of

B. Shi. The narrow band nonlinear dynamics experiments were conceived by myself and FH while data acquisition was performed by myself and S. Xu. The Gen. 3a source was constructed by C. Huang (CH), C. M. Hough (CMH), and myself. The cylindrical zoom lens was conceived by myself and constructed with the assistance of CH. The study of Kapton tape as an AR coating was performed by myself.

The work in Chapter 6 is an extension of results from my MSc thesis. Preliminary work was completed in collaboration with M. Na and A. Longman. Part of the material has been published in Applied Physics Letters (DOI: 10.1063/1.5009470). Data acquisition for this work was performed in part during my MSc studies and is labeled as such where relevant. The data in InP was acquired with the assistance of CH and feedback from M. A. B. Narreto. All interpretations and modeling was entirely by myself as part of my doctoral work with guidance from FH and LT.

A version of chapters 7 and 8 has been published in Advanced Materials (DOI: 10.1002/adma.202100978). This project was conceived by myself and E. Üzer (EU) and expanded with input from C. Ott (CO) and M. R. P. Pielmeier (MP). Raman and XRD measurements were performed on my behalf by A. Vogel (AV) and A. Degg (AD), respectively, while interpretation and data analysis was performed by myself. Materials growth was performed in part by myself with assistance from CO and EU. Samples for initial TRTS measurements were provided by EU and the primary sample for HIM and TRTS was synthesized by CO. PDS measurements were performed with the assistance of AZ and FE in the lab of Professor Martin Stutzmann. The photoluminescence spectra and Rietveld refinement calculations were provided by T. Nilges. DFT calculations were performed on my behalf by MP while extended analysis of the calculations was performed by myself with feedback from MP. TRTS data was acquired by myself and Naaman Amer (NA) while analysis and interpretation of these results were performed by myself with feedback from Charles Jensen and NA. FH and TN provided extensive guidance and feedback in all stages of this work.

To my grandfather,

Norman Purschke, 1929-2021

Acknowledgements

I would like to begin by thanking my parents, Eunice and Garry, have been my most consistent supporters. I would especially like to thank my partner, Tatiana. Tata, you have loved, supported, and encouraged me through it all. I am lucky to have you.

Funding for equipment used in this work was provided by the Canada Foundation for Innovation, iCore, the Natural Sciences and Engineering Research Council of Canada (NSERC), Alberta Innovates Technology Futures (AITF), the AITF Strategic Chairs Program, and the University of Alberta. My own funding was provided through the Queen Elizabeth II Scholarship, the Alberta Graduate Excellence Scholarship, the Doctoral Recruitment Scholarship, teaching assistant positions primarily with undergraduate labs, the NSERC Discovery Grant Program and the NSERC CREATE grant for the Alberta/Technical University of Munich International Graduate School for Hybrid Functional Materials (ATUMS), and by the Willa and Stuart B. Woods Graduate Scholarship in Physics.

I am grateful to my current and former colleagues Vedran Jelic, Peter Nguyen, Ayesheshim Ayesheshim, Zhenyou Wang, Alex Marin-Calzada, Howe Simpson, Glenda de los Reyes, Nils Refvik, and Aran McDowell. I owe special thanks to my colleagues Mary Narreto and Charles Jensen, with whom I collaborated with a great deal. Finally, I would like to thank my colleague Cameron Hough, who has been my closest collaborator over the years. I would like to thank former undergraduates Daniel Mildenberger, Patricia Jule Oliva, Hannah Louis, Christopher Mannes, and Haille Sharum. I would especially like to thank former undergraduates Ketty Na and Chenxi Huang. I would also like to thank former postdocs Yang Luo and Tianwu Wang and former research associates Naaman Amer and Lyuba Titova, who taught me a great deal. I am also grateful to several visiting researchers including Hannah Schamoni, Josef Mock, Shujuan Xu, and Naotaka Yoshikawa.

From the University of Alberta I would like to thank Professors Joseph Maciejko and Rick Sydora, who have sat on my supervisory committee, Professors Frank Marsiglio, Mark Freeman, Carsten Krauss, and Don Page. I also extend my gratitude to the Undergraduate Laboratory team of Taylor Rogers, Lorne Roth, Kyle Foster, and William Morrish. I would also like to thank Sarah Derr, Kailey Robertson, and Rae Beaumont for administrative assistance and Beipei Shi, Greg Popowich, and James Chaulk for technical support. I would also like to thank to my former colleagues Jens Boos and Mason Protter for organizing student seminars and Joel Hutchinson, Brad Hauer, and Hugh Ramp for stimulating discussions, and my former colleagues from the Graduate Physics Students Association.

From the Laboratory for Laser Energetics, I owe thanks to Dustin Froula, Greg Jenkins, John Palastro, Jake Bromage, and Khanh Linh Nguyen. From NORCADA, to Hooman Hosseinkhannazer and Yeubin Ning. From the University of Northern British Columbia, to Matt Reid for use of his thermal imager and Patrick Kilcullen.

From the ATUMS collaboration I would like to thank Professors Jon Veinotand and Bernhard Rieger for starting the collaboration, Professors Al Meldrum and Karthik Shankar for stimulating discussions, and Leah Veinot and Sergey Vagin for administrative assistance. I would also like to thank my colleagues at the Walter Schottky Institute Andreas Zeidler, Felix Eckmann, Hannah Schamoni, and Theresa Hoffman, and my colleagues from the chemistry department Ebru Üzer, Claudia Ott, Markus Pielmeir, Annabelle Degg, and Anna Vogel.

I would like to thank the hosts of my German research exchanges, Professors Tom Nilges and Martin Stutzmann. To Martin, I am grateful for my time in your lab as I always learned a great deal from conversations with you and your group. To Tom, I am greatly indebted to you for welcoming me into your group and teaching me a great deal about solid-state chemistry. I am especially grateful to you for your guidance as my co-supervisor within the ATUMS joint PhD program.

Finally, and most importantly, I would like to thank my supervisor Professor Frank Hegmann. Frank, you pushed me to question every aspect of the problem at hand (as one should), which pushed me to develop a much deeper and broader understanding of physics. I am grateful for everything you taught me.

Table of Contents

List of Tables

List of Figures

List of Acronyms

AD angular dispersion

ALS asymmetric least squares

APD avalanche photodiode

AR anti-reflection

BZ Brillouin zone

CBM conduction-band minimum

CEP carrier-envelope phase

CPKS coupled-perturbed Kohn-Sham

DC direct current

DFG difference-frequency generation

DFT density-functional theory

DNA deoxyribonucleic acid

DOS density of states

EFL effective focal length

EM electromagnetic

EMA effective-mass approximation

EO electro-optic

EOS electro-optic sampling

FEL free-electron laser

FFT fast Fourier transform

FTIR Fourier-transform infrared

FWHM full width at half maximum

GDD group-delay dispersion

GVD group-velocity dispersion

HIM helium-ion microscopy

HSE Heyd–Scuseria–Ernzerhof

IR infrared

LN lithium niobate

LO longitudinal optical

LST Lyddane-Sachs-Teller

MDT minimum-duration tilt

NIR near infrared

OPA optical parametric amplifier

OR optical rectification

PBE Perdew–Burke-Ernzerhof

PDS photothermal-deflection spectroscopy

PFT pulse-front tilt

PL photoluminescence

RCWA rigorous coupled-wave analysis

SFG sum-frequency generation

SRH Shockley-Reed-Hall

TDS time-domain spectroscopy

THz terahertz

TO transverse optical

TOD third-order phase

TPF tilted-pulse front

TRTS time-resolved terahertz spectroscopy

UNL Ultrafast Nanotools Lab

USP ultra-short pulse

UV-Vis ultraviolet-visible

VBM valence-band maximum

vdW van der Waals

XRD x-ray diffraction

Chapter 1

Introduction

1.1 Materials Science and Modern Technology

The role of materials in technology is paramount, for example a modern microprocessor contains more than 60 elements [1]. In the last century, rapid technological progress has been facilitated by an increasingly diverse range of materials available to scientists and engineers [2]. Today, materials science is an enormous interdisciplinary field of utmost importance to solving many challenges facing humanity, ranging from the climate crisis [3] to quantum computing [4]. As important as the development of new materials, as well as the improvement of existing ones, is the ability to characterize their properties and understand the fundamental physical processes underlying their behavior [5]. Shown in Figure 1.1 is a visualization of the workflow of innovation in materials science, illustrating the interplay between synthesis, characterization, and application along the path to real-world applications. Highlighted in this flowchart is the step of probing the basic materials physics, which is the central theme of this thesis with a focus on the exploration of new materials and the development of new techniques.

Semiconductors are one of the most important classes of materials. This is reflected in both the range of applications, from microprocessors to solar cells, and the market cap: direct revenue in the semiconductor industry in 2020 was over 430 Billion USD. Moreover, computers, which would not be possible without the semiconductor transistor, are an integral part of virtually all facets of modern society. Despite the incredible focus on research and development in this field, there remains

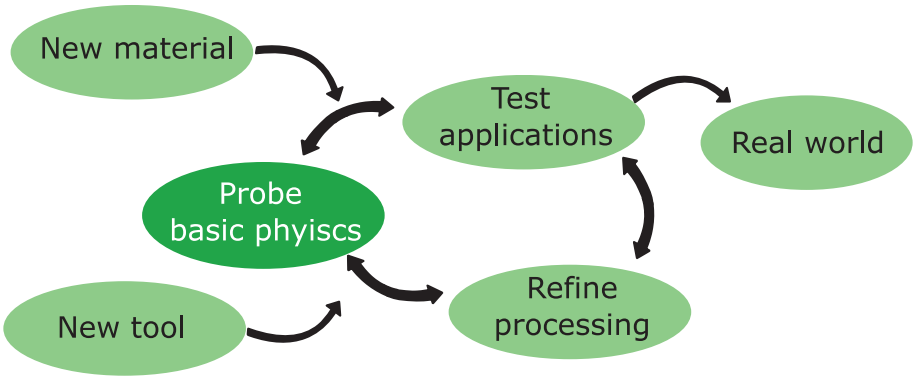

Fig. 1.1: Innovation cycle in materials science. Development of materials involves a complex interplay between new-material discovery, testing applications, refining synthesis and processing to achieve a desired function, and probing of the underlying fundamental physics, with the ultimate goal of reaching real world applications. This work is concerned primarily with the problem of probing the underlying physics, which is highlighted in the flowchart.

a steady push to develop both new spectroscopic probes to better understand the chemical, electronic, and vibrational properties of standard materials such as silicon and gallium arsenide and to develop new semiconductor materials with complementary properties. One of the most useful tools for characterizing optical, vibrational, and electronic dynamics in semiconductors is ultrafast spectroscopy. More specifically, ultrafast terahertz (THz) spectroscopy is the most powerful tool available to directly probe and drive transport phenomena on subpicosecond timescales. Here, this capability will be exploited to reveal a new window into the relaxation dynamics in the well established III-V semiconductor class and also to provide deep insight into the transport and photophysics in the exciting new material SnIP.

1.2 Why Ultrafast?

The development of laser technology over the last several decades has resulted in an incredible range of techniques to generate, manipulate, and control light. As this field expanded, researchers began to push to shorter pulse duration [6] and higher intensity [7]. The two enabling technologies for much of this development were modelocking and chirped-pulse amplification. Ultrafast lasers have helped drive innovation in fields as diverse as laser fabrication [8], precision metrology [9], biomedical optics [10], nuclear fusion [11], and materials science [12].

For applications in materials science, it is natural to question the importance of probing on such remarkably short timescales. In Figure 1.2, we illustrate the timescale associated with a variety of electronic, optical, and vibrational processes. Clearly, in order to capture the time evolution of processes in materials, which is critical to understanding their behavior, ultrafast lasers are an indispensable tool.

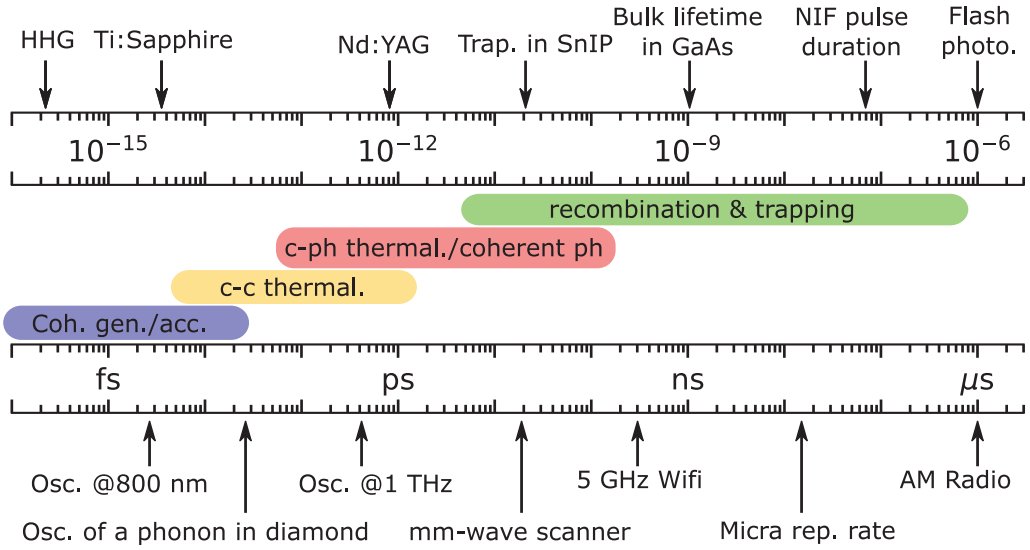

Fig. 1.2: Ultrafast Timescales. In the middle: An estimate of the electronic/vibronic processes occurring on various timescales. As a rough criteria, timescales less than approximately tens to hundreds of picoseconds, which are difficult to probe with conventional electronics, are considered ultrafast. Along the top, the timescale of pulse duration for various types of laser/light sources is indicated. The trapping time in SnIP, a material important in this work, is also indicated on this plot along with the bulk lifetime in GaAs, one of the most important optoelectronic materials. Along the bottom, timescale of the oscillation period of several important wavelengths of light. Here, the term Micra rep. rate refers to the repetition rate of the laser oscillator in the Ultrafast Nanotools Lab.

1.3 What is Terahertz Spectroscopy?

More than just requiring faster light sources to probe dynamics in materials, the frequency of light dictates the nature of the excitations that are probed. Shown in Figure 1.3 is the electromagnetic (EM) spectrum, from microwaves to ultraviolet, along with a rough classification of the types of excitations in each frequency range for a hypothetical solid.* To date, ultrafast laser sources with suitably high power

*These classifications were adapted from Fox, ref. [13].

pulse duration exist with only a relatively small number of different center frequencies. One of the frontiers in ultrafast optics is therefore bringing ultrafast optics to new frequency bands. This can be done either by introducing new laser sources or, alternatively, by using nonlinear optics to perform frequency conversion.

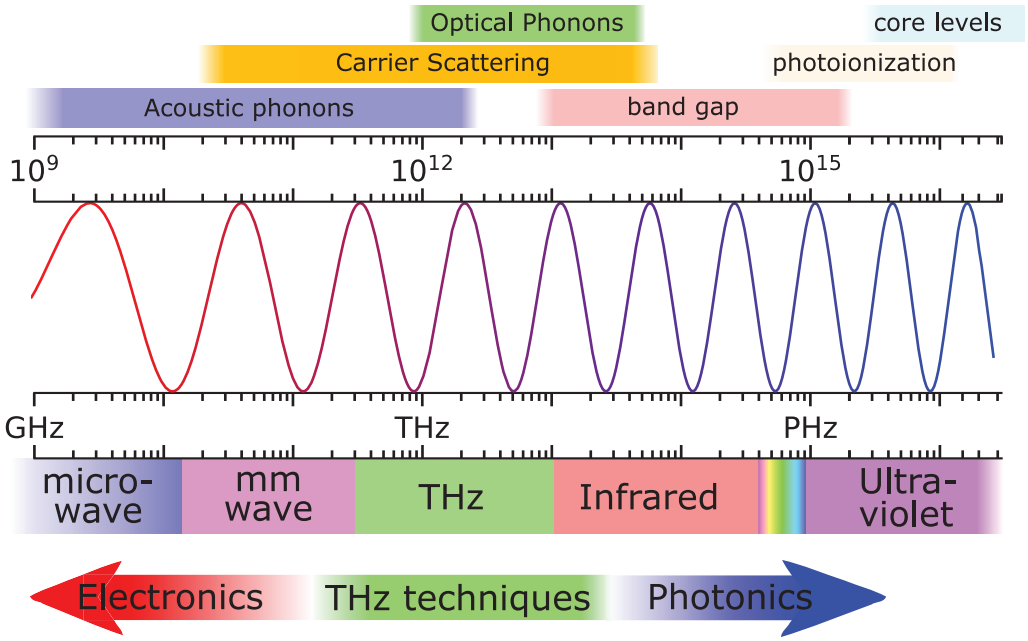

Fig. 1.3: The electromagnetic spectrum. The various bands of the electromagnetic spectrum are indicated. The THz part of the spectrum, between 0.3 and 10 THz, is indicated in green and is located between the microwave/mm wave and infrared portions of the spectrum. In this region, a unique set of technologies was developed to complement the conventional electronics and photonics technologies. Along the top, the frequency scale of fundamental excitations in semiconductors are listed. The labels of the top axis are in units of Hz.

In the THz region of the EM spectrum, both conventional optics and electronics based radiation sources based are inefficient. For this reason, the area between approximately 0.3 and 10 THz was historically known as the THz gap. A variety of tools relying on photoconductive and electro-optic (EO) processes were developed to fill this gap and today a variety of sources and detectors exist that have essentially filled the gap. THz pulses with more than a decade of bandwidth can be routinely generated, resulting in picosecond pulses with just a single cycle electromagnetic transient oscillation.

Notably, the THz pulses generated from EO and photoconductive processes have

a stable carrier envelope phase, so that the electric field waveform from shot to shot is the same. Moreover, the half-cycle duration of, *e.g.*, a 1 THz field is 500 fs, which is significantly longer than the duration of typical ultrafast laser pulses, facilitates the stroboscopic sampling of the electric field as a function of time delay, as shown in Figure 1.4a. This facilitates time-domain spectroscopy, where the discrete Fourier transform of the waveform gives access to spectral information. This is highlighted in Figure 1.4b, which shows the fast Fourier transform (FFT) of the waveform from Figure 1.4a and reveals characteristic water-vapor absorption lines.

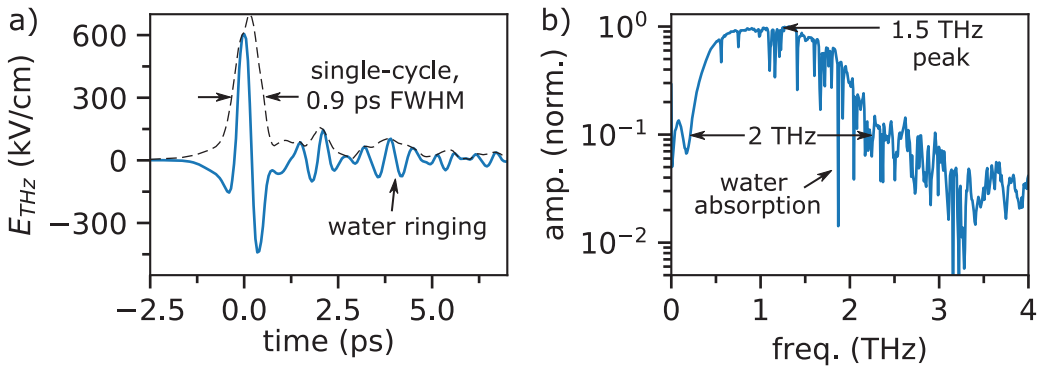

Fig. 1.4: Picosecond THz pulses. **a** A single-cycle THz pulse measured in the time domain with a peak electric field at focus over 600 kV/cm. The dashed line indicates the envelope of the THz pulse. **b** The corresponding amplitude spectrum from the discrete Fourier transform, with frequencies ranging from 0.1 to 3 THz and several characteristic dips from water vapor absorption lines.

The phase-resolved measurement of the electric field is especially useful for spectroscopy, as it allows one to extract both the real and imaginary part of the optical constants directly without the need to resort to Kramers-Kronig relations. Another powerful aspect of THz spectroscopy is the sub-picosecond temporal resolution that comes along with the coherent detection as measurements are not limited by the pulse envelope as with conventional ultrafast probes. These principles are illustrated in Figure 1.5a and b, where we plot the differential THz transmission as a function of time delay and the conductivity spectrum 4 ps after photoexcitation, respectively. The temporal resolution of the measurement in Figure 1.5a is high enough to resolve the carrier cooling*, which delays the rise time to the peak of the differential trans-

*Or, more relevant to this work, the temporal resolution is sufficient to probe the trapping and recombination of carriers in new materials with high trap densities.

mission. Simultaneously, the spectral bandwidth of the conductivity measurement in Figure 1.5b is large enough to extract the carrier scattering time, which gives access to the mobility on picosecond timescales. These capabilities make THz spectroscopy a powerful tool for exploring ultrafast photocarrier dynamics in energy materials, a field of extreme importance to current challenges faced by humanity.

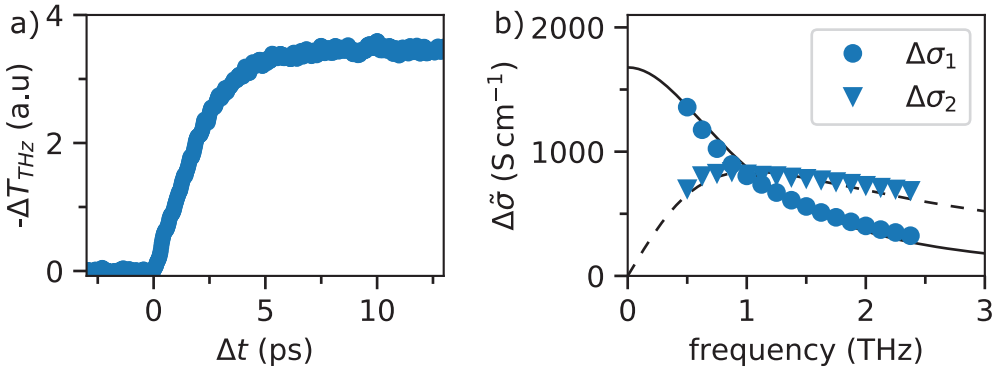

Fig. 1.5: Time-resolved THz spectroscopy. **a** Onset of the photoconductivity in germanium after excitation with a femtosecond laser pulse with sub-picosecond time resolution. The rise time of several picoseconds is in this case limited by carrier-cooling dynamics. **b** Complex conductivity spectrum acquired approximately 30 ps after photoexcitation overlaid with a Drude fit. The carrier scattering time can be read directly from the crossover point of the real and imaginary components, in this case yielding a scattering time of 153 fs.

Exploration of new materials remains one of the most important frontiers of THz spectroscopy [14]. Moreover, similar to the push to higher intensities with ultrafast lasers, the recent development of table-top strong-field THz sources enabled a revolution in the field of nonlinear THz dynamics [15, 16, 17]. New types of spectroscopies probing nonlinear THz dynamics have yielded a great deal of insight into the fundamental properties of light and matter [18] and remains a thriving field today [19, 20]. The work presented in this thesis contributes to each of these three areas through the development of strong-field THz pulse sources based on tilted-pulse-front (TPF) optical rectification (OR), the application of intense THz pulses to drive hot-carriers in semiconductors, and finally the study of ultrafast photophysics in the exciting new material tin iodide phosphide (SnIP).

1.4 Thesis Outline

Chapter 1 begins with an introduction to the field of ultrafast THz science and applications to materials science, Chapter 2 provides a theoretical basis for THz pulse generation, propagation, and coherent detection. The theory of optical rectification is developed in detail, providing a basis for understanding the studies of TPF THz generation.

Chapter 3 details the use of pulse-front tilt (PFT) as a tool in nonlinear optics and closely examines the correspondence between PFT in the time domain and angular dispersion (AD) in the frequency domain. A detailed consideration shows that the usual equation governing this correspondence, which accounts for first-order AD, fails to capture the full spatiotemporal intensity of a tilted-pulse front. The theory of spatiotemporal coupling in the plane-wave approximation to arbitrary order in the AD, and therefore pulse-propagation dynamics, is developed and a novel technique is discussed that could enable new types of spatiotemporal control of pulse propagation. Moreover, the conditions in which the 2D problem of TPF THz generation can be formally mapped to 1D are discussed and the expected THz pulse spectrum from lithium niobate is calculated. Finally, the design of a novel TPF THz source based on a surface relief grating in GaN is presented that could enable high-power THz generation in the 5-12 THz gap, which remains one of the more underdeveloped regions of the THz gap [21].

Chapter 4 discusses the development of lithium niobate-based TPF THz sources in the Ultrafast Nanotools Lab over the last several years. It introduces several modifications to the TPF and THz optics used to increase the source performance, culminating in the most recent design that demonstrated peak electric fields exceeding 600 kV/cm. It also discusses several minor modifications to the sources, such as a Kapton tape based antireflection coating, a dry-nitrogen purge box and the effect of water absorption lines, and the exciting potential for these sources in narrow band nonlinear dynamics.

The second part of the thesis, involving applications of ultrafast THz spectroscopy to materials, begins in Chapter 5. The fundamentals of semiconductor dynamics and

ultrafast excitation relevant for understanding the exploration of semiconductor photoluminescence (PL) in GaAs and carrier transport in SnIP are developed. Chapter 6 discusses the modulation of semiconductor PL with intense THz pulses, THz-ΔPL [22], which is shown to arise by THz-driven carrier heating. An intense THz pulse coincident with a photoexcitation pulse in direct-gap semiconductors simultaneously quenches near-gap PL and enhances PL from the high-energy luminescence tail. An effective model for this phenomenon based on THz-field-induced carrier heating and diffusion is introduced and is shown to simultaneously capture both the PL quenching and enhancement with a single free parameter, the initial hot-carrier temperature. This work provides a framework for understanding THz-ΔPL that could be useful in a variety of direct-gap semiconductors. Additionally, it provides a new window into hot-carrier physics in semiconductors and highlights a new method of ultrafast control over carrier dynamics.

Finally, chapters 7 and 8 detail studies of the recently discovered tin iodide phosphide (SnIP), the first inorganic double-helix semiconductor. This interesting material has extraordinary mechanical properties and has shown promise for water splitting, suggesting it could find application in flexible electronics or photocatalysis, however, to date, relatively little is known about its optoelectronic properties. Chapter 7 discusses the synthesis of SnIP nanowire thin films and characterizes their optical properties, crystallinity, electronic structure, and infrared active (IR) vibrational modes using a variety of experimental probes along with quantum chemical calculations. Chapter 8 presents a comprehensive exploration of SnIP using time resolved THz spectroscopy (TRTS) [23]. As the first ultrafast optical study of any kind in SnIP, these results provide enormous insight into the photophysics and transport properties in this material. These results suggest that elimination of bulk defects could significantly increase the photocatalytic activity in SnIP. Most importantly, we extract a carrier mobility that is remarkably high for such a soft and flexible material, which highlights the potential of SnIP as a new material for flexible electronics.

Chapter 2

Terahertz Generation, Propagation, and Detection

2.1 Historical Perspective

In this chapter, the fundamentals of terahertz (THz) pulse generation, propagation, and detection are developed in detail, however, we begin with a brief historical note on THz science and technology. The exposition of the THz field begins almost as early as the field of nonlinear optics [24, 25, 26], which itself was facilitated by the first demonstration of the laser in 1960[27].[†] Before the laser, investigations of light-matter interaction had been performed almost exclusively in the linear regime, *i.e.*, low enough intensity that the potential-energy surface explored by light-driven charges was parabolic. The first demonstration of difference-frequency mixing was reported in 1965 in what can be considered the first example of THz generation by OR [29].[‡] Several years later, generation of far-infrared radiation from more stable picosecond pulses was achieved in lithium niobate (LN) in a configuration closer to that used today [30]. More familiar THz crystals were used in 1973 with difference frequency generation in ZnTe using dye lasers and a generation scheme quite similar to a modern THz spectrometer [31].

[†]Interestingly, Maiman, who first observed lasing on May 29, 1960, initially planned to publish his results in Physical Review, however, his manuscript was rejected. Instead, he announced his work in a press release in July and within weeks, his results had been duplicated by several groups [28]

[‡]At this time, this was referred to as far-infrared generation as the THz classification did not come along until several years later.

Over the next decade, development of ultrafast laser technology and nonlinear optics progressed steadily, however, early progress in the THz region did not. The radiation generated in these early experiments was detected incoherently with liquid-helium cooled bolometers and weak enough that it was not useful for far-infrared spectroscopy. While there was some interest in optical generation of fast electronic pulses analogous to THz methods of today [32, 33, 34], it was not until the mid 1980's that significant progress was made on THz pulse generation and detection as we know it today. In 1984, Auston reported the *in situ* electro-optic sampling (EOS) of a THz pulse in lithium tantalate, producing perhaps the first example of a THz waveform and corresponding Fourier amplitude spectrum familiar in modern research [35]. The field grew enormously in the subsequent years with the development of time-domain [36] and time-resolved [37] THz spectroscopy and innovations such as free-space EO sampling [38]. In the mid 2000's, another revolution in the field occurred with the development of table-top high-intensity THz sources [15, 16], which facilitated studies of nonlinear optics in the far-infrared. Today, the THz region of the spectrum remains a thriving area of research with applications in (but not limited to) materials science [39], communications [40], medicine [41], security [42], and industrial applications [43].

2.2 Electromagnetic Wave Equation

To understand the fundamental physics of THz generation essentially amounts to studying how optical nonlinearities in materials act as sources of electromagnetic radiation. Our starting point is the wave equation in matter,

$$\nabla^2 \mathbf{E} - \mu_0 \epsilon_0 \partial_t^2 \mathbf{E} = \mu_0 \left(\partial_t \mathbf{J} + \partial_t^2 \mathbf{P} \right), \tag{2.1}$$

where $\mathbf{E}$ is the electric field, μ_0 and ϵ_0 are the vacuum permeability and permittivity, respectively, $\mathbf{J}$ is the free current density, and $\mathbf{P}$ is the polarization.* The terms on the right can be generally categorized as current sources and polarization sources, which couple to the electric field at the level of their first and second derivatives,

*To get to this point requires the approximation that that the gradient of the charge density is zero [44], which arises from the relationship $\nabla \times \nabla \times \mathbf{E} = \nabla(\nabla \cdot \mathbf{E}) - \nabla^2 \mathbf{E}$. From Gauss' law, $\nabla \cdot \mathbf{E} = \rho/\epsilon_0$, if the gradient of the charge density is zero the first term on the right-hand side is zero.

respectively. From here, we can already see why accelerating charges emit radiation while static, *i.e.*, constant velocity so that $\partial_t \mathbf{J} = 0$ and $\partial_t^2 \mathbf{P} = 0$, do not radiate.

Solution of this equation for arbitrary geometry and material response requires sophisticated numerical techniques and is a field of physics and engineering unto itself, known as computational electromagnetics. However, we can gain a great deal of insight into the problem of THz generation using simplified models. First, we rewrite the wave equation in the frequency domain,

$$\nabla^2 \tilde{\mathbf{E}} + \omega^2 \epsilon_0 \mu_0 \tilde{\mathbf{E}} = \mu_0 (-i\omega \tilde{\mathbf{J}} - \omega^2 \tilde{\mathbf{P}}), \tag{2.2}$$

where the bold face indicates a vector quantity and the tilde is used to indicate a complex quantity in the frequency domain. This equation holds two key insights into the difference between current sources and polarization sources. First, the factor of i indicates that the emission from current sources is ninety degrees out of phase with respect to the emission from polarization sources.* Second, the polarization source term has an extra factor of frequency in comparison to the current source term. This has a direct effect on the THz spectrum of optical-rectification based sources, which are more efficient at higher frequencies, as opposed to photoconductive sources, which are more efficient at low frequencies.

To further simplify the equation, we assume translational symmetry in the y and z directions and move to a reference frame travelling at velocity c/n_g, where c is the speed of light and n_g is the group velocity, with the substitution $\tilde{\mathbf{E}} = e^{in_g k_\omega x} \tilde{A}\, \hat{\mathbf{z}}$,

$$\partial_x^2 \tilde{A} + 2in_g k_\omega \partial_x \tilde{A} + k_\omega^2 (1 - n_g^2) \tilde{A} = \mu_0 \left(-i\omega \tilde{J} - \omega^2 \tilde{P} \right) e^{-in_g k_\omega x}, \tag{2.3}$$

where k is the terahertz wave vector, $\tilde{A}$ is the spatially varying amplitude coefficient, and we have dropped the bold-face type for the current and polarization assuming they also obey y and z translational symmetry. At this point, equation 2.3 is still agnostic regarding origin of the electromagnetic source. In the next section we will specialize it to polarization sources based on OR, which is the nonlinear optical process most relevant to this work.

*This can be understood intuitively if we think of an oscillating bound charge, where the polarization is proportional to the position and the current is proportional to the velocity.

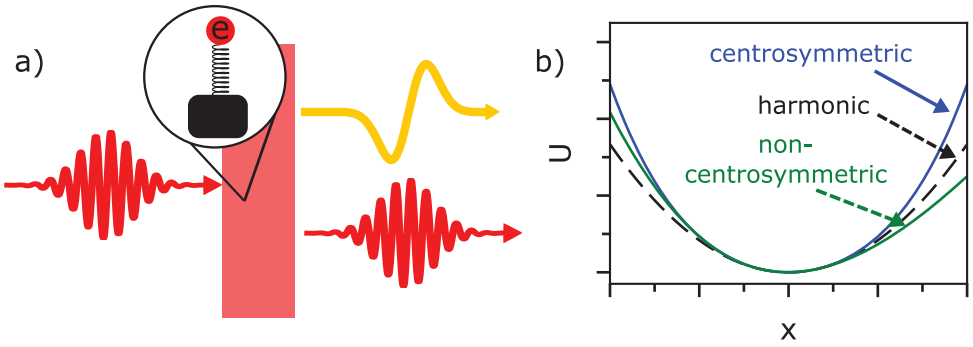

Fig. 2.1: Principle of Optical Rectification in Nonlinear Crystals. **a** Schematic layout of the THz generation layout. An optical pulse is incident on a crystal with bound electrons that can be considered microscopically as oscillators. **b** Illustration of the potential landscape experienced by the electron for a harmonic potential (black dashed line , $U = ax^2$) as well as for anharmonic centrosymmetric (blue line, $U = ax^2 + bx^4$) and non-centrosymmetric (green line, $U = ax^2 + bx^3$) potentials. The non-centrosymmetric potential is required for THz generation by optical rectification.

2.3 Optical Rectification of Femtosecond Pulses

2.3.1 Nonlinear Polarization

In this section, we will assume there are no free charges so that the current source is zero. The problem of an ultrafast laser pulse interacting with electrons in a material to emit a THz pulse is shown in Figure 2.1a. We can consider the material to be composed of a field of oscillators that, in the absence of an applied field, are in equilibrium so that the potential, $U(z)$, can be expanded with the lowest order term being quadratic.* We can calculate the trajectory of an electron in such a potential from the equation of motion [45],

$$\frac{d^2z}{dt^2} + \gamma\frac{dz}{dt} + \frac{dU}{dz}z = eE(t), \tag{2.4}$$

where e is the elementary charge, $E(t)$ is the applied electric field, and γ is a phenomenological damping that drives the system back to equilibrium. To see how the polarization, $P = ez$, behaves in this simple picture we consider three different functional forms for the potential: a harmonic potential (quadratic), an anharmonic centrosym-

*The equilibrium potential, a constant, does not affect the dynamics. Additionally, in this section we assume the field is applied in the z direction.

metric potential (quadratic plus quartic), and anharmonic non-centrosymmetric potential (quadratic plus cubic), as shown in Figure 2.1b.

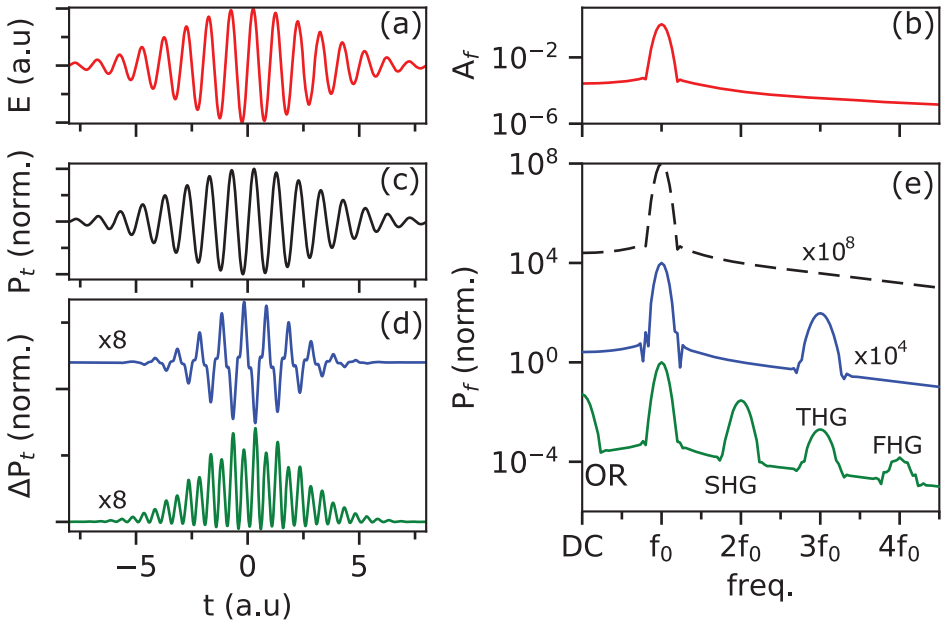

Fig. 2.2: Nonlinear polarization induced by an ultrafast pulse. Applied optical field in **a** the time domain and **b** the frequency domain. **c** Time-dependent polarization for the harmonic potential. **d** Difference between the anharmonic polarization and the harmonic polarization for the centrosymmetric (blue) and non-centrosymmetric (green) cases. **e** The discrete Fourier transforms of the nonlinear polarizations. The optical rectification term responsible for THz generation peaks at DC and rolls off as a function of frequency on a logarithmic scale. Here, OR refers to optical rectification and SHG, THG, and FHG second, third, and fourth harmonic generation, respectively.

With a Gaussian pulse for $E(t)$,* as shown in Figure 2.2a with the corresponding amplitude spectrum in Figure 2.2b, we can easily solve the equation of motion in equation 2.4 for the three different potentials to study the polarization. The time-dependent polarization in the harmonic potential, shown in Figure 2.2c, follows the oscillations of the applied field. Introducing anharmonicity modifies the resulting time-domain polarization in what appears to be a complex, as seen in Figure 2.2d where the difference between the calculated polarization for the anharmonic potentials from the harmonic potential is plotted.

While the time-domain structure looks complex, things are much simpler in the

*Here, the term Gaussian pulse refers to a sin wave modulated by a Gaussian envelope.

frequency domain as shown by the discrete Fourier transforms of the polarizations in Figure 2.2. Here, the polarization in the harmonic potential (black dashed line) is proportional to the driving field amplitude, *i.e.*, the response is linear. Conversely, the polarization in the centrosymmetric anharmonic potential, while peaked at the driving field frequency, develops an additional lobe at the third harmonic. The polarization in the non-centrosymmetric anharmonic potential is even more exciting as it develops lobes peaked at DC (optical rectification), as well as at the second, third, and fourth harmonics.* Recalling equation 2.2, where the polarization acts as a source term in the wave equation, the polarizations at new frequencies in Figure 2.2e imply that a driving field can generate new frequencies of light. It also shows that inversion asymmetry is a requirement for THz generation crystals. This can be seen with a symmetry argument as follows. In the centrosymmetric case, because $U(x) = U(-x)$, $P(E) = -P(-E)$ so that the integral $\int dt P(t) = 0$ for a harmonic driving field, indicating the lack of DC polarization.

Instead of the time-domain approach to studying the polarization, which is useful to help develop intuition for the origin of nonlinearity, it is advantageous to start from a frequency-domain description. Rather than expanding the potential, the polarization can be expanded in powers of the driving field, which for a single field/polarization can be written as

$$P = \epsilon_0 \left(\chi^{(1)} E(\omega) + \chi^{(2)} E^2 + \chi^{(3)} E^3 + \cdots \right), \tag{2.5}$$

where the coefficients $\chi^{(n)}$ indicate the n^{th} order susceptibility. With $E = E_0 e^{i(kx-\omega t)} + c.c$, where $c.c$ indicates the complex conjugate, the polarization therefore contains all harmonics of the driving field, which explains the appearance of harmonics in the Fourier transform of the time-domain polarization. Moreover, in order to satisfy symmetry, $\chi^{(2)}$ (and all even susceptibilities) must be zero for centrosymmetric materials.† Assuming a non-centrosymmetric material, this can be generalized to second

*Of course this trend continues to all the higher harmonics; the spectrum is truncated here for illustrative purposes.

†The susceptibilities for the anharmonic potentials in Figure 2.1b can be extracted from perturbation theory as is discussed, for example, in Boyd Nonlinear Optics [44]. For real materials, they are usually measured experimentally, although they can sometimes be computed with reasonable accuracy using quantum-chemical calculations.

order to include multiple fields and polarizations with,

$$\frac{\tilde{P}_{i,\omega}}{\epsilon_0} = \chi^{(1)}_{ij}\tilde{E}_{j,\omega} + \int_{-\infty}^{\infty} d\omega_1 \int_{-\infty}^{\infty} d\omega_2 \chi^{(2)}_{ijk}\tilde{E}_{j,\omega_1}\tilde{E}_{k,\omega_2}\delta(\omega_1+\omega_2-\omega) + \cdots \tag{2.6}$$

were the Einstein summation notation is used and, following convention in nonlinear optics, there is no distinction between upper and lower indices and it is understood that the fields/susceptibilities are upper/lower indices where the susceptibilities are tensorial elements.* For example, $\chi^{(2)}_{xyz}$ is the proportionality coefficient from mixing fields in the y and z directions to create a polarization in the z direction. The Dirac delta term selects the pairs of applied fields that drive a polarization at frequency ω.

The nonlinear polarization, as in the second term in equation 2.6, is still quite general and can be specialized further to only include the difference-frequency generation (DFG) term as,†

$$\frac{\tilde{P}^{DFG}_{i,\omega}}{\epsilon_0} = \int_0^{\infty} d\omega_1 \int_0^{\infty} d\omega_2 \chi^{(2)}_{ijk}\tilde{E}_{j,\omega_1}\tilde{E}^*_{k,\omega_2}\delta(\omega_1-\omega_2-\omega). \tag{2.7}$$

and, assuming the different fields are derived from the same pulse so they have the same polarization, this can be further simplified to,

$$\frac{\tilde{P}^{DFG}_{\omega}}{\epsilon_0} = \int_0^{\infty} d\omega' \chi^{(2)}_{eff}\tilde{E}(\omega'+\omega)\tilde{E}^*(\omega'), \tag{2.8}$$

where $\chi^{(2)}_{eff}$ is the effective second order susceptibility based on the polarization of the pulse and the resulting polarization. The subscripts have been dropped as we now assume that the polarizations are known *a priori*. Finally, with a similar substitution as in the previous subsection, with $\tilde{\mathbf{E}} = e^{in_g k_\omega x}\tilde{A}\,\hat{\mathbf{z}}$, the DFG term becomes,

$$\frac{\tilde{P}^{DFG}_{\omega}}{\epsilon_0} = \int_0^{\infty} d\omega' \chi^{(2)}_{eff}\tilde{A}(\omega'+\omega)\tilde{A}^*(\omega')e^{in_g(k_{\omega'+\omega}-k_{\omega'})}. \tag{2.9}$$

For completeness, the SFG term can similarly be written as,

$$\frac{\tilde{P}^{SFG}_{\omega}}{\epsilon_0} = \int_0^{\infty} d\omega' \chi^{(2)}_{eff}\tilde{A}(\omega-\omega')\tilde{A}(\omega')e^{in_g(k_{\omega-\omega'}+k_{\omega'})}. \tag{2.10}$$

*Although it would appear that there are generally n^3 constants for the n^{th} order susceptibility, this number can be dramatically reduced by symmetry considerations [44].

†The nonlinear polarization generated by DFG within a femtosecond pulse is peaked at DC and rolls off, hence it is referred to as OR.

In addition to THz generation via DFG, in LN sources the THz field can coupled back to the optical pulse through cascaded nonlinear optical processes [46, 16, 47], which can be considered SFG and DFG processes mixing the optical and THz frequencies. Moreover, the detection of THz pulses via EO sampling can be considered as the generation of coherent sidebands via mixing optical and THz fields with DFG and SFG [48]. In this work, only the DFG processes that generate THz radiation are considered, *i.e.*, mixing frequencies within the optical pulse.

2.3.2 Pulse-Propagation Equation

The amplitude coefficients, $\tilde{A}$, are complex quantities with a phase and amplitude that evolves based on the complex refractive index in the generation crystal. Starting from equation 2.3, assuming there the current term is zero and separating the linear and nonlinear polarizations so that $\tilde{P} = \epsilon_0 \chi^{(1)} \tilde{A} e^{i n_g k_\omega x} + \tilde{P}_{NL}$, the propagation equation becomes,

$$\partial_x^2 \tilde{A} + 2 i n_g k_\omega \partial_x \tilde{A} + k_\omega^2 (\tilde{n}_\omega^2 - n_g^2)\tilde{A} = -\omega^2 \mu_0 e^{-i n_g k_\omega} P_{NL}, \tag{2.11}$$

where the complex refractive index at frequency ω is defined as $\tilde{n}_\omega^2 = \sqrt{\tilde{\epsilon_\omega}} = \sqrt{1 + \chi_\omega^{(1)}}$. With the slowly-varying amplitude approximation, where $\partial_x^2 \tilde{A} = 0$, which is valid when $\partial_x \tilde{A}$ does not vary rapidly in space, the pulse-propagation equation becomes,

$$2 i n_g k_\omega \partial_x \tilde{A} + k_\omega^2 (\tilde{n}_\omega^2 - n_g^2)\tilde{A} = -\omega^2 \mu_0 e^{-i n_g k_\omega} P_{NL}. \tag{2.12}$$

This is the form that will be used in the following section for THz generation. Following Agrawal [49], for the optical pulse propagation we approximate $\tilde{n}_\omega^2 - n_g^2 \approx 2 n_g (\tilde{n}_\omega - n_g)$, which is valid when $n_\omega \approx n_g$, define $\beta_g = n_g k_\omega$ and $\beta = n_\omega k_\omega$ so that the zero-order term becomes $\beta_g(\beta - \beta_g)$, and expand around the center wavevector, $k_0 \equiv k_{\omega_0}$ of the optical pulse,

$$\begin{aligned} \beta_g &= n_g k_0 + n_g(\omega - \omega_0)/c = n_g k_0 + v_g^{-1}(\omega - \omega_0), \\ \tilde{\beta} &= \tilde{\beta}_0 + (\omega - \omega_0)\tilde{\beta}_1 + \frac{1}{2}(\omega - \omega_0)^2 \tilde{\beta}_2 + \frac{1}{6}(\omega - \omega_0)^3 \tilde{\beta}_3 + \cdots, \end{aligned} \tag{2.13}$$

where $\tilde{\beta}_i = \left. \frac{\partial^i (\tilde{n} k)}{\partial \omega^i} \right|_{\omega_0}$. Noting that the group velocity is defined as $v_g^{-1} = \partial(nk)/\partial\omega = Re\,[\beta_1]$, we can write,

$$\tilde{\beta} - \beta_g = (\tilde{n} - n_g)k_0 + (\omega - \omega_0) Im[\tilde{\beta}_1] + \frac{1}{2}(\omega - \omega_0)^2 \tilde{\beta}_2 + \frac{1}{6}\tilde{\beta}_3 + \cdots. \tag{2.14}$$

With this substitution, equation 2.12 becomes,

$$\partial_x \tilde{A} = i\left[(\tilde{n}-n_g)k_0 + (\omega-\omega_0)Im[\tilde{\beta}_1] + \frac{1}{2}(\omega-\omega_0)^2\tilde{\beta}_2 + \frac{1}{6}(\omega-\omega_0)^3\tilde{\beta}_3 + \cdots\right]\tilde{A} + i\frac{\omega^2\mu_0 e^{-in_g k}}{2\beta_g}P_{NL}, \tag{2.15}$$

which is the pulse-propagation equation in the reference frame of the group velocity of the optical pulse. Assuming the nonlinear polarization at optical frequencies is zero, which is a good approximation in many cases involving THz generation,* this is a simple first order differential equation with the solution,

$$\tilde{A}(x) = \tilde{A}_0 \exp\left(i\left[(\tilde{n}-n_g)k_0 + (\omega-\omega_0)Im[\tilde{\beta}_1] + \frac{1}{2}(\omega-\omega_0)^2\tilde{\beta}_2 + \frac{1}{6}(\omega-\omega_0)^3\tilde{\beta}_3 + \cdots\right]x\right). \tag{2.16}$$

Each of these terms corresponds to a standard feature of pulse propagation in dispersive media, which highlights the usefulness of the wavevector expansion method, each of which illustrated in Figure 2.3a and b. The wavevector-expansion formalism is also applied in the following chapter discussing the propagation of angularly-dispersing pulses and will be useful for mapping the 2D tilted-pulse front THz generation problem to 1D.

The first term yields a constant phase shift with frequency that grows with propagation distance, which corresponds to a continuously evolving carrier-envelope phase due to mismatch between the group and phase indices (blue vs orange curves in Figure 2.3). For completeness, a linear phase with frequency would result in a propagation of the envelope (green curves in Figure 2.3), however, in this formalism we have moved to a reference frame traveling with the optical envelope. The second order term results in Gaussian broadening in time (red curves in Figure 2.3). β_2 is known as the group-velocity dispersion (GVD). The third term leads to cubic phase, which results in an asymmetric temporal envelope (purple curves in Figure 2.3) and β_3 is known as the third-order dispersion (TOD).

*This is true when the optical pulse intensities are insufficient to drive self-phase modulation and the THz field does not significantly couple back to the optical pulse. The second condition notably breaks down in the case of tilted-pule front THz generation in lithium niobate, however, the approximation made here still yields a great deal of insight into the problem.

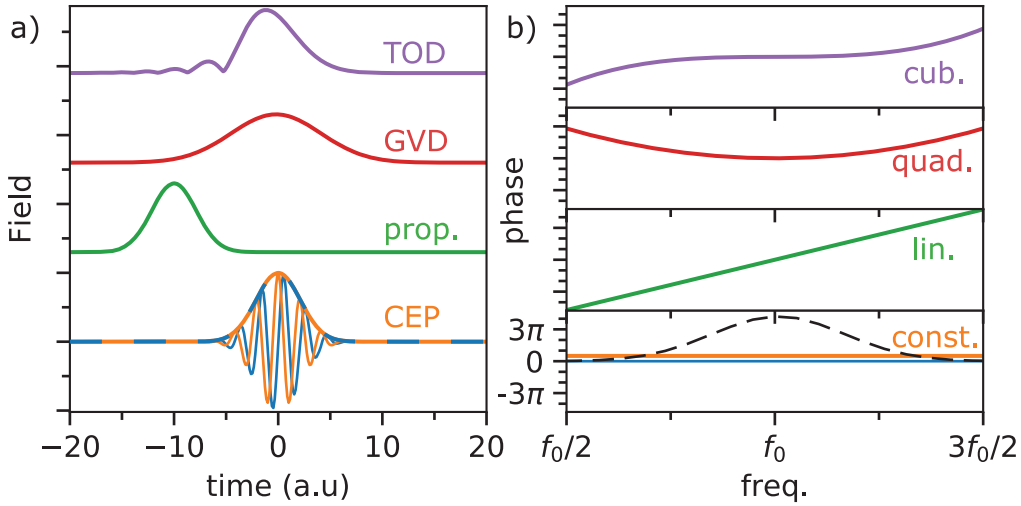

Fig. 2.3: Propagation effects in the wavevector expansion approach. **a** Electric field envelope for various functional forms of the phase as shown in **b**. Here TOD, GVD, prop., and CEP indicate the third-order dispersion, group-velocity dispersion, propagation, and carrier-envelope phase, respectively. The electric field itself is plotted for the blue (zero phase) and orange (phase=$\pi/2$) cases to highlight the changing carrier envelope phase. In **b**, the field amplitude, centered at f_0, is plotted as the dashed black line. These curves were calculated from a Fourier transform with a Gaussian envelope using an angular frequency of 3 and an e^{-1} point of 3. The phase shifts were applied in the frequency domain and an inverse Fourier transform was used to find the corresponding field. The envelope was calculated as the absolute value of the Hilbert transform.

2.3.3 Dispersion and the Nonlinear Polarization

In Figure 2.4 we study the effect of propagation in a ZnTe crystal up to the TOD term for several transform limited pulse durations. Here, the quadratic phase was minimized for the 1 mm point in the crystal, which is analogous to pre-compensating for GVD with the laser compressor. To exaggerate the effects of cubic phase and make it easier to visualize, the calculation propagates through 2 mm of crystal thickness in total, which is more than a typical experiment. However, in a real experiment there are typically multiple optical elements that contribute to TOD between the laser amplifier and THz generation crystal.

Figure 2.4**a-c** shows the time-domain envelopes for three different transform limit pulses. For the 90 fs pulse in **a**, the effect of propagation is minimal and the peak amplitude and pulse duration of the pulse at each location in the crystal is similar.

The effects of GVD are, however, highly nonlinear with minimum pulse duration and we see that for a 30 fs transform limit pulse, the pulse broadening is significant enough that the amplitude of the pulse with 1 mm of group-delay dispersion (GDD), which is second order phase, *e.g.*, the product GVD$\times x$ for an initially fully-compressed pulse propagating in a dispersive medium, is enough to reduce the amplitude by more than a factor of 4. This effect is even more pronounced for a 15 fs pulse.

Furthermore, we can see that cubic phase results in an asymmetric pulse shape. This effect is not visible for the 90 fs pulse and small for the 30 fs pulse, however, for the 15 fs pulse it becomes important. Again, we note that in typical experiments, there could be significant TOD in the optical elements preceding the THz generation crystal, so that it could be more important for both the 30 fs and 90 fs pulses. In each case, we have plotted the transform limit pulse (dashed black line) along with the orange curve in Figure 2.4**a-c**. If we focus on the orange curve in Figure 2.4**c**, we see that the pulse envelope develops multiple peaks and the peak intensity is significantly reduced with respect to the transform limit pulse. At the exit face of the crystal, the multiple peaks are no longer visible (green curve) and instead the result is an asymmetric pulse envelope.

We now focus on the effect of the GVD and TOD on the frequency-domain nonlinear polarization, which is shown in Figure 2.4**d-f** for the 90 fs, 30 fs, and 15 fs transform limit pulses, respectively. The range of the frequency axis is scaled separately in each case because the spectrum of the nonlinear polarization is much narrower for the longer pulse duration. Unsurprisingly, we see that the nonlinear polarization at each location in the crystal is essentially unchanged for the 90 fs pulse. Alternatively, we see that the roll off with frequency is much sharper at the entrance and exit faces of the crystal for both the 30 fs and 15 fs pulses with respect to the center of the crystal where the quadratic phase is minimized. The amplitude of the DC nonlinear polarization is unaffected by pulse broadening.*

We can also see the effect of the TOD in the frequency domain: the asymmetry of the pulse envelope maps to a frequency-dependent phase shift, *i.e.*, the angle of the

*This is a somewhat counter-intuitive result. One way to think about it is that because the DC term arises from mixing a single frequency with itself, the relative phase between frequencies should not matter.

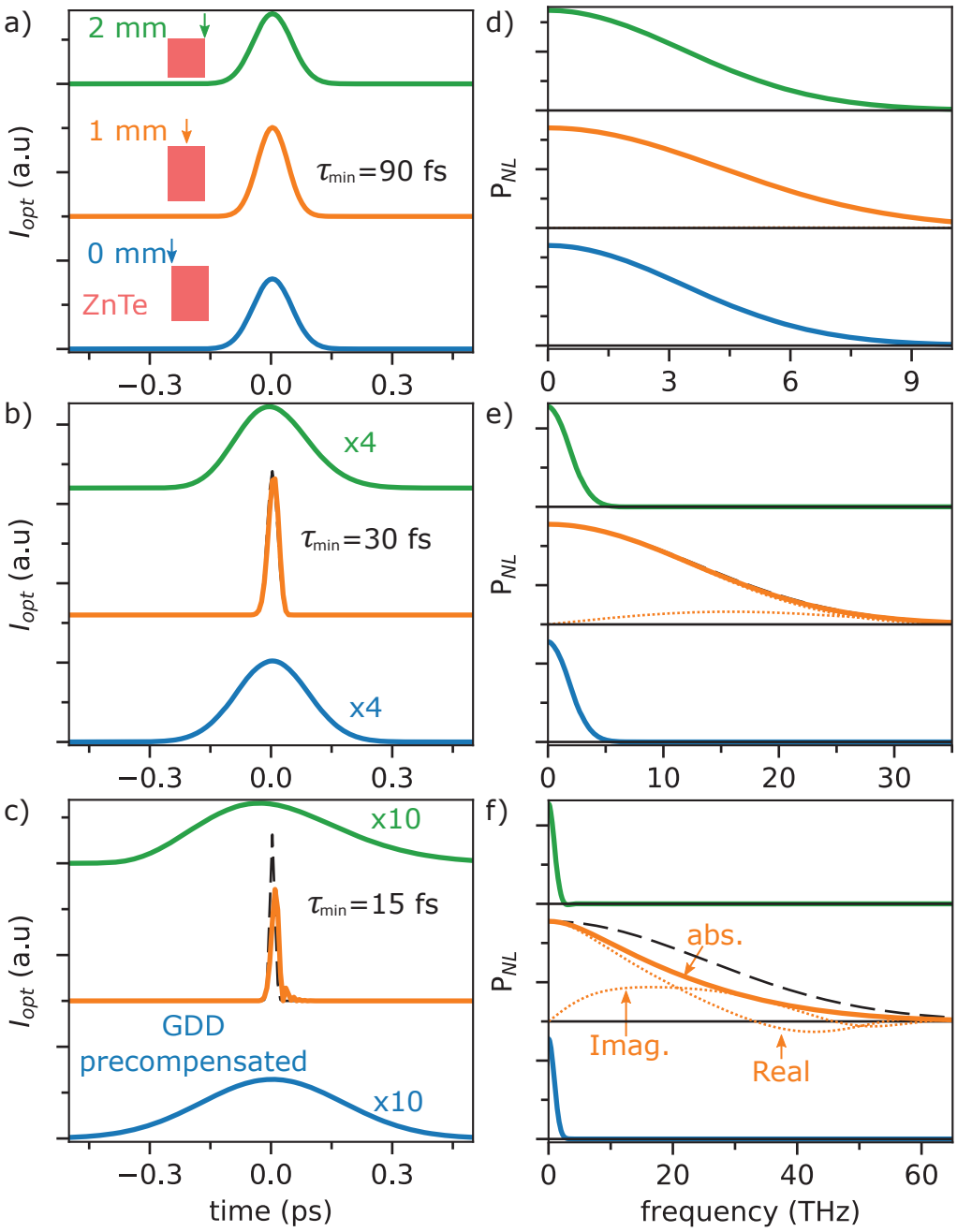

Fig. 2.4: Propagation effects on the nonlinear polarization from OR. Intensity envelope of an transform-limit **a** 90 fs **b** 30 fs and **c** 10 fs pulse for 3 different propagation distances in a ZnTe crystal up to the cubic (third order) phase. As indicated by the insets in **a**, the blue curve corresponds to the entrance face, *i.e.*, 0 mm, the orange curve to 1 mm, and the green curve to 2 mm. The group-delay dispersion is pre-compensated so that the quadratic phase is minimized at 1 mm. **d-f** The corresponding nonlinear polarizations due to OR for the pulses in **a-c**. The dashed black lines are the nonlinear polarization from the transform limited pulse.

nonlinear polarization becomes a function of frequency. In Figure 2.4**f**, we indicate the real and imaginary parts of the nonlinear polarization (dotted lines) for the 15 fs pulse, where the effect is quite dramatic. Moreover, it is already apparent for the 30 fs pulse, as can be seen in Figure 2.4**e**. If we focus on the low-frequency regime, which is the region we observe experimentally, this effect is less pronounced, however, it becomes more prominent for larger TOD and could be important in real experiments with a large number of optical components.

2.3.4 THz Generation

Starting from equation 2.12 and substituting in the expression for the nonlinear polarization in equation 2.9 yields an expression for the THz field amplitude at frequency ω as a function of propagation distance,

$$\partial_x \tilde{A} - i\frac{k_\omega}{2n_g}(\tilde{n}_\omega^2 - n_g^2)\tilde{A} = \frac{\omega^2\mu_0\epsilon_0}{2in_g k_\omega}\int_0^\infty d\omega' \chi_{eff}^{(2)}\tilde{A}(\omega'+\omega)\tilde{A}^*(\omega')e^{in_g(k_{\omega'+\omega}-k_{\omega'}-k_\omega)}, \quad (2.17)$$

and rearranging we are left with,

$$\partial_x \tilde{A}_\omega = ik_\omega(\tilde{n}_\omega - n_g)\tilde{A}_\omega + i\frac{k_\omega}{2n_g}\int_0^\infty d\omega' \chi_{eff}^{(2)}\tilde{A}(\omega'+\omega)\tilde{A}^*(\omega'), \quad (2.18)$$

where the exponential term in the integral was equal to 1 because we are using the free-space wavevectors. In this formulation, the phase matching between optical and THz is captured in the phase relationship between the nonlinear polarization integral, which captures the phases of the optical fields, and the THz field amplitude $\tilde{A}_\omega$. Equation 2.18 is differential equation governing the growth of a THz field co-propagating with a femtosecond optical pulse in a non-centrosymmetric medium, *i.e.*, the equation governing THz generation by optical rectification.*

To study the effect of co-propagation on the generated THz spectrum and waveform, in Figure 2.5**a** we plot the time domain THz waveform with three different crystal thicknesses with a refractive index profile as shown in Figure 2.5**b**. This corresponds to the the index of a toy model with a single optically active phonon with

*As an aside, it is interesting to study the solution in the case where the nonlinear polarization is zero. The solution to the first-order equation is given by $\tilde{A}_\omega = \tilde{A}_0 \exp[i(\tilde{n}_\omega - n_g)k_\omega x]$ so that the electric field is given by $E_\omega = \exp(in_g k_\omega x)\tilde{A}_\omega = \tilde{A}_0 \exp(i\tilde{n}k_\omega x)$ as expected. This exact correspondence with what is expected from linear optics is somewhat mysterious given the two approximations made to get to equation 2.18. However, it does lend support to the validity of these approximations.

f_0 = 5.3 THz, ϵ_{st} = 10, ϵ_∞ = 7.4, and γ = 0.025 THz, which yields a complex refractive index as seen in Figure 2.5**a**. This is similar to ZnTe, however, it does not include the contribution of higher-order phonon processes to the complex refractive index. For the calculation, we set the group refractive index to 3.2.

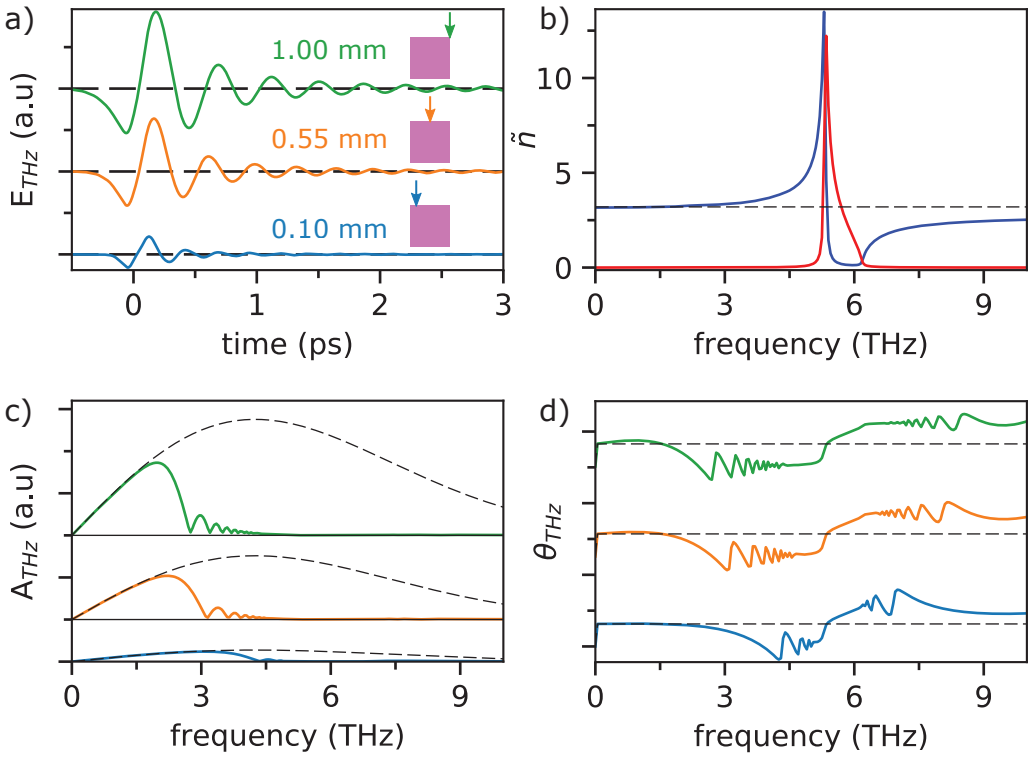

Fig. 2.5: Co-propagation effects on THz generation. **a** Time-domain waveforms for three different crystal thicknesses with a real (blue) and imaginary (red) parts of the complex refractive index, shown in **b**, calculated in a toy model with a single optically-active phonon. The dashed line in **b** is the group index of the generation pulse. **c** The corresponding amplitude and **d** phase spectra. The dashed black lines in **c** and **d** represent the amplitude and phase for a non-dispersive crystal. The transform-limited pulse duration for these calculations was 90 fs.

In fig 2.5**c, d** we show the corresponding amplitude and phase spectra, respectively. From the amplitude spectra, we see that the THz pulse spectrum is broadest when the optical pulse has only propagated 0.1 mm into the crystal. As seen in the 0.55 mm spectra (orange), when the optical pulse propagates deeper into the crystal the spectrum develops several peaks in the 3 to 5 THz regime. This indicates that at these frequencies the optical pulse has propagated beyond the coherence length and the amplitude oscillates with distance [44]. Even deeper into the crystal, at 1 mm

(green curve) the peaks in the spectrum shift further to the left.

This effect can also be seen in the phase, which develops sharp oscillations in the frequency regime where the pulse has propagated beyond the coherence length. There are two more regions where the phase is smooth, one in the region where the extinction coefficient is large, which occurs because the absorption is large and the field is attenuated on a comparable length scale as the coherence length, and one in the high frequency regime. While strong absorption limits the THz generation in the former region, there is significant enough THz generation in this latter region that some groups have used this part of the spectra in time-domain spectroscopy [50].

2.4 THz Pulse Propagation: Gaussian Optics

So far, we have considered the case of translational symmetry in the yz-plane. This approximation is good as long as the optical generation pulse is collimated with a beam waist such that the Rayleigh range of the generated THz pulse is significantly larger than the generation crystal length. This is often the case in THz spectroscopy systems, where THz pulses are often generated in a collimated section of a beam path. However, the pulses are generally then focused onto a sample or detection crystal so that the plane-wave approximation breaks down. The measured THz pulse is then affected by two factors related to Gaussian optics: first, the high frequencies focus tighter than the low frequencies, and second, there is a constant phase shift with frequency, *i.e.*, a carrier-envelope phase (CEP) shift, known as the Guoy phase. The amplitude of a Gaussian pulse as a function of distance x from the focus is given by,

$$A(r) = A_0 \exp\left(-r^2/w^2\right), \tag{2.19}$$

where w is the beam waist, r is the radial distance from the peak, and A_0 is the peak intensity. The beam waist as a function of distance from the focus is given by,

$$w(x) = w_0 \left[1 + \left(\frac{x}{x_R}\right)^2\right]^{1/2}, \tag{2.20}$$

where $x_R = w_0^2/\pi\lambda$ is the Rayleigh range, which gives an indication of the length over which the beam with beam-waist at focus w_0 can remain collimated. This equation can be inverted using the quadratic-root formula to find the w_0^2 and then w_0 can be

calculated directly given the beam-waist at position x. Care must be taken to choose the correct root in the first step as there are generally two ways the equation can be satisfied. We can see how the amplitude of the field, A_0, changes at the focus with respect to a collimated section by enforcing energy conservation. Integrating the intensity, which is proportional to the field amplitude squared, over space we see that to enforce energy conservation we find the condition,

$$A_{0,1} w_1 = A_{0,2} w_2, \tag{2.21}$$

where $A_{0,i}$ and w_i are the field amplitude and beam waist at position i. It is important to note that this estimate provides an upper bound on increase in amplitude achieved by focusing. In real systems there will be aberrations, such as non-Gaussian beam profile, that increase the size of the beam waist at the focus.

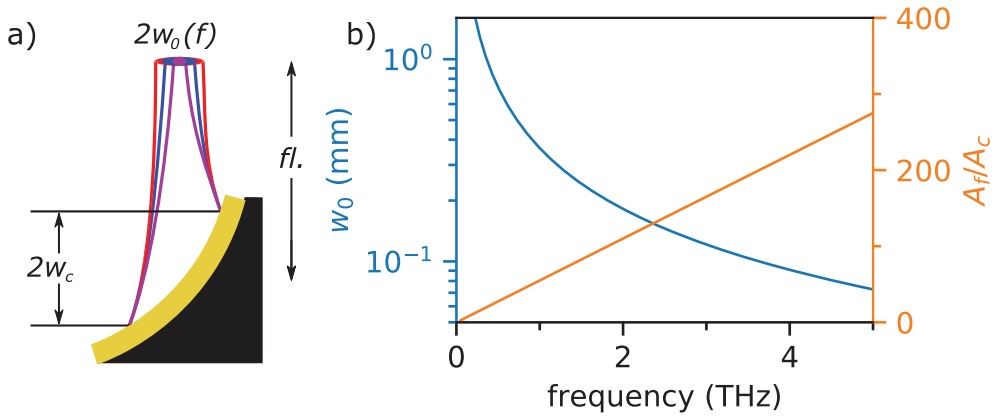

Fig. 2.6: Gaussian optics: THz focal spot size. **a** Schematic illustration of the calculated physical situation. **b** Frequency-dependent beam waist (blue) at the focus of the parabolic mirror in **a** along with the corresponding ratio between focused and collimated amplitude (orange). The beam waist incident on the parabolic mirror was taken to be 20 mm and the focal length of the mirror was taken to be 76.2 mm.

To see how focusing affects the amplitude spectrum, we consider a situation of a THz pulse with a frequency-independent beam waist of $w = 20\,\text{mm}$ focused to a spot with a parabolic mirror with a focal length of 76.2 mm (3"). This situation is illustrated schematically in Figure 2.6**a** along with the beam waist and focused/collimated amplitude ratio at the focus calculated using equations 2.20 and 2.21. To a very good approximation, the beam waist at the focus is given by,

$$w_0 \approx \left(\frac{c}{\pi f} \frac{F}{w} \right), \tag{2.22}$$

where F is the focusing optic focal length, so that the beam waist at the focus scales as f^{-1}. This results in an amplitude enhancement that increases linearly with frequency. The high frequencies are therefore enhanced in amplitude significantly more than the low frequencies. Notably, experimentally we have not observed such a significant reduction in the beam waist of the high frequencies (see Ref. [51]). This is likely due in part to a reduced wavefront quality at higher frequencies and in part to a breakdown of the assumption of a frequency-independent beam waist in the collimated section.

We now turn our attention to the CEP shift, which results from the constant phase shift with frequency of a focusing Gaussian pulse. The Guoy phase, θ_G, which is the anomalous phase shift of a focusing Gaussian pulse, is given as a function of distance from the focus by ,

$$\tan(\theta_G) = \frac{x}{x_R}. \tag{2.23}$$

According to equation 2.23, each frequency accumulates a 90° phase shift with respect to the beam at infinity. It therefore acquires a full 180° phase shift between positive and negative infinity. In real experiments, while the collimated section is not at infinity with respect to the focus, it is typically far enough that there is a full 90° phase shift with respect to the collimated beam.

In Figure 2.7**a, b**, we show the Guoy phase of a focusing Gaussian pulse for three different frequencies. Notably, the beam undergoes a rapid phase shift over a length scale proportional to the Rayleigh range. Beyond that, there is only a small variation with distance, which justifies our previous statement that there is a full 90° phase shift between the focused and collimated sections of the beam. In Figure 2.7**c**, we show the full effect of focusing on the Gaussian pulse including both the frequency-dependent Guoy phase shift and the changing beam waist. For a detailed experimental characterization of the effects of Gaussian optics on THz pulse propagation, see ref. [51].

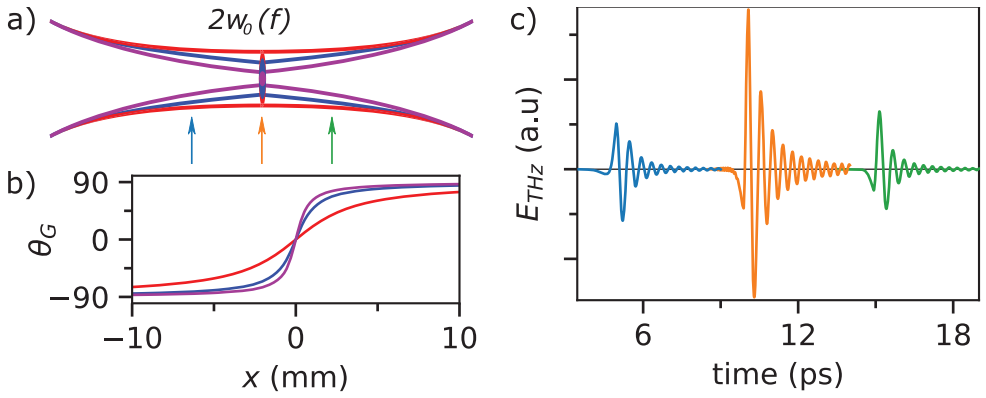

Fig. 2.7: Gaussian optics: Guoy phase and CEP shift. **a** Illustration of the focusing Gaussian pulse. **b** Guoy phase as a function of distance from the focus for 0.5 THz (red), 1.5 THz (blue) and 2.5 THz (magenta). **c** THz waveform at three distances near the focus including both the amplitude and phase affects from Gaussian optics.

2.5 Electro-Optic Sampling

2.5.1 Measurement of the THz-induced phase shift

The final step in our THz spectroscopy system involves EO sampling of the THz pulse waveform. A typical EO sampling setup, a linearly polarized femtosecond optical probe pulse co-propagates with a THz pulse in an EO crystal, as shown schematically in Figure 2.8a. The crystal is oriented such that the THz field modulates the refractive index along the y' axis. The polarization of the optical pulse can be tracked through four stages. First, the THz-field-induced modulation of the refractive index induces a phase shift that changes the polarization state of the probe pulse. Second, an additional $\pi/2$ phase shift is imprinted on the y' axis with a quarter waveplate so that the fields can be written as,

$$\begin{aligned} \tilde{E}_{x'} &= \tilde{E}_{0,opt} e^{i\pi/2+\phi}/\sqrt{2}, \\ \tilde{E}_{y'} &= \tilde{E}_{0,opt}/\sqrt{2}. \end{aligned} \tag{2.24}$$

Third a Wollaston prism projects the polarization states onto the $x-y$ polarizations, which are rotated by 45° with respect to the $x'-y'$ axes, and spatially separates the pulse into linear polarizations, so that $\tilde{E}_x = \tilde{E}_{x'}\cos(\pi/4) - \tilde{E}_{y'}\sin(\pi/4)$ and $\tilde{E}_y = \tilde{E}_{x'}\cos(\pi/4) + \tilde{E}_{y'}\sin(\pi/4)$. Finally, photodiodes are used to measure the intensities of each polarization, which are proportional to the square of the optical

fields and can be written after some manipulation as,

$$I_x \propto \frac{1}{4}\tilde{E}^2_{0,opt}\left(1+\sin(\phi)\right), \\ I_y \propto \frac{1}{4}\tilde{E}^2_{0,opt}\left(1-\sin(\phi)\right). \tag{2.25}$$

giving the ratio,

$$(I_x - I_y)/(I_x + I_y) \equiv I_{EO} = \sin(\phi) \approx \phi, \tag{2.26}$$

which relates experimentally accessible quantities directly to the phase shift induced by the THz field. The following discussion elaborates on how ϕ can be related to the THz field. The frequency-dependent response of the system is affected by the same factors that impact the THz generation process: dispersion and phase mismatch of the optical and THz pulses as well as the strength of the EO coefficient. A complete Fourier-domain description of the EO sampling process was first derived in ref. [48]. The derivation presented in this section is less rigorous but more intuitive and yields the same final expression.

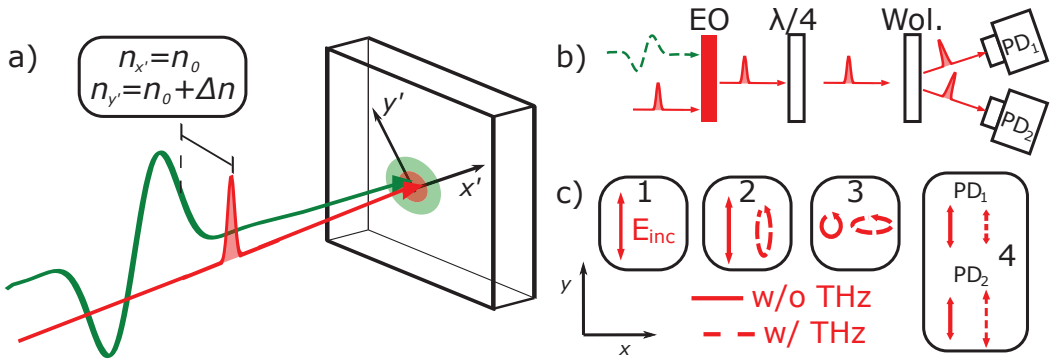

Fig. 2.8: Electro-optic sampling. **a** Schematic illustration of an EO sampling experiment. A THz pulse and optical pulse are coincident on an EO crystal. The THz field modulates the index along the y' axis through the EO effect. **b** Diagram of the stages of EO sampling along with the corresponding polarization states with (dashed lines) and without (solid lines) indicated in **c**. The $x-y$ coordinates shown in **c** are rotated 45° with respect to the x' and y' axes in **a**.

2.5.2 Phase shift in the delta-function approximation

We first consider the case of a delta function pulse co-propagating with a THz field. This experimental configuration is shown in the top schematic of Figure 2.9**a**. Due to the THz-field induced birefringence, the rate of change with length is given

by [44],

$$\frac{d\phi}{dx} = k_{0,opt}\Delta n_{opt} = k_{0,opt} r_{eff} n_{0,opt}^3 E_{THz}, \tag{2.27}$$

where $k_{0,opt}$ and $n_{0,opt}$ are the wavevector and phase index, respectively, at the center wavelength of the optical pulse, and r_{eff} is the EO coefficient relevant for the experimental configuration. Neglecting the THz emission due to the optical pulse, which we can do because the probe pulse is assumed to be weak, the THz field seen by the delta function pulse at position x in the crystal is $E_{THz} = \tilde{A}_0 e^{i(n-n_g)kx}$, where n_g is the group index of the delta function pulse. Inserting this expression into equation 2.27 and integrating over the crystal thickness, we find,

$$\begin{aligned} \int_0^x d\phi &= k_{0,opt} r_{eff} n_{opt}^3 \tilde{A}_0 \int_0^x dx e^{i(\tilde{n}-n_g)kx} \\ \phi(x) &= k_{0,opt} r_{eff} n_{opt}^3 \tilde{A}_0 \frac{e^{i(\tilde{n}-n_g)kx} - 1}{i(\tilde{n}-n_g)k}, \end{aligned} \tag{2.28}$$

which is the phase shift induced by a single THz frequency. Note that if $\tilde{n} = n_g$, the phase factor must be eliminated prior to integration to avoid the pole in the denominator. To account for the total phase shift we must integrate over the full THz spectrum,

$$\phi(x,t) = k_0 r_{eff} n_0^3 \int_{-\infty}^{\infty} d\omega e^{i\omega t} \tilde{A}_0(\omega) \frac{e^{i(\tilde{n}-n_g)kx} - 1}{i(\tilde{n}-n_g)k}, \tag{2.29}$$

where t is the time-delay between the THz pulse and delta-function sampling pulse at the entrance face of the EO crystal.

2.5.3 Including a Gaussian envelope

To this point, the calculation has overlooked one aspect of the problem: the finite duration of the optical sampling pulse. As illustrated in the middle schematic of Figure 2.9**a**, the effect of the finite pulse duration is that different parts of the optical envelope see different time delays, which results in a smearing of the THz field. To include this effect in our calculation, we first rewrite equation 2.29, as the convolution of a delta function and the response function,

$$\phi(x,t) = k_0 r_{eff} n_0^3 \int_{-\infty}^{\infty} d\tau \delta(t-\tau) \int_{-\infty}^{\infty} d\omega e^{i\omega\tau} \tilde{A}_0(\omega) \frac{e^{i(\tilde{n}-n_g)kx} - 1}{i(\tilde{n}-n_g)k}, \tag{2.30}$$

and generalize this to the case of an optical pulse with finite duration, we replace the delta function with the optical intensity envelope,

$$\phi(x,t) = k_0 r_{eff} n_0^3 I_{int}^{-1} \int_{-\infty}^{\infty} d\tau I_{opt}(t-\tau) \int_{-\infty}^{\infty} d\omega e^{i\omega\tau} \tilde{A}_0(\omega) \frac{e^{i(\tilde{n}-n_g)kx}-1}{i(\tilde{n}-n_g)k}, \qquad (2.31)$$

where $I_{int} = \int_{-\infty}^{\infty} dt I_{opt}(t)$ is a normalization constant. Since the Fourier transform of a delta function is a constant, for $I_{opt}(t) = \delta(t)$ we recover the expression in equation 2.28. In the case of a Gaussian envelope, which is a good approximation in many experiments, equation 2.28 is modified to include a Gaussian roll off with frequency,

$$\phi(x,\omega) = k_{0,opt} r_{eff} n_{opt}^3 I_{int}^{-1} \tilde{A}_0 \frac{e^{i(\tilde{n}-n_g)kx}-1}{i(\tilde{n}-n_g)k} e^{-\tau^2\omega^2/4}, \qquad (2.32)$$

where τ is the e^{-1} point of the time-domain intensity envelope and ω is the THz frequency. In the case of a more general pulse shape, as might be obtained due to higher order dispersion, as we showed previously the nonlinear polarization is directly proportional to the optical envelope. As a result, the tools we have developed for calculating nonlinear polarization in the previous sections can be applied to EO sampling and we can rewrite this expression as,

$$\phi(x,\omega) = k_{0,opt} r_{eff} n_{opt}^3 \tilde{A}_0 \frac{e^{i(\tilde{n}-n_g)kx}-1}{i(\tilde{n}-n_g)k} \tilde{C}(\omega), \qquad (2.33)$$

where,

$$\tilde{C}(\omega) = I_{int}^{-1} \int_0^{\infty} d\omega' \tilde{A}(\omega'+\omega) \tilde{A}^*(\omega') \qquad (2.34)$$

and $\tilde{A}$ and $\tilde{A}^*$ are the optical amplitudes as the equation for the nonlinear polarization via OR. This expression is now equivalent to the approximate solution of Gallot *et al.* [48], which is commonly used for determining the response function of an EO sampling system [52].

2.5.4 Co-propagation effects

We can go one step further and include the effect of GVD on the EO signal. As illustrated in the bottom schematic of Figure 2.9**a**, GVD acts to broaden the pulse as it propagates, which results in further smearing of the THz field. We will include the effect of pulse broadening by assuming that we can simply modify equation 2.27 by including the term proportional to the Fourier transform of the envelope,

$$\frac{d\phi(x,\omega)}{dx} = k_{0,opt}\Delta n_{opt} = k_{0,opt} r_{eff} n_{0,opt}^3 \tilde{A}_0 e^{i(\tilde{n}-n_g)kx} \tilde{C}(\omega,x). \qquad (2.35)$$

In the case where there is no GVD or higher-order dispersion, $\tilde{C}(\omega, x) = \tilde{C}(\omega)$ and this integral can be calculated analytically to recover equation 2.33. Alternatively, we can numerically integrate equation 2.35 using similar structure as that developed in the previous sections for THz generation.

2.5.5 Examples

The normalized amplitude and phase response function for the three situations considered here are shown in Figure 2.9 **b** for the same refractive index as that of the toy crystal use previously with a 1 mm crystal thickness. The response is dominated by the group/phase index mismatch term, *i.e.*, the response from the delta function pulse (blue curve). There is a dramatic roll off of responsivity above 2.5 THz followed by a series of peaks at higher frequencies for reasons similar to those of the peaks in the THz generation.

Including the envelope term (orange curve) results in a slightly reduced amplitude response of the higher frequencies. This effect is more dramatic for, *e.g.*, a 100 fs pulse. Finally, the numerical integration of equation 2.35 that includes GVD results in a more significant reduction in response for the higher frequencies and a dampening of the oscillations in the 2.5-4 THz range. We also see that, unlike the non-dispersive case, the phase response is affected by GVD.

It is important to note that for these calculations, we have used a Gaussian pulse with a 50 fs full-width at half maximum (FWHM) transform-limited pulse duration. This duration was chosen as it allows us to see both the effect of finite pulse duration and GVD. For longer pulses, the roll off due to finite pulse duration is more dramatic but the effect of GVD is smaller. Conversely, for faster pulses the effect of finite duration is less pronounced, however, the effect of GVD becomes more important.

2.6 Comparison to experiment

2.6.1 Sampling Crystal

Having developed the basic structure to understand THz generation and detection by OR and EO sampling, this section describes several experiments to validate the theories starting with the effect of the response function of the EO sampling crystal

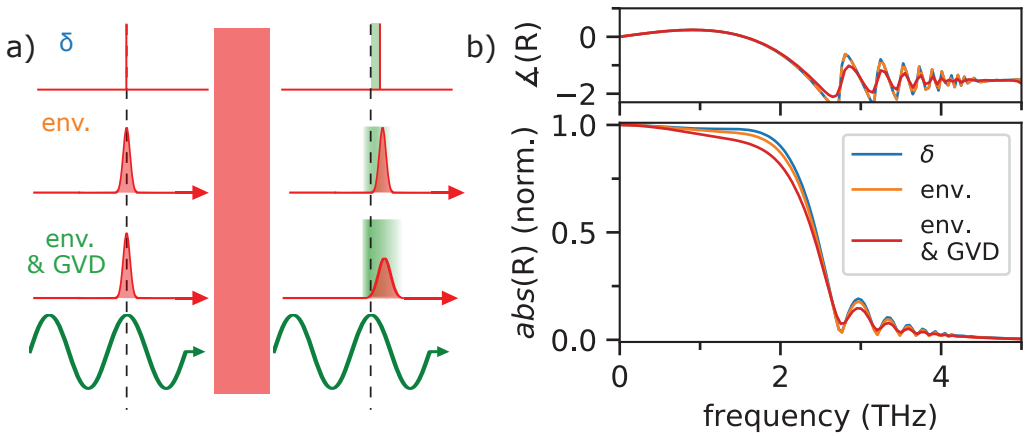

Fig. 2.9: Various approximations of the EO sampling response function. **a** Illustration of the processes affecting EO sampling in the delta function (top), envelope (middle) and envelope plus GVD approximations. The green sine wave represents the electric field of a single THz frequency. **b** The corresponding amplitude (bottom) and phase (top) responses as a function of frequency for the delta function approximation (blue), the Gaussian envelope approximation without GVD (orange curve) and the envelope approximation with GVD (red curve). The calculations were performed for a 1 mm toy-model crystal similar to ZnTe (see Figure 2.5).

on the spectrum/waveform, as shown in Figure 2.10. A 1 mm ZnTe emitter was used in combination with a 1 mm ZnTe detector and a 0.25 mm GaP detector. Note that in this section, no attempt was made to precisely control the pulse durations in the emission and detection crystals. The refractive indexes in the THz range of the two crystals (solid lines) are shown along with the group optical indexes at 820 nm (the center wavelength of the USL amplifier). The normalized detector response functions, calculated from equation 2.32 with a 100 fs FWHM, is shown in Figure 2.10b. GVD of the optical pulse was not considered due to the relatively long pulse duration (see Figure 2.4a). The two important effects governing the relative amplitude of the response function in this system are therefore the pulse duration, which affects the roll off of the signal at high frequencies, and phase mismatch.

Phase mismatch in the ZnTe crystal becomes important at frequencies above approximately 2 THz, where the signal strength rolls off rapidly and then oscillates. The 0-2 THz regime is dominated by the Gaussian roll off. In GaP the relatively smaller normalized response in the 0-2 THz range is due to the phase mismatch as GaP is phase matched at 8 THz so the mismatch gets smaller with increasing frequency. On

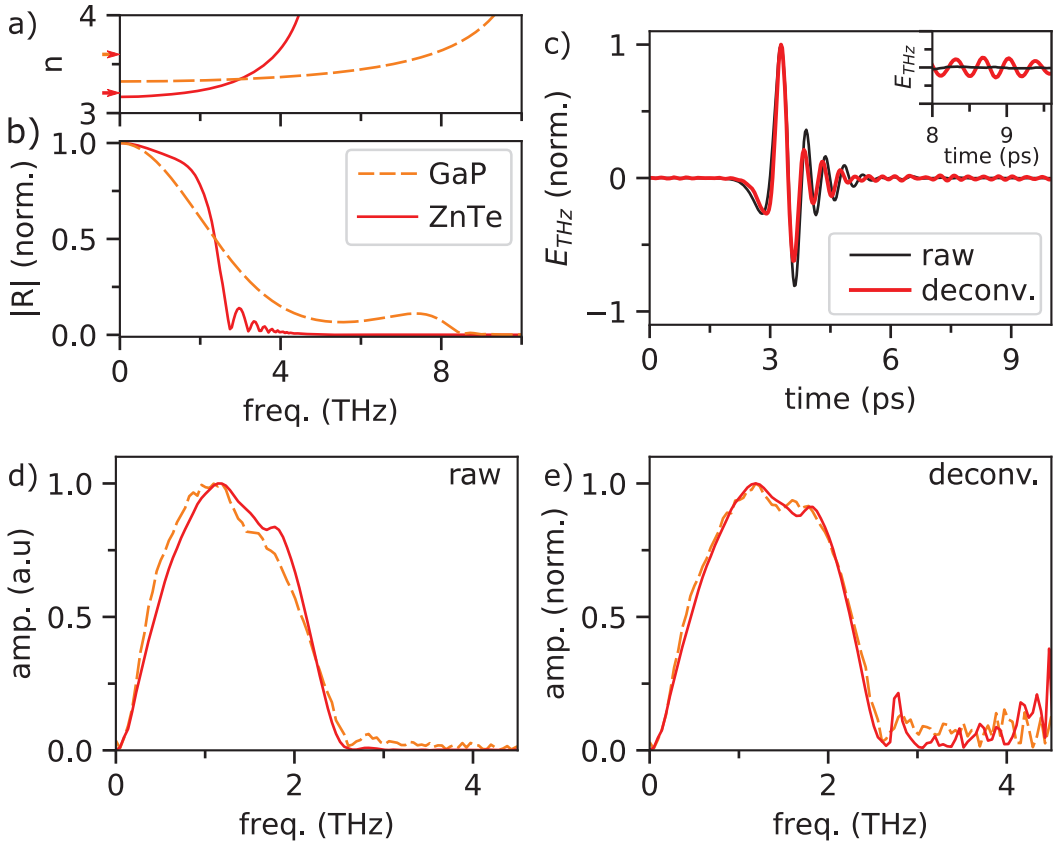

Fig. 2.10: Effect of sampling crystal on the THz waveform and spectrum. **a** THz refractive index for ZnTe (red solid line) and GaP (orange dashed line) The group index at 820 nm is indicated with an arrow to the left of the axis. **b** Amplitude of the detector response function for 1 mm ZnTe (red) and 0.25 mm GaP (orange) sampling crystals. **c** Raw (black) versus deconvoluted (red) waveforms for the ZnTe sampling crystal. The inset highlights the artifacts induced by the deconvolution procedure. The y-axis is in a.u. **d** Raw and **e** deconvoluted spectra for the ZnTe and GaP sampling crystals.

the other hand, in the higher THz frequency range the roll off of the response-function amplitude is due to the finite pulse duration.

The deconvoluted time-domain response (red) is overlaid on the raw signal (black) for the ZnTe detector in Figure 2.10c. Here, the spectrum was limited to only the region less than 3.5 THz to reduce the amplification of noise. The deconvolution results in a small change to the CEP and a reduction of the ringing immediately after the main peak of the pulse. However, it also results in non-physical ringing in the longer time region as shown in the inset. This highlights the fact that care must

be taken in deconvoluting signals in order to avoid misinterpreting artifacts as real behavior.

The raw spectra for the GaP (orange) and ZnTe (red) detectors are shown in Figure 2.10d. Notably, the low frequencies in the orange curve are enhanced relative to the higher frequencies. Intuitively, this makes sense based on the calculated response functions in Figure 2.10b. Furthermore, in Figure 2.10e the deconvoluted spectra are plotted and show much better agreement with one another. Even still, there are notable differences between the curves, especially near the feature at 1.5 THz and in the >2.5 THz region where the pulses have propagated beyond the coherence length in ZnTe.

It is not surprising that the high-frequency regime does not agree well as the detector response function in this regime is quite sensitive to the group velocity of the optical pulse, which can vary depending on the Sellmeier coefficients used in its calculation.* It is also sensitive to the precise THz refractive index. Moreover, the differences near 1.5 THz can be attribute to the small variations in the refractive index and absorption coefficient due to combination phonon modes at these frequencies [54]. This again highlights the difficulty with deconvoluting the detector response in EO sampling as extremely detailed information about the sampling crystal and optical pulse are required to precisely perform the calculation.

2.6.2 ZnTe versus GaP Emitter

Next, we study the effect of the dispersion of the THz refractive index on the emitted spectrum. In Figure 2.11a is the spectrum from a 1 mm ZnTe emitter with a 0.25 mm GaP detector and in Figure 2.11b is the normalized calculated spectrum (dashed line) along with the calculated spectrum after accounting for the transmission coefficients at the emitter/detector exit/entrance faces and the response function of the GaP sampling crystal (solid line). Here, we chose to convolute the calculated spectrum rather than deconvolute the experimental spectrum as the latter method is more likely to amplify noise.

*Sellemeier coefficients are parameters used in a phenomenological fit to the dispersion refractive index for a given material, see, *e.g.*, ref. [53].

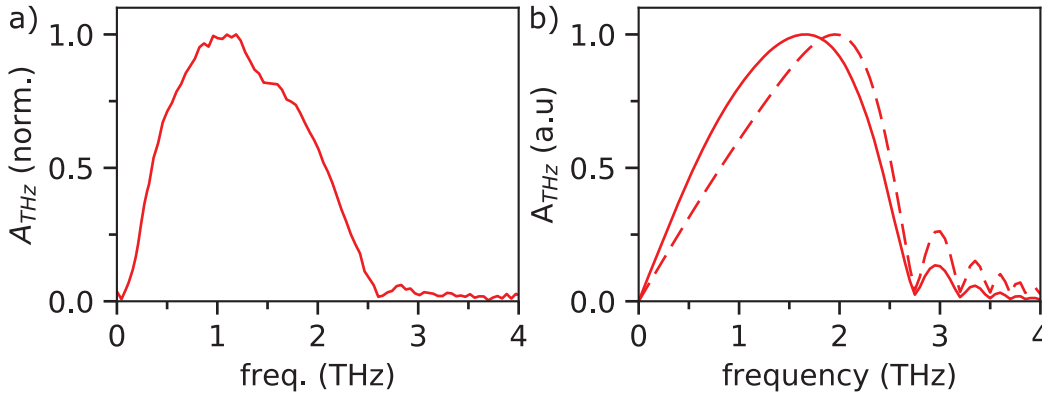

Fig. 2.11: Effect of emitter dispersion on THz spectrum: ZnTe. **a** Experimentally measured THz spectrum from a 1 mm ZnTe emitter measured with a 0.25 mm GaP sampling crystal. **b** Calculated THz waveform (dashed line) and calculated waveform taking into account the detector response function and transmission coefficients from the emitter to free space and back into the GaP sampling crystal (dashed line).

The calculation reproduces many of the features in the experimental spectrum faithfully. The bandwidth is contained mainly in the 0.5-2 THz range in both the experimental and calculated spectra. Just above 2.5 THz, both spectra reach a minimum. The oscillations in the calculated spectrum above this point are much more prominent than the experimental data, although there is a single peak located at approximately 2.8 THz in the latter. This lack of higher frequency oscillations could be due to many experimental factors, such as inhomogeneity of the refractive index or curvature of the optical wavefront. The finer details of the experimental spectra are also not present in the calculated spectrum, namely, the roll off at low frequency and the feature in the spectrum near 1.5 THz. The former is an effect due to Gaussian optics, where the lower frequencies are not focused as tightly and some of the their amplitude is lost due to diffraction.

In Figure 2.12a, the experimental spectrum from a 0.25 mm GaP emitter combined with the same 0.25 mm GaP detector is shown. Here, the spectrum is peaked near 2 THz and contains bandwidth up to 6 THz. Similar to before, in Figure 2.12b the calculated spectrum (dashed line) is shown along with the calculated spectrum

multiplied by the transmission coefficients and detector response function* The detector response more dramatically reshapes the spectrum due to the broader bandwidth. The convoluted spectrum has similar character to the experimental spectrum, with most of the bandwidth between 0.5 and 3 THz and a roll off of the main lobe that extends to 6 THz. Once again, the low frequency character of the experimental spectrum is different than the calculation due to Gaussian optics effects.

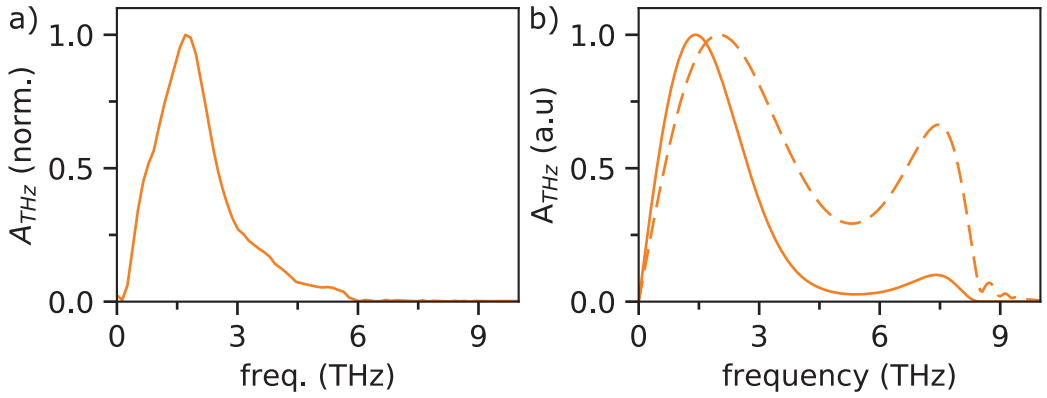

Fig. 2.12: Effect of emitter dispersion on THz spectrum: GaP. a Experimentally measured THz spectrum from a 1 mm ZnTe emitter measured with a 0.25 mm GaP sampling crystal. **b** Calculated THz waveform (dashed line) and calculated waveform taking into account the detector response function and transmission coefficients from the emitter to free space and back into the GaP sampling crystal (solid line).

The most dramatic difference between the experiment/theory is in the region above 6 THz. The calculation predicts a secondary lobe peaked near 7.5 THz, which is clearly not visible in the experimental spectrum, which cuts of sharply at 6 THz. In the calculation, the primary and secondary lobes are again due to the coherence length. However, in contrast to the ZnTe case where the secondary lobes occur at frequencies that have gone beyond one coherence length, in GaP the group velocity is phasematched to approximately 7.5 THz and no frequencies below this have reached the second coherence length yet. The absence of the secondary lobe in the experimental spectrum is unclear and we speculate on several possible origins. First, in the THz beam path a thin Teflon and black polyethylene sheet are used to filter the

*Note that the range of the $x-$axis has been extended relative to the ZnTe case, causing the spectrum to appear narrower even though it is broader.

optical pump pulse, which could have reduced transmission at high THz frequencies [55]. It is also possible that the pump and probe pulses from the laser were not optimized at the emitter/detector locations, which would reduce the signal strength in the high-frequency regime or that the Sellmeier coefficients used to calculate the GaP group index were imprecise.

2.6.3 Generation Crystal Thickness

Finally, in Figure 2.13 the effect of the emitter thickness on the THz spectrum is examined. Figure 2.13a shows the experimentally normalized experimental spectra with 0.5 mm (solid line) and 1 mm (dashed line) emitters and a 0.25 mm GaP detector. The calculated spectra, accounting for the transmission and detector response, are shown in Figure 2.13b.

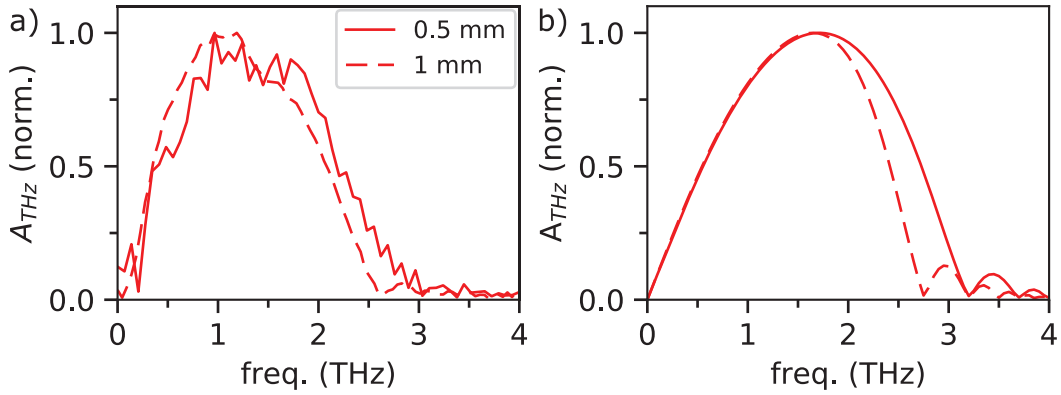

Fig. 2.13: Effect of generation length on the THz waveform. a Experimentally measured THz spectrum with a 0.5 mm (solid line) and 1 mm (dashed line) emitter and a 0.25 mm GaP detector. **b** Calculated THz spectra from a 0.5 mm (solid) and 1 mm (dashed) ZnTe emitter taking into account the sampling crystal response function and transmission coefficients from the interfaces.

The Experimental spectrum from the 0.5 mm emitter is slightly broader and peaked at a similar frequency. The signal strength is also lower, leading to a decreased signal to noise ratio. The first secondary lobe in the spectrum from the 1 mm emitter is visible from experiment while it is not distinguishable from noise in the spectrum from the 0.5 mm emitter. The calculated spectra in Figure 2.13b shows similar to features, as the spectrum 0.5 mm emitter (solid line) is slightly broader than for the 1 mm emitter (dashed line).

Chapter 3

New Perspectives on Tilted-Pulse Fronts and Terahertz Generation

Chapter 2 discussed the theory of terahertz (THz) pulse generation by optical rectification (OR) in phase-matched crystals such as GaP and ZnTe. However, the generation efficiency and peak electric fields from these emitters are limited due to their small band gaps and electro-optic (EO) coefficients. It is therefore desirable to use a crystal such as lithium niobate (LN), which has a large band gap ($\sim$3.7 eV [56]), high damage threshold, and EO coefficient much larger than GaP and ZnTe. However, there is a large group/phase index mismatch in LN that prevents collinear THz generation, as seen in Figure 3.1a, b. The technique of tilted-pulse front (TPF) OR was developed to overcome this limitation [57, 58, 16, 17]. The principle of TPF excitation is illustrated in Figure 3.1c.

A time-domain description of TPF-OR, including the geometrical calculations of pulse-front tilt (PFT), has been presented in several recent theses [59, 60, 61, 62, 51]. To add a new perspective, this chapter discusses a frequency-domain description of the TPF technique and develops the theory of the correspondence between PFT and angular dispersion (AD) [63]. Moreover, the importance of higher-order AD in determining the full spatiotemporal dynamics of TPF propagation is highlighted, which, to the best of the author's knowledge, has not been addressed in the literature. Moreover, we present a novel technique for higher-order AD management and discuss the relevance to TPF THz generation.

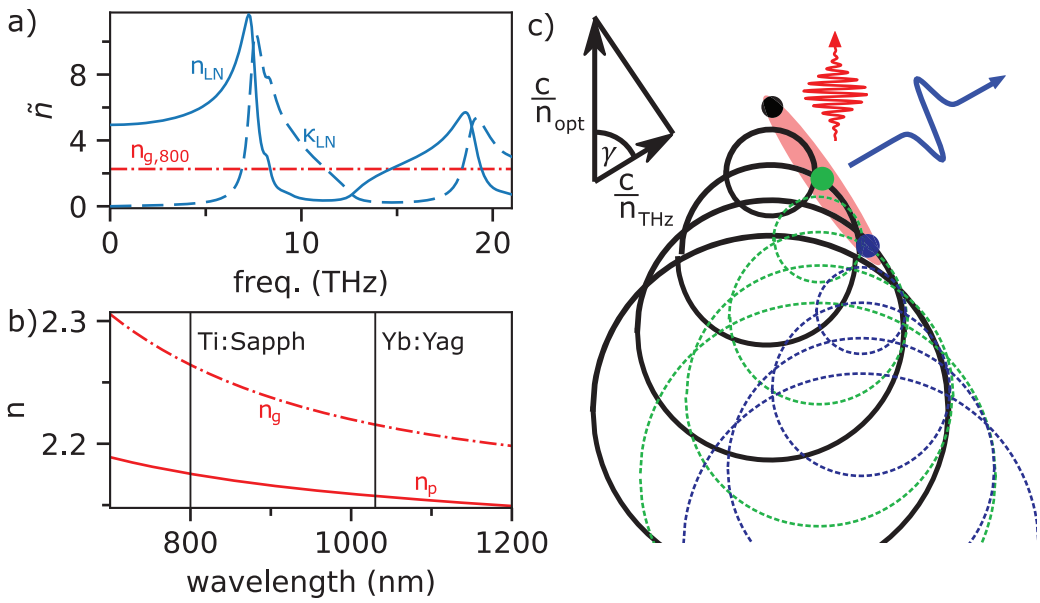

Fig. 3.1: Principal of tilted-pulse front THz generation. **a** Real (solid) and imaginary (dashed) parts of the THz complex refractive index in LN along the c-axis, calculated using the parameters in ref. [64]. The dot/dashed red line indicates the group refractive index at 800 nm. **b** Phase (solid) and group (dot/dashed) refractive index in LN in the NIR. The vertical lines indicate the center wavelengths of Ti:Sapphire and Yb:YAG lasers, which are commonly used for TPF THz generation. The indexes were calculated from the Sellmeier coefficients provided by ref. [53]. **c** Illustration of the principle underlying TPF THz generation. The small circles inside the shaded red region represent individual beamlets of the intensity envelope. The large black, green, and blue circles represent the THz wavefronts emitted from several propagation points along the beamlet path. The wavefronts from each individual beamlet superpose constructively along the Cherenkov cone angle while the wavefronts from separate beamlets superpose constructively along one of the cone wavefronts, resulting in non-collinear THz generation. The phase-matching triangle in the top left can be used to determine the required PFT, γ given some group optical index, n_{opt}, and THz phase index, n_{THz}.

We also determine the conditions necessary to rigorously map the 2D problem of TPF THz generation to 1D, which yields corrections to the propagation constants to group-velocity dispersion (GVD) from AD (GVD-AD) not considered in other work (see, *e.g.*, refs. [47, 65, 66]) and use the machinery of chapter 2 to study OR in LN. Finally, we propose the use of GaN as a novel EO crystal for TPF OR, which could be a useful new source of THz radiation in the 5-12 THz region due to its large bandgap and high phonon frequency. Rigorous coupled-wave analysis is used to design a high-efficiency surface-relief grating capable of producing the correct PFT.

3.1 Non-Collinear Difference Frequency Generation

3.1.1 Two-Color

We begin by considering the case of two pump fields at frequencies ω_1 and ω_2, which create a difference-frequency polarization at frequency $\omega_3 = \omega_1 - \omega_2$ as introduced in Chapter 2. In order to have an efficient nonlinear process, we want the field at ω_3 to be in phase with the difference-frequency polarization. If we are confined to 1D, the fields are given by $e^{i(n_1 k_1 x - \omega_1 t)}$, $e^{i(n_2 k_2 x - \omega_2 t)}$, and $e^{i(n_3 k_3 x - \omega_3 t)}$. The difference-frequency polarization is at $e^{i(n_1 k_1 - n_2 k_2)x - \omega_3 t)}$.* From this, the phase difference between the nonlinear polarization and the difference frequency is given by $(n_1 k_1 - n_2 k_2 - n_3 k_3)x = \Delta k_x$, which sets the maximum length the difference-frequency amplitude grows before it is out of phase with the nonlinear polarization. It is common to define the coherence length, which quantifies the length at which the difference-frequency amplitude is maximized, as $L_{coh} = \pi/\Delta k$.† For example, if we consider LN with $\omega_1 = 2\pi\,(375)$ THz and $\omega_2 = 2\pi\,(374)$ THz (799.4 and 801.6 nm, respectively), which have refractive indices of $n_1 \approx n_2 \approx 2.18$. The index at $\omega_3 = 1$ THz is approximately 5.0 and the phase mismatch is large and the coherence length is just 53 μm.

This short interaction length greatly limits the efficiency of nonlinear processes, however, if we remove the restriction of 1D and we allow our optical fields to propagate at an angle with respect to one other, as illustrated schematically in Figure 3.2**a**,

*This can be seen from the second order term in equation 2.6 specialized to the case of two fields.

†Note that various definitions of the coherence length exist in the literature (see *e.g.* ref. [44] section 2.2 or [67] equation 1.

we have some additional control over the nonlinear polarization. We can write the equation for a field propagating at an angle θ with respect to the x direction as,

$$E(x,y) = \tilde{A}_0 e^{ik(\cos(\theta)x + \sin(\theta)y) - i\omega t}, \tag{3.1}$$

where k is the length of the wavevector. We can write the difference-frequency polarization as,

$$P_{NL}(\omega_3) = \tilde{A}_{0,\omega_1} \tilde{A}^*_{0,\omega_2} e^{i(k_1 \cos(\theta) - k_2)x + ik_1 \sin(\theta)y - i\omega_3 t}. \tag{3.2}$$

The resulting nonlinear polarization can be written as a plane wave with a wavevector at angle,

$$\tan(\phi) = \frac{\sin(\theta)k_1}{\cos(\theta)k_1 - k_2}. \tag{3.3}$$

In Figure 3.2**b** we plot the nonlinear polarization along the direction, ϕ, as defined in equation 3.3, with the fields and indexes defined by the previous example of the collinear coherence length. Three different crossing angles were considered. In Figure 3.2**c** we show the THz field at the difference frequency of 1 THz. As the crossing angle increases, the wavelength of the nonlinear polarization decreases and at $\theta = 1.2°$, it is nearly the same as the THz polarization, indicating a long coherence length. A 2D map of the nonlinear polarization for the same three angles is shown in Figure 3.2 **d-f**, where the increasing angle ϕ can be clearly seen. The inset shows the phase-matching triangles, where for a specific angle θ the triangle is closed and the coherence length is infinite. This is satisfied when $|n_3\vec{k}_3| = |n_1\vec{k}_1 - n_2\vec{k}_2|$, which can be rewritten as,

$$n_3^2 k_3^2 = n_1^2 k_1^2 + n_2^2 k_2^2 - 2n_1 n_2 k_1 k_2 \cos(\theta). \tag{3.4}$$

For our example, with the values used in our previous calculation of the collinear coherence length, we find $\theta = 0.315°$, which is close to the graphically determined value from Figure 3.2**b**.

3.1.2 Broadband

While this two-color calculation is useful for single-frequency THz emission, as a next step, we would like to generalize this to accommodate the broad bandwidth of a femtosecond pulse. The situation we would like to study is illustrated in Figure 3.3 **a, b**, where several fields are incident on a crystal with different propagation angles.

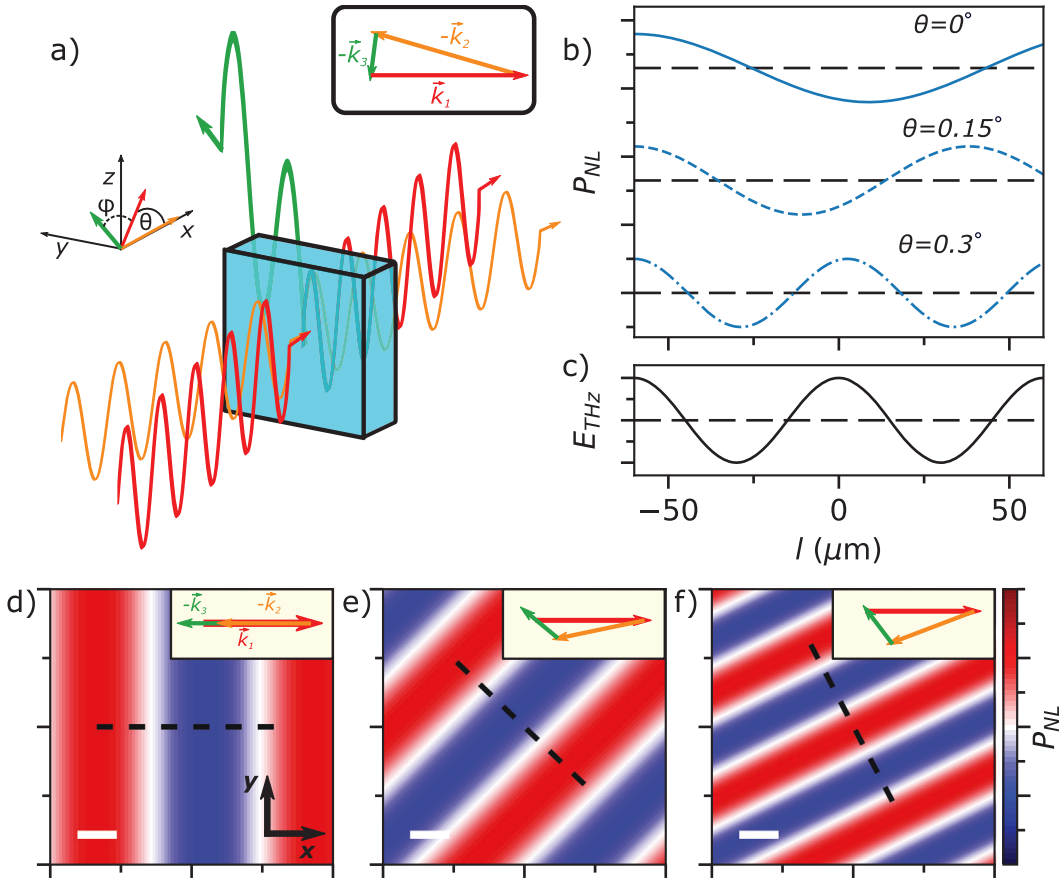

Fig. 3.2: Non-collinear phasematching. **a** Two optical fields (orange and red) incident on a nonlinear crystal propagating at angle θ with respect to one another. The left inset indicates the coordinate system while the top inset indicates the phase matching condition that determines the angle of emitted THz radiation (green). **b** P_{NL} evaluated along the dashed black lines in **d-f** for three different values of θ. **c** Field at the $\omega_1 - \omega_2$, which is close to the same wavelength as the nonlinear polarization with $\theta = 1.2°$. Colormap of the spatial dependence of the nonlinear polarization evaluated with equation 3.2 for **d** $\theta = 0°$, **e** $\theta = 0.6°$, and **f** $\theta = 1.2°$. The white scale bar in the bottom left of each figure is 20 μm. The colored vectors in the insets indicate the vector sum of the optical and THz fields, where the sum is 0 in **f**. In each case, the length of k_3 and angle θ is exaggerated for illustrative purposes.

We assume a constant AD with wavelength* over the bandwidth of the pulse, *i.e.*, that the propagation angle can be written as,

$$\theta(\lambda) = (\lambda - \lambda_0)\left(\frac{d\theta}{d\lambda}\right), \tag{3.5}$$

where we define θ such that $\theta(\lambda_{min}) = 0$.

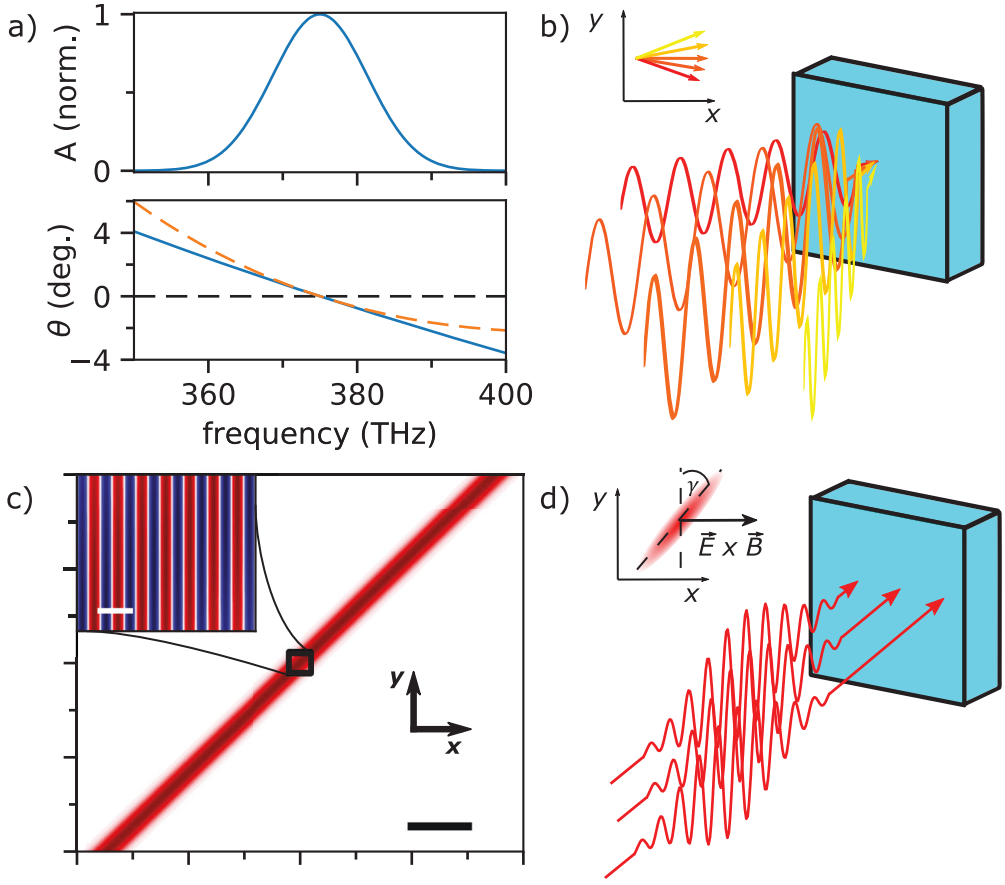

Fig. 3.3: Angular dispersion/Pulse-front tilt relationship. a Amplitude spectrum (top) and angular spectrum (bottom). **b** Schematic description of the problem in the frequency domain. **c** 2D map of the intensity envelope as a function of x and y. The black scale bar is 50 μm. Inset: electric field as a function of x and y in the boxed region of the main figure. The white scale bar is 1 μm. **d** Schematic illustration of the spatiotemporal time-domain waveform incident on the crystal.

Once again assuming an optical index of 2.18 and a THz index of 5.0, we can

*Here, the theory is developed using a linear angle with wavelength rather than with frequency, which allows us to analytically retrieve the usual correspondence between PFT and AD. A linear angle with frequency also maps to PFT in the time domain.

evaluate the AD term numerically from equation 3.4 by considering,

$$\left.\frac{d\theta}{d\lambda}\right|_{\lambda_0=800} = \lim_{(\lambda_0-\lambda_1)\to 0} \left.\frac{\theta(\lambda_1)}{\lambda_0-\lambda_1}\right|_{\lambda_0=800}. \tag{3.6}$$

we find an AD of $-0.148°/\text{nm}$. If we convert this to frequency using,

$$\left.\frac{d\theta}{df}\right|_{f_0} = -\frac{c}{f_0^2}\left.\frac{d\theta}{d\lambda}\right|_{\lambda_0}, \tag{3.7}$$

we find an AD of $0.315°/\text{THz}$, as expected from our 2-color calculation.

At this point, it is quite interesting to make a connection back to the time domain. Obviously, without prior knowledge of the correspondence between AD and PFT is nearly impossible to visualize the superposition of the angularly dispersed waves. To study the time-domain field of an angularly dispersing pulse we can construct the waveform using a Fourier transform,

$$E(x,y,t) = \int_{-\infty}^{\infty} d\omega \tilde{A}_0(\omega) \exp\left(i(\cos(\theta_\omega)x + \sin(\theta_\omega)y)k_\omega - i\omega t\right). \tag{3.8}$$

A spatial map of the pulse envelope calculated at $t = 0$ using equation 3.8 with an amplitude and angle spectrum as shown in Figure 3.3**a** is shown in Figure 3.3**c**. At first glance, this appears to be a pulse propagating at an angle with respect to the chosen coordinate system. However, if we zoom in on a small portion of the pulse and plot the electric field rather than the intensity, as shown in the inset, we see that the phase fronts are perpendicular to the x direction.

This is the defining characteristic of PFT, where the intensity envelope is at an angle with respect to the propagation direction (normal to the phase fronts). In Figure 3.3**d** we show an analogous schematic to frequency schematic in Figure 3.3**b**, however, the fields propagating at different angles with respect to one another are replaced by collinear time-delayed pulses. The inset illustrates the idea of a tilted-pulse front, where the intensity is at an angle with respect to the Poynting vector, $\vec{E} \times \vec{B}$, which indicates the direction of the flow of energy.

3.2 Angular Dispersion/Pulse-Front Tilt Correspondence

3.2.1 First Order Angular Dispersion

We can develop an analytic description of the tilted-pulse front from 3.8. Expanding the sinusoids in equation 3.8 to first order in θ and rearranging we have,

$$E(x,y,t) = \int_{-\infty}^{\infty} d\omega \tilde{A}_0(\omega) \exp\left(i(k_\omega x - i\omega t) \exp\left(-i\lambda_0 \frac{d\theta}{d\lambda} k_\omega y\right) \exp\left(i2\pi \frac{d\theta}{d\lambda} y\right)\right). \tag{3.9}$$

There are now three exponential terms. The first is the regular phase factor for a plane wave propagating in the x direction. The second is a linear phase shift with frequency (note that $k_\omega \propto \omega$) where the slope is proportional to y. Since a linear phase shift in the frequency domain represents a propagation in the time domain, this implies that the peak of the envelope translates in x direction as y changes, which is exactly what we see in Figure 3.3**c**. The third exponential term involves a constant phase shift proportional to y, *i.e.*, the translation of the envelope is accompanied by a shifting carrier-envelope phase (CEP). This term has very little effect with the many-cycle pulses used in our work, however, it could be important for few-cycle pulses.

We can derive the relationship between the angle of the PFT, γ, and the AD, $d\theta/d\lambda$. From the linear portion of the phase factor, $(x - \lambda_0(d\theta/d\lambda)y)k_\omega$, we see that lines of constant phase occur when $x = \lambda_0(d\theta/d\lambda)y$. With the pulse front tilt as defined in Figure 3.3d, we find,

$$\tan(\gamma) = \lambda_0(d\theta/d\lambda) \tag{3.10}$$

which is the same as the expression derived by Hebling in a non-dispersive medium [63].

Recalling that one of the goals of this chapter is to understand the TPF THz generation using a frequency-domain approach, we take a step back and reconsider the two-color difference frequency generation. If we look at the angle of emission (equation 3.3) near the center wavevector, k_0, as the wavevector difference approaches zero we can make an additional connection between the time domain and frequency

domain,

$$\tan(\phi) = \lim_{\Delta k \to 0} \frac{\sin(\Delta\theta)k_0}{\cos(\theta)k_0 - (k_0 + \Delta k)} = -k_0 \frac{d\theta}{dk}, \\ \tan(\phi) = \lambda_0 \frac{d\theta}{d\lambda}, \tag{3.11}$$

which is equivalent to the expression for the correspondence between the PFT and the AD.

3.2.2 Pulse Broadening From Angular Dispersion

Notice that the expression for the tilted pulse front in equation 3.9 predicts that the tilted pulse can propagate indefinitely without broadening. This is an approximation that arises from neglecting the higher order terms in θ when expanding the sinusoids. This approximation is most accurate for narrow-band pulses or pulses with small AD. If we now choose to keep terms order θ^3 we find,

$$E(x,y,t) = \int_{-\infty}^{\infty} d\omega \tilde{A}_0(\omega) \exp\left[i \left(1 - \frac{1}{2} \left(\frac{d\theta}{d\lambda} \right)^2 (\lambda - \lambda_0)^2 \right) k_\omega x \right] \times \\ \exp\left[i \left(\frac{d\theta}{d\lambda}(\lambda - \lambda_0) - \frac{1}{6} \left(\frac{d\theta}{d\lambda} \right)^3 (\lambda - \lambda_0)^3 \right) k_\omega y \right] \exp\left[-i\omega t \right]. \tag{3.12}$$

Previously, we quantified the higher order dispersion terms using an expansion in the wavevector and considered quadratic phase (GVD) and cubic phase (TOD) in detail. The terms $(\lambda - \lambda_0)^n k_\omega$ term results in a different relationship between phase and frequency than we have considered so far as it contributes to the phase to all orders of $(\omega - \omega_0)^n$. However, it turns out that to a very good approximation only the GVD and TOD terms contribute significantly. We can see why with a slight rearrangement using the expansion,

$$(\lambda - \lambda_0)^n k = (2\pi)^n c^{n-1} (-1)^n \frac{(\omega - \omega_0)^n}{\omega_0^n \omega^{n-1}} \\ \approx (2\pi)^n c^{n-1} (-1)^n \left[\frac{(\omega - \omega_0)^n}{\omega_0^{2n-1}} - (n-1) \frac{(\omega - \omega_0)^{n+1}}{\omega_0^{2n}} + \cdots \right], \tag{3.13}$$

where we used the expansion $x^{-1} \approx x_0^{-1} - x_0^{-2}(x - x_0) + \cdots$. This shows that each $(\lambda - \lambda_0)^n$ term contributes to the n^{th} order phase and higher on expansion of the sinusoids.

The first exponential in equation 3.12 (the x term) therefore contains a linear phase from the zero-order term in θ, and a quadratic and cubic phase from the second-order term. From the quadratic term, we find an effective GVD of $\beta_{2,x} = -\frac{(2\pi)^2 c}{\omega_0^3}\left(\frac{d\theta}{d\lambda}\right)^2$ and a TOD of $\beta_{3,x} = \frac{3(2\pi)^2 c}{\omega_0^4}\left(\frac{d\theta}{d\lambda}\right)^2$. In practice, the pulse broadening is dominated by the GVD term and the TOD term has only a small effect. Combining the $\beta_{2,x}$ term with the relationship between AD and PFT, equation 3.10, we can see that the effective GVD is proportional to $\tan^2(\gamma)$ (similar to ref. [65]), *i.e.*, the GVD is larger for larger PFTs. To third order, the second exponential in equation 3.12 (the y term), we have only a first order term, which governs the PFT, and a cubic phase term that grows with distance in the y direction with an effective TOD of $\beta_{3,y} = -\left(\frac{d\theta}{d\lambda}\right)^3 \frac{(2\pi)^3 c^2}{\omega_0^5}$.

3.3 Higher-Order Spatiotemporal Coupling

3.3.1 Minimum-Duration Tilt

If we look more closely at the equations for the tilted-pulse front, we note that the point of minimum pulse duration lies along the $x = 0$ line regardless of the y position. This implies that the tilted-pulse front intensity is maximum only along the portion of the pulse currently crossing the $x = 0$ plane. This is illustrated in Figure 3.4 **a**, where we plot the optical envelope at an instant in time in a skewed coordinate frame along the tilted-pulse front. The pulse duration is minimized only along near $y = 0$.

With our current framework, there is no mechanism for compensation of GVD with y as there are only constant, linear, and cubic terms coupled to the y direction.

The key difference between the situation described previously and the formalism we have developed so far is the introduction of higher-order terms in the AD,

$$\theta(\lambda) = (\lambda - \lambda_0)\left(\frac{d\theta}{d\lambda}\right)\Big|_{\lambda_0} + \frac{1}{2}(\lambda - \lambda_0)^2\left(\frac{d^2\theta}{d\lambda^2}\right)\Big|_{\lambda_0} + \cdots \tag{3.14}$$

The addition of the quadratic term in $\lambda - \lambda_0$ contributes only at third order in $\omega - \omega_0$ in the expansion of the cosine term, however, in the expansion of the sine term the leading order effect is to pick up a term quadratic in $\omega - \omega_0$. With a suitable choice of $\left.\frac{d^2\theta}{d\lambda^2}\right|_{\lambda_0}$, we can compensate the GDD term from the relative propagation of the optical envelope with y. In other words, we can design our AD such that the entire tilted-pulse front is maximally compressed at the same instant in time, or alternatively

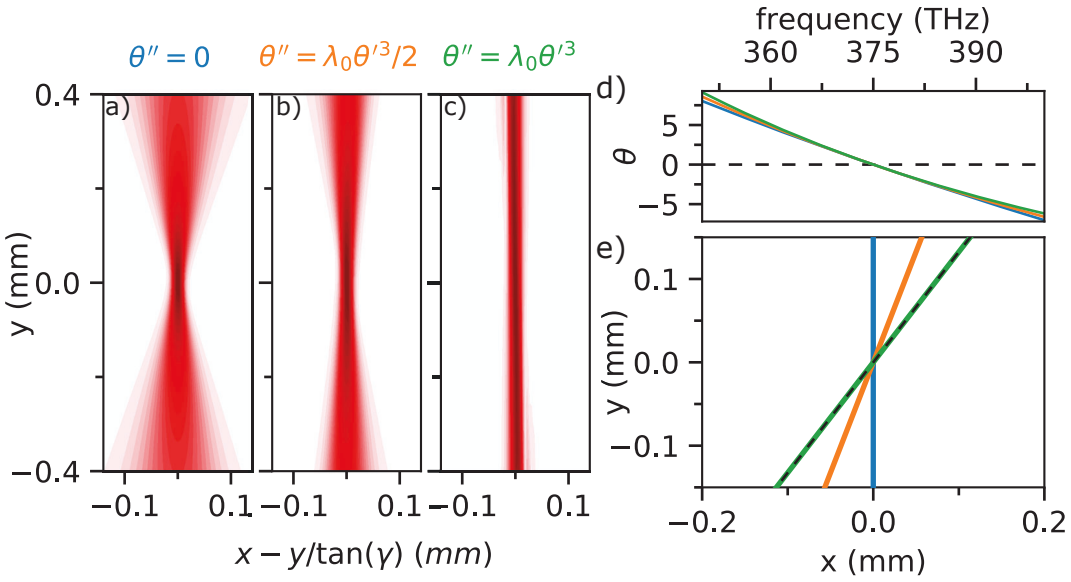

Fig. 3.4: Effective of higher-order AD on PFT. Optical envelope in a skewed coordinate frame along the tilted-pulse front with **a** $\theta'' = 0$, **b** $\theta'' = \lambda_0\theta'^3/2$, and **c** $\theta'' = \lambda_0\theta'^3$. **d** Angle as function of wavelength for quadratic AD corresponding to **a** (blue), **b** (orange), and **c** (green). **e** Lines corresponding to the tilt angle of the pulse front (black dashed) and the minimum-pulse-duration line for **a** (blue), **b** (orange), and **c** (green).

along a line in the xy-plane with a slope equivalent to the PFT. We also include a third order term in order to maintain our accuracy to the level of TOD. This idea is illustrated in Figure 3.4**b,c**, where a quadratic term with wavelength has been included in the AD. We see that there is a specific value of the quadratic term that best minimizes the pulse duration along the tilted-pulse front.

To deal with this analytically, when we include the quadratic term in our expression for $\theta(\lambda)$ we find several new terms to deal with,

$$\begin{aligned} \cos(\theta)kx &\approx \left[k - \frac{1}{2}\theta'^2(\lambda-\lambda_0)^2k - \frac{1}{2}\theta'\theta''(\lambda-\lambda_0)^3k\right]x, \\ \sin(\theta) &\approx \left[\theta'(\lambda-\lambda_0)k + \frac{1}{2}\theta''(\lambda-\lambda_0)^2k + \frac{1}{6}\theta'''(\lambda-\lambda_0)^3k - \frac{1}{6}\theta'^3(\lambda-\lambda_0)^3\right]y, \end{aligned} \tag{3.15}$$

where the primed superscripts indicate derivatives with respect to λ to simplify the notation and, once again, we have kept terms only to order $(\lambda-\lambda_0)^3$. Using equation 3.13, we find an effective GVD in the y direction of $\beta_{2,y} = \frac{4\pi^2 c\theta''}{\omega_0^3}$. Additionally, we find corrections to the TOD in the x and y directions, so that $\beta_{3,x} = \frac{12\pi^2 c\theta'^2}{\omega_0^4} + \frac{24\pi^3 c^2\theta'\theta''}{\omega_0^5}$

and $\beta_{3,y} = \frac{8\pi^3 c^2 \theta'^3}{\omega_0^5} - \frac{8\pi^3 c^2 \theta'''}{\omega_0^5} - \frac{12\pi^2 c \theta''}{\omega_0^4}$.

In order to have the pulse duration minimized along the same angle as the pulse front we require, *i.e.*, to have the minimum-duration tilt (MDT) match the PFT

$$\exp\left(i\frac{1}{2}\beta_{2,x}(\omega-\omega_0)^2 x\right) = \exp\left(i\frac{1}{2}\beta_{2,y}(\omega-\omega_0)^2 y\right), \tag{3.16}$$

for $x = y\tan(\gamma)$, *i.e.*, along the direction of the PFT. This leads us to the expression,

$$\frac{d^2\theta}{d\lambda^2} = \left(\frac{d\theta}{d\lambda}\right)^2 \tan(\gamma) = -\lambda_0 \left(\frac{d\theta}{d\lambda}\right)^3. \tag{3.17}$$

In addition to balancing the GVD term, because we are keeping terms to third order in $\omega - \omega_0$, we also need to find a relationship between the $\beta_{3,x}$ and $\beta_{3,y}$. We find,

$$\theta''' = 3\lambda_0^2 \theta'^5 + \theta'^3 \tag{3.18}$$

3.3.2 Intuitive Picture of Higher-Order Angular Dispersion

While we have shown analytically that the higher-order AD is necessary to fully encapsulate the tilted pulse propagation, we can use a simple picture to gain a more intuitive understanding of situation, shown in Figure 3.5. Moreover, we can use this picture to easily find the condition to minimize the pulse-front duration along the PFT (or any desired angle) to all orders in the phase. Interestingly, a similar intuition was used by Kreier and Baum to minimize the pulse duration along the axis perpendicular to the propagation direction [68].

We consider an optical pulse normally incident on a transmission grating. In this case, the pulse front tilt is equal to the diffraction angle, as illustrated in Figure 3.5**a**.* Moreover, if the incident pulse is maximally compressed, we know that the diffracted pulse is also maximally compressed along the grating surface, which is parallel to the PFT. From the grating equation for this condition, we can find the n^{th} order AD as,

$$\frac{d^n\theta}{d\lambda^n} = \frac{d^n}{d\lambda^n}\sin^{-1}\left(\frac{\lambda}{\Lambda},\right) \tag{3.19}$$

where Λ is the groove density. Alternatively, if the ultrafast pulse is not normally incident things change: the pulse duration is still minimized along a line parallel to

*Here we consider the situation where the pulse is diffracted entirely into the $m = +1$ order for simplicity.

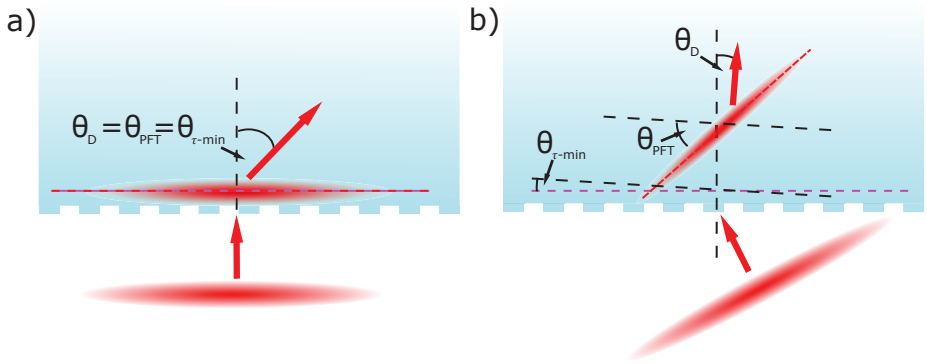

Fig. 3.5: Decoupling of PFT and minimum pulse duration. **a** An ultrafast pulse normally incident on a grating. In this case the diffraction angle equals the pulse front-tilt angle and the line of minimum pulse duration coincides with the PFT angle. **b** An off-normal incidence ultrafast pulse, where the diffraction angle, PFT, and line of minimum pulse duration no longer coincide.

the grating surface, however, the grating surface is neither parallel to the propagation direction nor the PFT, as illustrated in Figure 3.5**b**. Similarly to the normal-incidence case, the grating equation gives us the conditions necessary to minimize the pulse duration along the grating surface to all orders.

3.3.3 Effect of Material Dispersion

The theory presented so far is valid in free space. As the final step before we can map the problem to 1D, we want to include material dispersion in our calculation. This introduces an additional degree of complexity to an already complex calculation. To recap, there are 3 expansions involved in our calculation: we first expand the wavelength as a function of angle, then the sinusoids, and finally after rearranging the term $(\lambda-\lambda_0)^n$ terms we expand ω^{-n} about ω_0. To include the material dispersion, we would like to introduce another expansion of the wavevector as we did in the pulse-propagation equation, with $nk \approx\equiv \beta \approx \beta_0 + \beta_1(\omega-\omega_0) + \frac{1}{2}\beta_2(\omega-\omega_0)^2 + \cdots$, where $\beta_i = d^i(nk)/d\omega^i$. As a result, we pick up a large number of additional terms and the algebraic calculation becomes rather unwieldy. As a result, we chose to perform this calculation using the SymPy computer algebra package for Python, with which the expansion is easily extended to arbitrary order in $\omega-\omega_0$.

Table 3.1: Propagation constants for angularly dispersing pulses to third order in $\omega - \omega_0$ and $d^n\theta/d\lambda^n$. β_i is the i^{th} derivative of the wavevector in the material with respect to ω and the primed superscripts indicate derivatives of the propagation angle with respect to λ. Both the ω and λ derivatives are evaluated at ω_0.

Order	x	y
0	β_0	0
1	β_1	$-\frac{2\pi\beta_0 c\theta'}{\omega_0^2}$
2	$\beta_2 - \frac{4\pi^2\beta_0 c^2\theta'^2}{\omega_0^4}$	$\frac{4\pi^2\beta_0 c^2\theta''}{\omega_0^4} + \frac{4\pi\beta_0 c\theta'}{\omega_0^3} - \frac{4\pi\beta_1 c\theta'}{\omega_0^2}$
3	$\beta_3 + \frac{24\pi^3\beta_0 c^3\theta'\theta''}{\omega_0^6} + \frac{24\pi^2\beta_0 c^2\theta'^2}{\omega_0^5} - \frac{12\pi^2\beta_1 c^2\theta'^2}{\omega_0^4}$	$\frac{8\pi^3\beta_0 c^3\theta'^3}{\omega_0^6} - \frac{8\pi^3\beta_0 c^3\theta'''}{\omega_0^6} - \frac{24\pi^2\beta_0 c^2\theta''}{\omega_0^5} - \frac{12\pi\beta_0 c\theta'}{\omega_0^4} + \frac{12\pi^2\beta_1 c^2\theta''}{\omega_0^4} + \frac{12\pi\beta_1 c\theta'}{\omega_0^3} - \frac{6\pi\beta_2 c\theta'}{\omega_0^2}$

Starting from equation 3.8 with k_ω replaced by the expansion of the wavevector, we can write the equation for the angularly-dispersing pulse as,

$$E(x,y,t) = \int_{-\infty}^{\infty} d\omega \tilde{A}_0(\omega) \exp\left(i\left[\beta_{x,0} + \beta_{x,1}(\omega-\omega_0) + \frac{1}{2!}\beta_{x,2}(\omega-\omega_0)^2 + \cdots\right] x \right.$$
$$\left. + i\left[\beta_{y,0} + \beta_{y,1}(\omega-\omega_0) + \frac{1}{2!}\beta_{y,2}(\omega-\omega_0)^2 + \cdots\right] y - i\omega t \right), \tag{3.20}$$

where $\beta_{i,j}$ is the i^{th} expansion coefficient in the j direction. The expressions for $\beta_{i,j}$ are summarized in Table 3.1. There are several important features of note. First, after including material dispersion $\beta_{2,y}$ contains terms proportional to the first order AD, which at first glance appears to discredit the arguments of the previous section regarding the requirement of second-order AD. However, in a non-dispersive medium the terms proportional to θ' cancel. Moreover, without the θ'' term there is no way to independently control the angle of minimum-duration tilt. Second, we see that the GVD-AD is of opposite sign to that of the material (material GVD is positive assuming normal dispersion). Note that the expression for GVD-AD can be rewritten as,

$$\beta_{2,x} = -\frac{n_g^2}{\omega_0 n(\omega_0) c}\tan^2(\gamma), \tag{3.21}$$

which is equivalent to the definition of ref. [66].

Third, we see that the AD of order i couples to the propagation constants at lowest order to $\beta_{i-1,x}$ and $\beta_{i,y}$. This second feature is especially useful as it implies

that, in principle, higher-order AD terms can be added to compensate, for example, the PFT or MDT without disturbing the lower-order tilts. The angle of the i^{th} tilt, γ_i,* can also be found by looking at the lines of constant i^{th} order phase,

$$\tan(\gamma_i) = -\frac{\beta_{i,y}}{\beta_{i,x}}, \tag{3.22}$$

so that the PFT in a medium is given by,

$$\tan(\gamma_1) = \frac{2\pi\beta_0 c\theta'}{\beta_1\omega_0^2} = \frac{n_0}{n_g}\lambda_0\theta', \tag{3.23}$$

which is the same as that derived by Hebling [63]. The MDT in a medium is given by,

$$\tan(\gamma_2) = -\frac{\lambda_0^2(\lambda_0 n_0\theta'' + 2\theta'(n_0 - n_g))}{2\pi\beta_2 c^2 - \lambda_0^3 n_0\theta_1^2}, \tag{3.24}$$

and the condition for the MDT to lie along the PFT is,

$$\theta'' = \frac{\lambda_0 n_0\theta'^3}{n_g} + \theta_1\left(-\frac{2\pi\beta_2 c^2}{\lambda_0^2 n_g} - \frac{2}{\lambda_0} + \frac{2n_g}{\lambda_0 n_0}\right). \tag{3.25}$$

3.3.4 Prism/Grating Pair for Quadratic Angular Dispersion Management

The decoupling of the tilt angle of the line of minimum pulse duration and the tilted-pulse front has consequences on the spectrum and spatial mode in THz-pulse generation, as has been discussed recently by Bodrov *et al.* [69]. In standard TPF setups, the minimum duration angle is corrected by the demagnification of the grating imaging optics as discussed by Fülop *et al.* [65]. However, this is well known to introduce imaging errors, which limits the possible lateral size of the generation beam. To overcome the imaging errors, the contact-grating technique was proposed [70]. However, with the contact grating technique there is no way to insure that the MDT is coincident with the PFT other than with a normally-incident pulse where the beam necessarily diffracts into multiple orders, which reduces quality of the spatial mode of the THz pulse [71].

Here, we introduce a new method for independently controlling the PFT and MDT using a prism-grating pair, as shown schematically in Figure 3.6**a**. In this scheme, a

*For example, γ_1 is the PFT and γ_2 is the MDT. γ_0 can also be thought of as the phase-front tilt which, of course, is zero.

prism introduces a small AD into the pulse before the contact grating. In this simple configuration, there are already a large number of tunable parameters: the incidence angle, glass, and apex angle of the prism and the period and incidence angle of the grating (we assume the grating substrate is LN).

Shown in Figure 3.6b are the PFT (solid lines) and MDT (dashed lines) as a function of prism incidence angle for 4 different grating incidence angles. The black horizontal line indicates the PFT required for phase-matched THz generation in LN. The prism glass for this calculation was N-SF11 and the grating period was 870 nm. Here, we see that for each grating incidence angle, there is a prism angle such that the solid and dashed lines simultaneously intersect the horizontal black line, *i.e.*, the MDT and PFT are equal to the 63° angle required for THz generation.

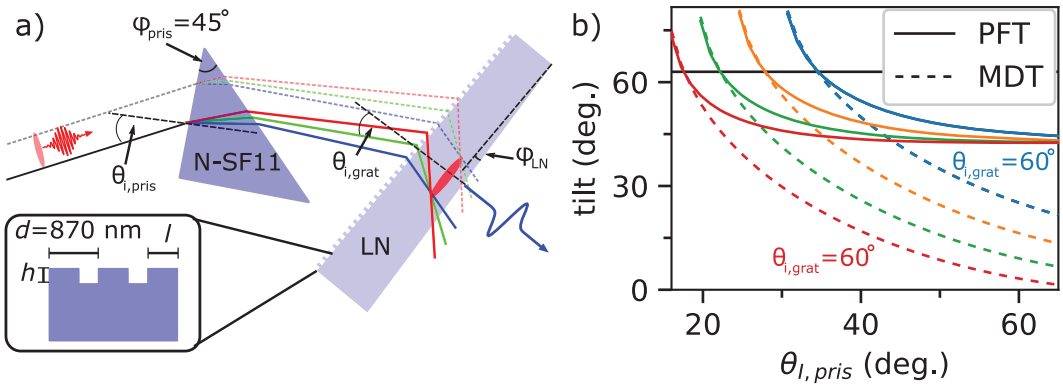

Fig. 3.6: Compensation of second-order angular dispersion. a Prism-grating scheme for control of quadratic AD. An optical pulse is pre-dispersed by a prism with apex angle Φ_{pris} and incidence angle $\theta_{i,pris}$. In this example, the prism glass is N-SF11. The angularly-dispersed pulse is incident on a grating deposited on LN with a grating period d=870 nm. The height, h, and ridge width, l, can be used as tunable parameters to optimize the grating efficiency. **b** Pulse-front tilt (solid line) and minimum-duration tilt (dashed line) as a function of prism incidence angle for 4 different grating incidence angles. The horizontal dashed line indicates the 63° pulse-front tilt required for phase-matched TPF THz generation in LN. The LN crystal should be cut at angle Φ_{LN} to optimize the THz output coupling.

It is somewhat surprising that the intersection of the MDT and PFT is near 63° for each grating incidence angle. Interestingly, the crossing angle appears to be most sensitive to the grating period for any combination of the other parameters. This raises the concern of whether it is possible to design an efficient grating for 800

nm with an 870 nm period. Moreover, the tilt angle of the grating with respect to the prism introduces a variable magnification as a function frequency, which could negatively affect THz generation.

Nevertheless, we have shown that it is theoretically possible to independently control the PFT and MDT using a simple prism/grating pair. This capability could enable large aperture TPF THz generation with zero imaging error. Moreover, it is possible that this technique could facilitate independent control of the generation pulse wavefront, which could be useful for enhancing the focusing power of TPF THz sources. Furthermore, TPFs are important in several other areas of ultrafast optics, including non-collinear optical-parametric amplification [72], ultrafast electron diffraction [73], attosecond photonics [74], X-Ray free-electron lasers [75], and emerging THz pulse-shaping technologies [76]. Finally, we note that this is the only simplest configuration for PFT/ management. It is likely that more sophisticated schemes, for example using mismatched prism pairs or grisms for pre-dispersal would yield a larger range of control.

3.4 2D to 1D Tilted-Pulse Front Mapping

Having considered the propagation of tilted-pulse fronts in detail, it is now possible to formally map the 2D problem of tilted-pulse front THz generation to 1D in order to study the TPF THz generation in using the machinery of chapter 2. This mapping was first performed in ref. [47], however, the effective GVD due to AD was not considered. It was also performed in refs. [65, 66], however, these works did not consider the change in effective GVD from the coordinate transformation as will be shown here. Starting from equation 3.20, by rotating to a reference frame with coordinates x' and y' in the direction perpendicular to the PFT. With $x = \cos(\gamma)x' - \sin(\gamma)y'$ and $y = \sin(\gamma)x' + \cos(\gamma)y'$,* the effective propagation constants in the x' direction are given by $\beta_{i,x'} = \beta_{i,x}\cos(\gamma) - \beta_{i,y}\sin(\gamma)$.

To understand how we can map the 2D problem to 1D we consider the tilted pulse front as a set of infinitesimally spaced sources of spherical wavefronts. In analogy to a phased array, the infinite set of spherical wavefronts propagates forwards as a plane

*In this section we refer to γ_1 as γ, which is typically used to refer to the PFT.

wave in the direction normal to the line of polarization sources, *i.e.*, perpendicular to the pulse front. In order for this analogy to hold, the polarization sources must be translationally invariant along the THz wavefront or, in other words, the angles γ_i should all equal the PFT. From equation 3.22 we find $\beta_{i,y} = -\tan(\gamma)\beta_{i,x}$ so that,

$$\beta_{2,x'} = \beta_{2,x}(\cos(\gamma) + \sin(\gamma)\tan(\gamma)) = \frac{\beta_{2,x}}{\cos\gamma}, \tag{3.26}$$

which implies that the effective GVD-AD along the THz propagation direction is larger than along the TPF propagation direction.* This rigorous mapping therefore introduces a correction already at second order in $\omega - \omega_0$, which is not taken into account by previously published 1D models and further limits the effective generation length. For a 63° PFT the effective GVD-AD is approximately 2.2 times higher than the GVD-AD.

Similarly, we can find the group velocity from the first order term,

$$\beta_{1,x'} = v_{eff}^{-1} = \frac{\beta_1}{\cos(\gamma)}, \tag{3.27}$$

and, since we know that $\beta_1 = (c/n_g)^{-1}$, we find an effective index of $n_{g,eff} = n_g/\cos(\gamma)$, which is what we expect from the diagram in Figure 3.1b.

As suggested previously, to complete the mapping from 2D to 1D the source term must obey translational invariance in the y' direction, which is parallel to the THz wavefronts. To verify that this is the case, note that the propagation constants in the y direction are given by and $\beta_{i,y'} = \beta_{i,x}\sin(\gamma) + \beta_{i,y}\cos(\gamma)$. When the condition in equation 3.22 is satisfied, $\beta_{i,y'} = 0$ for all i with the notable exception of the $\beta_{0,y'}$ term. This term governs the CEP, which changes along the tilted pulse front in the y' direction. There is no way around this, which at first appears to contradict the claim that it is possible to map from 2D to 1D. However, the CEP cancels out in the difference-frequency generation process that drives optical rectification so that the source term is indeed translationally invariant and the mapping from 2D to 1D is complete.

*It is interesting that we can calculate this correction term without explicitly calculating the second order AD. Of course, for the correction term to the TOD we must calculate the second order AD explicitly.

3.5 Tilted-Pulse Front THz Generation in Lithium Niobate

In this section, we use the THz-generation formalism from Chapter 2 along with the effective propagation constants from the previous section to second order in $\omega - \omega_0$ to study TPF THz generation in LN. In the literature, theoretical studies of TPF THz generation typically place emphasis on the energy-generation efficiency [65, 66, 69]. In this section, we show how energy-generation efficiency is decoupled from the peak electric field generation even before considering focusing effects. Furthermore, using a Gaussian optics approximation we show how optimizing for peak electric field strengths favors shorter transform-limited generation pulses.

As shown in Figure 3.1 the refractive index mismatch for 800 nm versus 1 THz is large and TPF phase matching is required for THz generation. Shown in Figure 3.7a is the refractive index in the range of 0 to 5 THz. The nonlinear scale on the top axis shows the PFT required to phase match to the corresponding frequency on the bottom axis. We see that a range of pulse front tilts between 62 and 68° enable tuning through the whole 5 THz range.* Figure 3.7b shows the corresponding GVD-AD in the TPF propagation direction (blue) as well as the GVD-AD$_{eff}$ in the THz propagation direction as a function of phase-matched frequency. Note that the material GVD at 800 nm along the extraordinary axis is 368 fs^{2}mm^{-1} so that the pulse broadening is dominated by GVD-AD.

The pump-pulse duration as a function of distance along the THz propagation direction is shown in Figure 3.8a for several different transform-limit pulse durations. As expected, the pulse-broadening is significantly worse for the shorter transform-limit pulses. For the 30 fs pulses, the pulse width is already larger than 0.75 ps (half-cycle duration at 0.7 THz near the peak emission frequency of many LN sources) so that GVD-AD dramatically limits the effective generation length for fast pulses. This can be seen by studying the THz pulse energy, which here is defined as the integral of the power spectrum from calculations using the model described in Chapter 2, as a function of propagation length, as shown in Figure 3.8b. The calculation began

*This range of tuning was proven experimentally by Hebling *et al.* [77].

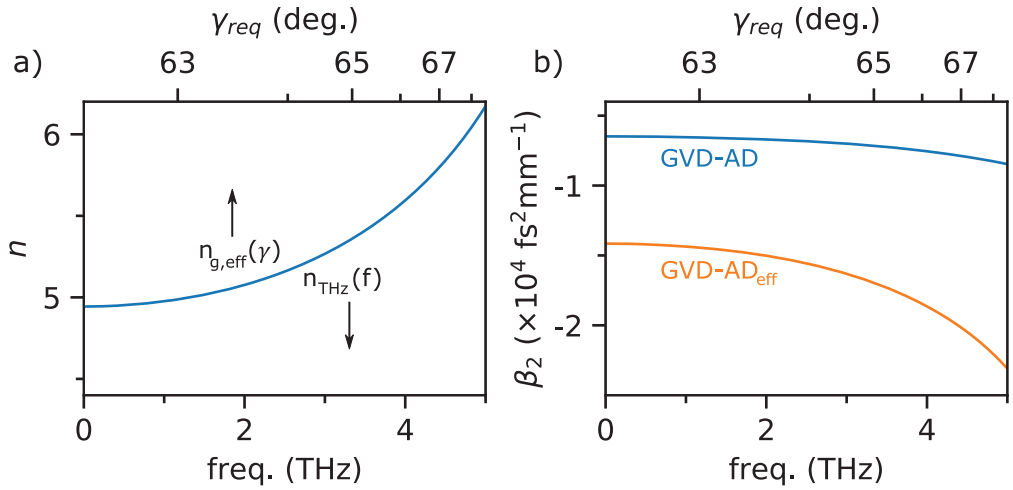

Fig. 3.7: Tilted-pulse front in lithium niobate. a Refractive index in LN as a function of frequency from 0-5 THz. The nonlinear scale along the top axis indicates the required PFT to phase-match the effective group velocity perpendicular to the pulse front to the corresponding THz frequency. **b** GVD-AD (blue) along the TPF propagation direction (normal to phase fronts) and effective GVD-AD (orange) along the THz propagation direction as a function of phase-matched frequency. The top axis again indicates the PFT required for phase matching at this frequency.

between the locations where $x'(\tau_{opt} = 0.75 \text{ ps})$, *i.e.*, the locations where the curves in Figure 3.8a cross the horizontal dotted line in the negative and positive x' regions. The green curve, corresponding to a 300 fs transform-limit pulse duration, shows the largest peak energy, which is expected from the results of ref. [65].

The 300 fs transform-limit calculation also shows the largest peak electric field in the time domain, as shown in Figure 3.8c. However, the field grows and peaks over a shorter distance than the pulse energy. The colored ticks along the bottom and top axes in Figure 3.8b and c indicate the locations where the pulse energy and field reach their maximum, respectively. The narrowing spectrum with increasing propagation distance, which was shown in Section 2.6 for collinear sources, results in a pulse broadening in the time domain so that the location with maximum energy is decoupled from the location of maximum field.

Although the calculation in Figure 3.8c suggests that the 300 fs transform limit pulse is still favorable for THz generation over faster pulses, however, this calculation has not yet taken into account the field enhancement from the tighter-focusing power

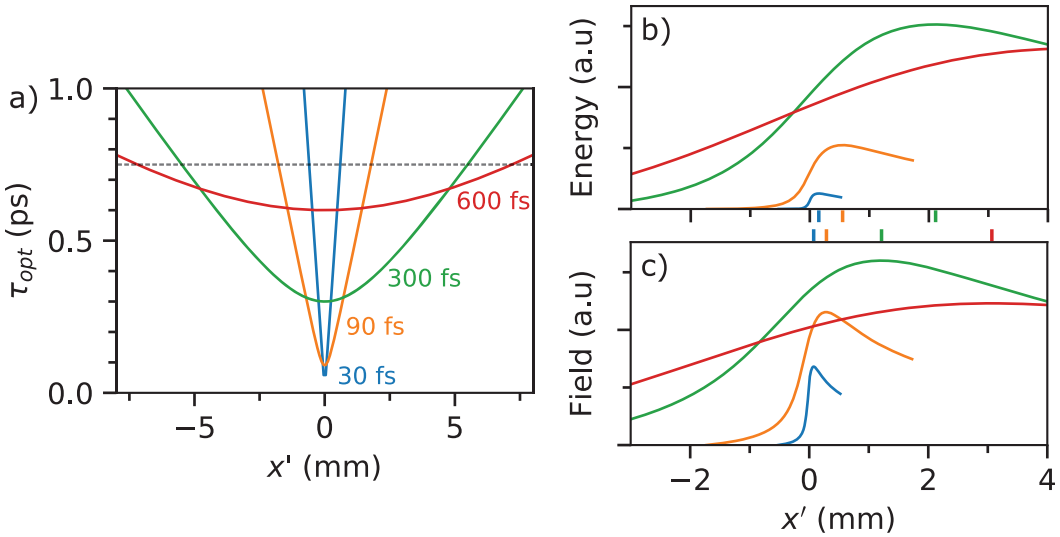

Fig. 3.8: TPF THz generation in LN. a Optical-pump pulse duration as a function of x', the THz propagation direction with the effective GVD from equation 3.26 for 4 different transform-limited pulse durations. The horizontal dashed line indicates a pulse duration of 0.75 ps. **b** THz pulse energy, defined as the integral of the power spectrum, as a function of propagation length. **c** Peak THz electric field in the time domain as a function of propagation length. The ticks along the top/bottom axes in **c**/**b** are the locations of maximum field/energy. For each transform-limit pulse duration the calculation was performed in the region where the pulse duration was less than 0.75 ps. The optical pulse energy was the same for each calculation.

of the broader spectrum. We can estimate the effect of focusing on the spectrum using a Gaussian optics approximation (see section 2.4). Assuming a pulse with a frequency-independent beam waist of 6 mm incident on a parabolic mirror with a 15 mm effective focal length,* the beam waist at focus is shown in Figure 3.9a. This calculation suggests a beam waist of approximately 0.28 mm at 1 THz.

The amplitude spectra taken from the x' location of the peak electric field for the 300 fs and 90 fs transform limit pump pulses are shown in Figure 3.8b (solid lines) along with the spectra found by assuming a focused field enhancement using the beam waist in Figure 3.8a. A more dramatic enhancement from focusing is observed in the 90 fs pump pulse due to its broader spectrum in comparison to the 300 fs source. Again plotting the peak-field as a function of x', however, including the enhancement from focusing, we see that the largest electric field is instead achieved with the 90 fs

*These values were chosen based on results from the Gen. 3a TPF source (see Chapter 4) in the Ultrafast Nanotools Lab. For further details see [51].

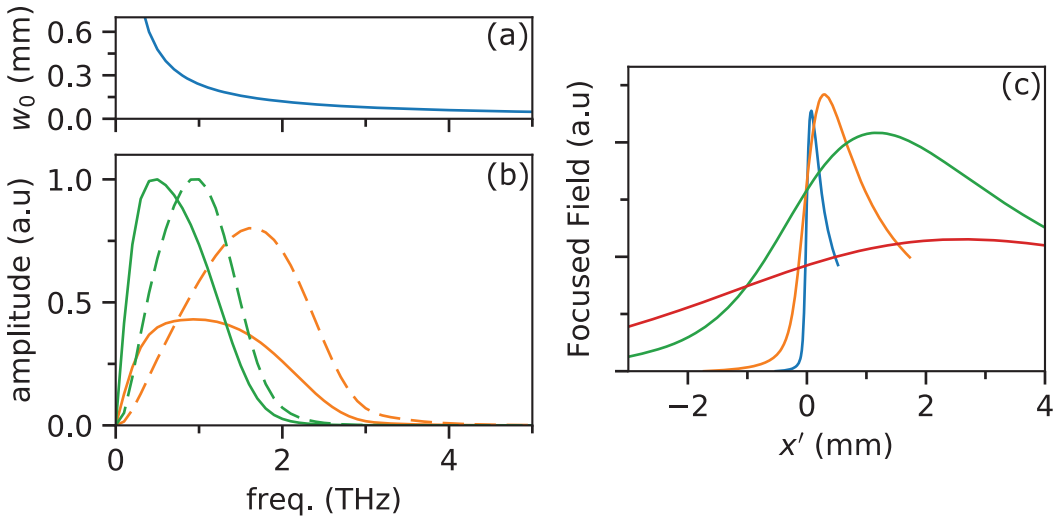

Fig. 3.9: Effect of focusing on the peak electric field. **a** Gaussian beam waist at the focus, w_0, assuming the pulse has a 6 mm beam waist incident on a mirror with a 15 mm EFL, similar to the Gen. 3a source (see Chapter 4). THz spectra for 90 fs (orange) and 300 fs (green) pump pulses taken at the x' location of the peak field from the calculations in Figure 3.8**c** normalized to the peak of the 300 fs spectrum (solid lines). The dashed lines indicate the spectrum at focus assuming the Gaussian beam waist in **a**, again normalized to the peak of the 300 fs spectrum. **c** Peak focused electric field as a function of THz propagation distance assuming a Gaussian beam waist as in **a**.

pump pulse, as seen in Figure 3.8c.

It is of course interesting to compare the calculated spectra and waveforms to experiment, which is done in Figure 3.10 for a 30 fs pump pulse. The calculated waveform in Figure 3.10a shows a similar carrier envelope phase to the experimental waveform shown in 3.10b.* Note that a $\pi/2$ phase shift was applied to the calculated waveform to account for the Guoy phase as the source was placed in a collimated region of the parabolic mirror arrangement.

Shown in Figure 3.10c and d are the calculated and experimental spectra, respectively, in the range of 0 to 5 THz. The calculation correctly predicts a peak frequency somewhere in the range of 1-2 THz with a broad spectrum. It appears to overestimate the bandwidth, showing spectral content beyond 4 THz as opposed to the data,

*This waveform/spectrum was taken from the Gen. 3a THz source (see Chapter 4). The ringing in the waveform after the main peak, as well as the sharp dips in the spectrum, are water absorption lines.

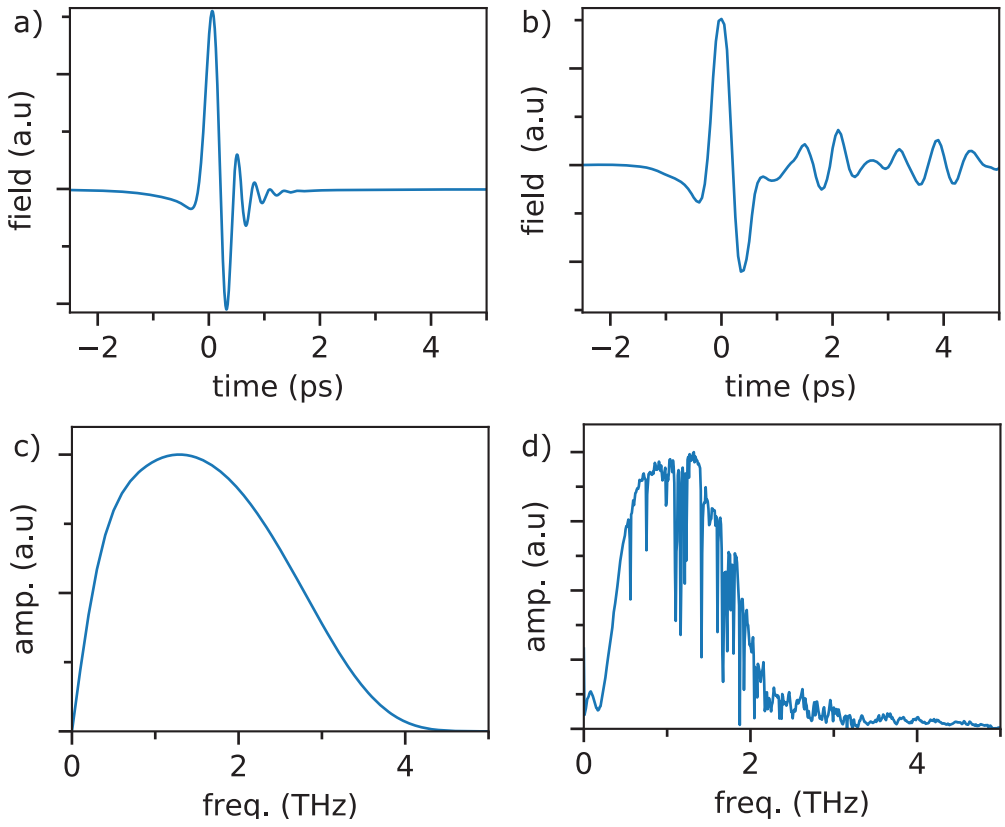

Fig. 3.10: THz generation in lithium niobate: theory versus experiment. a Calculated and **b** experimentally measured waveform from the Gen. 3a TPF source (see Chapter 4). The CEP of the THz waveform was shifted by $\pi/2$ to account for the Guoy phase. **c** Calculated and **d** experimentally measured THz spectrum.

which appears to cut off just beyond 2 THz on the linear scale (a logarithmic scale shows more high-frequency content). This is likely because the model underestimates the LN absorption in this region. MgO doping, which is necessary to mitigate the photorefractive effect, has the side effect of increasing absorption in this region [78]. Moreover, the 2-oscillator model of the dielectric function does not account for combination modes, which also could increase the absorption coefficient in this region [54, 79].

3.6 Tilted-Pulse Front THz Generation in Gallium Nitride

3.6.1 GaN as a Novel THz Emitter

Intense and narrow-band THz generation in the low-THz range is possible with LN [17] and organic crystals [80] as well as in the multi-THz range with GaSe sources using type-II phasematching, currently the most effective pulsed emitters in the 5-12 THz range are based on air-plasma sources, which have low spectral brightness [21]. While the TPF technique has been applied extensively in LN, it has also been used in alternative EO crystals such as GaAs [81] and GaP [82]. These works show that the TPF could enable THz generation in a much wider variety of materials than previously thought possible, which could present an opportunity for novel THz sources effective in the 5-12 THz range.

Of the binary semiconductors, GaN is particularly attractive as a novel TPF source because of its high phonon frequency, facilitating a broad THz bandwidth, its large band gap, facilitating high intensity (and therefore efficient) pumping, and relatively high EO coefficient. The properties of several EO crystals are summarized in table 3.2. GaN shows an EO coefficient 2 times smaller than ZnTe and significantly smaller than LN, however, its phonon frequency is 3 times higher than ZnTe and 2 times higher than LN so that its refractive index is essentially flat over a much broader range of frequencies. Alternatively, of the commonly used collinear EO crystals, GaP has the highest phonon frequency, however, its EO coefficient is half that of GaN. Moreover, the bandgap of GaN is comparable to that of LN so that 2-photon absorption is suppressed, which should enable pumping at significantly higher intensity compared to ZnTe and GaP. Moreover, as shown in chapter 2, the nonlinear source term in OR is proportional to the frequency. With such a high phonon frequency, the spectrum from a GaN-based emitter should be centered at a comparably much higher frequency. Finally, the high frequency spectrum should enable better spatiotemporal focusing, which would lead to higher peak electric fields.

Table 3.2: EO coefficient, TO phonon frequency, bandgap, 1 THz refractive index, and optical group index at 800 nm for several common EO crystals and GaN.

Crystal	r pm/V	f_{TO} THz	E_g eV	n(1 THz)	n_g(800 nm)
ZnTe	4.25	5.3	2.26	3.18[83]	3.23
GaP	1	10.98	2.24	3.41	3.67
LN	32	7.7	3.7	5.0	2.25
GaN	1.91[84]	15.93[50]	3.4[85]	3.22[50]	2.49[85]

3.6.2 Tunable THz Generation from 0 to 12 THz

As an additional advantage compared to LN, the PFT required for phase matching is much smaller in GaN, as shown in Figure 3.12a. Even phase matching to 13 THz, the PFT is only 53° so that the GVD-AD for a GaN TPF source is significantly smaller than that for a LN source. As we have already suggested that one of the benefits of the GaN emitter could be the high-frequency emission, the lower GVD-AD is especially useful to maintain a shorter pulse duration over a larger propagation distance. We also note that the material GVD in GaN is 490 fs^2mm^{-1}. Once again, this implies that the effective GVD of the TPF is dominated by GVD-AD.

To show the capability of TPF THz generation in GaN, in Figure 3.12a the THz waveforms calculated with 3 different PFTs and a 250 μm propagation length are plotted. The highest field strength occurs for the PFT matched to 4 THz (blue), which shows a nearly single-cycle pulse. Moving to a PFT matched to 8 THz (orange), the field strength is nearly as large as in the 4 THz case, however, it contains multiple cycles. Finally, with the PFT matched to 12 THz (green), the field strength is significantly lower and the field contains many cycles. Looking to the frequency domain, shown in Figure 3.12b, the spectrum from the PFT matched to 4 THz is quite broad, extending all the way to 10 THz. This suggests the potential for GaN-based THz sources in time-domain and time-resolved THz spectroscopy. The spectrum for the PFT matched to 8 THz develops a double-peaked spectrum. This occurs because the effective-generation length for lower frequencies is larger than for 8 THz

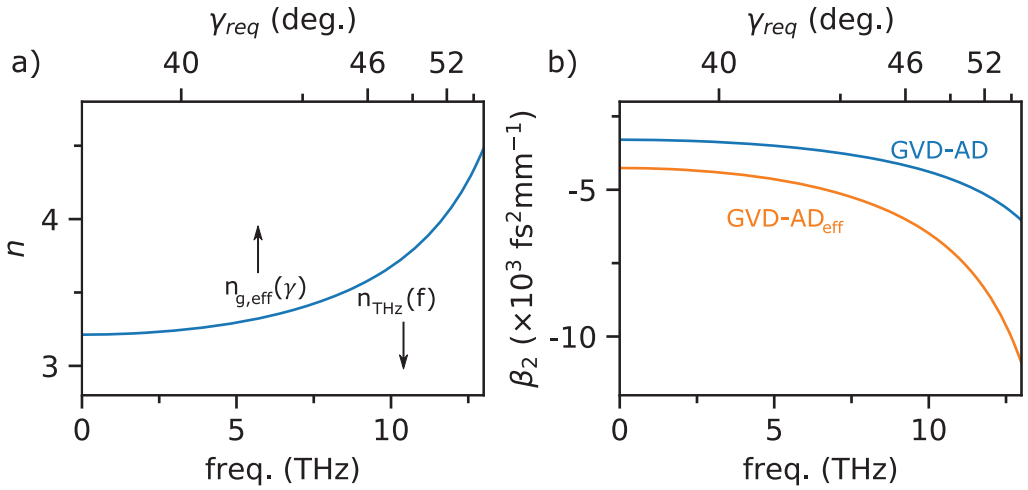

Fig. 3.11: Pulse-front tilt required in GaN. a Refractive index as a function of frequency from 0-13 THz in GaN. The nonlinear scale along the top axis indicates the required PFT to phase-match the effective group velocity perpendicular to the pulse front to the corresponding THz frequency. **b** GVD-AD (blue) along the TPF propagation direction (normal to phase fronts) and effective GVD-AD (orange) along the THz propagation direction as a function of phase-matched frequency. The top axis again indicates the PFT required for phase matching at this frequency.

because the nonlinear polarization remains large at low frequencies even after pulse-broadening to the effective GVD. Finally, the spectrum for the PFT matched to 12 THz is quite narrow. Notably, however, while the field strength in this case is several times smaller, the amplitude at the desired wavelength in the frequency domain is nearly half that of the 4 THz and 8 THz cases. This suggests that a GaN based TPF could be useful in applications that require narrowband resonant excitation such as nonlinear phononics.

We can learn more about the limitations of the generation process by studying the amplitude of the spectrum at the design wavelength as a function of distance in the crystal, as shown in Figure 3.13a. The amplitude at 4 THz grows over approximately 0.8 mm, which is a comparable effective generation length to ZnTe. At 8 THz, the effective generation length is smaller and at 12 THz, the field amplitude only grows for approximately 100 μm before. In standard THz generation by optical rectification, the three factors limiting effective generation length are phase-mismatch, absorption, and pulse broadening. In these simulations, we can rule out the phase-matching, as

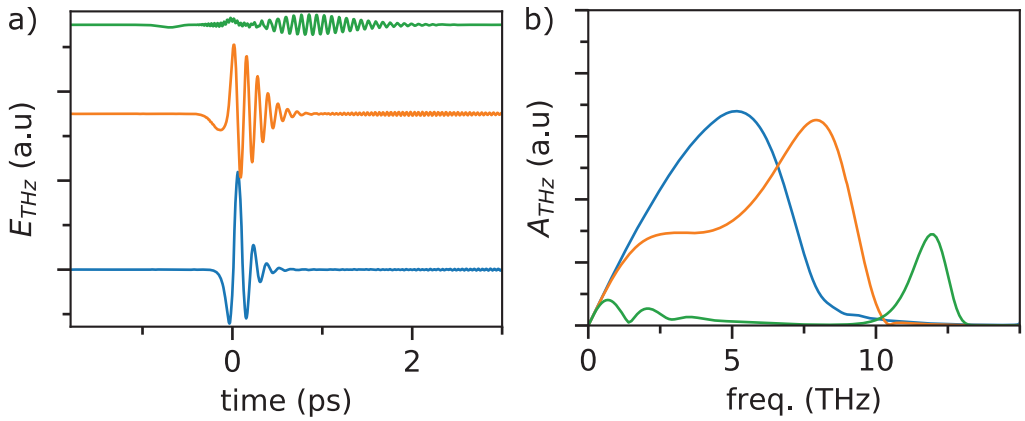

Fig. 3.12: Calculated high-frequency THz generation in GaN. a Waveforms and **b** spectra calculated for a GaN emitter with 800 nm excitation and various effective indexes.

the PFT technique implies an infinite coherence length. Moreover, the absorption at 12 THz is still quite low (this can be seen from the rate the amplitude decreases after its peak).

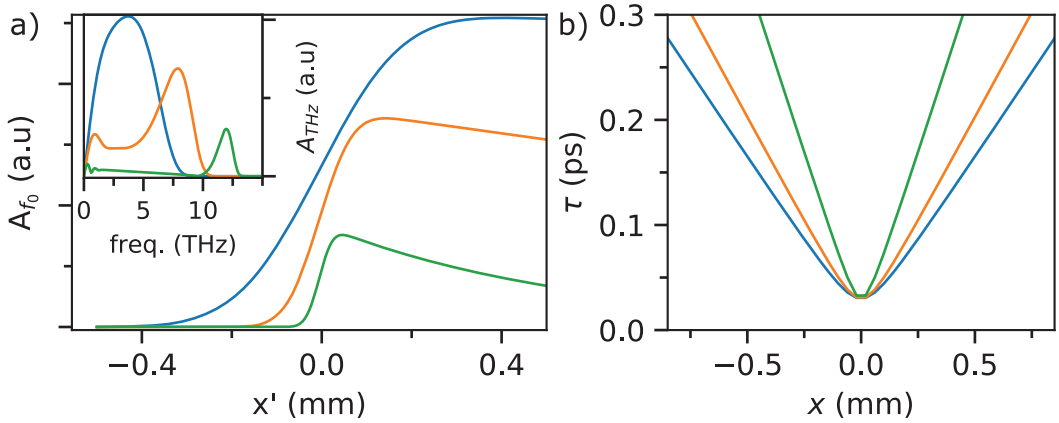

Fig. 3.13: Effective generation length in GaN. a Pulse duration along the THz propagation direction, x', for three different pulse front tilts designed to phase match at 4 THz (blue), 8 THz (orange), and 12 THz (green). **b** Field amplitude at the design frequency as a function of THz propagation distance. The inset shows the full spectrum at the location where the amplitude is maximum.

Therefore, despite the lower GVD-AD compared to LN, the strongest factor limiting THz generation at high frequencies is still the GVD-AD. This can be seen from the pulse duration as a function of distance, as shown in Figure 3.12a for PFTs matched to 4, 8, and 12 THz, again with a 30 fs transform-limit pulse duration. To efficiently

generate nonlinear polarization at, *e.g.*, f =10 THz the pulse duration must be less than approximately 0.05 ps (1/2f). Clearly, this only holds for a very narrow region near $x' = 0$.

3.6.3 Design of an Efficient Surface-Relief Grating in GaN

In addition to the phase mismatch between optical and THz, another reason that GaN has been overlooked as a potential THz emitter is the lack of suitable prisms for TPF THz generation in the standard geometry. Commercially available substrates with thicknesses of several hundred micrometers have only recently become available. This leads us to propose the design and construction of a contact-grating based TPF THz source. The simplest design for such a source involves etching a grating directly into the GaN surface, known as a surface-relief grating.

In order to design an efficient phase-grating, we used rigorous coupled-wave analysis (RCWA) [86] as implemented in a Stanford Stratified Structure Solver (S^4) [87]. S^4 is freely available software written in c++ with simple interfaces written in Lua and Python.* RCWA is a semi-analytic technique applicable to systems with periodicity in 2D, such as optical diffraction gratings. In the simplest grating design, with rectangular ridges, for a given line spacing, d, the ridge height, h, and width, l, can be varied to maximize the diffraction efficiency, as shown in Figure 3.14a. To find the optimal parameters for a GaN contact-grating THz source, for a given incidence angle the required line spacing is fixed based on the desired PFT.

For an incidence angle of 37°, as shown in Figure 3.14b, we find a line spacing of 424 nm to phase match to 1 THz. A 1 THz frequency was chosen for a proof-of-concept device instead of the higher frequencies because most EO sampling setups are most efficient in the low THz region. A parameter sweep of the ridge height and width is shown in Figure 3.14c, where darker red color indicates a higher diffraction efficiency. We found that ridge widths and heights of 190 nm and 300 nm provide the optimal conditions for high diffraction efficiency with large room for fabrication error. Cross sections of the efficiency along the dashed black lines in Figure 3.14c are plotted in Figure 3.14d and e to highlight the tolerances of the final device.

*Notably, the Python interface does not work very well and, at the time of writing, the Lua interface is recommended.

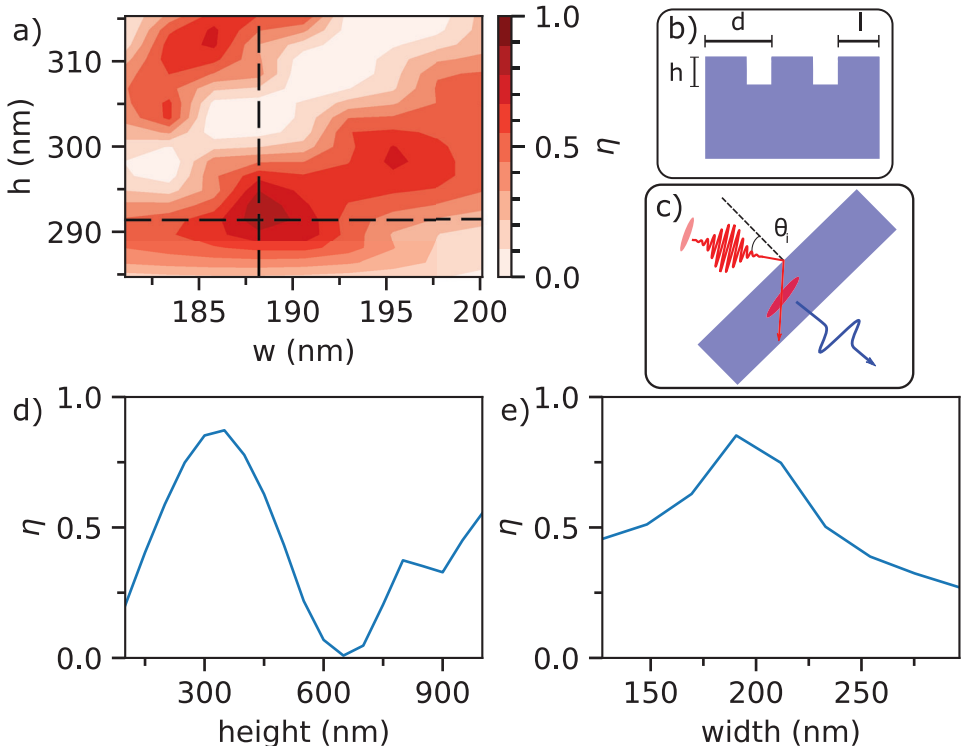

Fig. 3.14: Surface-relief grating for TPF THz generation in GaN. a Contour plot of the efficiency of a surface-relief grating in GaN as a function of ridge height and width. The grating period is 424 nm and the calculations were performed for an incidence angle of 37°. **b** Schematic layout of the grating. The design parameters were w=190 nm and h=300 nm, yielding the tolerance for experimental error. **c** Schematic illustration of the TPF layout. Calculated efficiency along **d** the dashed vertical line and **e** the dashed horizontal line on the contour plot in **a**.

Chapter 4

THz Source Development in the Ultrafast Nanotools Lab

In this chapter we discuss the development of intense terahertz (THz) pulse sources in the Ultrafast Nanotools Lab (UNL) using the Coherent Legend USP Ti:Sapphire amplifier (1 kHz, 3.6 mJ, 35 fs, 800 nm.[†]. This chapter provides an overview of the evolution of the source designs, which we categorize as Gen. 1, Gen. 2, and Gen. 3.[‡] The key innovations for new generation and the capabilities of each source are elaborated on. Furthermore, this chapter details the attempted application of flying focus [88, 89, 90] to THz generation in lithium niobate (LN), where the effective propagation velocity of an ultrafast pulse is controlled by exploiting chromatic aberration. Unfortunately, this first attempt was a null result. The reasons for this failure are discussed and future strategies for THz generation exploiting spatiotemporal control of laser intensity are introduced. Finally, several small projects involving intense THz pulse sources are detailed, including a Kapton-tape based antireflection (AR) coating for LN sources, the affect of water absorption on the peak electric field from TPF sources, and studies of narrowband high-field transport in photoexcited GaAs.

[†]Regarding the laser source, this system has also been discussed in refs. [59, 60, 51] Several additional aspects of this system that have not been addressed in other works are discussed in Appendix B.)

[‡]The individual tilted-pulse-front (TPF) THz sources have also been discussed in previous theses, refs. [59, 60, 61, 62, 51].

4.1 Tilted-Pulse-Front THz Sources

4.1.1 Overview

An overview of the various sources in the lab is shown in Figure 4.1. In total there are four TPF sources, which we loosely categorize based on their design principles as Generation 1, 2, 3a, and 3b. An additional THz source using flying focus was also constructed and will be outlined in the next section. Each TPF source has different characteristics and capabilities, which will be outlined in the following. In general, there are several figures of merit for intense THz sources, *e.g.*, the peak electric field, pulse energy, bandwidth, and peak frequency. The peak-electric field can be calculated in two ways. With knowledge of the pulse duration, spot size, and pulse energy the field can be calculated as,

$$E_{THz,pk} = \sqrt{\frac{2\eta_0 W}{A\tau}}, \tag{4.1}$$

where W is the pulse energy, $\eta_0 = 377\,\Omega$ is the free-space impedance, A is the area of the spot size, and τ is the pulse duration.*. Alternatively, the peak electric field can be calculated directly from the electro-optic (EO) sampling measurement. For the special case of zero phase mismatch, equation 2.29 can be simplified to,

$$\sin^{-1}\left(\frac{I}{I_0}\right) = \frac{2\pi}{\lambda} L n_0^3 r_{41} t_{GaP} t_{Si}^n E_{THz}, \tag{4.2}$$

where I/I_0 is the modulation ratio, λ is the probe beam center wavelength, L is the length of the active region of the EO crystal, n_0^3 is the phase index at the probe wavelength, t_{GaP} is the field transmission coefficient at the air-GaP interface, t_{Si} is the single-pass transmission of a high-resistivity silicon wafer, n is the number of silicon wafers, and r_{41} is the EO coefficient of the sampling crystal. The high-resistivity silicon wafers are used as they have a known transmission coefficient.

Each of the sources also has a different grating/imaging lens combination. A useful relation for calculation the PFT is given by [60],

$$\tan(\gamma) = \frac{N\lambda_0 D}{n_{opt}\cos(\theta_d)}, \tag{4.3}$$

*Several variations of this equation exist in the literature (see [91, 92, 59]) The peak field calculated from each method is generally similar up to a factor of $\sqrt{2}$

where γ is the PFT, n_{opt} is the optical group index, D is the demagnification of the imaging setup, N is the grating groove density, λ_0 is the center wavelength of the optical pulse, and θ_d is the diffraction angle.

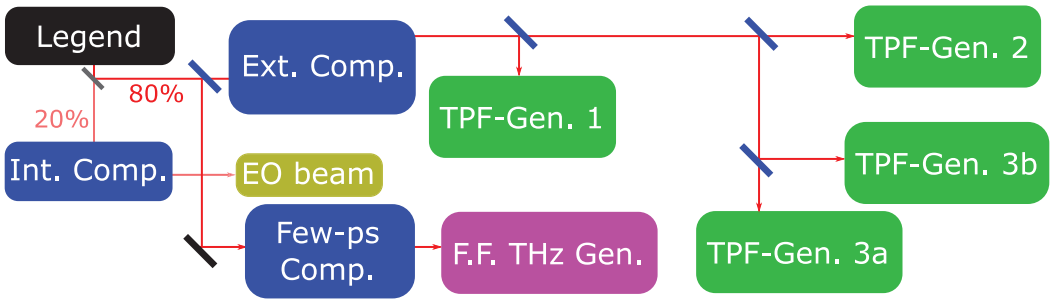

Fig. 4.1: Intense THz sources at UNL. Schematic layout of the THz sources coupled to the kHz amplifier. An 80/20 beamsplitter outside the Legend cavity is used to distribute the pulse energy to two compressors. The external compressor is used to control the pulse duration of the THz generation beams for TPF THz generation while the internal compressor is used to control the pulse duration of the EO gating beam for each source. The blue mirrors are insertable/flip mount mirrors to direct the compressed pulse to the various beamlines. The pulse can also be redirected before the external compressor to a few-picosecond compressor to provide pulse durations from 120 ps to 140 ps for flying focus.

4.1.2 Generation 1

The first-generation TPF source was constructed by A. K. Ayesheshim [59] and was based on the design of ref. [16]. The schematic layout of this source is shown in Figure 4.2a, where an 1100 ln mm^{-1} diffraction grating is imaged with a single 75 mm focal-length bi-convex lens into a LN prism. Heuristically, the source is assumed to be a point source of THz radiation and a parabolic mirror system is designed for transmission measurements with the sample location at a primary focus followed by an EO system at a secondary focus. An important innovation of this system was the construction of an external pulse compressor that enabled simultaneous control of the EO sampling pulse duration and the THz generation pulse duration (see ref. [59] for further details on the compressor and section 2.5 for details on the effect of pulse duration on EO sampling).

Shown in Figure 4.2b is the THz pulse waveform from this source along with the

corresponding amplitude spectrum in Figure 4.2b.* The peak frequency from this source was typically 0.5 THz with bandwidth from 0.2-2.5 THz. The spot size was measured using a thermal imager consisting of a pyroelectric array (Electrophysics) and was found to be approximately circular with e^{-2} diameters of 1.46x1.48 mm. The pulse energy of this measurement was 1.6 μJ and, using equation 4.1 along with the e^{-1} pulse width of 0.85 ps, the electric field is calculated to be 287 kV/cm.

With this source, there was a very large discrepancy between the peak field calculated using equations 4.1 and 4.2, *e.g.*, in Appendix C.1 of ref. [59], the field measured by EO sampling was found to be 88 kV/cm as opposed to 154 kV/cm as calculated from the energy, spot size, and pulse duration. Subsequently, this source was reconfigured to perform EO imaging. Interestingly, a similar field calibration was achieved with the EO imaging setup to that of the spot size/energy calculation [61]. This suggests that the difference was due to misalignment of the EO system or sub-optimal alignment of the recollimating/focusing parabolic mirrors, as the EO imaging was performed at the first focus.

4.1.3 Generation 2

In the second generation TPF source, which was first presented in ref. [60], the parabolic mirror arrangement remained the same as the Gen. 1 source, however, the grating imaging system was changed to a 4f system, as shown in Figure 4.3a, with an 1800 ln mm^{-1} line-spacing grating and bi-convex lenses with focal lengths 125 mm and 75 mm. The 4f setup is designed to minimize imaging error that reduces the efficiency of THz generation, a concept that was first introduced in the context of TPF-THz generation in a series of papers from the group of J. Hebling [93, 70, 65] and first implemented by Hirori *et al.* [17]. The three design criteria that should be satisfied for optimal THz generation, shown in Figure 4.3, are that the pulse-front tilt (PFT) should satisfy the velocity-matching condition (see Chapter 3), the pulse duration should be minimized along the same angle as the PFT,† and the curvature

*The data in this figure was reproduced from ref. [59]. It is included here as the head-to-head comparison of the best-case parameters of the various sources is useful and similar peak fields have not been obtained from this source by the present author.

†As a side note, this condition has been recently reexamined by Bodrov *et al.*, who suggest that in some cases the energy generation efficiency can be increased with different conditions [69].

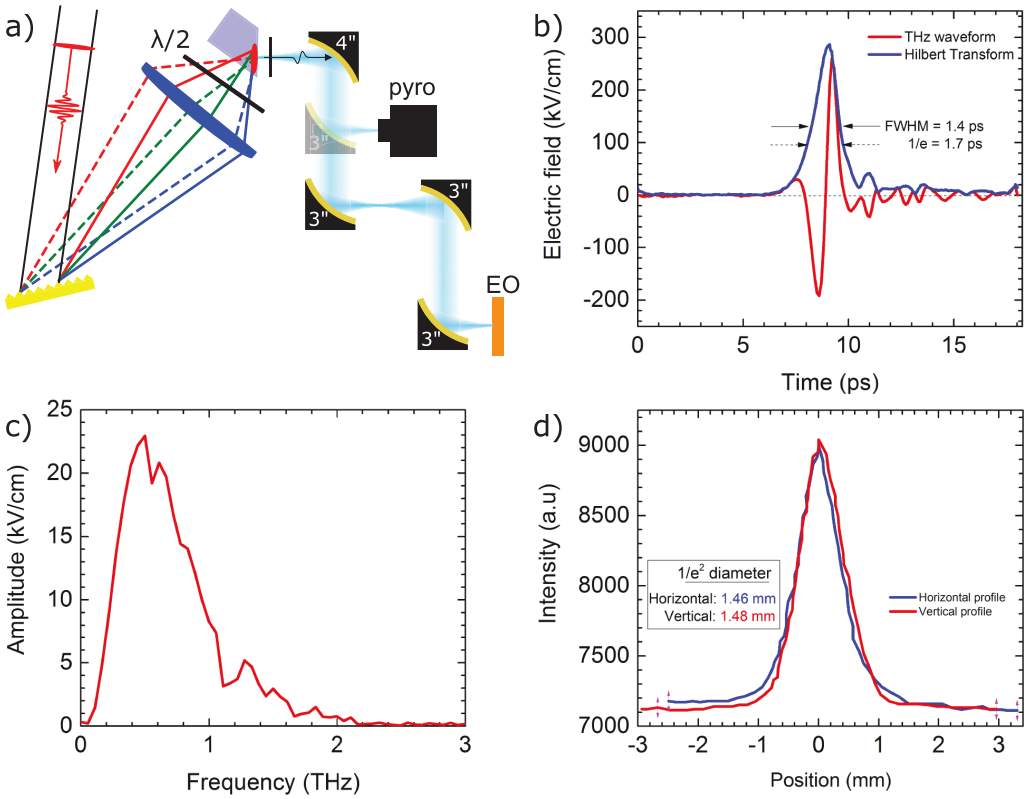

Fig. 4.2: First generation TPF source at UNL. a Schematic layout of the Gen. 1 TPF source, where the TPF from a 1200 ln mm^{-1} diffraction grating is imaged into an LN prism with a single 75 mm focal-length bi-convex lens. A half waveplate is used to rotate the polarization by 90° prior to the crystal as the diffraction grating efficiency is highest with horizontal polarization while the THz generation is maximized with vertical polarization. A 4" EFL 90° off-axis parabolic mirror collects the emitted THz radiation and a 3" parabolic focuses it to the sample location. A secondary focus is used for EO sampling. A black polyethylene sheet is used to filter the scattering 800 and 400 nm radiation from the generation pulse and second harmonic. **b** Electric field of measured by EO sampling in a 0.5 mm ZnTe EO crystal. The field was calibrated from the spot size, pulse energy, and pulse duration. **c** Amplitude spectrum from the Fourier transform of the time-domain waveform in **b**. **d** Beam profile measured from the pyroelectric imager. The plots in **b** to **d** were reproduced from ref. [59].

of the phase fronts should be small. Notably, while the first two conditions can be simultaneously achieved with a single-lens system, in the 4f system the wavefront curvature is much smaller, enabling much larger lateral size for the THz generation pulse [65].

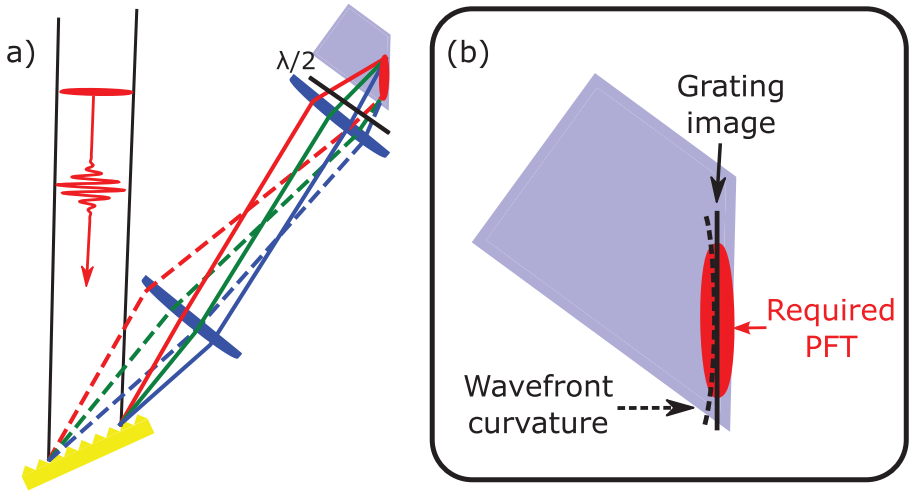

Fig. 4.3: Modified grating imaging. a Updated grating imaging optics, with an 1800 ln mm^{-1} grating and a two-lens imaging scheme (focal lengths 125 mm and 75 mm) to reduce image distortion. **b** Illustration of the three important parameters for TPF THz generation: the PFT, the grating image, and the wavefront curvature.

Subsequently to the work in ref. [60], the pulse characteristics of the Gen. 2 source were improved significantly. As shown in Figure 4.4, the source has achieved a peak electric field of 400 kV/cm, as measured by EO sampling in a GaP crystal with 250 μm (110) active layer and a 2 mm (100) inactive layer along with 3 field-attenuating high-resistivity silicon wafers to ensure the EO sampling remains in the linear regime (see section 2.5.1). The corresponding amplitude spectrum is shown in Figure 4.4b, showing bandwidth from 0.2-4 THz.* The peak frequency of this source is typically in the range of 0.6-0.9 THz. The background-subtracted spot profile at the focus (location of the pyroelectric detector in Figure 4.2a) is shown in Figure 4.4c and to fit the beam profile we use a 2D Gaussian fit, as shown in Figure 4.4d, using the amplitude, x/y width, and x/y location as free parameters. The image was taken with the pyroelectric imager and the background, acquired with the THz pulse

*This is quite broad for a TPF source in LN. However, it is possible to generate bandwidth beyond 5 THz in LN, as show for example in narrowband sources using parametric generation [94] or later in this chapter with a dry-nitrogen purged system.

blocked, was subtracted in post processor. The difference between the data and fit is shown in Figure 4.4e, revealing the non-Gaussian features of the beam profile, where the red regions indicate an underestimate of the fit and blue regions an overestimate. Clearly, we see that the data is more sharply peaked than a Gaussian function. In ref. [51], the beam profile was studied through a series of THz band-pass filters, revealing essentially Gaussian beam profiles with a a frequency-dependent focal spot size. This shows that the non-Gaussian nature of the broadband pulse results from the tighter focusing of higher frequencies. Interestingly, this work also revealed a frequency-dependent focal spot location, which could be indicative of spatiotemporal aberrations such as PFT.

From the fits, the e^{-2} diameters were found to be $d_x = 1.3$ mm and d_y=1.8 mm. The pulse duration was found to be a 0.8 ps* from a Gaussian fit to the amplitude of the Hilbert transform of the waveform in Figure 4.4a. With the pulse energy of 1.5 μJ, measured directly from the pyroelectric detector, this corresponds to a peak electric field of 340 kV/cm from equation 4.1, which is reasonably close to the value of 400 kV/cm measured by EO sampling. It is interesting that for this source, the field measured by EOS is even higher than that measured by the energy/spot size calculation, which is likely a result of several things. First, the calibration of the pyroelectric detector could be incorrect and the THz pulse energy could be higher. Second, the Gaussian approximation to the beam profile underestimates the peak intensity, as seen in Figure 4.4e, so that the field calculation of equation 4.1, which is based on Gaussian optics, underestimates the peak field. Third, an alternative to equation 4.1 was proposed in ref. [59] that results in an electric field that is larger by a factor of $\sqrt{2}$, which would imply that the peak field this spot size, energy, and pulse duration would be 480 kV/cm. In this case, it is the EOS calibration that underestimates the peak field, however, as discussed in chapter 2.5, the phase-mismatch of sampling/THz pulses, the finite duration of the sampling pulse, and the phase shift on transmission of the THz pulse can affect the EOS measurement so that the EOS calibration is likely an underestimate of the peak field. Based on this discussion, it is clear that precision metrology of the THz field remains an ongoing

*Here the pulse duration is considered to be the e^{-1} full width to remain consistent with refs. [15, 59]. The e^{-1} half-width is used for the field calculation.

challenge.

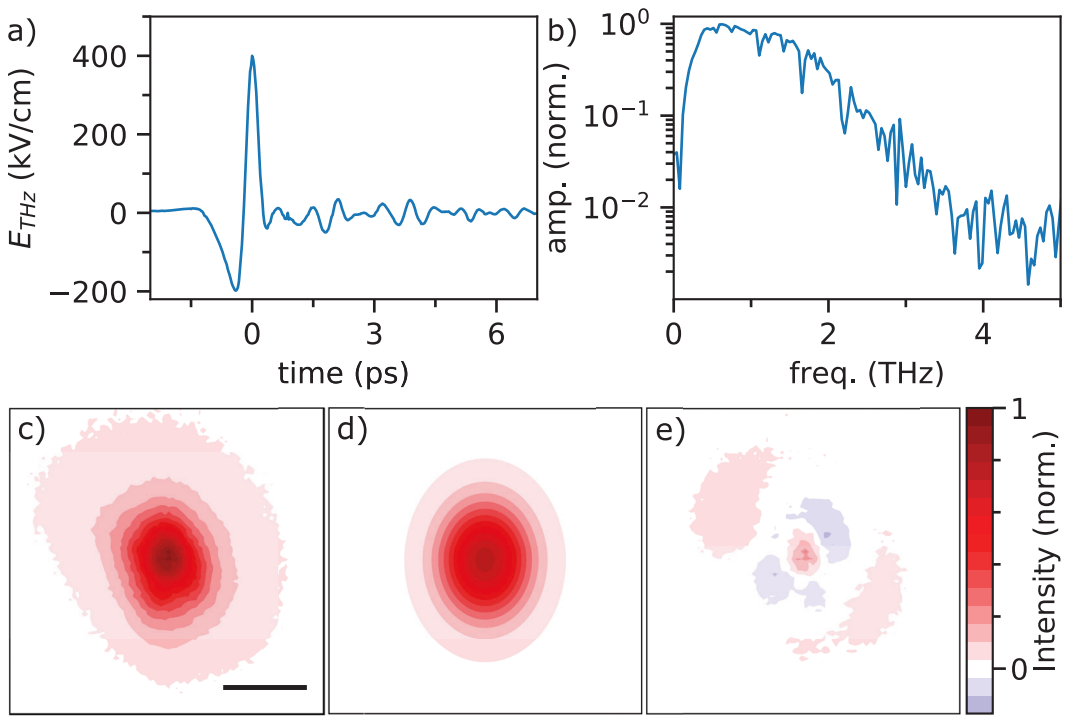

Fig. 4.4: Second generation TPF THz source. **a** THz waveform measured by EO sampling in a 0.25 mm GaP sampling crystal with a field strength calibrated from the modulation in EO sampling. **b** Corresponding amplitude spectrum, with frequency content up to 4 THz. **c** THz beam profile measured with the pyroelectric imager. **d** 2D Gaussian fit to the profile in **c** and **e** difference plot of the beam profile and the Gaussian fit. The scale bar in **c** is 1 mm.

4.1.4 Generation 3

In the third generation (Gen. 3) of the tilted pulse front sources in UNL, there were three main innovations. The first was a change to the parabolic mirror arrangement, which is shown in Figure 4.5a. The heuristic for this layout is that the THz source is assumed to be collimated at the exit face of the LN prism. The first mirror in the system is a 1/2" diameter 90° off-axis parabolic with a 15 mm effective focal length (EFL) that is used as a beam expander. The second is a 2" diameter collimating mirror with a 4" EFL. The second innovation for this generation was the use of cylindrical lenses in the grating imaging optics, the idea being that there is no need to introduce additional wavefront curvature in the vertical dimension as only the hor-

izontal dimension must be imaged. Both of these modifications were first introduced by Hirori *et al.* in ref. [17]. Additionally, a silicon brewster window was also used in place of black polyethelyne to filter the pump beam and its second harmonic, as shown in Figure 4.5b, which resulted in a small increase in the peak electric field as the black polyethylene attenuates and disperses the THz pulse a small amount. The focal lengths in this setup were 100 mm and 60 mm and the diffraction grating groove density was 1800 ln mm^{-1}.

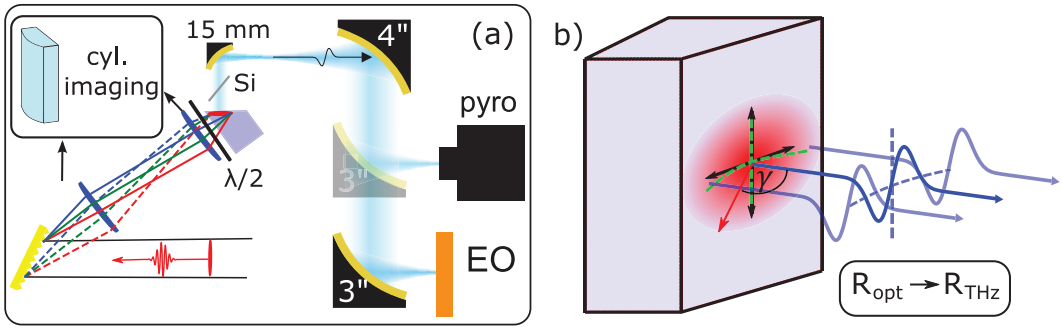

Fig. 4.5: Redesigned THz optics. a Schematic layout of the Gen. 3 THz sources. The grating images, which were spherical in the Gen. 1 and 2 sources, were replaced with cylindrical lenses. The focal lengths in this setup were 100 mm and 60 mm and the grating groove density was 1800 ln mm^{-1}. The parabolic mirror arrangement was updated to include a 15 mm EFL beam expanding mirror. A silicon brewster window is also used to remove the scattered optical pulse in place of a black polyethylene filter. **b** Illustration of the principle of collimated TPF THz generation, where the wavefront of the THz pulse (blue dashed lines) inherits the wavefront curvature of the optical pump pulse (green dashed lines).

The third innovation was the introduction of a cylindrical zoom lens to provide a tunable vertical spot size of the THz generation pulse before the grating-imaging optics, as shown in Figure 4.6a. The idea behind the zoom lens is that the THz generation efficiency of TPF sources in LN shows an optimal fluence [95, 96, 97] so that a tunable spot size is desirable. At the same time, we found that it was more difficult to achieve collimated THz emission in the horizontal dimension as opposed to the vertical dimension so that a large horizontal spot size, and therefore more uniform beam, was desirable. The zoom lens consisted of 3 cylindrical lenses with focal lengths 25 cm, -5 cm, and 20 cm. The magnification as a function of lengths l_{12} and l_{13}, as defined in Figure 4.6a, is shown in Figure 4.6b. The THz pulse energy as

a function of magnification is shown in Figure 4.6c, showing a clear maximum.*

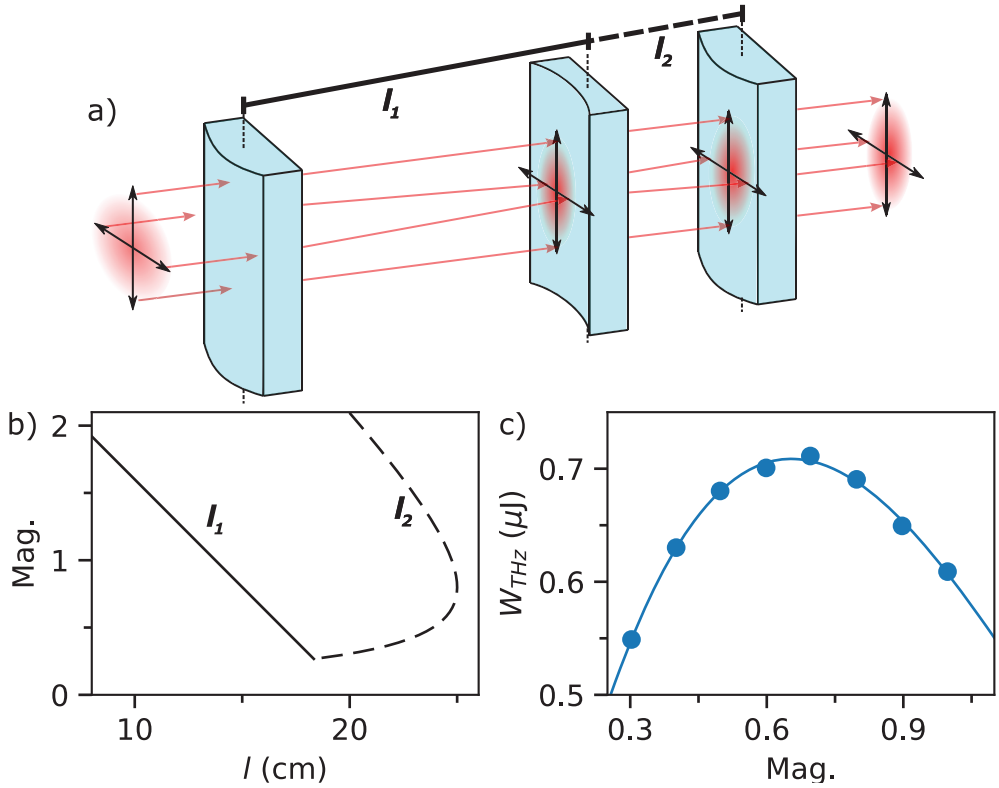

Fig. 4.6: Beam-shaping optics. a Cylindrical zoom lens arrangement. **b** Magnification as a function of lens lengths, tunable down to a magnification of approximately 4. **c** THz energy as a function of zoom-lens magnification, acquired without realigning the source at each magnification.

Two sources were constructed with this layout, referred to here as source Gen. 3a and 3b (these sources were first described in ref. [51] and [62], respectively.). Gen. 3a was designed for biological exposures to study the effects of pulsed intense THz radiation of biological systems and is coupled to a visible microscope aligned longitudinally to the THz beam path at the focus. Gen. 3b was designed for investigation of THz-modulation of luminescence in low-bandgap materials [98] and is coupled to an IR spectrometer. It is also configured for transmission measurements.

The two sources differed in the optics used to image the grating into the LN prism.

*This data was collected from source Gen. 3b, which is described in detail in ref. [62], without realignment of the grating imaging at each magnification. Similarly to the effect of compressor setting, the source must be realigned at each magnification to achieve the best output. It is likely that the maximum at M=0.7 is not a global maximum.

In Gen. 3a, a 4f imaging system using cylindrical lenses focal lengths $f_1 = 10$ cm and $f_2 = 6$ cm was used. The same configuration was used in Gen. 3b, however, the focal lengths were $f_1 = 25$ cm and $f_2 = 15$ cm. The peak electric field obtained with Gen. 3a was 640 kVcm while for Gen. 4b it was just 290 kV/cm. The origin of this large difference in peak electric field is unclear, however, we speculate on several possibilities here. For example, the wavefront curvature from the Gen. 3b imaging optics could be larger than for the Gen. 3a system, which would fundamentally limit the peak fields attainable from this source. Moreover, the larger focal lengths of the Gen. 3b optics with respect to the Gen. 3a optics necessitates larger aperature, and therefore thicker, lenses, which are likely to introduce additional aberrations that distort the tilted-pulse front and reduce generation efficiency. Alternatively, we note that the THz pulse in source Gen. 3b propagates through an additional focus before EO sampling. Anecdotally, this secondary recollimation step can be difficult and relies on precise alignment of both the parabolic mirror system and of the THz pulse with respect to the system, which could make it much more sensitive and therefore more difficult to achieve high peak fields.*

As the Gen. 3a source had a significantly higher field than the Gen. 3b source, in Figure 4.7 we characterize its properties in detail. Shown in Figure 4.7a is the THz waveform calibrated to the peak field measured by EO sampling with a GaP wafer with a 200 μm (110) active layer and 2 mm (100) inactive layer.† The corresponding amplitude spectrum is shown in Figure 4.7b, showing an extremely broad spectrum with a peak well above 1 THz. Note that simulations of TPF generation predict a similarly broad/high frequency spectrum with sub-50 fs generation pulses [65]. The beam profile with this source, shown in Figure 4.7c, is significantly smaller than that of the Gen. 2 source in Figure 4.4c. The spot size from the 2D Gaussian fits, shown in Figure 4.7d was found to be 1.25 x 1.43 mm^2. The difference plot, shown in Figure 4.7e, shows similar non-Gaussian features as the Gen. 2 source, where the data is more sharply peaked than a Gaussian profile.

*This is a common sentiment shared informally with a number of other researchers. However, some groups have successfully constructed transmission setups using this parabolic mirror configuration that have electric fields greater than 500 kV/cm (see, *e.g.*, ref. [99].

†For this waveform, the peak field was only 605 kV/cm as opposed to the record high of 640 kV/cm.

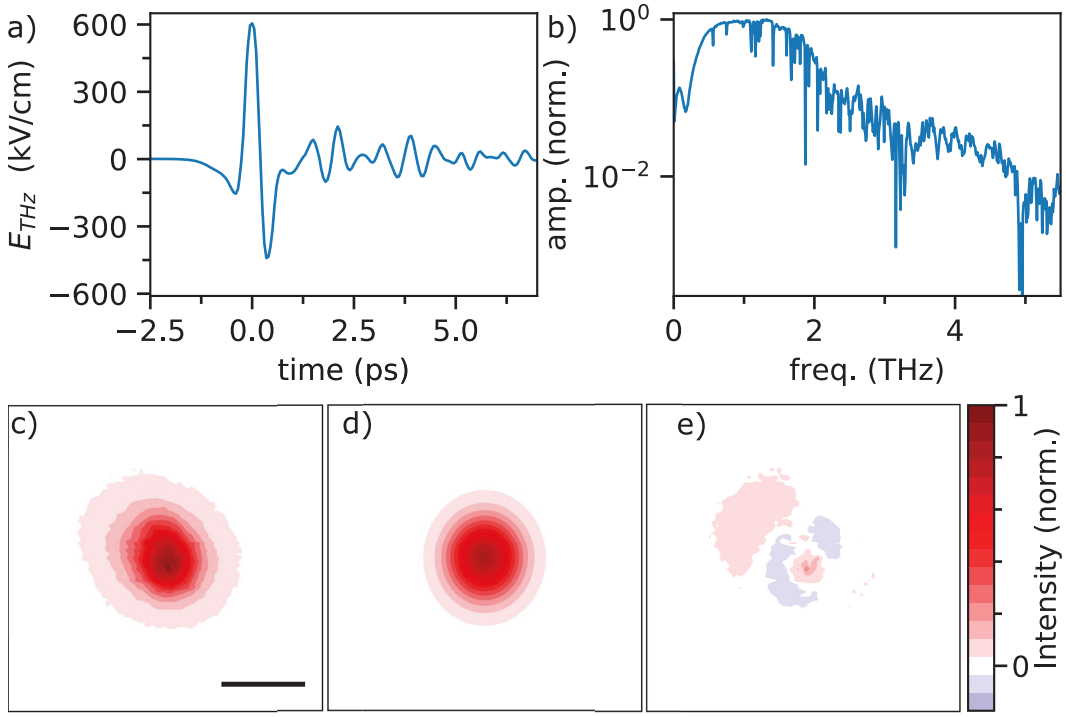

Fig. 4.7: Third generation TPF THz Source. **a** THz waveform measured by EO sampling in a 0.2 mm GaP sampling crystal calibrated with the signal modulation from EO sampling. **b** Corresponding amplitude spectrum, with frequency content up to 4 THz. **c** THz beam profile measured with the pyroelectric imager. **d** 2D Gaussian fit to the profile in **c** and **e** difference plot of the beam profile and the Gaussian fit. The scale bar in **c** is 1 mm.

Along with the pulse duration of 0.45 ps (e^{-1} point of the Hilbert transform) and pulse energy of 1.45 μJ, from equation 4.1 we find a peak electric field of 412 kV/cm, which, similarly to the Gen. 2 source, is again lower than that measured by EO sampling. The discussion of possible factors leading to this discrepancy in the previous source could also apply to the Gen. 3 source.

4.1.5 Outlook

The properties of the four TPF THz sources are summarized in table 4.1. The strongest fields obtained were from source Gen 3a, of up to 640 kV/cm, however, we note that it took a great deal of effort to achieve this value. With day-to-day operation, field strengths exceeding 500 kV/cm were quite commonly achieved. This sensitivity is quite common in the field and highlights the complexity of these sources.

Table 4.1: Parameters for each of the TPF THz sources in UNL. W_{max}, the highest energy achieved, W_{opt}, the energy of the source with optimum field, $r_x \times r_y$, the Gaussian e^{-2} full width, τ, the e^{-1} full width of the absolute value of the Hilbert transform, $E_{max,EO}$, the peak electric field measured by EO sampling, $E_{max,pyro}$, the peak electric field measured from equation 4.1, f_{max}, the peak frequency of the amplitude spectrum, and Δf, the full bandwidth of the source.

Gen.	W_{max}	W_{opt}	r_x/r_y	τ	$E_{max,EO}$	$E_{max,pyro.}$	f_{max}	Δf
-	μJ	μJ	mm^2	ps	kV/cm	kV/cm	THz	THz
1	2.2	1.6	1.46/1.48	1.7	164	287	0.5	0.2-2.5
2	4.0	1.6	1.55/2.01	0.8	400	340	0.8	0.2-4
3a	2.0	1.45	1.25/1.43	0.9	640	412	1.3	0.2-4.5
3b	-	0.7	1.26/1.16	-	290	-	0.9	0.2-3.5

To facilitate the use of strong fields, in the future it would be extremely useful to have more complete and automated characterization of the laser pulse parameters, especially the laser mode and beam pointing. Another issue with these sources is that small changes in pointing can lead to timing fluctuations that are large with respect to the cycle duration, which results in increased phase noise (see ref. [51]). It is therefore possible that the signal-to-noise in these systems could be significantly improved with stabilized beam pointing, which would facilitate the precise alignment required to achieve strong fields.

Looking to the literature, we see that there are several reports in the literature of TPF sources using similar lasers that produce field strengths approaching or greater than 1 MV/cm [17, 100, 101] and, in a select few cases, greater than 1.5 MV/cm [102] and even 2 MV/cm [103]. There are several improvements that could be made immediately to improve the electric field of the UNL sources. As will be discussed in a following section a dry nitrogen purge of the Gen. 2 source improved the electric field by approximately 10%. Due to the broader bandwidth and higher peak frequency of the Gen. 3a source, improvements of at least 10% could be expected, bringing the peak field to over 700 kV/cm. Moreover, the final focusing mirror in the Gen. 3a source has a 3" effective focal length, which could easily be replaced with a 2" focal length mirror. A simple estimate using Gaussian optics suggests that this could

decrease the focal spot e^{-1} point from 0.7 mm to 0.5 mm, which would represent an increase in the peak electric field of 1.5 times based on equation 4.1.* While in practice it is possible that such a large enhancement would be achieved, taking this calculation at face value suggests peak fields in excess of 1 MV/cm. Finally, although the GaP detector has a broad bandwidth, there is still phase mismatch that reshapes the measured THz field and deconvoluting the detector response [103] or using an ultra-thin sampling crystal [102] are likely to reveal even higher values of the electric field.

It is also worth noting that the THz generation pulse in the Gen. 3a source has an energy of 2 mJ at the LN crystal, while many of the previous citations report nearly double this value. While scaling up the generation-pulse energy represents the most direct way of improving the peak field, it should be noted that care must be taken to avoid pump-pulse reshaping, which significantly distorts the emitted THz wavefront and reduces the focusing power of the beams [95, 104]. It is quite typical to see large red-shifting of the center frequency with multi-millijoule pump lasers. As seen in table 4.1, the pulse energies from the various sources in UNL are quite comparable, however, the ones with larger bandwidth, and therefore shorter pulse duration, produce significantly higher peak electric fields.† For this reason, it is possible that emerging sources using a discretely tilted pulse front with a stair-step echelon, which facilitates ease of alignment, could be more well suited to high-power THz generation [97]. However, the limitations of this technique remain unclear and the highest fields to date have been obtained with the conventional grating based sources.

4.2 Flying Focus

As discussed in Chapter 3, the frequency-domain analogue of PFT is angular dispersion, which, historically, was seen as an optical aberration and care was taken to avoid it in, *e.g.*, prism and grating compressors. TPF THz generation can therefore

*This calculation assumes a Gaussian beam with a 0.7 mm e^{-1} radius at 1 THz.

†Note that the value for the peak electric field from EO sampling for the Gen. 1 source was not reported in ref. [59] for the alignment with the highest field from the spot-size measurement. The value in this table calculated using the reported ratio of the field strength from EO sampling to the energy/spot size calculation reported in the appendix of that work.

be seen as a method of exploiting optical aberrations to control the spatiotemporal propagation of laser pulses. A new method of spatiotemporal control, dubbed the flying focus, was recently introduced that exploits chromatic aberration and pulse chirp to control the effective focal velocity of laser pulses [88, 89, 90].

The principal of the flying focus is illustrated in Figure 4.8a, where a chirped optical pulse is incident on a chromatic lens* with a longitudinal dispersion of $dz/d\lambda$ so that each frequency is focused to location $z_0(\lambda) = dz/d\lambda(\lambda - \lambda_0)$. We consider the chirped pulse as a superposition of wavepackets, where the relative arrival time of each wavepacket is given as $\tau_0(\lambda) = d\tau/d\lambda(\lambda - \lambda_0)$† so that each wavepacket arrives at its focus at time $\tau(z_0) = \tau_0(\lambda) + z_0(\lambda)/c$, as illustrated in Figure 4.8b. We assume the intensity is maximum at any given z when the corresponding wavepacket arrives, which holds as long as it is high enough intensity compared to the combined contributions of the off-focus wavepackets, and we can directly write the flying focus velocity as,

$$\frac{v_{FF}}{c} = \frac{1}{c}\frac{z_0}{\tau(z_0)} = \left(c\frac{d\tau}{d\lambda}\frac{d\lambda}{dz} + 1\right)^{-1}, \tag{4.4}$$

which is equivalent to the expression in ref. [89].

Shown in Figure 4.8c is a calculation of the flying focus intensity for three z locations as a function of time (solid lines) using Gaussian optics (see section 2.4). The intensity of the focusing chirped pulse with no chromatic aberration is also plotted for comparison. Relative to the zero-chromatic aberration chirped pulse, the intensity envelope of the flying focus travels more slowly. In fact, by controlling the pulse duration and/or chromatic aberration, the flying focus velocity can be continuously tuned and, for example, matched to the THz pulse velocity in an EO crystal. While large temporal chirp is required to provide this control, which we have seen is detrimental to THz pulse generation (see chapter 2), however, another consequence of the flying focus is that the effective pulse duration of the focus is decoupled from that of the zero-chromatic aberration chirped pulse. Plotted in Figure 4.8c are the intensity envelopes of the flying focus which is also seen in Figure 4.8c where the pulse duration is much shorter for the flying focus than the zero-chromatic aberration pulse. Fur-

*Here, a diffractive lens is used due to its inherently large chromatic dispersion, however, this is not a requirement.

†For simplicity we have chosen $z_0(\lambda_0) = 0$ and $\tau_0(\lambda_0) = 0$.

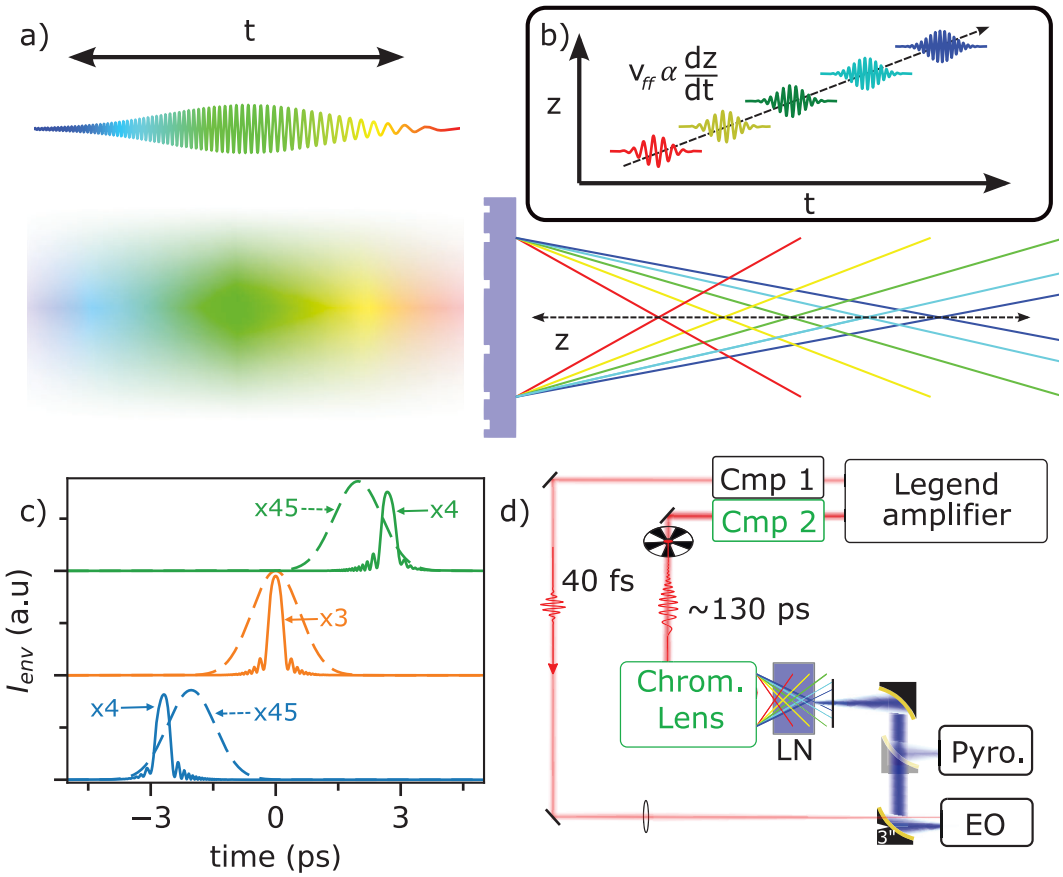

Fig. 4.8: Spatiotemporal control of pulse-propagation with flying focus. **a** Principle of the flying focus: a chirped pulse, where the instantaneous frequency (color) changes with time (t), is incident on a diffractive lens with large chromatic dispersion. The focus of each wavelength is located at a different depth (z location) with respect to the lens. The field as a function of time at each spatial location is shown schematically on the top right, where a pulse of varying center frequency arrives at a different time for each depth. **b** Calculation of the pulse envelope along the propagation axis for zero chromatic dispersion (chirped pulse propagating at the speed of light) and for large chromatic dispersion (flying focus propagating slower than the speed of light). **c** Schematic layout of the flying focus THz generation setup. A transmission grating compressor (Cmp 2, green) capable of few-ps compression enables tuning the optical pulse duration (chirp) by 10-20 ps while the chromatic lensing system enable control of the chromatic dispersion. 80% of the Legend power was used for the flying focus while a small part of the remaining power, which was fully compressed using the internal compressor, was used for EO sampling.

thermore, the peak intensity as a function of position away from the focus behaves different than that of the zero-chromatic aberration pulse. In Figure 4.8c, the intensities of the chirped pulse (dashed green and blue curves) and the flying focus (solid blue and green curves) were scaled to equal the peak intensity of the zero-chromatic aberration pulse. This shows that the intensity remains high along the propagation direction of the flying focus.

Together, these properties led us to speculate that the flying focus could be used to efficiently generate THz over a large propagation length, and we constructed an apparatus to test this idea. A simplified version of the setup is shown in Figure 4.8d. As suggested by equation 4.4, the focal velocity can be controlled by both tuning the pulse duration or chromatic aberration. To this end, a tunable compressor providing an intermediate range of compression (10-20 ps) was designed and constructed at UNL while a tunable chromatic lensing system was designed and constructed by G. W. Jenkins at the Laboratory for Laser Energetics (Cmp 2 and Chrom. Lens in Figure 4.8d). A parabolic mirror system consisting of a collimating mirror and a focusing mirror was used to direct the beam to either a pyroelectric detector coupled to a lock-in amplifier or an EO detection setup using the fast pulse from the internal Legend compressor.

As the flying focus required pulse durations of over 100 ps, we started with the uncompressed output of the Legend amplifier. To test the pulse duration and compressor operation, we constructed a cross correlation setup as shown in Figure 4.9a. The compressor consisted of two transmission gratings followed by a tilted retroreflector to couple out the beam. Shown in Figure 4.9b is an example of a spectrally-resolved cross correlation, which we can use to either measure the duration of the envelope directly or to extract the instantaneous wavelength of the chirped pulse using,

$$\lambda_{SFG,pk}^{-1} = \lambda_0^{-1} + \lambda_{inst}^{-1}, \tag{4.5}$$

where $\lambda_{SFG,pk}$ is the time-dependent peak of the spectrum of the sum-frequency generation (SFG) cross-correlation, λ_0 is the center wavelength of the gate pulse, and λ_{inst} is the instantaneous wavelength of the chirped pulse. λ_{inst} is plotted as a function of time delay for the minimum and maximum compression in Figure 4.9c,d, with a slope

ranging from 0.21 nm/ps to 0.24 nm/ps. With the 30 nm full-width at half maximum (FWHM) bandwidth of the Legend amplifier, this corresponds to FWHM pulse durations of 143 ps and 121 ps, respectively. The pulse durations calculated from the intensity were 110 ps and 92 ps, respectively, which implies a similar amount of pulse compression but disagrees quantitatively with the calculation from the instantaneous wavelength. The origin of this discrepancy is not fully understood, which presented some ambiguity in the required chromatic dispersion to achieve phase matching of the flying focus to the THz pulse. This was achieved using a multi-lens chromatic aberration system, which will be discussed in detail here.

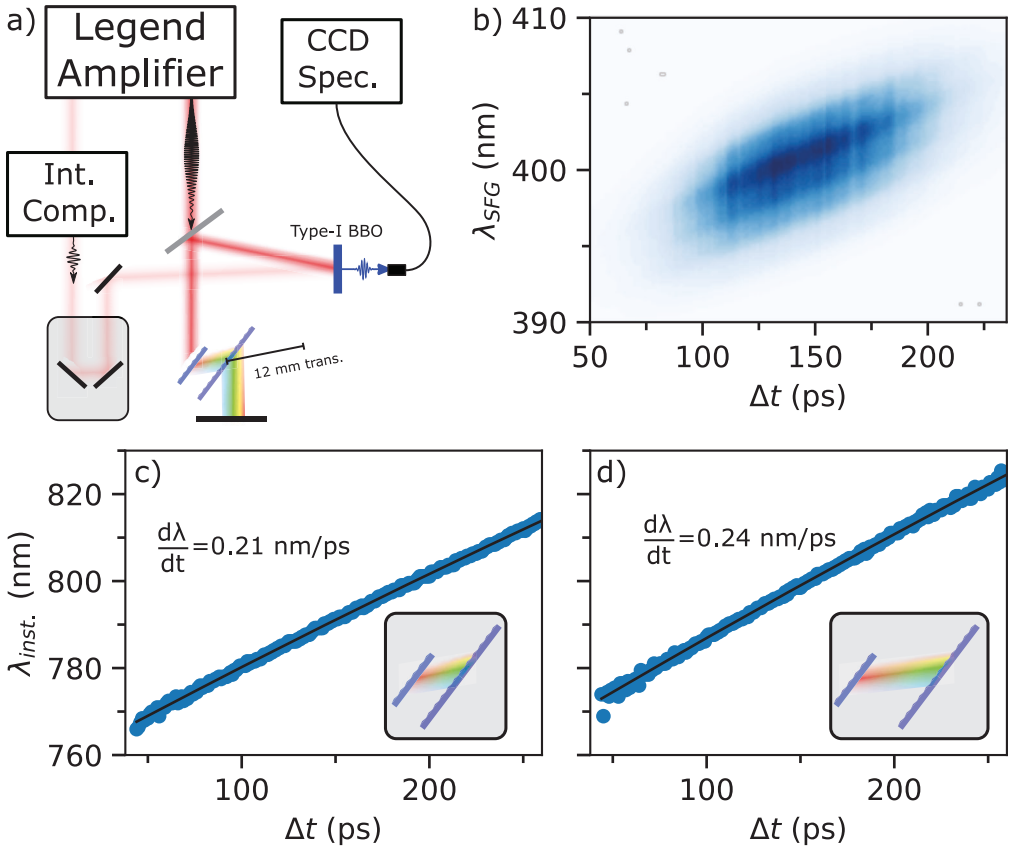

Fig. 4.9: Uncompressed pulse measurement. **a** Schematic layout of the cross-correlation setup and the few-picosecond transmission-grating compressor. **b** Representative spectrogram from the cross-correlation. Instantaneous center wavelength as a function of time extracted from the spectrogram at **c** the minimum compression and **d** the maximum compression achievable from the transmission grating compressor.

The incoherent detection with the pyroelectric detector coupled to the lock-in amplifier enabled us to rapidly scan a large range of pulse durations and chromatic

aberrations. Based on experience with TPF sources, we estimate this configuration is sensitive to nJ level pulse energies, however, we were unable to find any evidence of THz generation. Knowing that coherent detection is much more sensitive, we attempted to measure the THz generation with EO sampling. In order to validate the EO system, we first measured the sampled the THz pulse generated from the entrance and exit faces of the LN prism using the compressed pulse, as shown in Figure 4.10a. Here, both the entrance (right) and exit (left) face pulses were clearly visible despite the fact that the generation pulse energy was 20 times less than that of the flying focus pulse and the effective generation length near the interfaces was many times smaller than what we expected from the flying focus. Having validated the sensitivity of our EO system, we scanned the EO signal of a large number of combinations of pulse duration/chromatic aberration, however, in each case we measured only noise, as shown, *e.g.*, in Figure 4.10b.

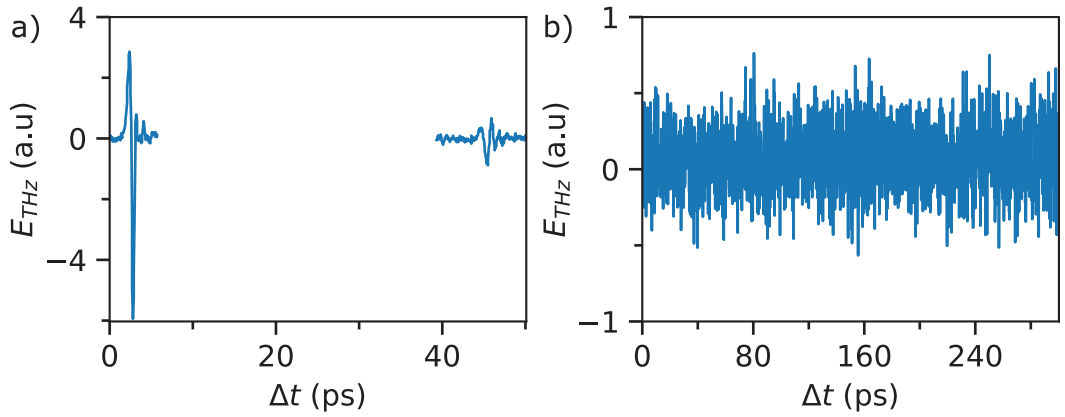

Fig. 4.10: Flying-Focus THz generation: Null result. **a** THz emission from the LN prism with the low-energy compressed pulse. The first peak below 10 ps corresponds to the emission from the exit face of the LN prism while the trailing peak after 40 ps corresponds to the emission from the entrance face. **b** Representative scan of the attempted THz generation with flying focus, showing noise across the full range of time-delays.

The most likely reason that this attempt failed is that the effective pulse duration was too long. Although it is, to an extent, decoupled from that of the incident chirped pulse, we estimate the effective pulse duration to still be several picoseconds. As a result, we were not able to drive sufficiently large nonlinear polarization at THz frequencies to observe any THz generation. Nevertheless, this work provides an inter-

esting starting point for future experiments generating THz pulses with alternative techniques of aberration exploitation. For example, a modified flying focus technique exploiting spherical aberration has recently been reported, which could in principle be adapted to THz generation [105].

4.3 Kapton Tape AR Coating

One of the factors limiting THz generation in LN is the large reflection coefficient. With a refractive index of 5.05 at 1 THz [106], 45% of the pulse energy is lost due to reflection at the LN/air interface. Wu *et al.* suggested that Kapton tape, a polymer tape commonly used in low-temperature studies, provides a convenient AR coating. We investigate this possibility in more detail here.

Shown in Figure 4.11a is the THz pulse transmitted through a bare 1 mm thick LN substrate (black) and the same wafer with 1 layer (blue) and 2 layers (orange) of 60 μm thick Kapton tape. Looking closely, we can see a small delay in the waveform with an increasing number of layers, as expected from the increased optical path length due to the refractive index of the Kapton tape. The corresponding amplitude spectra are shown in Figure 4.11, where we see small differences between each spectrum. We can also potentially see evidence of multiple beam. interference effects, as the addition of an extra layer of Kapton tape changes the frequency of enhanced transmission.

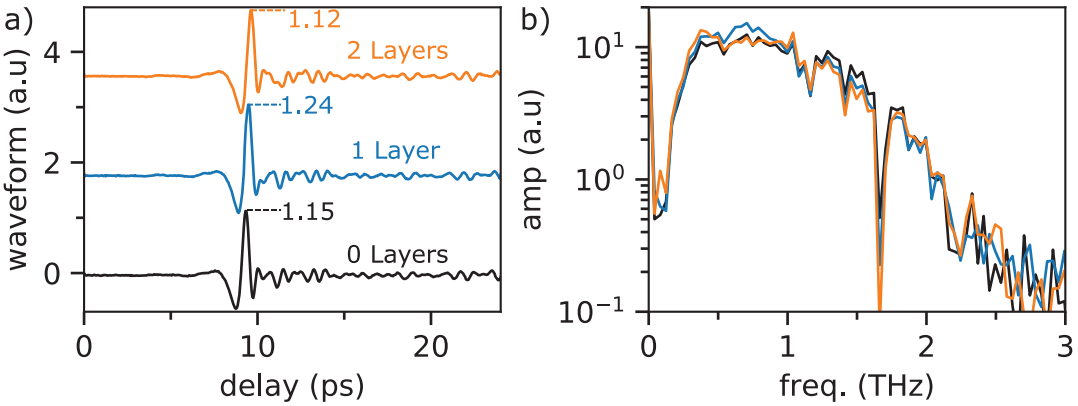

Fig. 4.11: Kapton-tape on LN: transmission enhancement. a Time-domain waveform transmitted through a 0.5 mm LN substrate with no Kapton tape (black), 1 layer of Kapton tape, and 2 layers of Kapton tape. The thickness of each layer was approximately 60 μm. **b** The corresponding amplitude spectra.

We can be more quantitative by plotting the ratio of the change in amplitude to the reference amplitude, as seen in Figure 4.12a, b. In these figures, the solid line is a smoothed version of the data (circles) using a Savitsky-Golay filter. Similar to Figure 4.11, the blue corresponds to a single layer of Kapton tape while the orange corresponds to two layers. Here, we can more clearly see oscillations in the transmission with a smaller period for the case of two layers, as expected. The transmission through Kapton tape on LN can be calculated using the thin-film transmission equation (see Appendix A.5),

$$t_{tf} = \frac{4n_{LN}n_{Kap}(n_K + n_{LN})(n_K + 1)}{(n_K + n_{LN})(n_K + 1)e^{-in_K kx} + (n_K - n_{LN})(n_K - 1)e^{in_K kx}}, \tag{4.6}$$

where n_{LN} is the refractive index of LN, n_K is the refractive index of Kapton, and x is the Kapton tape thickness (different for one and two layers).

Figure 4.12c and d show plots of $(t_{tf} - t_{LN-air})/t_{LN-air}$, where t_{tf} is the transmission with 1 and 2 layers of Kapton tape calculated from equation 4.6, respectively, and t_{LN-air} is the transmission from LN to air. This quantity is analogous to the absorbance that is measured experimentally. The calculation was performed with a constant refractive index of 5.05 for LN [106] and an index and absorption coefficient of 1.875 and 20 cm^{-1}, respectively, for Kapton tape [107]. In the region from 0.2-1.5 THz, the calculation shows good agreement with data, giving a reasonable estimate of the change in amplitude and successfully predicting location of the transmission minima/maxima. At frequencies above 1.5 THz, the calculation performs worse and fails to predict the observed reduction in transmission. This could be because the absorption of Kapton in this region is larger than our simple estimate or, alternatively, because the adhesive is absorbing at these frequencies.

After testing the effect of the Kapton tape on transmission through a LN substrate, we applied a single layer to the Gen. 3a THz source. While we did not immediately observe an enhancement in the electric field, after realignment of the source we saw an increase in the peak electric field from 605 kV/cm to 640 kV/cm. We note that Wu *et al.* reported that 96 μm layer of Kapton was used for an AR coating. Due to the high pump-pulse energy (70 mJ), the peak frequency in their source was below 0.5 THz and most of their bandwidth was in the range of 0.25 to 0.75 THz. From

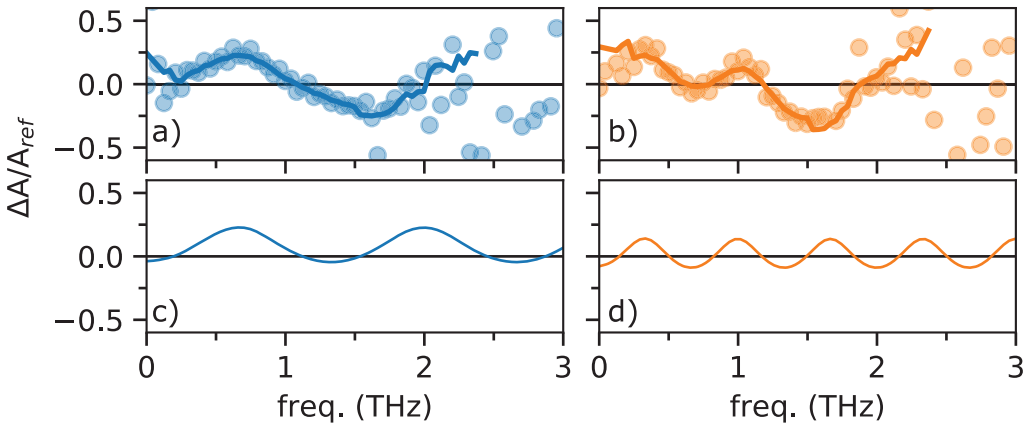

Fig. 4.12: Kapton AR coating: experiment versus theory. Experimentally measured change in THz amplitude, $\Delta A = A_{Kapt.} - A_{ref.}$ normalized by the reference spectrum, A_{ref} for **a** 1 layer and **b** 2 layers of 60 μm thick Kapton tape. Calculated change in transmission, $\Delta t = t_{Kapt.} - t_{ref.}$ for **c** 1 layer and **d** 2 layers of Kapton tape.

our calculations, the 96 μm layer is essentially optimized for increasing transmission in this region. For the UNL sources, with bandwidth of several THz, it is possible that even thinner layers of Kapton tape could improve the AR properties further. For example, from our simple calculation a 40 μm layer would increase transmission in the range from 0 to 1.8 THz with a peak at 1 THz. The thinner layer would also have less absorption, further improving the AR properties. Nevertheless, the long term effects of high-power laser exposure to Kapton are unclear and the polymer could become damaged over time, which could potentially negatively effect the output coupling of THz radiation.

4.4 Narrowband Nonlinear Dynamics

Recently, a great deal of focus has been placed on nonlinear THz dynamics using intense few or multicycle pulses, for example to explore excitonic dressed states [108], in compact charged-particle accelerators [109], or in resonantly driving Higg's mode in superconductors [110, 111]. Of special interest in the last several years is THz high-harmonic generation in Dirac [19, 112] and Weyl [113] semimetals, where the harmonic generation is rooted in high-field transport effects as opposed to the coherent acceleration [114] and recollision [115] of electrons and holes.

While the THz emission from TPF sources in LN is broadband and therefore single

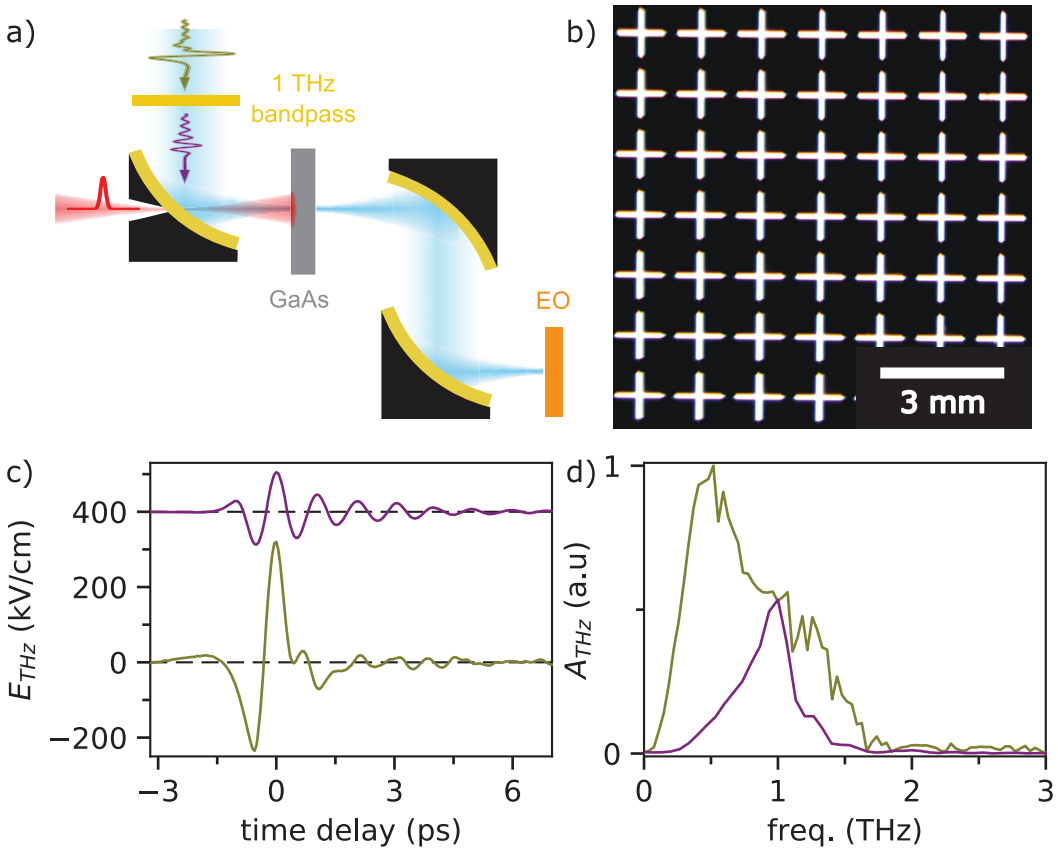

Fig. 4.13: Strong-field quasi-narrowband THz pulses. **a** Schematic layout of the pump-probe experiment. A removable 1 THz band pass filter reshapes the incident pulse, which is focused onto a GaAs wafer. A coincident femtosecond pulse at 800 nm photoexcites electron-hole pairs with a variable time delay. The THz transmission is measured with EO sampling at a secondary focus. **b** Transmission microscope image of the plasmonic resonators that act as band pass filters for THz radiation. **c** THz waveform measured before (gold) and after (purple) the insertion of a 1 THz band pass filter with peak fields of 320 kV/cm and 105 kV/cm, respectively, and **d** the corresponding amplitude spectra.

cycle, narrowband few-to-multicycle pulses can be obtained by spectrally filtering the broadband emission, as shown schematically in Figure 4.13a. The THz filter used here is based on nanostructured plasmonic resonators, as shown in Figure 4.13b for a 1 THz center frequency. The incident broadband THz pulse, with a peak field of 320 kV/cm, and the few-cycle THz pulse transmitted through the 1 THz filter, with a peak field of 105 kV/cm, are shown in Figure 4.13c. Here the source was not realigned after placing the filter, however, it is likely that an even higher narrowband field could be obtained with realignment. The corresponding amplitude spectra are shown in Figure 4.13d.

To validate the field strength, we performed a pump-probe THz-transmission experiment in GaAs similarly to refs. [116, 59]. The experiment is shown schematically in Figure 4.14a, where we use both broadband and narrowband excitation. The normalized THz transmission as a function of pump-THz time delay is shown for broadband excitation in Figure 4.14a and narrowband excitation in Figure 4.14b for several values of the peak electric field. The EO sampling delay was fixed to the peak of the THz pulse (see the insets). If we look to the positive time region, when the pump arrives before the THz, we see that as the field strength increases (the more transparent curves imply lower fields), the normalized transmission increases for both the broadband and narrowband data.

This can be seen more explicitly if we plot the ratio of positive-time transmission transmission to negative-time transmission versus incident field, as shown in Figure 4.14c. The transmission of both the narrowband (purple) and broadband (gold) data increase with increasing field, as expected, proving that the field strength with the narrowband pulses is sufficiently large to explore high-field transport. The dominant mechanism underlying this absorption bleaching is intervalley scattering, where the strong THz field drives electrons high in the conduction band where they can scatter to low mobility satellite valleys, as shown schematically in Figure 4.14d.

As indicated previously, of recent interest is the generation of harmonics due to high-field transport mechanisms. In general, one can expect harmonic emission to result from any departure from harmonic motion. We therefore speculate that the intervalley scattering mechanism could lead to harmonic emission, which we explore

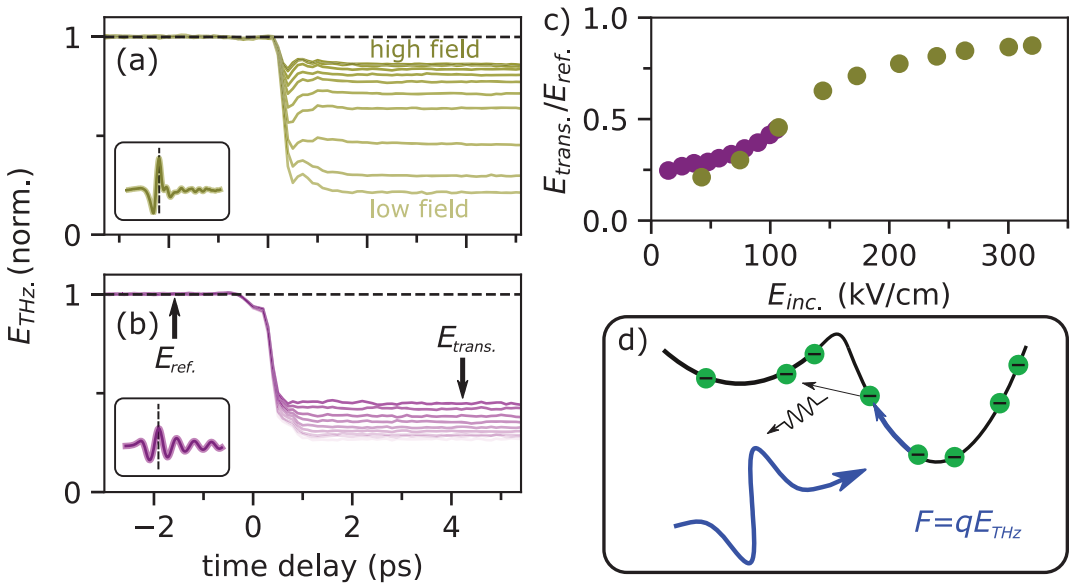

Fig. 4.14: Narrowband nonlinear dynamics. **a** Normalized THz transmission through photoexcited GaAs as a function of time delay at low (transparent) and high (bold) field strength with the broadband THz pulses. **b** Similar curves to **a** with the narrowband THz pulses that result from the broadband pulse transmission through a 1 THz bandpass filter. The transmission was measured by EO sampling with the time delay set to the vertical dashed line in the insets of **a** and **b**. **c** Transmission as a function of incident field strength for the broadband and narrowband spectra. The transmission was defined as the ratio of the EO signal at positive time to that at negative time, at the time delays indicated in **b**. **d** Illustration of the intervalley scattering process responsible for absorption bleaching, where carriers are driven by the strong electric field high in the bands where they can scatter to low-mobility satellite valleys.

in Figure 4.15. Here, a reference waveform was measured without photoexcitation and while anther waveform was measured with photoexcitation, as shown in Figure 4.15a along with the corresponding amplitude spectra in Figure 4.15b. As the data in Figure 4.15b (transparent circles) was noisy and contained several water-absorption lines, we used a Savitsky-Golay filter to smooth the data (solid lines). Here, we see the clear emergence of signal at the third harmonic, which does not appear as prominently in the un-pumped waveform.

These results represent the first steps towards exploration of narrowband high-field transport and the resulting harmonic emission in UNL. Future work should focus on confirming the presence of harmonic emission by, *e.g.*, using sharper or higher

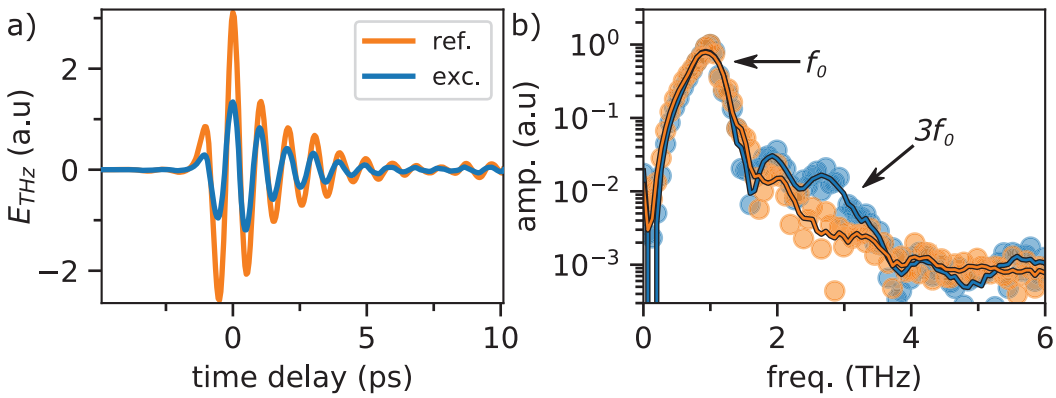

Fig. 4.15: Evidence for harmonic generation from high-field transport mechanisms. a Transmitted THz waveform with (blue) and without (orange) photoexcitation along with **b** the corresponding amplitude spectra. The spectrum from the photoexcited waveform shows evidence of an additional lobe at approximately 3 THz, which could be indicative of third harmonic generation.

contrast filters to more adequately remove incident spectra at the third harmonic. After verification, exploring the electric field, center frequency, and excitation density of the harmonic emission could yield enormous insight into the mechanisms of high-field ultrafast transport.

4.5 Dry-Nitrogen Purge

4.5.1 Electric field Enhancement

To facilitate future studies of nonlinear dynamics that require detailed spectroscopic information, such as THz harmonic emission, we constructed a dry-nitrogen purge box for the Gen. 2 TPF source. The ambient and purged waveforms are shown in Figure 4.16a and b, respectively. We can see that the ringing from water absorption is significantly reduced after the purge. The small peak at approximately 3 ps is a reflection from the black polyethylene filter. We see that the field increases by approximately 9%. The corresponding amplitude spectra are shown in Figure 4.16c. Here we see a dramatic reduction in the water absorption peaks, especially in the 2-4 THz range.

From the ratio of the sum of the power spectra, we see that there is approximately a 5% increase in energy after purging. This is likely also an overestimate as the water

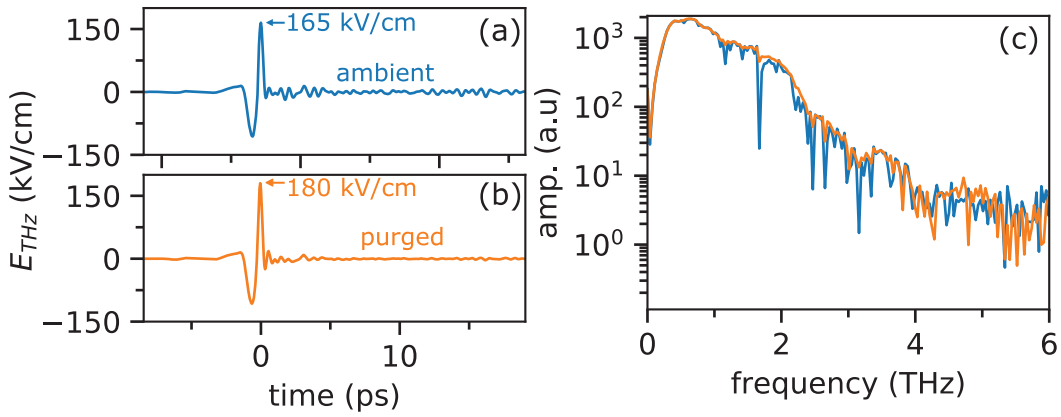

Fig. 4.16: Effect of water absorption on the field strength. Time-domain waveform in **a** an ambient environment with a peak field of 165 kV/cm with a humidity of approximately 20% and **b** a dry-nitrogen purged environment with a peak field of 180 kV/cm. **b** The corresponding amplitude spectra.

absorption lines are not resolved, *i.e.*, we have not captured the full ring down of the re-emission in the time domain. From equation 4.1, we should expect less than a 2.5% increase in the peak electric field, which is significantly less than the 9% observed from the EO sampling calibration. This suggests that the largest contribution to the water-vapor induced reduction in field strength is from dispersion rather than absorption. Note that the field enhancement from purging can depend on the ambient humidity, which in this case was approximately 20%. Moreover, it depends on the THz pulse spectrum and propagation length. As an interesting aside, the nonlinear response of water vapor lines has recently been explored by Rasekh *et al.* [117], showing an increase in amplitude with field at peak fields on the order of 1 kV/cm.

4.5.2 Water Absorption

We can also quantify the water absorption by plotting the absorbance, defined as the ratio of the purged to unpurged spectra power spectra, where, *e.g.*, $P_{amb} \equiv |A_{THz,amb}|^2$. The measured absorbance is shown in Figure 4.17a. Here, the water absorption peaks manifest as peaks. In the low frequency regime, away from the absorption lines the absorbance is approximately zero, as expected. However, in the high-frequency regime there appears to be a baseline fluctuation. This is likely due to drift in the source over time.

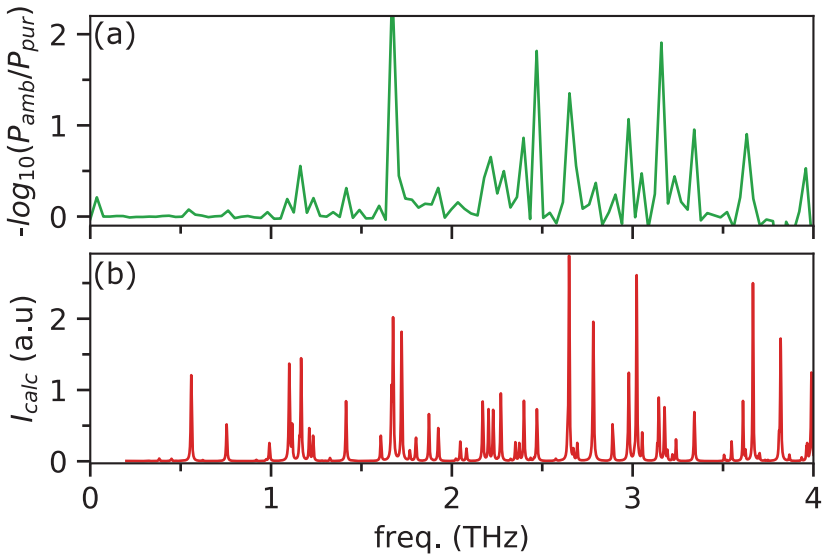

Fig. 4.17: Water vapor absorbance. a Water-vapor absorbance from the TPF-THz source, where the absorbance is defined as the negative base-10 logarithm of the ratio of the transmission. The amplitude spectrum taken in the purged (ambient) environment was the reference (transmitted) spectrum. **b** Intensity of water absorption as a function of frequency calculated using the HITRAN database.

We can compare this to the expected atmospheric water absorbance using the high-resolution transmission molecular absorption (HITRAN) database [118], as seen in Figure 4.17b. Here, we see reasonable agreement between the location of absorption lines in experiment versus theory. Moreover, in regions with well-separated absorption lines (*e.g.*, the modes at 0.6 and 0.75 THz) the relative amplitudes from experiment resemble that from theory. However, it is clear that much higher resolution is needed to resolve the absorption lines. Moreover, in regions with a large number of closely-spaced lines, as well as at higher frequency where the spectrum is noisier, it is more difficult.

In the range from 0.2 to 4 THz, the HITRAN database has indexed 7368 unique transitions, however, the number of relevant transitions can be dramatically reduced. This number is reduced to 1813 if only $H_2{}^{16}O$, which has an abundance of 99.7% so its spectral lines overwhelm the contributions from the other isotopologues of water. If we also enumerate only the transitions with intensities larger than calculated transition

just below 1 THz,* which appears to be near the limit of experimental detection, the number is further reduced to 68. Just 20 transitions lie in the range of 0.2 to 2 THz, above which the LN spectrum is less than one tenth its maximum amplitude.

*The calculation of intensity considers both the Einstein coefficient and thermal occupancy at 295 K [119].

Chapter 5

Conductivity, Recombination, and Luminescence in Semiconductors

This chapter provides a brief introduction to the physics of ultrafast excitation of semiconductors important for the exploration of THz dynamics in materials, as discussed in the subsequent chapters. It begins with a schematic outline of the process of ultrafast excitation and relaxation in a two band semiconductor in real-space and k-space. This is followed by a basic description of optical transitions that encompasses both absorption and luminescence. A discussion of the real-space dynamics using the ambipolar diffusion equation is then developed including terms for radiative and non-radiative recombination.

5.1 Ultrafast Excitation of Semiconductors

The processes of ultrafast excitation and relaxation in a simple two-band semiconductor are illustrated in Figure 5.1. Note that the approximate timescale of each stage is indicated by the scale bar on the far right of the figure. In the initial step, shown in Figure 5.1a, a femtosecond pulse (indicated by the waving red arrow) with energy in excess of the band gap generates electron-hole pairs at well defined energies, creating a non-thermal distribution (indicated by the deviations from Fermi-Dirac statistics to the right of the band diagram) [120, 121]. On a timescale similar to the duration of the excitation pulse, carrier-carrier scattering (indicated by the curved red arrows) drives the electrons and holes towards quasi-equilibrium hot-carrier distributions that can be described with separate quasi-Fermi levels and even temperatures for electrons and

holes [122]. In the next stage, illustrated in Figure 5.1b, hot-carriers exchange energy with the lattice through carrier-phonon scattering (outgoing black waving arrows) [123]. The strong coupling with specific phonon modes leads to hot-phonon effects that can act to slow the carrier cooling by increasing the rate of phonon absorption (incoming black waving arrows) [124]. The lifetime of hot-carriers and phonons can vary significantly based on the material and excitation conditions. In GaAs cooling to the lattice temperature occurs on a timescale of a few to tens of picoseconds [125, 126]. In this stage, some ultrafast trapping and hot-carrier photoluminescence (PL) also occurs, indicated by the the vertical transition to the mid-gap state and vertical transitions between electrons and holes along with outgoing photons, respectively. Finally, in the last stage of relaxation, illustrated in Figure 5.1c, the carriers have thermalized with the lattice and are described by quasi-Fermi distributions with temperatures equal to the lattice. Here, the drive towards equilibrium is governed by radiative emission, with a luminescence temperature equal to that of the lattice, and non-radiative recombination via localized states in the gap [127].

Simultaneously to the relaxation in k-space, the spatial distribution of carriers is evolving. At low enough intensities, the optical pulse decays exponentially as it propagates in the material, suggesting that the initial density profile is also exponential, as shown in Figure 5.1d. Due to the high trap density at the surface, the density profile rapidly becomes non-exponential with a local minimum near the surface [128], as seen in Figure 5.1e. In this regime, the hot-carrier temperature yields high energy luminescence that is more likely to be reabsorbed before emission into the air/vacuum, as shown in the inset. At later times, the carriers have diffused deeper into the bulk of the material, as shown in Figure 5.1f. In this stage, the carriers have cooled to the lattice temperature and rate of photon reabsorption is reduced due to the lower photoluminescence (PL) temperature.

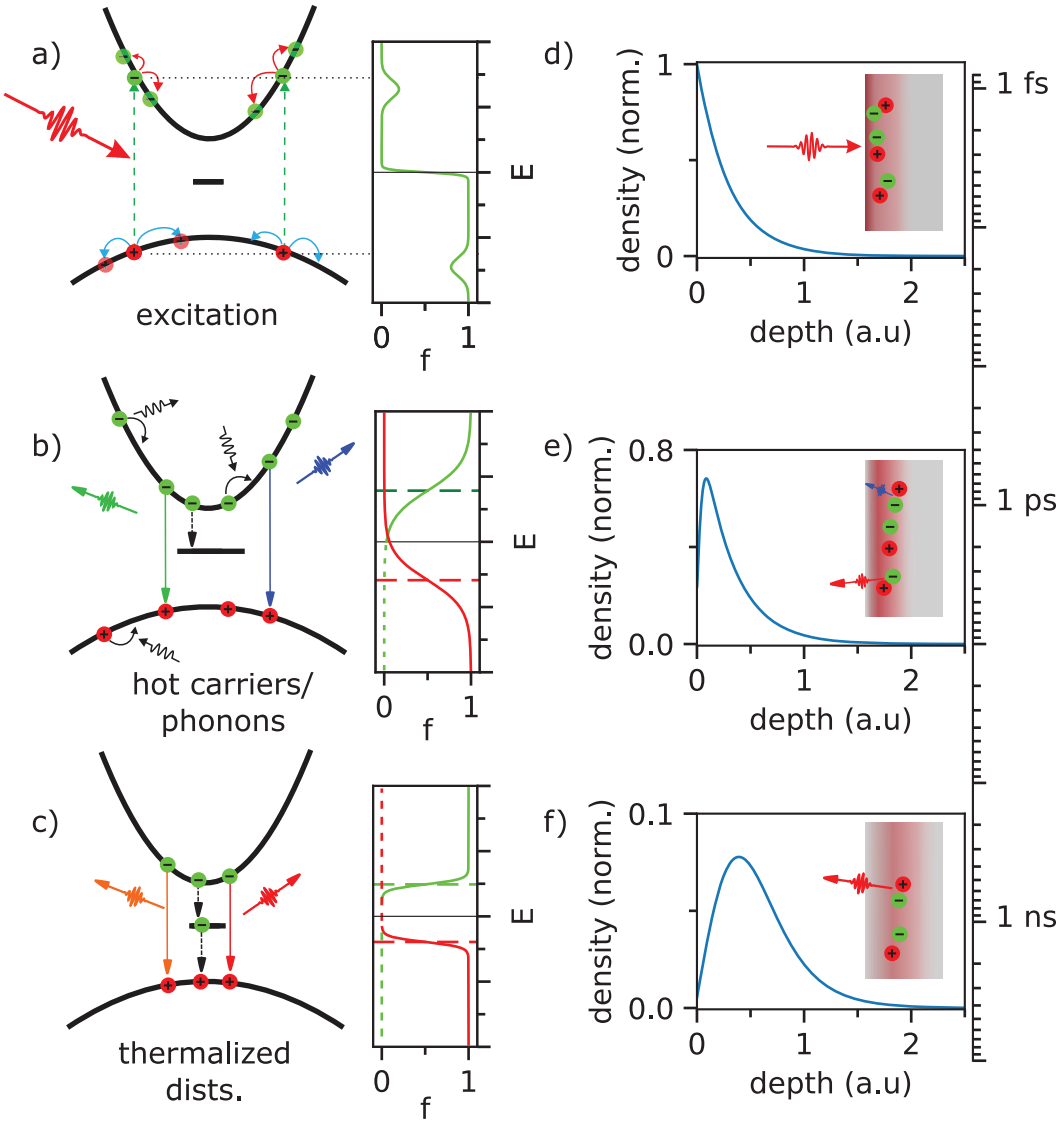

Fig. 5.1: Ultrafast excitation and relaxation in a two-band semiconductor. Stages of excitation and relaxation for a two-band semiconductor in k-space, from non-thermal distributions in **a**, to hot quasi-thermal distributions in **b**, to quasi-thermal distributions in equilibrium with the lattice in **c**. The corresponding real-space densities are shown in **d-f**. The scale bar on the right indicates the approximate timescale of each stage.

5.2 Theory of Optical Transitions

5.2.1 Transition rates

In general, the transition rate between two unique states is governed by Fermi's golden rule,

$$\Gamma_{ij} = \frac{2\pi}{\hbar} |\langle \Phi_j | H' | \Phi_i \rangle|^2 f_i(1 - f_j), \tag{5.1}$$

where Φ_i and Φ_f are the wave functions of the initial and final states, $\hbar$ is the reduced Planck constant, H' is the perturbing Hamiltonian, and f_i and f_j are the occupancies of state i and j, respectively. The occupancy factors are included because the initial state must be occupied and the final state must be unoccupied for a transition to occur. In the electric dipole approximation with a semiclassical picture where the matter is quantum and the light is classical, the perturbing Hamiltonian takes the form,

$$H_{ED} \propto \vec{E}_0 \cdot \vec{r}, \tag{5.2}$$

where $\vec{E}_0$ is the vector amplitude of the electric field, $\vec{r}$ is the radial vector, and H_{ED} is the electric-dipole Hamiltonian. From this, we can easily see that the initial and final states must have opposite parity for the transition rate to be non-zero, *i.e.*, for the transition to be dipole allowed. Because the matrix element in Fermi's golden rule is squared, we can also easily see the symmetry between absorption and stimulated emission. However, as the field amplitude goes to zero the transition rate vanishes. This would appear to preclude the phenomenon of spontaneous emission. A common way to introduce spontaneous emission is via the Einstein coefficients, where it is possible to find a relationship between the spontaneous emission rate and stimulated emission/absorption rate using the principle of detailed balance.*

In retrospect, the lack of spontaneous emission in the semiclassical theory is not surprising. It is well known that spontaneous emission is a result of vacuum fluctuations, which is a quantum-mechanical aspect of the electromagnetic field. A natural step would then be to extend the semiclassical theory by inserting the vacuum am-

*It is interesting that historically, Einstein's postulate of stimulated emission was a significant leap beyond standard empirical knowledge, however, in attempting to calculate the transition rates using the semiclassical theory, with classical light, it is instead spontaneous emission that must be introduced *ad hoc*.

plitude into equation 5.2. While this is somewhat satisfying, we note that both spontaneous and stimulated emission processes occur even when the field is not in the ground state. It is therefore not immediately clear why the vacuum amplitude is still important in this case. Moreover, due to the symmetry between the initial and final states this method appears to allow for spontaneous absorption, which is a clear violation of the conservation of energy.

Instead, if we work with a fully quantum theory of the light-matter interaction we can see how spontaneous emission arises naturally. Following Loudon [129], we redefine the electric-dipole Hamiltonian in second-quantized notation as,

$$H_{ED} \propto D_{if} \left(\hat{\pi}^\dagger \hat{a} + \hat{\pi} \hat{a}^\dagger \right), \tag{5.3}$$

where $D_{ij} = \langle \Phi_j | \vec{r} | \Phi_i \rangle$ is the transition dipole moment, $\hat{\pi}^\dagger$ and $\hat{\pi}$ are the transition operators, which act on the electronic part of the wavefunction, and $\hat{a}^\dagger$ and $\hat{a}$ are the usual raising and lowering operators, respectively, which act on the photonic part of the wavefunction. The first term in this Hamiltonian can be thought of as acting to move the electron from the ground state to the excited state by removing a photon while the second term acts to move the electron from the excited state to the ground state by creating a photon. This can be written as,

$$\begin{aligned} \hat{\pi}^\dagger \hat{a} \left| n_\gamma, \Phi_1 \right\rangle &= n_\gamma^{1/2} \left| n_\gamma - 1, \Phi_2 \right\rangle, \\ \hat{\pi} \hat{a}^\dagger \left| n_\gamma, \Phi_2 \right\rangle &= (n_\gamma + 1)^{1/2} \left| n_\gamma + 1, \Phi_1 \right\rangle. \end{aligned} \tag{5.4}$$

The first of these equations indicates the absorption of a photon while the second indicates emission. As the prefactors on the right hand side of these equations are just numbers, it is easy to calculate the matrix elements. If we insert these into Fermi's golden rule we find,

$$\begin{aligned} r_{21} &= C(1 + n_\gamma) \left| D_{12} \right|^2 f_2 (1 - f_1) \equiv r_{sp} + r_{st}, \\ r_{12} &= C n_\gamma \left| D_{12} \right|^2 f_1 (1 - f_2) \equiv r_a \end{aligned} \tag{5.5}$$

where C is a proportionality constant,* f_2 and f_1 are the occupancies of the upper and lower states. We see that if the photons are in the ground state ($n_\gamma = 0$) the

*This constant can be found from the electric-dipole Hamiltonian in a material, however, it appears that its value is not consistent in the literature. For our purposes, the constant is not important as we are interested in the qualitative rather than quantitative aspects of the theory of optical transitions.

transition rate from the ground state to the excited state is zero, *i.e.*, there is no spontaneous absorption. On the contrary, because of the $(n_\gamma + 1)^{1/2}$ term that arises from the operation of the creation operator on the state there are two contributions to the rate of emission. The first, r_{sp}, that is independent of occupancy and corresponds to the spontaneous emission process and the second, r_{st}, which is proportional to n_γ and corresponds to the stimulated emission process. Note that $r_{st} = n_\gamma r_{sp}$. We therefore see how absorption, stimulated emission, and spontaneous emission all arise naturally in a fully quantum mechanical theory.

5.2.2 Relating absorption and emission rates

Using equations 5.5, we can also study the relationship between the rates of absorption, stimulated emission, and spontaneous emission. While the relationship between r_{sp} and r_{st} it is easy to see, because of the different occupancy factors in the absorption and emission rates in equation 5.5 it is not as easy to find such a relationship between emission and absorption. Following Würfel [130], we define the absorption coefficient as,

$$\frac{c}{n} n_\gamma \alpha \equiv r_a - r_{st} = C n_\gamma |D_{12}|^2 (f_1 - f_2) \tag{5.6}$$

where $v = c/n$ is the speed of light in a medium. The factor of velocity times photon occupation can be thought of as the photon current so that the total rate of transitions is equal to the rate of photons entering the system times the absorption coefficient. We can now write the total rate of transitions as,

$$r_{tot} = r_{st} - \frac{c}{n} n_\gamma \alpha. \tag{5.7}$$

By studying the steady-state situation, with $r_{tot} = 0$, we find a relationship between the absorption coefficient and rate of spontaneous emission,

$$r_{sp} = \frac{c}{n} n_{\gamma,eq} \alpha \tag{5.8}$$

where $n_{\gamma,eq}$ is the equilibrium photon occupancy.* To find an equation for $n_{\gamma,eq}$, we note that the occupancies, f_i, in experimental situations can often be derived from a

*In this formulation, the absorption coefficient is occupancy dependent and can even be negative (amplification). However, this does not imply that the spontaneous emission rate is negative. In order for amplification to occur, the population must be inverted, which occurs when the quasi-Fermi splitting is larger than the photon energy. In this case, we will see that the equilibrium occupancy is also negative so the rate of spontaneous emission is positive.

quasi-equilibrium situation and are given by,

$$f_i(E_i) = \frac{1}{\exp\left(\frac{E_i - \epsilon_i}{kT}\right) + 1}, \tag{5.9}$$

where ϵ_i is the quasi-Fermi level of state i, k is the Boltzmann constant, and T is the temperature. Here, we have assumed thermal equilibrium between the two states but not chemical equilibrium. Once again, we study the steady state solution to equation 5.7, however, this time we insert the calculated rates, equation 5.5, and solve for the photon occupancy,

$$n_{\gamma,eq} = \frac{1}{\exp\left(\frac{E_\gamma - (\epsilon_2 - \epsilon_1)}{kT}\right) - 1}, \tag{5.10}$$

where $E_\gamma = E_2 - E_1$ is the photon energy. This equation was originally derived by Lasher *et al.* [131] and bears a striking resemblance to the Bose-Einstein distribution with a chemical potential given by $\mu = \epsilon_2 - \epsilon_1$.* The spontaneous emission rate can now be written as,

$$r_{sp} = \frac{c}{n} \frac{\alpha}{e^{\frac{E_\gamma - \epsilon_2 - \epsilon_1}{kT}} - 1}. \tag{5.11}$$

5.2.3 Band-edge absorption

This derivation has been performed for the simple case of a two-level system, however, this relationship between absorption and spontaneous is significantly more general and provides an excellent description of semiconductor luminescence. In order to understand semiconductor luminescence spectra, we will therefore develop the theory of band-edge absorption in more detail. To generalize the absorption coefficient to a multi-level system, we consider the total rate of stimulated transitions summed over all combinations of levels,

$$\frac{r_a(E) - r_{st}(E)}{n_\gamma} = \sum_i \sum_j \delta(E_i - E_j - E) C |D_{ij}|^2 (f_j - f_i). \tag{5.12}$$

Considering a two-band direct-gap semiconductor with parabolic bands, the k selection rule implies that the matrix element is zero for all but vertical transitions.† The

*Würfel takes this similarity further and defines the chemical potential of radiation as $\mu_\gamma = \epsilon_2 - \epsilon_1$. It is commonly assumed that the chemical potential of photons must be zero due to the non-conservation of photon number. This is addressed by Würfel in his original manuscript, where he provides an interesting discussion of luminescent processes in terms of chemical reactions between electrons and holes [130]. This idea has also been explored by other authors [132]

†Here we assume that the photon momentum is significantly smaller than the crystal momentum, which is a very good approximation

number of terms in the sum is equal to the joint density of states (the number of states with allowed transitions separated by energy E) so that, assuming the matrix element for direct transitions near the band edge is approximately a constant, we find,

$$\frac{r_a(E) - r_{st}(E)}{n_\gamma} = C|D_{cv}|^2 g(E)\left[f_v - f_c\right], \tag{5.13}$$

where D_{cv} is the interband matrix element, f_c and f_v are the conduction and valence band occupancies calculated at energy given by,

$$E_{c,v} = \frac{m_{red}}{m_{c,v}}(E - E_g) + E_{c,v}, \tag{5.14}$$

and $g(E)$ is the joint density of states given by,

$$g(E) = \frac{8\pi\sqrt{2}m_{red}^{3/2}}{\hbar^3}\sqrt{E - E_g}, \tag{5.15}$$

where E_g is the band gap and $m_{red}^{-1} = m_c^{-1} + m_v^{-1}$ is the reduced mass. For low excitation levels, when the valence band occupancy is near one and the conduction band occupancy is near zero, we therefore expect the absorption coefficient to follow the square root dependence of the joint density of states.

However, in real materials, disorder and thermal broadening distort this ideal square root behavior and an exponentially decaying absorption coefficient is typically seen in the sub-band gap range.* This sub-gap absorption, commonly known as the Urbach tail, can arise from several different mechanisms. In general, it is difficult to determine the correct microscopic model for any given system. Instead, following Katahara *et al.* [133] we will use a phenomenological model of the sub-gap absorption to find an effective joint density of states by using a stretched exponential function convoluted with the square root density of states,

$$g_{eff}(E) = \frac{1}{\gamma\theta\Gamma(\theta^{-1})}\int_0^\infty dE' \exp\left[\left(\frac{E'}{\gamma}\right)^\beta\right] g_0(E' - E), \tag{5.16}$$

where $g_0(E)$ is the parabolic joint density of states from equation 5.15, and γ and θ are phenomenological constants related to the characteristic width and profile of the

*Even for a perfect semiconductor, *i.e.*, one with no disorder and at low temperature, this square-root behavior breaks down due to the Coulomb interaction between electrons and holes (excitonic effects), however, in the materials and temperature ranges studied in this work these effects are not important.

band tail respectively. The prefactor is a normalization constant . Several microscopic models of band tailing exist that can in some cases be linked to specific values of the constant θ, however, a full discussion of these models is beyond the scope of this work [133]. We are left with an equation for the absorption coefficient in terms of the effective joint density of states,

$$\alpha = \frac{c}{n} C |D_{cv}|^2 g_{eff}(E) \left[f_v - f_c \right]. \tag{5.17}$$

5.2.4 Phenomenological model of absorption bleaching

The occupancy terms in equation 5.17 suggest that with high-fluence excitation, where the conduction band occupancy becomes non-zero, the absorption coefficient, α, is smaller than the equilibrium value [134]. A comprehensive theoretical description of this behavior is quite involved [122, 135], however, for the purpose of this work a simple phenomenological description can capture salient aspects of the problem. Considering a simple picture where the conduction (valence) band population increases (decreases) as the excitation intensity increases. A saturation model is often used to mimic this behavior, where the intensity dependent absorption coefficient is written as [136],

$$\alpha(I) = \frac{\alpha_0}{1 + I/I_{sat}}, \tag{5.18}$$

where α_0 is the linear absorption coefficient, I is the light intensity, and I_{sat} is a phenomenological saturation intensity that is related to the intensity at which the occupancy factors in equation 5.17 become important.

With this, we can write a differential equation governing the change in optical intensity as a function of propagation distance within a crystal,

$$\frac{dI}{dz} = -\alpha(I) I = \frac{\alpha_0}{1 + I/I_{sat}} I, \tag{5.19}$$

which we can use to find the initial density of carriers at depth z,

$$N_0(z) = \frac{1}{E_\gamma} \frac{dI}{dz}, \tag{5.20}$$

where $N_0(z)$ is the carrier density and E_γ is the photon energy at the center frequency of the generation pulse.

5.2.5 Luminescence spectrum and photon reabsorption

From equations. 5.11 and 5.17, we therefore find an energy-dependent emission rate given by,

$$r_{sp} = \frac{c}{n} C |D_{cv}|^2 \frac{g_{eff}(E)\left[f_v - f_c\right]}{\exp\left(\frac{E_\gamma - (\epsilon_2 - \epsilon_1)}{kT}\right) - 1}. \tag{5.21}$$

As an important note, the total rate of radiative recombination can be extracted from this equation as a function of carrier density and, for an intrinsic semiconductor with a square root density of states, it is proportional to the square of the carrier density so that,

$$\left.\frac{dN}{dt}\right|_{rad} = -BN^2, \tag{5.22}$$

where B is the radiative rate constant [137]. This is connected to the idea that both the concentration of electrons and of holes is important for determining the reaction rate and is therefore considered a bimolecular recombination process [138].

While this equation can give the PL intensity at any point in the crystal, the emitted spectrum is modified by photon reabsorption as the PL propagates to the surface. The luminescence intensity at any point in the sample satisfies the equation,

$$\frac{dI(z,E)}{dz} = -\alpha(z,E)I + Cr_{sp}(z,E), \tag{5.23}$$

where I is the luminescence intensity, z is the distance from the semiconductor surface, and C is a constant relating the photon emission rate to the luminescent intensity. This equation can be solved with the boundary condition of zero luminescence intensity deep in the sample. In the case where the quasi-Fermi splitting and temperature are uniform throughout the sample, this solution to this equation can be calculated analytically so that the external luminescence spectrum is given by,

$$I_{PL}(E) = \left[1 - \exp(-\alpha(E)d)\right] \frac{Cr_{sp}}{\alpha(E)}, \tag{5.24}$$

where d is the thickness of the sample or, alternatively, the thickness of the excited (emitting) layer near the surface. This approximation of a uniform quasi-Fermi splitting and carrier temperature often provides good fits to experimental data [133]. It also facilitates a qualitative understanding of PL reabsorption. In the limit where d is large, the emitted PL spectrum reduced by a factor of $1/\alpha$ with respect to the

spectrum of equation 5.21. Alternatively, in the limit where αd is small, the exponential can be expanded with $\exp(-\alpha d) \approx 1 - \alpha d$. In this case, the factors of α in the numerator and denominator cancel so that the effect of photon reabsorption is insignificant as expected.

5.3 Non-radiative recombination

5.3.1 Recombination through mid-gap states

In a luminescent recombination process, the full energy of the excited electron is transferred to a single photon. In a non-radiative process, the same amount of energy must be released. A first guess could be that the energy is transferred simultaneously to multiple phonons, however, in the semiconductors considered in this work, the band gap is many times larger than the phonon energy. For example, in GaAs the LO phonon energy is 36.2 meV while the band gap is 1.42 eV, implying that more than 39 phonons must be simultaneously emitted for the electron to recombine by multiphonon emission, which is extremely unlikely.* Instead, non-radiative emission typically occurs through extrinsic mid-gap states, which was schematically illustrated by the flat line in between the bands in Figure 5.1.

The statistics of non-radiative recombination through mid-gap states was first studied by Shockley Reed and Hall (SRH) [139] and the rate is given by,

$$R = \frac{NP - N_i^2}{\tau_n(P + P_1) + \tau_p(N + N_1)}, \tag{5.25}$$

where N and P are the number of electrons and holes and N_1 and P_1 are the number of electrons and holes in equilibrium. This equation can be specialized to a number of different scenarios, for example in an intrinsic semiconductor where $N_1 = P_1 = 0$. Assuming the trapping rates of electrons and holes are similar, in this case $N = P$ and this can be rewritten as,

$$\left.\frac{dN}{dt}\right|_{NR} = -\frac{N}{\tau_{NR}}, \tag{5.26}$$

which is considered a monomolecular term as the rate is proportional to a single concentration.

*More formally, this would represent an extremely high order perturbative process in quantum mechanics so that the transition rate would tend to zero.

5.3.2 Trap-filling dynamics

The non-radiative lifetime, τ_{NR}, can be associated with the number of available trap states. In some materials there can exist a recombination bottleneck where the traps become saturated. In this situation, the recombination dynamics show a characteristic fluence dependence where the lifetime increases with excitation density. Similarly to the case of absorption bleaching, a simple phenomenological model can be used to model this behavior use a coupled set of rate equations. The non-radiative dynamics can be rewritten as,

$$\begin{aligned} \frac{dN_1}{dt} &= G_{01} - (k_{12} + k_{10})\, N_1, \\ \frac{dN_2}{dt} &= k_{12} N_1 - k_{20} N_2, \end{aligned} \tag{5.27}$$

where N_1 and N_2 are considered a band-like and trap state, respectively. The k constants indicate the rate of population transfer between the levels and G_{01} indicates a carrier generation rate from the ground state. The trap state (subscript 2) can be made saturable by writing k_{21} as a function of N_2,

$$k_{12} = \left(1 - \frac{N_2}{N_{2,sat}}\right) k_0, \tag{5.28}$$

where k_0 is the rate with no filled traps and $N_{2,sat}$ is the maximum trap density, so that $k_{12} = 0$ when $N_2 = N_{2,sat}$.

5.3.3 Auger recombination

The non-radiative recombination through mid-gap states is an extrinsic phenomenon, *i.e.*, it requires imperfections in the semiconductor. Another channel for non-radiative recombination that does not require such states is Auger recombination. Auger processes involve at least three bodies, with the two most basic being are electron-electron-hole (eeh) and hole-hole-electron (hhe). In eeh (hhe) Auger recombination, two electrons (holes) in the conduction (valence) band interact with one being kicked to a higher energy state in the conduction (valence) band and the other recombining with an electron (hole). Auger processes must conserve both energy and momentum, which places restrictions on the possible energies in k-space where these Auger processes occur. Because Auger recombination is a three body process it obeys

third-order recombination kinetics so that,

$$\left.\frac{dN}{dt}\right|_{Aug} = CN^3, \tag{5.29}$$

where C is the Auger recombination constant. Due to the N^3 dependence of this term, it is typically dominant at high excitation densities.

5.4 Radiative efficiency

To develop an intuition for the radiative efficiency, which is helpful to understand the modulation of luminescence with intense THz pulses (Chapter 6), it is useful to see how the carrier density affects the PL efficiency. The total rate of recombination can be written as a sum over each recombination channel so that,

$$\left.\frac{dN}{dt}\right|_{tot} = AN + BN^2 + CN^3. \tag{5.30}$$

The radiative efficiency, η_r, can be defined as the ratio of the number of carriers that recombine radiatively versus the total number of carriers that recombine at any given time,

$$\eta_r = \frac{B\,N}{A + B\,N + C\,N^2}. \tag{5.31}$$

Shown in Figure 5.2 is the rate of radiative efficiency for a toy semiconductor with $A = 1\,\mathrm{ns}^{-1}$, $B = 1 \times 10^{-19}\,\mathrm{ns}^{-1}\mathrm{cm}^{-3}$, and $C = 1 \times 10^{-35}\,\mathrm{ns}^{-1}\mathrm{cm}^{-6}$. The blue, green, and red dashed lines represent the density dependence of the recombination rate due to the A, B, and C terms, respectively. We can see that there are three different regimes to this behavior. At the lowest density, the recombination rate is dominated by the A term (monomolecular, non-radiative) and is independent of density. At intermediate densities, the B term (bimolecular, radiative) becomes the dominant channel for recombination and, finally, at high density the C term (Auger, non-radiative) dominates.

In a transient PL experiment, the density changes as a function of time. The radiative efficiency for a transient luminescence experiment with a delta function excitation of density N_0 can be defined as,

$$\eta_r = \frac{1}{N_0}\int_{t_0}^{\infty} dt \frac{B\,N^2(t)}{AN + BN^2 + CN^3}, \tag{5.32}$$

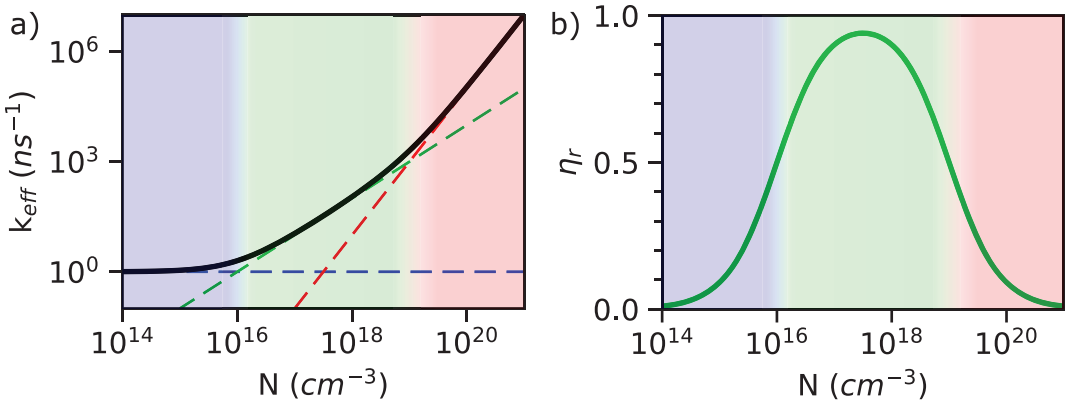

Fig. 5.2: Effective relaxation rate and PL efficiency. **a** Total recombination rate as a function of carrier density for a hypothetical semiconductor with $A = 1\,\mathrm{ns}^{-1}$, $B = 1 \times 10^{-19}\,\mathrm{ns}^{-1}\mathrm{cm}^{-3}$, and $C = 1 \times 10^{-35}\,\mathrm{ns}^{-1}\mathrm{cm}^{-6}$. **b** Radiative efficiency for the semiconductor in **a** calculated using equation 5.31.

which is the ratio of carriers that recombine radiatively versus non-radiatively. In general this equation cannot be solved analytically because the functional form of $N(t)$, is not analytic when all three terms contribute to recombination. However, it is clear that the radiative efficiency can be reduced either by increasing the rate of non-radiative recombination or by decreasing the rate of radiative recombination.

5.5 Spatial distribution of carriers

5.5.1 Ambipolar current

As seen in Figure 5.1, the spatial distribution of carriers also evolves in time after excitation. From equation 5.23, it is also clear that the spatial distribution can also is important for determining the external luminescence intensity. As the rate is proportional to the density, we must be able to model this spatial distribution. Considering a semiconductor with a distribution of electrons and holes in the linear-response regime in 1D,*

$$\begin{aligned} -\frac{J_N}{e} &= -N\mu_n E - D_N \frac{\partial}{\partial z} N, \\ \frac{J_P}{e} &= P\mu_p E - D_P \frac{\partial}{\partial z} P, \end{aligned} \tag{5.33}$$

*As discussed by Lundstrom [140], the diffusion equation can be either derived as a limiting case of the Boltzmann transport equation or postulated under the assumption that the current is linearly proportional to the electric field and the gradient of the charge density.

where $J_{N/P}$ is the electron/hole current density, E is the electric field, N and P are the spatially-dependent electron and hole densities, $\mu_{n/p}$ are the electron/hole mobilities, and $D_{N,P}$ are the diffusion coefficients. These equations apply to the density rather than charge current. In the absence of external fields the internal electric field can be found from Gauss' law,

$$\frac{\partial}{\partial z}E = \frac{P-N}{\epsilon}, \tag{5.34}$$

where ϵ is the semiconductor dielectric constant. Together this coupled system of equations are known as the semiconductor drift-diffusion equations.

With sufficiently high density the diffusion of electrons and holes is coupled by the internal electric field, which is called ambipolar diffusion.* Assuming that the strength of the internal field is sufficient to approximate $N = P$ and $-\frac{J_N}{e} = \frac{J_P}{e}$, *i.e.*, the number density currents are equal, from equations 5.33 and 5.34, the electric field coupling the electrons and holes is given by,

$$E = \frac{1}{N}\frac{(D_P - D_N)}{\mu_N + \mu_P}\frac{\partial}{\partial z}N, \tag{5.35}$$

which can be substituted into either of the current equations to find the ambipolar current,

$$-\frac{J_{ab}}{e} = \frac{(D_P\mu_n + D_N\mu_P)}{\mu_N + \mu_P}\frac{\partial}{\partial z}N, \tag{5.36}$$

and, using the Einstein relation, $D = k_B T\mu/e$, where k_B is the Boltzmann constant and e is the elementary charge, we can rewrite this as,

$$-\frac{J_{ab}}{e} = \frac{k_B T}{e}\frac{2\mu_N\mu_P}{\mu_N + \mu_P}\frac{\partial}{\partial z}n = D_{ab}\frac{\partial}{\partial z}N, \tag{5.37}$$

where we have defined the ambipolar diffusion coefficient, $D_{ab} \equiv 2k_B T\mu^*/e$, in terms of the reduced mobility, $\mu^* = \left(\mu_N^{-1} + \mu_P^{-1}\right)^{-1}$. The factor of two in the ambipolar diffusion coefficient has been left out in some publications [128] while it is present in others [142]. The factor of two makes sense if we consider the case where the electron and hole mobilities are equal. In this situation, even without the electric field electrons and holes diffuse at the same rate so that the internal field is zero. The factor of 2 is necessary to ensure that the ambipolar diffusion proceeds at the correct rate.

*For an interesting discussion of the meaning of ambipolar transport, see Champlain [141]

5.5.2 Diffusion equation

To see how the density evolves with time, which is the important parameter to determine the luminescence spectrum, we use the continuity equation,

$$\frac{\partial}{\partial t}N = \frac{\partial}{\partial z}\left(-\frac{J_{ab}}{e}\right) + G - R, \tag{5.38}$$

where G and R are the carrier generation and recombination rates, respectively. In our experiments, the generation rate can be approximated as a delta function because the diffusive timescale is significantly longer than the excitation pulse. The recombination rate is given by equation 5.30 while the generation rate can be assumed to be a delta function as the diffusive timescale is typically much slower than the photoexcitation pulse duration. Assuming that the ambipolar diffusion constant is independent of spatial location, the time evolution of the carrier density is given by,

$$\frac{\partial}{\partial t}N = D_{ab}\frac{\partial^2}{\partial z^2}N + N_0\delta(t-t_0) - A\,N - B\,N^2 - C\,N^3, \tag{5.39}$$

where t_0 is the arrival time of the excitation pulse and N_0 is the initial density, which is a function of z. This is recognizable as the diffusion equation with source and sink terms. In the case where the bimolecular and Auger terms are insignificant, there is an analytic solution for this equation, however, in general it is necessary to solve it numerically.

5.5.3 Surface recombination

The broken symmetry at the surface of a bulk crystal generally leads to a large concentration of mid-gap states that can act as non-radiative recombination centers. Within the diffusion model, this is general taken into account using a boundary condition where the density current at the surface is equal to the non-radiative recombination rate,

$$-\frac{J_{surf}}{e} = -\frac{N_{surf}}{s}, \tag{5.40}$$

which facilitates analytic solutions for the diffusion equation in some scenarios. It is also useful in the numerical simulations developed in the subsequent chapter. The constant s is known as the surface recombination velocity and is related to the carrier lifetime at the surface.

5.6 Carrier Transport

5.6.1 Optical Conductivity

The diffusion equation in the previous section considers an instantaneous response to the electric field, which means that the scattering time is short compared to the period of the applied electric field. This approximation is generally good for ambipolar diffusion, where the diffusive timescale is long compared to the scattering time. However, in THz spectroscopy, with high-frequency probes, it breaks down and a more sophisticated relationship between applied field and current is needed. To this end, the optical conductivity is defined as the proportionality between the applied electric field and the electric current density as a function of frequency,

$$\tilde{J}(\omega) = \tilde{\sigma}(\omega)\tilde{E}(\omega), \tag{5.41}$$

where $\tilde{\sigma}(\omega) = \sigma_1(\omega) + i\sigma_2(\omega)$ is the optical conductivity. Most importantly, the DC mobility can be extracted by modeling the dispersion of $\tilde{\sigma}(\omega)$. By inverse Fourier transform, equation 5.41 can also be written as an integral equation for the time-dependent current as,

$$J(t) = \int_{-\infty}^{t} \sigma(t-t')E(t')dt', \tag{5.42}$$

where $\sigma(t-t')$ is the current response function, which is the inverse Fourier transform of the Drude conductivity. This equation can be seen as a generalization of the first term on the right-hand side of equation 5.33.

5.6.2 Drude model

A simple model for the optical conductivity is the Drude model, which considers the material as an ensemble of independent electrons subject to a viscous force where the velocity of an electron can be written as,

$$\frac{dv}{dt} + \frac{v}{\tau} = \frac{qE}{m^*}, \tag{5.43}$$

where v is the velocity of a single carrier, and q, m^*, and τ are is its charge, effective mass, and scattering time, respectively. With the substitutions $v = \tilde{v}(\omega)e^{-i\omega t}$ and $E = \tilde{E}(\omega)e^{-i\omega t}$, this can be written in the frequency domain as,

$$(-i\omega + 1/\tau)\tilde{v}(\omega) = q\tilde{E}(\omega). \tag{5.44}$$

The current density can be written as $\tilde{J}(\omega) = Ne\tilde{v}(\omega)$ so that from equation 5.41 the Drude conductivity is,

$$\tilde{\sigma}_{Dr}(\omega) = \frac{Nq\tau}{m^*}\frac{1}{1-i\omega\tau}, \tag{5.45}$$

where $\tilde{\sigma}_{Dr}(\omega)$ is the Drude conductivity. In the Drude model, the carrier mobility can be defined as,

$$\mu_{Dr} = \frac{|q|\tau}{m^*}, \tag{5.46}$$

which is the mobility that can be used in equation 5.33 for sufficiently low-frequency fields.

5.6.3 Drude-Smith model

The Drude conductivity is often insufficient to describe the optical conductivity in nanomaterials where experimental spectra often show a suppression of low-frequency conductivity and a negative imaginary conductivity. In the THz community, the Drude-Smith model [143] is often used to interpret these spectra. Historically, the Drude-Smith conductivity was attributed to carrier backscattering at boundaries, however, an alternative picture was recently provided by our group pointing to a diffusive restoring force as the microscopic origin of the Drude-Smith model [144]. From equation 5.33, it should be unsurprising that diffusion could contribute to the conductivity response in non-uniform systems where currents lead to charge gradients.

Cocker *et al.* showed that the charge density gradient could be related to the integral of the current density by,*

$$\frac{dN}{dz} = \frac{a}{D}\int_{-\infty}^{t} J(t')dt', \tag{5.47}$$

where $a = 12D/qL^2$ and L is the length scale on which carriers are localized [144]. Using equations 5.42, 5.45, and 5.47, equation 5.33 can be written as,

$$J(t) = \int_{-\infty}^{t} \sigma_{Dr}(t-t')E(t')dt' - a\int_{-\infty}^{t} J(t')dt'. \tag{5.48}$$

Taking the derivative, Fourier transforming, and rearranging this can be written as,

$$\tilde{J}(\omega) = \tilde{\sigma}_{Dr}(\omega)\left(\frac{1}{a/i\omega - 1}\right)\tilde{E}(\omega). \tag{5.49}$$

*Note that Cocker *et al.* worked in the response function formalism so the notation differs from the present work, however, the underlying logic is the same. We speculate that the connection to the diffusion equation developed here could yield further insight in future studies.

The quantity multiplying the electric field on the right-hand side is the conductivity, which itself can be rewritten as,*

$$\tilde{\sigma}(\omega) = \frac{Nq^2\tau_{Dr}}{m^*}\frac{1}{1-i\omega\tau_{Dr}}\left(1-\frac{1}{1-i\omega\tau_{diff}}\right), \tag{5.50}$$

where $\tau_{diff} = a^{-1}$ is the diffusion time. This equation showed excellent agreement with Monte Carlo simulation of conductivity in localized systems with fully reflective boundaries. Note that in this equation the scattering time, τ_{Dr}, contains contributions both from the bulk scattering processes and scattering from boundaries. Furthermore, a phenomenological extension of this equation yields,

$$\tilde{\sigma}_{DS-mod}(\omega) = \frac{Nq^2\tau_{Dr}}{m^*}\frac{1}{1-i\omega\tau_{Dr}}\left(1+\frac{c}{1-i\omega\tau_{diff}}\right), \tag{5.51}$$

where c is a constant that varies from -1 to 0, yielded excellent agreement with Monte Carlo simulation with partially reflective boundaries. The constant c was shown to depend exponentially on the reflection coefficient with $c = -1$ corresponding to fully reflective boundaries and $c = 0$ corresponding to fully transmissive boundaries. In the special case where $\tau_{diff} = \tau_{Dr} \equiv \tau_{DS}$, equation 5.51 is equivalent to the usual Drude-Smith model [143],

$$\tilde{\sigma}_{DS}(\omega) = \frac{Nq^2\tau_{DS}}{m^*}\frac{1}{1-i\omega\tau_{DS}}\left(1-\frac{c}{1-i\omega\tau_{DS}}\right). \tag{5.52}$$

In the notation of Cocker *et al.*, equation 5.50 is the modified Drude-Smith model, equation 5.51 is the extended modified Drude-Smith model, and equation 5.52 is the truncated Drude-Smith model. In the Drude-Smith model there are two notions of carrier mobility. One characterizes how free charges are to move on length scales shorter than the localizing morphology, which is given by,

$$\mu_{DS} = \frac{q\tau_{DS}}{m^*}, \tag{5.53}$$

while the other, referred to here as the long-range mobility, characterizes how free charges are to move over distances longer than the localizing morphology and is given by,

$$\mu_{DS,l-r} = \frac{q\tau_{DS}}{m^*}(1+c). \tag{5.54}$$

*This step involves a neat trick of adding 0=1-1 to the term in brackets on the right-hand side in equation 5.49.

Chapter 6

THz control of hot-carrier photoluminescence

6.1 Introduction

Over the last several years, an interesting field of fundamental research has grown around the use of intense terahertz (THz) pulses to drive and modulate light emission in a variety of ways. This work has lead to a deeper understanding both of the interaction of THz radiation with matter and the nature of light emission in a variety of material systems. Early experiments were performed at low temperatures using two-color experiments using an optical or near-infrared excitation mixed with a multi-THz macropulse pump from a free-electron lasers (FELs) [145, 146, 147]. The photon energy from the FELs could be tuned to resonant transitions of luminescence centers in semiconductors in order to modulate the PL spectrum by population transfer into or out of radiative states. Studies using free electron lasers have progressed along with FEL technology, and more recent work using isolted multi-cycle THz pulses from an FEL have yielded new insights into dark trap states in quantum dots [148] and dynamics of internal transitions in excitons [149].

With the advent of the tilted-pulse front technique for intense THz pulse generation, experiments on THz driven or modulated luminescence have become possible with table-top sources. In GaAs quantum wells, intense THz pulses have been shown to drive carrier multiplication by cascaded impact ionization that leads to bright luminescence [150]. Followup studies in more uniform and high purity GaAs quantum

wells showed that the carrier multiplication was suppressed, however, bright luminescence flashes could be seen with simultaneous resonant continuous-wave illumination.* Here, the luminescence enhancement was attributed to ionization from trap states, similar to the earlier work done with FELs [148].

Several studies have explored the use of metamaterials to enhance the THz electric field, facilitating THz control of light emission. For example, using gold plasmonic antennae patterned on a bulk GaAs substrate enables bright and hot luminescence, which is attributed to Zener tunneling in atomically-strong THz fields [102]. Similar results are obtained in quantum dot systems with gold nanoslit arrays for field enhancement [151]. In this work, the luminescence was attributed to field induced tunneling between adjacent quantum dots. Moreover, using sub-gap optical excitation the authors demonstrated THz-assisted photoluminescence (PL) due to the dynamic Stark effect. This technique also enables characterization of the spatial distribution of the field enhancement, which was shown in recent work probing THz-assisted PL with several different antenna geometries and spatially resolving the near-field THz waveform [152]. With similar antenna structures, intense THz pulses can also be used to drive electron emission and excite ultraviolet fluorescence from a nitrogen plasma [153].

THz pulses can also be used to modulate atomic fluorescence directly without the field enhancement afforded by antenna structures. A number of studies have showed how plasma fluorescence induced by strong-field ionization is enhanced by intense THz pulses, enabling plasma characterization [154] and coherent sampling of the THz waveform [155, 156]. In these studies, the mechanism of modulation was proposed to be THz-induced heating resulting in impact ionization from high-lying Rydberg states. More recent work in gases using a narrowband electronics-based THz source to resonantly excite high-lying transitions and induce fluorescence shows a great deal of promise in THz imaging [157]. This technique, which shows incredible sensitivity and acquisition speed in comparison to conventional THz imaging, is currently limited to only a very narrow THz bandwidth. Nevertheless with the variety of atomic systems

*The authors suggest several possible origins of the suppression including an enhacement of the impact ionization rate due to disorder-induced relaxation of wavevector conservation and a reduction of the THz pulse electric field due to different sample structure.

there remains considerable hope that this method can be adapted to a variety of THz frequencies, which could enable rapid and high-sensitivity THz multi-spectral imaging.

In a different context, THz pulses have also been used to drive luminescence in the tunneling junction of a scanning-tunneling microscope (STM) [158]. Here, a variety of interesting measurements were performed showing both modulation of DC luminescence from the STM bias and zero-bias THz-induced luminescence due to inelastic tunneling via plasmons. This work is quite exciting as it highlights the potential for the study of time-resolved luminescence of, *e.g.*, few or single molecule systems [159].

Several studies have also been performed using intense THz pulses to modulate PL in bulk semiconductors. In early work, Liu *et al.* showed that intense THz pulses quench PL in bulk GaAs and CdTe [160]. The effect proved to be linear with THz intensity, which led the authors to suggest that THz-induced heating was the origin of the PL quenching, however, no detailed mechanism was elaborated. The authors reported that no PL quenching was observed in semiconductors with large excess energy on excitation, suggesting that cool carriers were more strongly affected by THz heating than hot carriers.

This problem was subsequently studied theoretically using Monte Carlo simulation and the PL quenching was attributed to non-radiative recombination due to the high-wavevector phonons participating in intervalley scattering [161]. However, the link between intervalley phonons and non-radiative recombination was not strongly motivated. Because non-equilibrium phonons have a lifetime of only a few picoseconds at room temperature, in order to achieve a high PL-quenching ratio a very large trapping rate in relation to the carrier lifetime must be assumed. If this were the case, one would expect a strong temperature quenching of luminescence, which is not observed experimentally. Moreover, the link between high-wavevector phonons and non-radiative recombination is not established in the literature.

In our own work, building on the results of Liu *et al.*, we discovered that in addition to PL quenching, intense THz pulses can be used to enhance high-energy

PL coming from hot carriers in the initial stages of relaxation [60]. We studied the THz-induced quenching and enhancement of PL, referred to from here as THz-ΔPL, over a range of experimental conditions in GaAs and also reported high-energy PL enhancement in InP.* We also observed the modulation of PL in Ge and studied an interesting and dynamic interplay between the direct- and indirect-gap [98, 62]. More recent work showing enhancement of high-energy PL has been reported in a metal-halide perovskite, where the high-energy PL enhancement was attributed to resonant excitation of phonon modes resulting in a hot-phonon bottleneck [162].

This chapter builds on our previous studies of THz-ΔPL in semiconductors [60, 22] beginning with a brief description of the salient features of the THz-ΔPL in GaAs. It then proceeds by developing a simple model that encompasses both the PL quenching near the band gap and the PL enhancement in the high-energy tail in bulk direct-gap semiconductors [22]. With a thermodynamic model of the PL emission and a diffusion-equation approach to calculate the spatio-temporal evolution of the carrier distribution, we show how both PL enhancement and PL quenching can arise from THz-induced carrier heating. With minimal assumptions regarding the complex interactions in the sub-picosecond regime (see section 5.1), this effective model facilitates a heuristic understanding of the THz-ΔPL, external PL spectrum, and transient radiative efficiency, providing qualitative and even semi-quantitative agreement with experiment.

6.2 THz-ΔPL in GaAs

The experimental layout for our studies of THz-ΔPL, the THz modulation of PL, is shown in Figure 6.1a, where a femtosecond optical pulse excites carriers across the band gap in a semiconductor, inducing PL, and an intense THz pulse simultaneously drives carrier heating via the strong electric field. The resulting PL was collected non-collinearly, to avoid the specularly reflected laser pulse, and directed to a spectrometer via an optical fiber. The THz-ΔPL in GaAs as a function of optical/THz time delay and PL photon energy is shown in Figure 6.1b. The THz-ΔPL occurs when the THz

*We note that the enhancement of high-energy PL was also seen in CdTe, however, the bandgap energy was significantly closer to the excitation photon energy making it more difficult to distinguish PL from scattered laser light.

and optical pulses are overlapped in the crystal. Note that the time delay is defined relative to the THz pulse, shown above. Near the band gap at 1.42 eV, which is also the peak of the PL spectrum as shown to the left, the THz pulse induces strong PL quenching. In the high-energy tail, however, the THz pulse induces enhancement in the region $\sim 2k_bT$ above the band gap. The photon energy at which the THz-ΔPL transitions from quenching to enhancement is defined as $E_{\gamma\times}$.

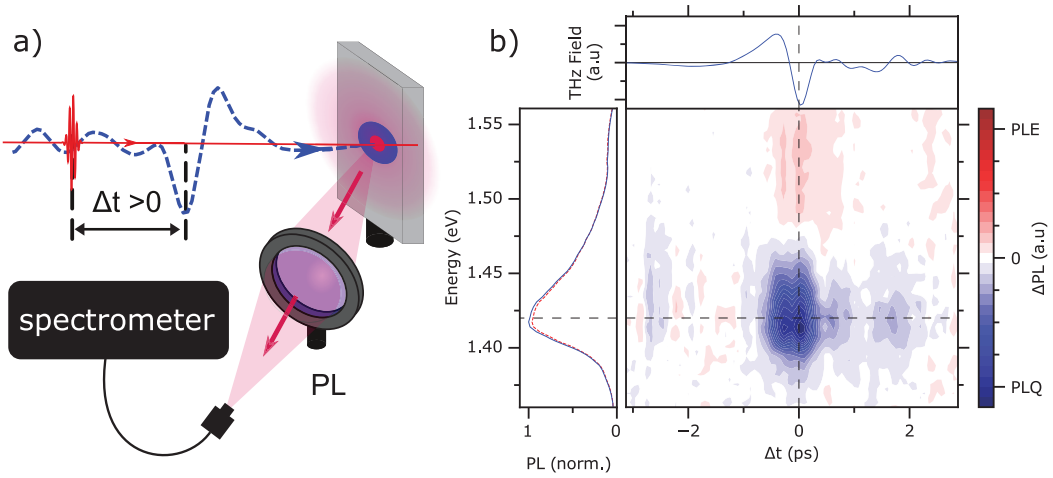

Fig. 6.1: THz-ΔPL: Experiment and salient features. **a** Schematic layout of the THz-ΔPL experiment, where a femtosecond optical pulse and intense THz pulse are coincident on a semiconductor. The resulting PL is collected non-collinearly and directed to a spectrometer via an optical fiber. **b** 2D scan of the THz-ΔPL as a function of PL photon energy and THz pump/femtosecond excitation pulse time delay. The instantaneous field of the THz pulse is shown along the top and the spectrally-integrated PL spectrum with (blue line) and without (red dashed line) are shown to the left. This figure was adapted from ref. [22]. The horizontal dashed line indicates the band-gap energy while the vertical dashed line is the time delay used for the cross section in Figure 6.2a. The optical fluence and THz electric field were 300 μJ cm^{-2} and 200 kV/cm, respectively. In the colormap, red indicates PL enhancement and blue PL quenching.

More quantitative information about the THz-ΔPL can be obtained by plotting a cross section of the 2D scan at the peak of the THz envelope, as shown in by the blue (absolute) and red (fractional) lines in Figure 6.2a, along with the normalized PL spectrum shown in black. From the blue line, it appears that the PL quenching is significantly stronger than the PL enhancement, which is due to the asymmetry of the PL spectrum. On the other hand, the red curve shows that the PL enhancement

is as large as the PL quenching relative to the spectrally-resolved PL intensity. The crossover energy is near 1.475 eV, which is approximately $2k_bT$ above the peak of the PL spectrum at the band gap. Figure 6.2b shows the spectrally integrated THz-ΔPL as a function of optical/THz time delay. The curve closely follows the envelope of the THz pulse. Note that positive time implies that the THz pulse, which is considered the pump in this case, arrives before the optical pulse. An integrated PL quenching of approximately 1% is observed.

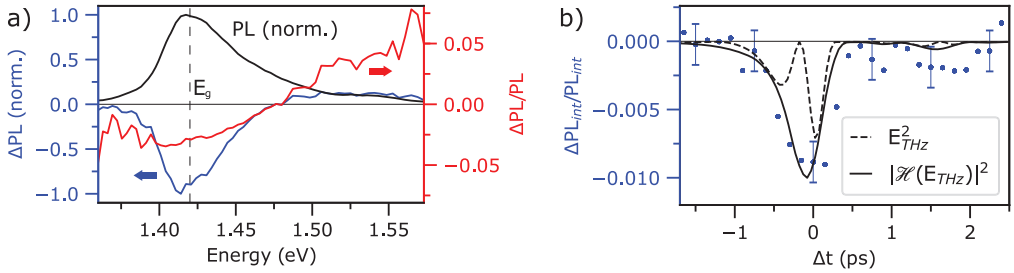

Fig. 6.2: Cross section and integral. **a** Cross section of the THz-ΔPL (blue) and THz-ΔPL/PL (red) taken at the time delay where the optical pulse is coincident with the peak electric field of the THz pulse. The black line indicates the normalized PL spectrum. **b** Integral of the THz-ΔPL as a function of optical/THz time delay (blue squares) with the THz intensity envelope, calculated from the absolute value of the Hilbert transform, overlayed. The dashed black lines indicate the negative absolute value of the THz electric field.

6.3 Diffusion model of PL

The essential physics of PL in bulk semiconductors was developed in chapter 5. Using the simplest model for the direct-gap absorption coefficient, where $\alpha \propto \sqrt{E_\gamma - E_g}$, and the Boltzmann approximation for the occupancies, the equation for the rate of radiative recombination as a function of energy, equation 5.21, can be written as,

$$r_{sp}(E_\gamma, z, t) = B \cdot n^2(z,t) \cdot \exp(-E_\gamma/k_bT) \cdot \sqrt{E_\gamma - E_g}, \tag{6.1}$$

where B is the radiative rate constant and n is the carrier density.* From this equation, it is clear that THz-induced carrier heating, which is a well established

*This equation assumes an undoped semiconductor so that the concentration of electrons and holes is equal.

phenomenon [163, 164, 116, 165, 166, 167, 102, 19], should lead to enhancement of high-energy PL [22]. However, it is not immediately clear why carrier heating should result in PL quenching. Note that carrier heating is distinct from lattice heating, which can itself lead to PL quenching [138], however, the energy in the THz pulse is insufficient to heat the lattice a significant amount.*

From a different perspective, the radiative efficiency (and PL spectrum) in bulk semiconductors is well understood in terms of radiative (bimolecular), Shockley-Reed-Hall (monomolecular), and surface recombination along with carrier diffusion [168, 169, 138]. A diffusion-equation based picture of relaxation dynamics in GaAs is also well established in ultrafast THz spectroscopy [128, 142]. It is therefore prudent to use this as a starting point for the investigation of THz-ΔPL. A 1D numerical model of relaxation including these elements was developed.†

Table 6.1: Literature parameters for the material constants used in the diffusion model for THz-ΔPL in the three experimentally relevant semiconductors.

Mat.	E_g (eV)	δ (μm)	v_{surf} ($\times 10^5\, cm/s$)	μ_{ab} ($\mathrm{cm^2 V^{-1} s^{-1}}$)	A ($\times 10^9 s^{-1}$)	B ($\times 10^{-10}\,\mathrm{cm^3\,s^{-1}}$)
GaAs	1.42	0.74	8.5	388	0.5	1.7
InP	1.34	0.30	1	192	0.01	0.5
CdTe	1.50	0.76	1.6	83	-	-

Shown in Figure 6.3a is the calculated integrated PL spectrum for a GaAs-like semiconductor (see table 8.2). An exponential density with depth based on the penetration depth, δ, was used. Surface recombination was included via the surface recombination velocity, v_{surf}. The density profile was evolved numerically in time using a Crank-Nicholson scheme [170] based on the diffusion equation with bi-molecular and monomolecular recombination terms until an insignificant fraction of carriers remained. At each time step, the emitted PL spectrum was calculated by integrating

*This argument does not preclude the possibility of hot phonon effects, where the effective temperature for a subset of the phonon modes is significantly higher than the lattice temperature, which can affect carrier-cooling times [122].

†While an analytic solution of the diffusion equation with monomolecular and surface recombination exists, to the best of the authors knowledge there are no known analytic solutions that can account for the bi-molecular term. Moreover, numerical solution allows for a time-dependent temperature, which is a key aspect of ultrafast PL experiments.

the luminescence intensity over the full density profile using equation 5.23. An exponential cooling of the hot-carrier temperature* with a time constant of 50 ps was used, as seen in the inset of Figure 6.3a. The 50 ps time constant was chosen for illustrative purposes. The PL spectrum was calculated for two different initial hot-carrier temperatures, 600 K (blue) and 900 K (orange). Clearly the hotter initial carrier temperature results in a decrease in the peak PL intensity.

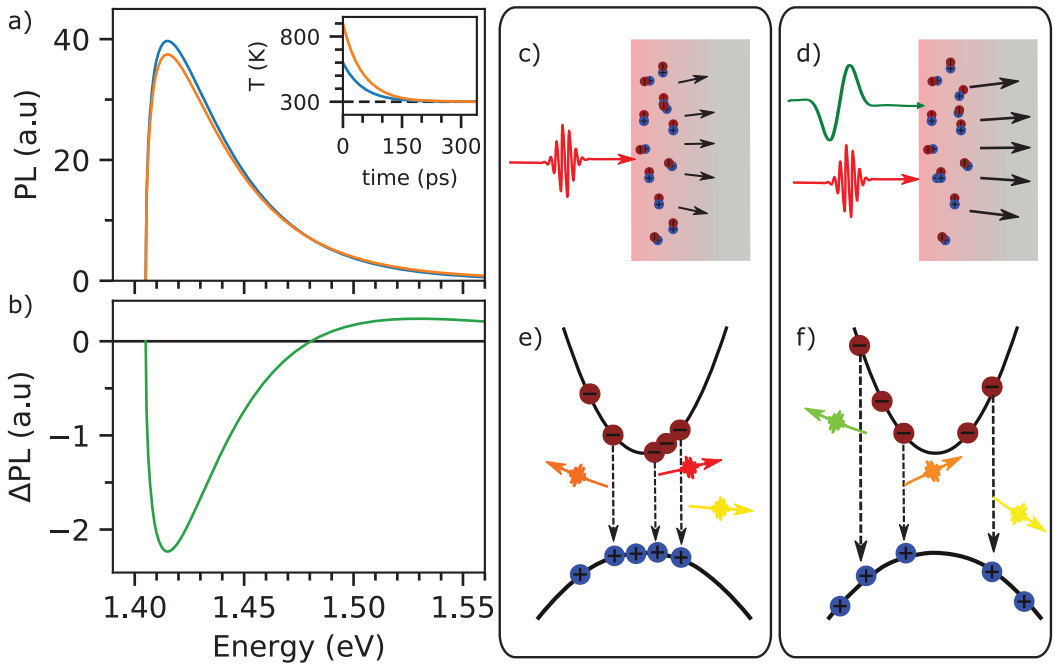

Fig. 6.3: THz-ΔPL model. **a** Integrated PL spectrum for a semiconductor calculated using the model described in the text using two different initial hot-carrier temperatures with an exponential carrier cooling. The simulation parameters are defined in table 8.2. **b** Differential PL spectrum from the two cases in **a**. Illustration of the processing affecting the PL efficiency and spectrum in real space (**c** and **d**) and k-space (**e** and **f**). In **c** and **e**, an optical pulse alone forms a distribution of electron-hole pairs in real space, with carriers diffusing into the substrate, and in k-space, with carriers thermally occupying the parabolic bands. In **d** and **f**, an intense THz pulse heats the distribution, which drives further diffusion into the substrate, reducing the carrier density, and drives carriers higher in the bands in k-space, increasing the amount of high-energy luminescence from hot carriers.

This can also be seen by plotting the difference between the two spectra, ΔPL, as shown in Figure 6.3b. Remarkably, the ΔPL spectrum closely resembles the ex-

*The cooling dynamics in real materials likely deviates from exponential behavior [125]. In the context of THz-ΔPL, non-exponential cooling will quantitatively change the spectrum, however, the qualitative features would remain unchanged.

perimental THz-ΔPL spectrum plotted in Figure 6.2a, which shows that both the THz-induced PL quenching and PL enhancement arise naturally due to carrier heating within the context of well established models of semiconductor PL. Nevertheless, a heuristic understanding of the origin of the integrated PL quenching remains less clear. As discussed in section 5.4 PL can be quenched either by increasing the rate of non-radiative recombination (*i.e.*, increasing A) or decreasing the rate of radiative recombination (*i.e.*, decreasing $BN(t)$). As the constants A and B remained unchanged throughout the calculation, based on equations 5.32 and 5.24 the density or spatial profile must be changing in order to quench the PL.

To see how this arises, the effect of the intense THz pulse on the distribution of carriers is illustrated in real space in Figure 6.3c, d. In Figure 6.3c, a femtosecond optical pulse photoexcites carriers in a region near the surface of the semiconductor. The concentration gradient leads to carrier diffusion deeper into the bulk at a rate determined by the carrier mobility and temperature. A similar situation is depicted in Figure 6.3b, however, an intense THz pulse additionally acts to heat the carrier distribution, which drives more rapid diffusion into the bulk of the material. This diffusion spreads the distribution out to reduce the density without recombination, which acts to reduce the radiative time constant, $BN(t)$, and leads to PL quenching.

Simultaneously, in k-space the hotter carriers tend to occupy higher-energy regions in the conduction/valence bands, which leads to emission of higher energy photons, as illustrated in Figure 6.3e, f. This leads to a additional mechanism for PL quenching, as the rate of photon reabsorption will be larger for a hotter PL spectrum. This reduces the rate at which photons are coupled out of the material into free space and therefore further reduces the external radiative efficiency.

6.4 THz-ΔPL in the Context of the Diffusion Model

6.4.1 Quenching-enhancement crossover

Most of the parameters in the diffusion model can be fixed by literature values for the material properties, which are summarized in table 8.2 for the three bulk

semiconductors for which THz-ΔPL has been reported.* The reported hot-carrier cooling times, however, can vary depending on the excitation photon energy [125], measurement technique [126], and excitation density [124], with values ranging from just several picoseconds to tens of picoseconds [125, 126]. Moreover, the initial hot-carrier temperature depends on the excitation photon energy as a carrier distribution generated with higher excess energy beyond the band edge yields a higher hot-carrier temperature. In the diffusion model, it is therefore useful to understand how these parameters affect the ΔPL.

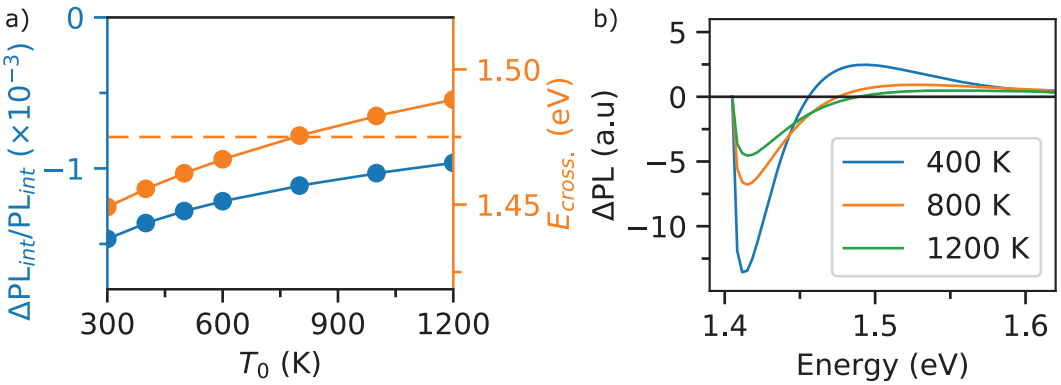

Fig. 6.4: Effect of initial hot-carrier temperature on ΔPL. a Calculated $\Delta PL_{int}/PL_{int}$ (blue) and $E_{\gamma\times}$ (orange), as a function of initial hot-carrier temperature. The horizontal dashed line indicates the experimentally observed crossover point in GaAs. **b** ΔPL spectra for three different initial hot-carrier temperatures. The calculations were performed using the parameters listed for GaAs in table 8.2 and an exponential hot-carrier cooling with a time constant of 5 ps.

Shown in Figure 6.4 is the integrated PL quenching (blue) and quenching-enhancement crossover energy for a GaAs-like semiconductor as a function of initial hot-carrier temperature. The differential temperature, heuristically considered the THz-induced heating, was chosen to be 100 K above the initial hot-carrier temperature. An exponential cooling with a 5 ps time constant was used. The horizontal dashed line indicates the quenching-enhancement crossover energy observed in GaAs, which appears to occur with an initial hot-carrier temperature of approximately 750 K. This is quite similar to the initial hot-carrier temperature of approximately 900 K reported by Clady *et al.* using time-resolved PL with 735 nm excitation [125]. Moreover, the

*The material properties themselves also vary depending on the reference. *E.g.*, for the radiative lifetime see ref. [171] versus ref. [172].

integrated PL quenching of approximately 0.1 % at this energy is similar to that of the experimentally observed THz-ΔPL. To see how the initial hot-carrier temperature affects the ΔPL spectrum, Figure 6.4 shows the ΔPL spectrum for 3 different initial hot-carrier temperatures. This suggests that within the diffusion model, the THz-induced heating more strongly affects cool carriers rather than hot carriers, which was suggested by Liu *et al.* based on their experimental results [160].

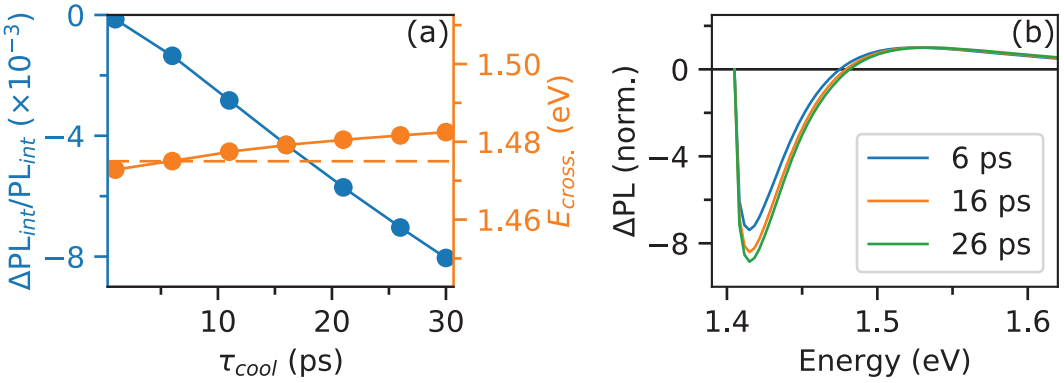

Fig. 6.5: Effect of hot-carrier cooling time on ΔPL. a Calculated integrated ΔPL (blue) and $E_{\gamma\times}$ crossover point (orange) as a function of hot-carrier cooling time. The horizontal dashed line again indicates the experimentally observed crossover point in GaAs. **b** ΔPL spectra for three different values of τ_{cool}. The calculations were performed with exponential cooling and using the parameters listed for GaAs in table 8.2 and an initial hot-carrier temperature of 800 K.

Similarly, the integrated ratio of the change in PL intensity to the integrated PL, $\Delta PL_{int}/PL_{int}$, is plotted in Figure 6.5a (blue) along with $E_{\gamma\times}$ (orange) as a function of cooling time, τ_{cool}, with an initial hot-carrier temperature of 800 K. The values of τ_{cool} from 1 ps to 30 ps cover more than the range of reported cooling times in the literature. Interestingly, the $E_{\gamma\times}$ is significantly less sensitive to τ_{cool} than it is to the initial hot-carrier temperature. The normalized ΔPL spectra for 3 different values of τ_{cool} are plotted in Figure 6.5b. Here, the spectra are normalized to highlight the fact that, qualitatively, larger τ_{cool} increases the ratio of the peak PL quenching to peak PL enhancement.

6.4.2 Scaling with THz energy

The dependence of the ΔPL spectrum on the increased hot-carrier temperature, defined as ΔT_{hc}, is shown in Figure 6.6a for three different values of ΔT_{hc}. With some assumptions, the this can be roughly mapped to the incident THz pulse energy. First, one must assume that the absorbed THz energy scales linearly with the incident THz field, which is a reasonable starting point. Second, one must assume that the heat capacity of the electron-hole plasma is independent of temperature, which holds in a non-degenerate system where the occupancies follow Boltzmann statistics and their heat capacities are that of an ideal gas. As a result of this first-order correspondence, in Figure 6.6b, the THz-ΔPL for three different incident THz pulse energies is plotted for comparison to the calculation from the diffusion model. The diffusion model correctly reproduces the qualitative behavior of the experimental data, where in the model $E_{\gamma\times}$ does not change significantly and only the ΔPL amplitude, not lineshape, changes significantly with ΔT_{hc}.

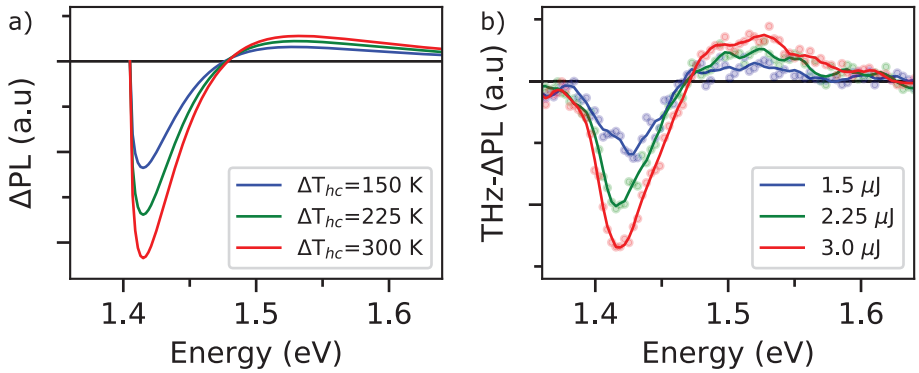

Fig. 6.6: THz heating dependence of the ΔPL. a Calculation of the ΔPL spectrum from the diffusion model using the parameters for GaAs and an initial hot-carrier temperature of 800 K with three different values of ΔT_{hc}. **b** Experimentally measured THz-ΔPL for three different incident THz pulse energies (reproduced from refs. [60, 22]).

Furthermore, in ref. [60], we showed that that integrated THz-ΔPL/PL scales linearly with incident THz pulse energy. The $\Delta PL_{int}/PL_{int}$ calculated from the diffusion model is plotted as a function of ΔT_{hc} in Figure 6.7 (blue dots) along with a linear fit through the first data point (black line). For comparison the experimental THz-ΔPL/PL is also shown in Figure 6.7b. The $\Delta PL_{int}/PL_{int}$ from the diffusion

model shows nearly linear scaling with ΔT_{hc}, however, at larger values the scaling is slightly sublinear. This sub-linear scaling, which does not appear to occur experimentally, could be due to an overestimation of the PL enhancement from the model at high energies, where the parabolic approximation to the density of states (DOS) breaks down, or it could be an indication that either the assumption of exponential (temperature independent) and density-independent cooling does not hold. Alternatively, it could be an indication that the assumptions about the linearity between THz energy and THz heating do not hold. Regardless of its origin, the deviation from linearity in the model is small. Moreover, the amplitude of the $\Delta PL_{int}/PL_{int}$ from the diffusion model is a similar magnitude to that of the experimental data, which further supports the validity of the diffusion model.

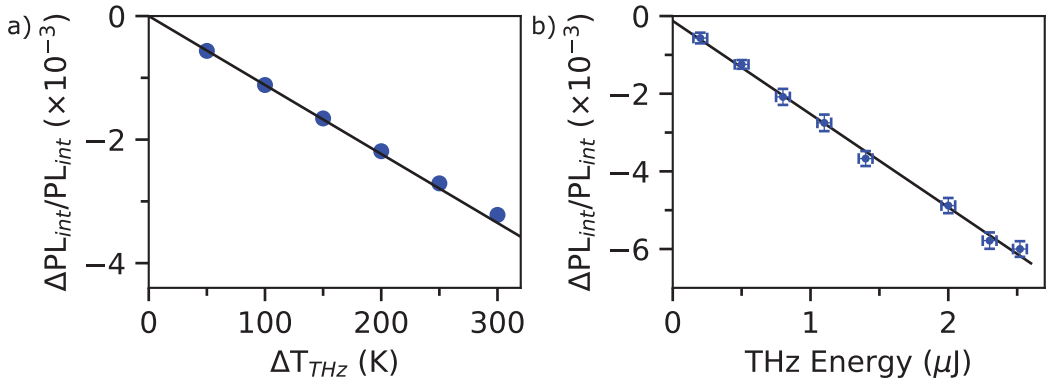

Fig. 6.7: THz heating dependence of the integrated ΔPL. Calculated $\Delta PL_{int}/PL_{int}$ as a function of ΔT_{hc} (blue circles) along with a linear fit through the first data point (black line). **b** Experimentally measured THz energy dependence of the $\Delta PL_{int}/PL_{int}$ (reproduced from Refs. [60, 22]).

6.4.3 THz-ΔPL in InP

In ref. [60], we also reported on the observation of THz induced PL quenching and enhancement in InP. The diffusion model developed in this chapter should also be applicable in this case. Shown in Figure 6.8a, b are the calculated and experimental PL in InP, respectively. The material parameters in the calculation were adjusted to reflect the values for InP reported in table 8.2. Note that both the non-radiative and radiative constants in InP are significantly lower than in GaAs. We found that the non-radiative rate constant did not significantly affect the calculated ΔPL, so

a shorter non-radiative lifetime was used in the calculations to facilitate more rapid calculation. Moreover, the band gap energy is 1.34 eV as opposed to 1.42 eV in GaAs so that the initial hot-carrier temperature should be larger.* From time-resolved PL studies, for a given excitation photon energy the hot-carrier temperature in InP can be several hundred Kelvin larger than in GaAs [125]. An initial hot-carrier temperature of 1200 K was therefore chosen. The cooling time was again assumed to be exponential with a 5 ps time constant. The calculation appears to overestimate the broadness of the PL peak in comparison to the experimental data, which could indicate either that the chosen hot-carrier temperature is too large or that the model does not properly account for the energy-dependent absorption coefficient in InP.

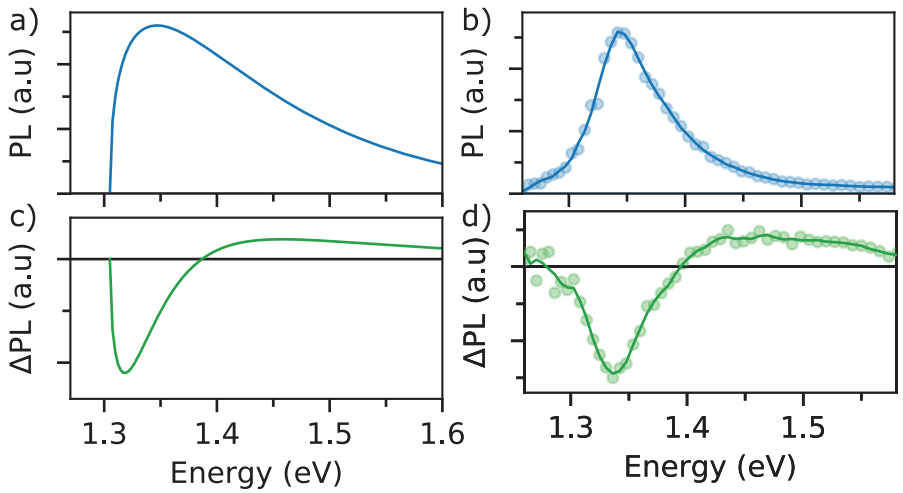

Fig. 6.8: ΔPL in InP. a Calculated and **b** experimental PL spectra in InP. **c** Calculated ΔPL and **d** experimentally measured THz-ΔPL in InP. The calculation was performed with the parameters for InP from table 8.2 with a 1200 K initial hot-carrier temperature and a 5 ps cooling time. The experimental spectrum was measured with a monochromator and avalanche photodiode (APD). A spectra correction accounting for the grating efficiency and APD responsivity was applied to the data.

Shown in Figure 6.8c, d are the calculated ΔPL and experimental THz-ΔPL spectra in InP, respectively. The ΔPL was calculated with ΔT_{hc}=300 K. As with GaAs, the model reproduces the qualitative behavior of the experimental data well, such as the approximate ratio of peak PL quenching to enhancement and the quench-

*Note that the band gap for calculations was also adjusted to account for band-tailing, as with the calculations for GaAs, so that the peak of the calculated spectrum coincided with that of the experimental spectrum.

ing/enhancement crossover energy. Interestingly, this crossover energy is located a similar distance from the peak of the PL spectrum as GaAs despite the larger initial hot-carrier temperature. This appears to be due to the lower radiative coefficient in InP with respect to GaAs [137]. A lower radiative coefficient tends to red-shift the quenching/enhancement crossover energy, which is less sensitive to the other material parameters, such as the non-radiative coefficient, ambipolar mobility, and surface recombination velocity.

6.5 New Insight at High-Injection Levels

This section examines the behavior of the PL and THz-ΔPL as a function of optical excitation fluence, which reveals interesting signatures in the PL and THz-ΔPL spectra that result from the high carrier density injection levels. The experimental results reported for GaAs are reproduced from ref. [60], however, the results are reinterpreted with new insight to the origin of observations [22]. New experimental results are reported for InP. The optical fluence dependence in the diffusion model is studied to help understand the experimental results, however, in its basic form the model is not able to reproduce all aspects of the data. Possible extensions to the model are proposed that could facilitate deeper understanding of the underlying physics.

6.5.1 Gallium arsenide

The spectrally integrated PL in GaAs as a function of fluence is shown in Figure 6.9. At low fluence (see the inset) the PL scales superlinearly with fluence due to the nature of bimolecular recombination (see chapter 5). At higher fluence, the PL scales sublinearly because of the onset of absorption bleaching due to state filling so that the optical pulse penetrates deeper into the sample and leads to an increased in the rate of photon reabsorption during the PL emission. The solid line was calculated using the diffusion model with a saturable absorption model for the initial carrier density [22], showing excellent agreement with the data.* The corresponding THz-ΔPL_{int} (blue) is shown along with the THz-$\Delta\text{PL}_{int}/\text{PL}_{int}$ (red) in Figure 6.9b. The

*Note that due to absorption bleaching, the carrier density is not sufficient to result in a significant contribution from Auger recombination. Moreover, fits to the data using the diffusion model are superior to those using rate equations with an Auger term.

amplitude of $\Delta\mathrm{PL}_{int}$ rapidly increases up to a fluence of approximately 500 $\mu\mathrm{J\,cm^{-2}}$, reaches a peak, then monotonically decreases. On the other hand, the fractional change is monotonically decreasing through the whole range.

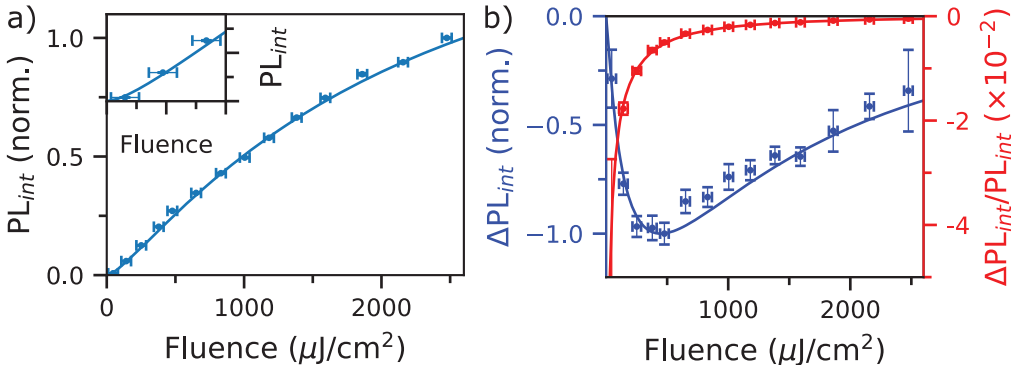

Fig. 6.9: Effect of Excitation Density on the Integrated PL in GaAs. a Integrated PL in GaAs as a function of optical excitation fluence. The data was fit with the diffusion model accounting for absorption bleaching using a saturation model to find the initial carrier density. Inset: enlargement of the first 3 data points showing the superlinear increase. **b** Corresponding $\Delta\mathrm{PL}_{int}$ (blue) and $\Delta\mathrm{PL}_{int}/\mathrm{PL}_{int}$ (red). The red solid line is a fit using a stretched exponential function of the form $\Delta\mathrm{PL}_{int}/\mathrm{PL}_{int} = C\exp\left[-(F/\gamma)^{\theta}\right]$, where C=0.46, γ=1.2, and $\theta = 0.25$ were used as free parameters. The blue curve is the stretched exponential fit times the PL fit from **a**. The data was acquired using a photodiode coupled to a lock-in amplifier triggered by a chopper modulating the THz beam.

The normalized PL spectra are shown in Figure 6.10a up to 650 $\mu\mathrm{J\,cm^{-2}}$. Surprisingly, the PL spectrum appears to narrow with increasing fluence, which is somewhat counterintuitive behavior. This is due to the onset of absorption bleaching, as the excitation pulse penetrates deeper into the substrate the corresponding increase in photon reabsorption acts to redshift the PL spectrum. Another possible contribution from absorption bleaching could be due to the reduced PL reabsorption that accompanies a degenerate system. The corresponding THz-ΔPL spectra are shown in Figure 6.10b. Along with the redshifting of the PL full-width at half maximum (FWHM), $E_{\gamma\times}$ shifts toward the band gap, suggesting that this behavior is also connected to the absorption bleaching. Up to 380 $\mu\mathrm{J\,cm^{-2}}$ the amplitude of both the PL quenching and enhancement increases after which the PL drops off, which is likely the origin of the reduction in integrated PL quenching in Figure 6.9b.

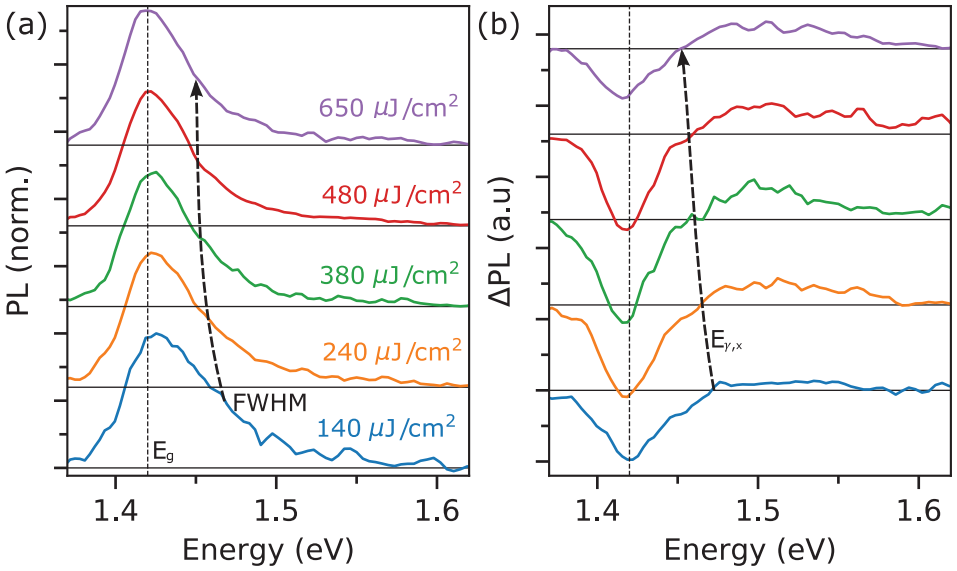

Fig. 6.10: PL redshifting with fluence in GaAs. a Normalized PL spectra for several excitation fluences in GaAs. The dashed black line indicates the FWHM energy while the vertical black line indicates the band-gap energy. **b** The corresponding ΔPL spectra. Here, the dashed black line indicates $E_{\gamma\times}$.

6.5.2 Indium Phosphide

The integrated PL as a function of excitation fluence in InP is shown in Figure 6.11a. This solid line is a fit using rate equations with only bimolecular and monomolecular terms, suggesting that the absorption bleaching due to state filling is less prominent in InP. This is expected as the excess energy is larger in this case so that both the DOS at the injection energy and the total number of states below the injection energy are both larger than in GaAs. In InP, the superlinear increase due to the nature of bimolecular recombination is more noticeable than in GaAs, which is likely due to the lower B coefficient.

The corresponding THz-$\Delta\mathrm{PL}_{int}/\mathrm{PL}_{int}$ is shown in Figure 6.11b along with the THz-$\Delta\mathrm{PL}_{int}$ in Figure 6.11c. Here, a qualitatively new regime exists in comparison to GaAs: at low fluence, the amplitude $\Delta\mathrm{PL}_{int}$ increases approximately quadratically with optical fluence as indicated by the dashed black line. At the same time, the amplitude of the $\Delta\mathrm{PL}_{int}/\mathrm{PL}_{int}$ increases nearly linearly with an intercept that projects to a non-zero value at zero fluence. At higher fluence, above approximately 800 $\mu\mathrm{J\,cm^{-2}}$, the amplitude $\Delta\mathrm{PL}_{int}/\mathrm{PL}_{int}$ recovers the monotonically decreasing

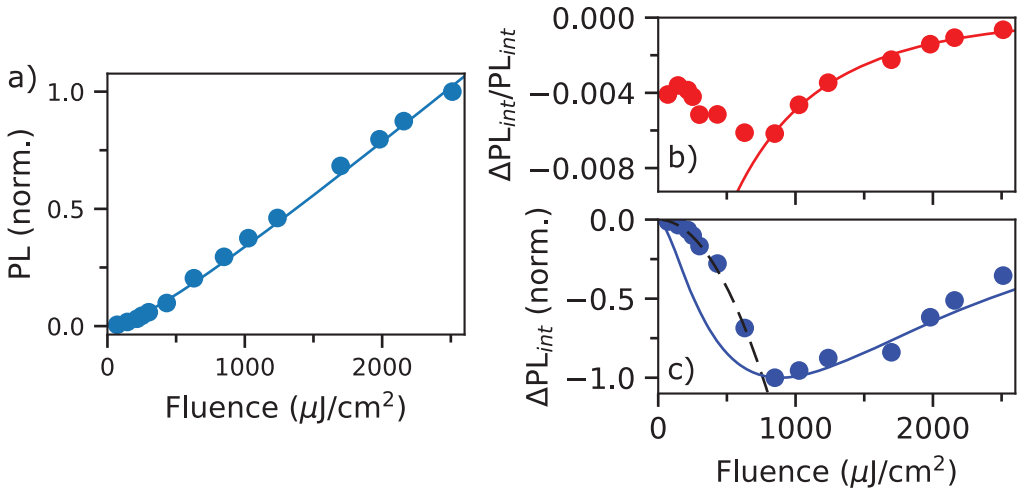

Fig. 6.11: Effect of Excitation Density on the Integrated PL in InP. a Integrated PL in InP as a function of optical excitation fluence. The data was fit with a rate equation including monomolecular and bimolecular terms. **b** Corresponding $\Delta PL_{int}/PL_{int}$ and **c** ΔPL_{int}. The red solid line in **b** is a fit using a stretched exponential function similar to that of GaAs. The blue solid line in **c** is the stretched exponential fit times the PL fit from **a** while the black dashed line is a quadratic fit.

stretched-exponential like behavior observed in GaAs.

The qualitatively different behavior carries over to the PL spectra, as shown in Figure 6.12a. In contrast to GaAs, where spectral narrowing was observed even at the lowest fluences, in InP the spectrum broadens significantly up to approximately 700 $\mu J\,cm^{-2}$. This could result from a hotter carrier distribution with increasing pump fluence or as the result of an enhanced radiative rate that results in more early-time PL before the distribution has cooled. The corresponding $E_{\gamma\times}$, which first blue shifts then red shifts with fluence, behaves similarly to the PL FWHM, as shown in Figure 6.12. This strengthens the connection already made for the GaAs data between the $E_{\gamma\times}$ and the width of the PL spectrum.

Finally, it is also interesting to study how the spectrally integrated PL quenching and enhancement scale. As illustrated in Figure 6.13a, the region of the spectrum with THz-induced PL quenching (shaded blue) and THz-induced PL enhancement (shaded red) are integrated and plotted as a function of optical excitation fluence, as shown in Figure 6.13b. Here, the line solid lines are drawn as guides to the eye. Up to approximately 700 $\mu J\,cm^{-2}$, both curves approximately quadratic scaling. At

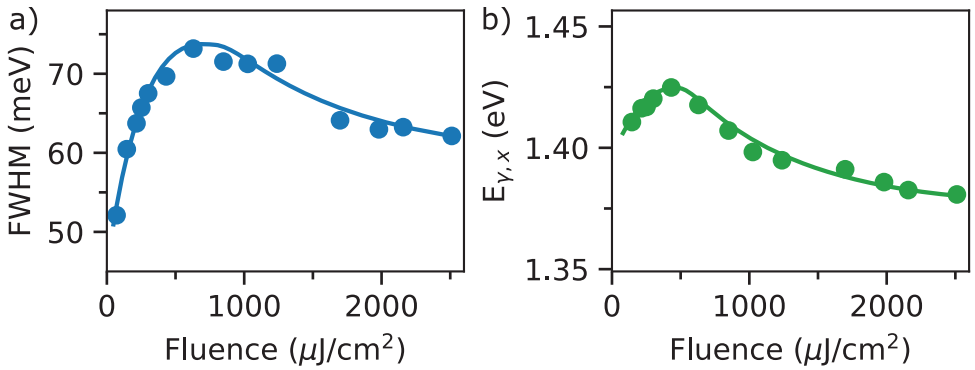

Fig. 6.12: High-fluence effects on the PL spectra in InP. a PL FWHM and **b** quenching/enhancement crossover as a function of excitation fluence in InP. The solid lines are drawn as guides to the eye.

higher fluence, the PL enhancement appears to saturate while the amplitude of PL quenching begins to decrease.

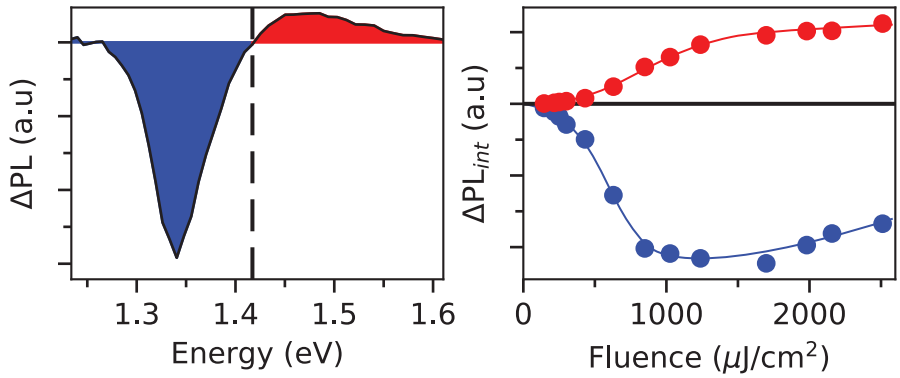

Fig. 6.13: Scaling of PL quenching and PL enhancement. a Representative THz-ΔPL spectrum with the areas integrated for the PL quenching (blue) and PL enhancement (orange) highlighted. **b** Integral of the PL quenching (blue) and PL enhancement (red) as a function of optical excitation fluence in InP.

6.5.3 Diffusion Model

Shown in Figure 6.16a is the integrated PL calculated from the diffusion model for a GaAs-like semiconductor with similar parameters as in section 6.4, showing the superlinear scaling at low fluence due to bimolecular recombination. The corresponding ΔPL_{int} and $\Delta PL_{int}/PL_{int}$ is shown in Figure 6.16b. Clearly, this behavior is contrary to that observed in GaAs (Figure 6.9) as both the absolute ΔPL and fractional ΔPL is monotonically increasing with fluence. However, this behavior is qualitatively

similar to the scaling at low fluence in InP (Figure 6.11). Note that here the curves only extend to 700 μJ cm^{-2}, however, calculations show that these trends continue to arbitrarily high fluences (not shown here).

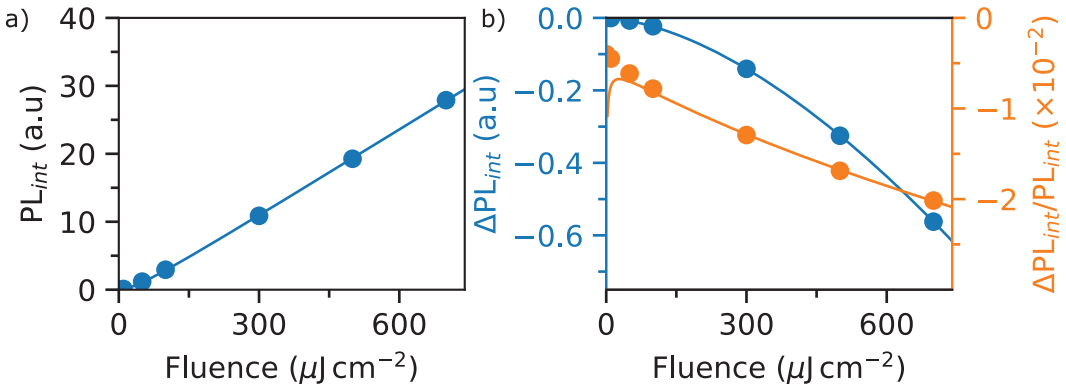

Fig. 6.14: Integrated PL and ΔPL in the diffusion model. **a** Integrated PL and **b** ΔPL_{int} (blue) and $\Delta PL_{int}/PL_{int}$ as a function of optical excitation fluence in the diffusion model.

Moving on to study the PL and ΔPL spectra, as seen in Figure 6.15a the normalized PL spectrum broadens with increasing fluence. As the carrier temperatures in the model are unchanged for each fluence, this broadening is the result of an enhanced radiative lifetime at high densities that results in a relatively larger contribution of hot-carrier PL. Looking to the ΔPL, shown in Figure 6.15b, $E_{\gamma\times}$ also appears to blueshift along with the broadening of the PL spectrum. Once again, this behavior is contrary to what was observed in GaAs, which showed a redshifting with fluence. However, similar broadening was observed experimentally in the low fluence regime in InP.

As a final point of comparison between the diffusion model and the experimental data, it is also interesting to study how the spectrally integrated PL quenching and enhancement scale with optical fluence. As for InP, illustrated in Figure 6.16a is the region of the spectrum with THz-induced PL quenching (shaded blue) and THz-induced PL enhancement (shaded red) that are integrated and plotted as a function of optical excitation fluence. As seen in Figure 6.16b, where the circles are calculated data points, both the integrated PL enhancement (red) and PL quenching (blue) scale approximately quadratically with excitation, as evidenced by the solid lines

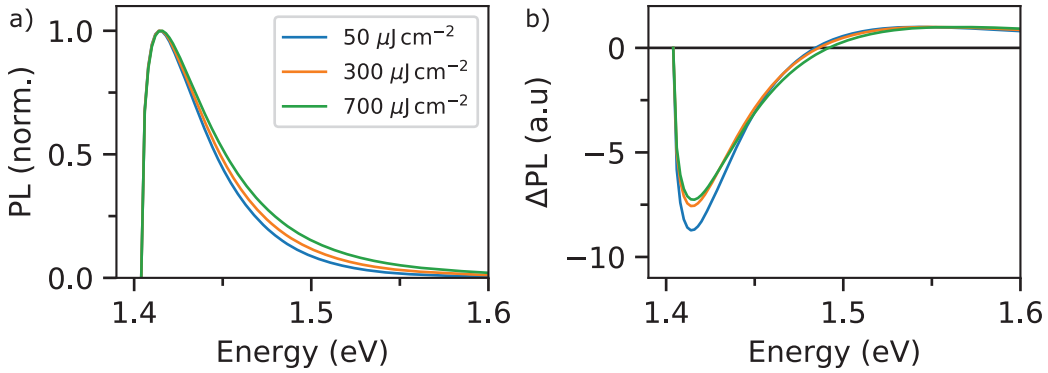

Fig. 6.15: Blue-shifting spectra in the diffusion model. **a** PL and **b** ΔPL spectra calculated for a GaAs-like semiconductor using the diffusion model.

which are quadratic fits. This behavior is similar to that observed in InP up to approximately 700 μJ cm^{-2} (see Figure 6.13), which shows that the diffusion model can reproduce the scaling of THz-ΔPL with fluence in some regime. However, this quadratic scaling holds to arbitrarily high fluence within the diffusion model, which is clearly not observed experimentally, suggesting that additional physical processes must be included in the future to fully understand the THz-ΔPL.

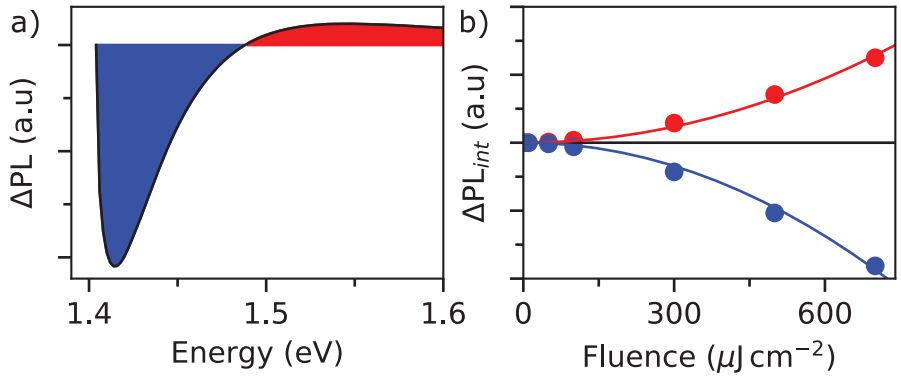

Fig. 6.16: Scaling of the PL quenching and enhancement in the diffusion model. **a** PL$_{int}$ and **b** ΔPL$_{int}$ (blue) and ΔPL$_{int}$/PL$_{int}$ calculated for a GaAs-like semiconductor using the diffusion model.

6.6 Discussion

This chapter has discussed the modulation of semiconductor PL with intense THz pulses with the goal of understanding experimental results in the context of a diffusion-based model of relaxation dynamics and PL. With a simple picture of

relaxation dynamics using proven theories and a phenomenological understanding of the interaction of intense THz pulses with free carriers in semiconductors, the THz-ΔPL was shown to arise naturally due to THz-induced carrier heating. Specifically, both the THz-PL quenching [160] and THz-PL enhancement [22], are reproduced qualitatively and semi-quantitatively by scaling a single free parameter in the simulation, the initial hot-carrier temperature. The model was also shown to capture the THz-ΔPL in both GaAs and InP.

While a great deal of new insight was attained, some aspects of the THz-ΔPL remain mysterious, namely, the scaling of the THz-ΔPL and PL with optical excitation fluence. It is likely that more insight could be obtained with extensions of the diffusion model. For example, the density-dependent carrier mobility should be included in the diffusion calculations to capture the inhibition of diffusion due to increased scattering rate [142]. Moreover, with a degenerate carrier system the simple model for the PL spectrum used in this chapter does not hold. Future development to the model should therefore include more sophisticated PL models for both the emission spectrum and reabsorption cross section. Finally, the assumptions of excitation-fluence-independent initial hot-carrier temperatures, THz-induced heating, and hot-carrier cooling times likely break down at some level. At high fluence, hot-phonon effects and state filling are likely to modify the carrier-cooling dynamics and initial hot-carrier temperature [122]. Finally, with increasing carrier density the heat capacity of the carrier system increases, suggesting that the THz-pulse-induced ΔT_{hc} should not be as large at high excitation fluence.

Nevertheless, we expect that the diffusion model of THz-ΔPL is more broadly applicable to the study of hot-carrier dynamics and should apply to a variety of direct gap semiconductors with photoexcitation below the satellite valleys.* To confirm this, future experiments could be performed, *e.g.*, with frequency-tripled light from a Ti:sapphire laser to photoexcite high bandgap semiconductors such as GaN or ZnS, or with the second harmonic of Yb:YAG-based TPF-THz systems [173], which would be suitable for THz-ΔPL experiments in CdSe or CdS. Furthermore, intense THz pulse

*Intervalley physics is not included in the model, however, it could be an interesting addition in future work.

systems in combination with an optical-parametric amplifier (OPA) could extend the THz-ΔPL studies to a variety of low band gap semiconductors. Alternatively, the OPA/THz-ΔPL combination could be useful to explore the scaling of hot-carrier dynamics with excess energy on excitation.

Chapter 7

Double-Helix SnIP: Synthesis, Properties, and Ab-initio Calculations

7.1 Introduction

The importance of the double helix structure in biology has led to significant fundamental interest in abiotic and inorganic analogues [174, 175, 176, 177, 178]. SnIP recently surprised the inorganic materials community as the first carbonless atomic-scale double helix [179]. Subsequently, several compounds were predicted to form with the SnIP structure, indicating that SnIP could be the first of a new class of inorganic double-helix materials [180, 181, 182]. With strong intra-helix covalent bonds and weak inter-helix dispersion forces, SnIP belongs to the group of newly emerging 1D van der Waals (vdW) materials with potential applications in nanoelectronics and photonics [183, 184, 185, 186]. In contrast to the DNA structure, which consists of two equal radius helices, SnIP forms with an outer $[SnI]^+$ helix wrapping around an inner $[P]^-$ helix, as pictured in Figure 7.1a. SnIP crystallizes monoclinically with a unit cell containing two opposite-handed double helices so that there is no net chirality.

It is composed of abundant and non-toxic elements and can grow uninhibited to cm-length needles with a low-temperature synthesis [179, 187], as seen in Figure 7.1b, or in nanotubes using vapor deposition [188, 189]. Its 1.86 eV band gap is well situated for solar absorption and photocatalytic water splitting [181, 183, 188].

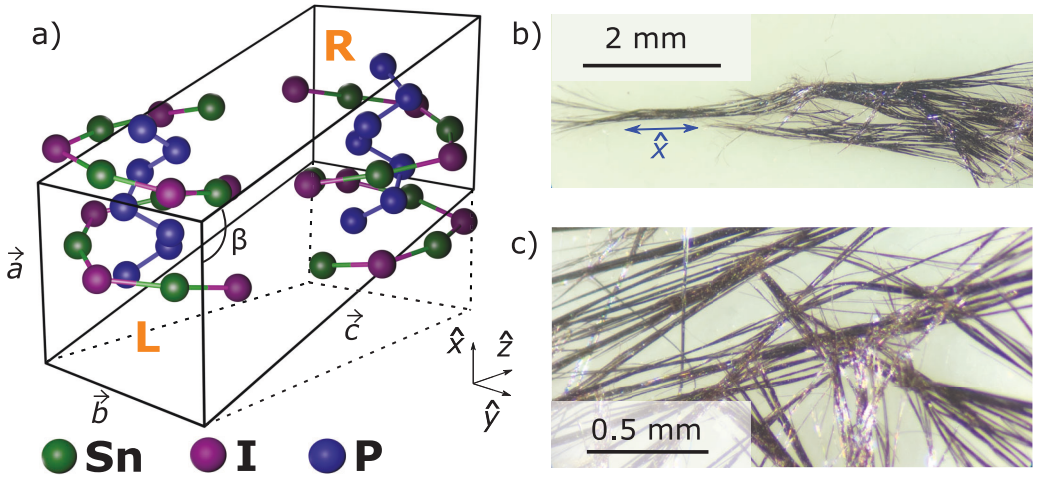

Fig. 7.1: Double-helix SnIP. a SnIP unit cell, consisting of a monoclinic unit cell (space group $P2/c$) with $|\vec{a}|$ ≈7.934 Å, $|\vec{b}|$ ≈9.802 Å, and $|\vec{a}|$ ≈18.439 Å, and $\beta \approx 110.06°$. The basis contains both a left- and right-handed strand with an outer $[SnI]^+$ helix wrapping around an inner $[P]^-$ helix. Each double-helix, which contains 7 of each constituent atom and two winds about its axis, has an outer diameter of approximately 9.8 Å[179]. The structure is inversion symmetric. **b** Bulk SnIP needles from annealing over a period of several months, indicating the large-scale morphology that can be expected from this material and highlighting the potential for growth of centimeter scale lengths. **c** Magnified version of the needles in **b.**

SnIP is also an extremely soft and flexible semiconductor and is therefore a promising material for applications in flexible electronics [179, 183], where these properties are highly desirable [190]. It is predicted to have a high carrier mobility [181], however, as-grown SnIP is highly resistive so that the current lack of doped samples has made it difficult to explore its electronic properties [179]. Moreover, despite the exciting properites and unique structure of SnIP, there have been no investigations probing its ultrafast photophysical properties.

This chapter details the synthesis and basic properties of SnIP nanowire thin films suitable for terahertz (THz) spectroscopy. It also provides a detailed discussion of the highly anisotropic electronic structure as calculated in the framework of density functional theory (DFT), providing a basis for interpreting our results from time-resolved THz spectroscopy (TRTS) in the following chapter. Moreover, the infrared (IR) active vibrational spectrum is calculated using DFT and the calculated average dielectric function shows excellent agreement with measurements of the THz dielectric

function in the region of 0.5 to 2.5 THz.

7.2 Synthesis

SnIP was grown by heating and annealing a stoichiometric mixture of SnI_4, Sn, and P_{red} in a vacuum-sealed argon-purged ampoule [179]. The ampoule was heated and cooled according to the recipe in Figure 7.2. Indicated on the right axis are the melting and boiling points of the reactants, where we see that only the SnI_4 reaches its boiling point. Moreover, the temperature does not even reach the melting point of P_{red}. Notably, the maximum temperature is significantly lower than even the melting point of P_{red}, indicating that sufficient vapor pressure for the reaction to occur is reached by sublimation. Recent gas-phase DFT calculations have elaborated on the reaction pathways of SnIP growth, which is closely related to the growth of black phosphorus [187]. The temperature of the ampoule is rapidly raised to 400 °C, which facilitates the dimerization of SnI_2 molecules to form Sn_2I_4, an important step in the SnIP reaction pathway that is not present at the higher temperatures used in the synthesis of black phosphorus. The ampoules are then slowly annealed over a timescale of approximately one week. Longer needles can be formed by annealing for a longer period of time. The thermal cycle reported here was used for the samples synthesized in this work.

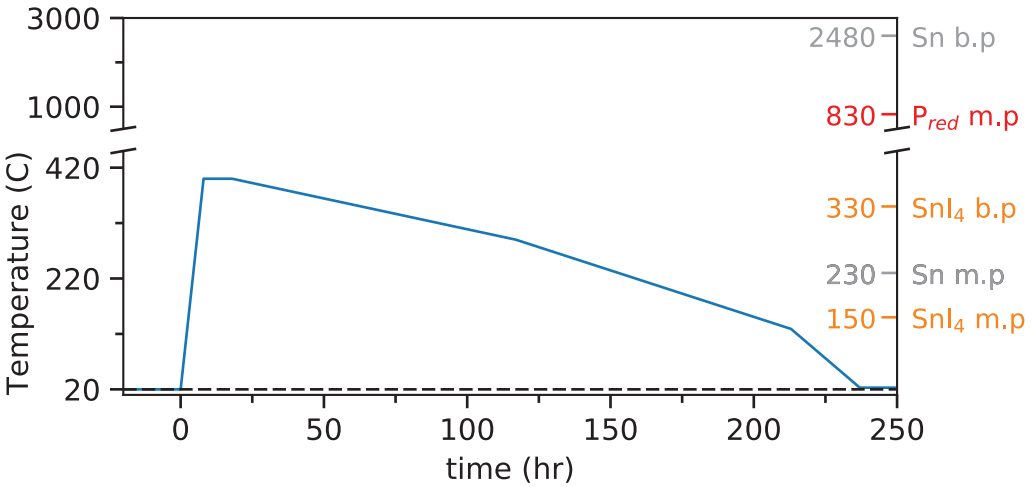

Fig. 7.2: Temperature cycle for SnIP synthesis. A vacuum sealed ampoule with the precursor materials is heated and annealed over approximately one week. The melting and boiling points of the reactants are indicated on the right axis.

A representative ampoule after the temperature cycle is shown in Figure 7.3, revealing that a complex mix of reactants and products are present. The bright orange regions are residual SnI_4 and the red regions are residual P_{red}. SnIP can be recognized by its needle-like morphology, and can be seen to have formed in several regions along the ampoule. In general, SnIP growth appears to nucleate at random locations along the ampoule.* In addition to the random nucleation sites, a polycrystalline SnIP pellet formed to the right of the ampoule, corresponding to the location of the precursor pellet. This pellet comprises the majority of the synthesized SnIP by volume.

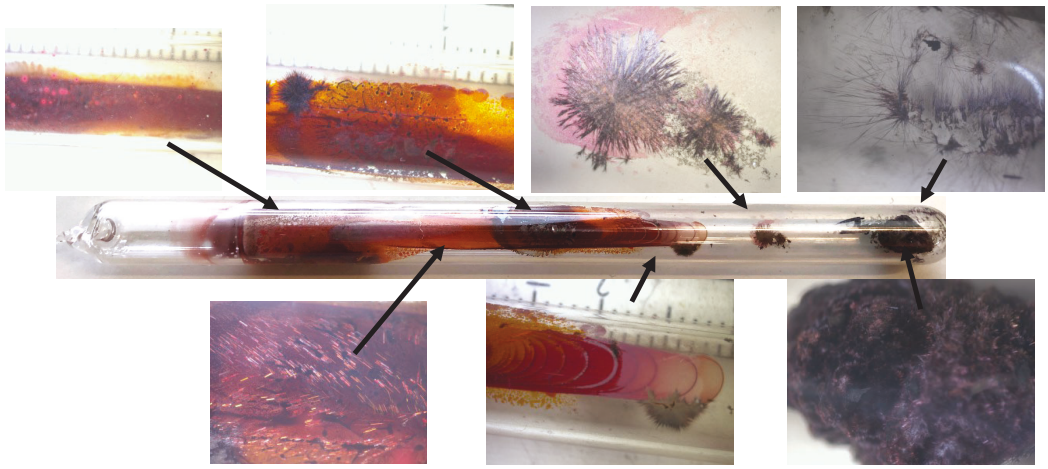

Fig. 7.3: SnIP and byproducts. A representative ampoule after the bake cycle from 7.2. The full ampoule is shown in the middle while the top row and bottom row are magnified images of the various reaction products corresponding to the locations along the ampoule indicated by the black arrows.

To create SnIP nanowires from the bulk material, the pellet was ground by mortar and pestle and suspended in toluene. The residual SnI_4 is dissolved by toluene, which is a useful method for purifying SnIP samples. Generally, several toluene rinses are required to remove all residual SnI_4. The SnIP suspension is then ultrasonicated, which gradually delaminates the weakly-bound needles into nanowires. Bundles as small as 20 nm have been observed by this method [179]. In general, ultrasonicating for a longer period of time yields a smaller diameter distribution. The nanowire suspension can be drop cast (in our case on quartz substrates) to produce a relatively

*In addition to the standard synthesis, we attempted to catalyze SnIP nucleation by depositing tin on quartz slides. While this specific technique was unsuccessful, such controlled growth methods could be useful for future devices based on SnIP.

uniform thin-film.*

7.3 Nanowire-Film Characterization

To better characterize the SnIP nanowire film, we performed several measurements to study the morphology, optical properties, and crystalline quality. Where possible, we include comparisons between measurements of the nanowires with respect to the bulk needles, providing a more complete picture of the effect of ultrasonication on the nanowires properties.

7.3.1 Microscopy

In Figure 7.4a, we show an image of the SnIP nanowire film on a quartz substrate.† The area circled red, which was used for THz-TDS, shows a uniform film thickness with high-density coverage. In this photo, the areas to the left and the right of the red circle were cleaned to facilitate acquisition of a reference waveform for THz-TDS.

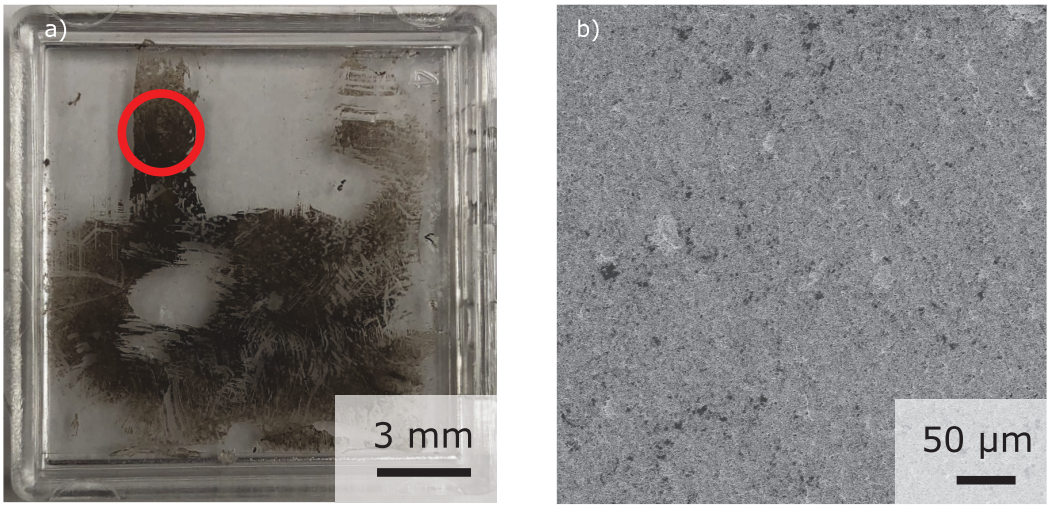

Fig. 7.4: Large-scale morphology of the SnIP thin film. a Image of the SnIP nanowire thin-film. The red circle indicates the region studied with THz spectroscopy. **b** Large-scale HIM image taken within the circled region in **a**.

This portion of the film was also imaged using a Zeiss helium ion microscope

*The films tend to be quite uniform, which could be a consequence of their cylindrical geometry, which has been shown to suppress the coffee ring effect in ellipsoidal systems [191].

†At the time this photo was taken, several areas of the film had been scratched by the 100x magnification objective, which had a tendency to drag small clumps of material along the film due to surface roughness.

(HIM). HIM was chosen over the more commonly used scanning electron microscope due to its ability to image samples on insulating substrates. This capability is especially advantageous for THz spectroscopy, as it enables direct imaging of the samples used for THz spectroscopy without the need to transfer to a conductive substrate or coat the sample with a thin metallic film. A large-scale HIM image is shown in Figure 7.4, showing that the film is indeed quite uniform over a large area. While there are several small gaps in the film, the surface coverage is quite high.

Much finer detail can also be seen with magnified HIM images, as seen in Figure 7.5. Figure 7.5a shows an area of the thin film approximately 20x20 μm^2. The film consists of randomly oriented nanowires with a tendency to lie with the long axis (along the double-helix direction) in the plane of the substrate, which is an important point for analysis later in this chapter involving ensemble averages over orientations. Figure 7.5 shows another magnified image with a rather large-diameter (700 nm) nanowire that reveals structure within the wire due to delamination of its constituent strands. To the right of the large-diameter nanowire is another feature that appears to have different morphology than SnIP. From analysis of x-ray diffractograms later in this chapter, we know that our thin films contain small amounts (approximately one part in one hundred) of the clathrate compound $Sn_{24}P_{19.3}I_8$.

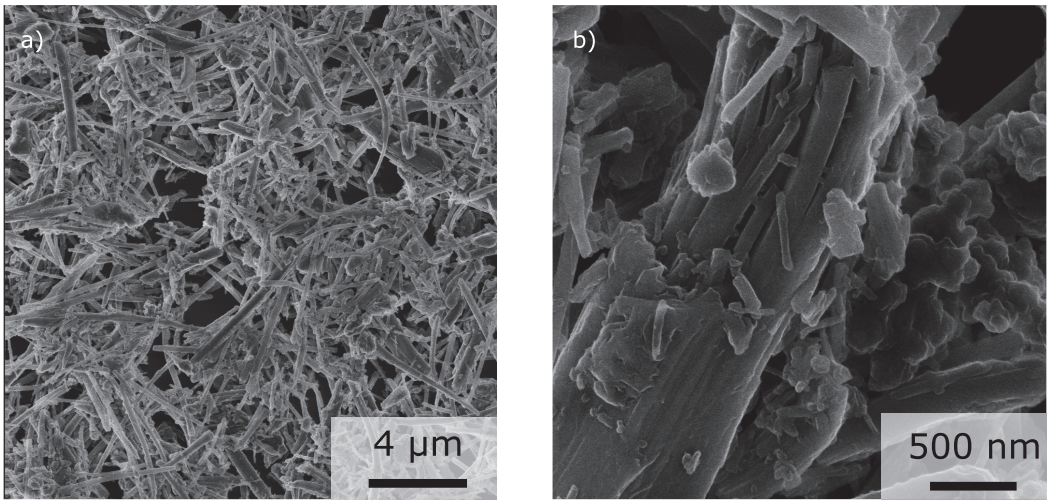

Fig. 7.5: Microscopic view of the SnIP nanowires. a Magnified HIM image of the film in Figure 7.4. **b** High-resolution image of a large nanowire. To the right of the nanowire a region with morphology distinct from that of SnIP is also seen.

It is also useful to estimate the filling fraction of the thin film. While we can see that the area filling fraction is high, it is more difficult to estimate the volume filling fraction from images alone. For a densely packed system of cylinders, the highest volume filling fraction attainable is 0.9, however, this requires highly ordered packing. However, as indicated previously, our film consists of randomly oriented nanowires. Numerical calculations of random packing for cylinders with large aspect ratio, similar to the nanowires in our films, yield a volume filling fraction of 0.35 to 0.45 [192], which provides us with a rough estimate of the volume filling fraction of our films.

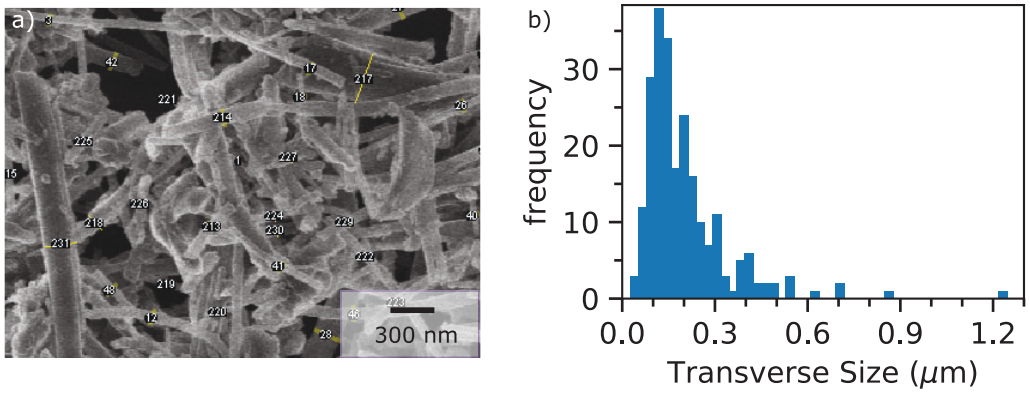

Fig. 7.6: Distribution of nanowire sizes. a) An enlarged section of the helium ion microscope image in Figure 7.5**a** showing how the diameters were measured. The numbered lines indicate nanowires that were measured using ImageJ. b) A histogram of the diameter of 230 nanowires sampled randomly from the image in Figure 7.5**a**.

HIM also facilitates semi-quantification characterization of the distribution of nanowire sizes, as shown in Figure 7.6a,b. The diameters of a randomly chosen subset of all the nanowires in the image in Figure 7.6a were measured using ImageJ. Approximately 230 nanowires were selected visually* and a histogram of the transverse nanowire diameter is shown in Figure 7.6b. Almost all of nanowires have diameter less than 500 nm and ignoring outliers (which we define as diameter greater than 500 nm), we find the average, median, and standard deviation of the distribution are 190 nm, 160 nm, and 100 nm, respectively. The most common nanowire size in the

*While effort was made to obtain a random selection representative of the full distribution, there was no rigorous criteria for this process. This distribution could therefore be biased, however, we note that the precise distribution of sizes has at most a minor impact on our interpretations.

histogram was from 100 nm to 110 nm. The largest nanowire measured was 1200 nm while the smallest was 40 nm. The distribution of nanowire lengths was quite broad, ranging from sub-micron up to 8 μm in the region examined. Most nanowires appear to be in the range of 1 to 5 μm in length. We expect the nanowires to be approximately cylindrical.

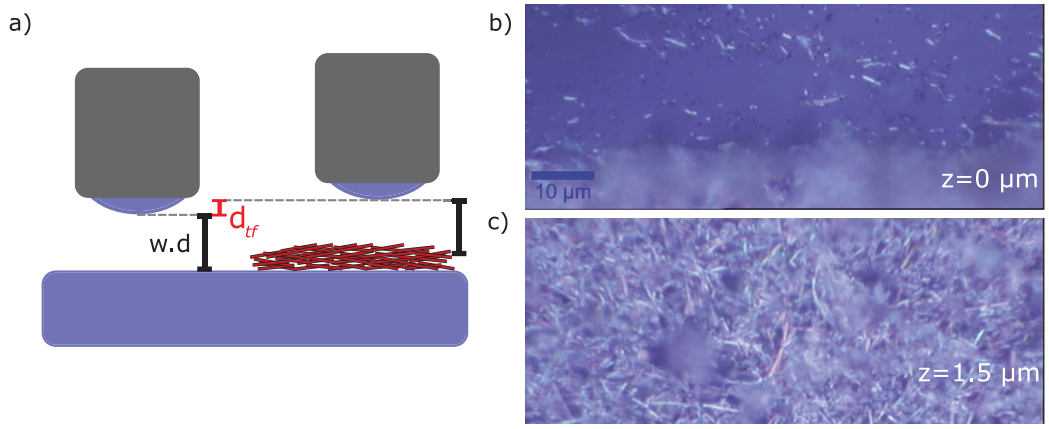

Fig. 7.7: Thin-film thickness from optical microscopy. **a** Illustration of the working principle for extracting the film thickness from optical microscopy. The 100x microscope objective has a depth of focus smaller than the film thickness. The difference in microscope height between focusing on the substrate and focusing on the sample yields the average film thickness. The microscope objective working distance is schematically indicated by *w.d.* Microscope images with the objective height z such that **b** the substrate in focus (defined as z=0)and **c** the largest fraction of nanowires in focus.

For THz-TDS, it is also important to quantify the film thickness, which we can find using optical microscopy, as indicated schematically in Figure 7.7a. The principle underlying this method is to exploit the small depth of field of an optical microscope and measure the difference in objective height with the substrate in focus versus with the film in focus. Figures 7.7b and c show images with the substrate and thin film in focus, respectively, using a 100x magnification optical microscope. For a given objective height, only a fraction of the nanowire film was in focus at any given time, so choosing the objective height with the most nanowires in focus in comparison to the height with the substrate in focus allows us to estimate the average film thickness, which we find to be 1.5 $\pm$ 0.5 μm.*

*Due to the granularity of the film, the precise position where the thin film is in focus is subjective, leading to the large uncertainty in film thickness.

7.3.2 Optical Spectroscopy

Due to the needle and nanowire geometries, measurement of the optical properties such as the absorption coefficient, and therefore optical band gap, is difficult. We therefore include several measurements on both bulk needles and nanowire thin-films to provide a compelling verification of the 1.86 eV gap. First, the diffuse-reflectance signal from a SnIP thin film was acquired with a UV-Vis spectrometer coupled to an integrating sphere. Shown in Figure 7.8a is the Kubelka-Munk transformation, $f(E)$, of the diffuse reflectance of the SnIP thin film [193],

$$f(E) \equiv \frac{\alpha(E)}{s(E)} = \frac{(1 - R_\infty(E))^2}{2R_\infty(E)}, \tag{7.1}$$

where $R_\infty(E)$ is the diffuse-reflectance signal, E is the photon energy, α is the absorption coefficient, and s is the scattering coefficient. Here, the reference spectrum was acquired using a white diffusely-reflecting standard reference sample. In the approximation of an energy-independent scattering coefficient and semi-infinite/homogeneous sample, $f(E)$ is proportional to the absorption coefficient. The sharp increase in $f(E)$ near 1.8 eV is due to the onset of absorption at the band edge. The small increase in the signal below the band edge is likely an artifact due to, *e.g.*, surface roughness or the energy dependence of $s(E)$.*

To estimate the band gap, we use a Tauc plot of $[E \cdot (f(E) - bl)]^h$, as shown in Figure 7.8b, where bl indicates the baseline (dashed line in Figure 7.8a) and h is an exponent that depends on the nature of transitions [193]. In SnIP, calculations suggest that the direct and indirect gaps are separated by only a few meV, making it difficult to determine the correct value of h for the Tauc plot. With the assumption of an indirect transition ($h = 1/2$), the extrapolated band gap is 1.81 eV. Alternatively, with the assumption of a direct transition ($h = 2$), the extrapolated band gap is 1.87 eV. These values are in good agreement with the diffuse-reflectance signals in ref. [179].

As can be seen, the band gap determination from diffuse-reflectance spectroscopy relies on assumptions about the baseline and nature of transitions. It is therefore

*For example, assuming an approximate functional form of the $s(E)$ given by Rayleigh scattering, where $s(E) \propto \lambda^4$, along with an exponential sub-gap absorption can be shown numerically to reproduce this behavior.

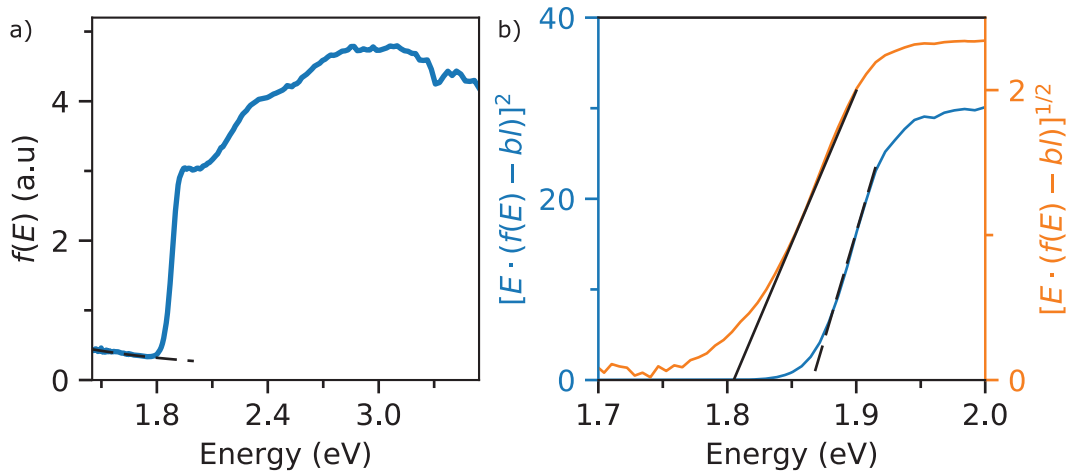

Fig. 7.8: Diffuse-reflectance spectroscopy. a) Kubelka-Munk transformation of the diffuse-reflectance signal. Dashed line: estimated baseline. b) Tauc plot assuming indirect transitions (orange) with an extrapolated band gap of 1.81 eV (solid black line) and assuming direct transitions (blue) with an extrapolated band gap of 1.87 eV (dashed black line). In each case the baseline extrapolated from the low-energy tail is subtracted from the spectrum.

helpful to use complementary techniques such as photoluminescence spectroscopy to probe the electronic structure, as shown in Figure 7.9a for a single bulk SnIP needle.* As expected, the PL spectrum is peaked near the extrapolated direct-gap energy at approximately 1.86 eV. The asymmetry of the spectrum, with a tail extending beyond 1.6 eV, is due to sub-gap transitions [133]. Shown in Figure 7.9b is a semi-log scale plot of the PL with an exponential function overlaid to show the width of the tail.

While together the diffuse-reflectance and PL spectra provide compelling verification of the band gap, neither is well suited to probe the sub-gap absorption. As noted, the diffuse reflectance can be affected by the dispersion of $s(E)$, surface roughness, and film homogeneity. Furthermore, the PL spectrum is biased to more heavily weight regions of the sample with high PL efficiency. Alternatively, photothermal deflection spectroscopy (PDS) provides a signal that is more directly proportional to absorption and is an extremely sensitive probe. An excellent discussion of the PDS technique and of the processes that contribute to sub-gap absorption is presented in ref. [194].

*We note that we were not able to observe PL from ultrasonicated nanowires.

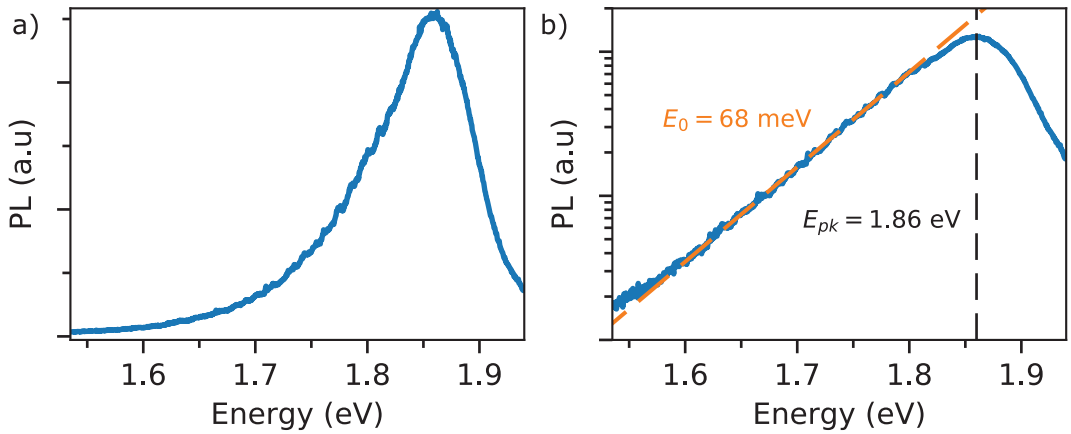

Fig. 7.9: Bandgap verification from photoluminescence. a) Photoluminescence of a single bulk SnIP needle with 633 nm excitation wavelength. b) Semi log-scale version of the PL from a). The dashed orange line is an exponential fit for the sub-gap PL with $PL \propto \exp(E/E_0)$. The peak of the PL spectrum, at E_{pk}, at 1.86 eV, is indicated with the vertical dashed line, which coincides with the extrapolated direct gap. The data for this figure was provided by T. Nilges.

Briefly, a monochromator with a broadband light source is used to selectively excite a thin-film sample immersed in C_6F_{14}, a liquid with a strong gradient index with temperature. Simultaneously, a probe laser propagates transverse to the film surface. Heat deposited by absorption of light is transferred to the liquid in the volume near the surface, resulting in a gradient index lensing effect that deflects the probe beam. PDS therefore directly probes the dissipated optical energy, providing a sensitive and direct probe of absorption.

In Figure 7.10, we show the PDS signal in the spectral range from 1.25 eV to 2.5 eV from a SnIP thin film that was prepared identically to that studied with TRTS in the subsequent chapter . This spectrum contains three important regions: First, the saturation regime above the band edge, which is a known feature of PDS and does not provide any additional information. Second, near the band edge (vertical dashed line at 1.86 eV), we see an exponential absorption tail with a width (Urbach energy) of 70 meV. The width of this tail is similar to that of the PL tail, though we note that the PL tail is affected by both the energy dependence of sub-gap absorption and the thermal occupancy [133]. At lower energies, and notably at 1.55 eV (800 nm), there is a broad absorption feature that increases with frequency, which we speculate

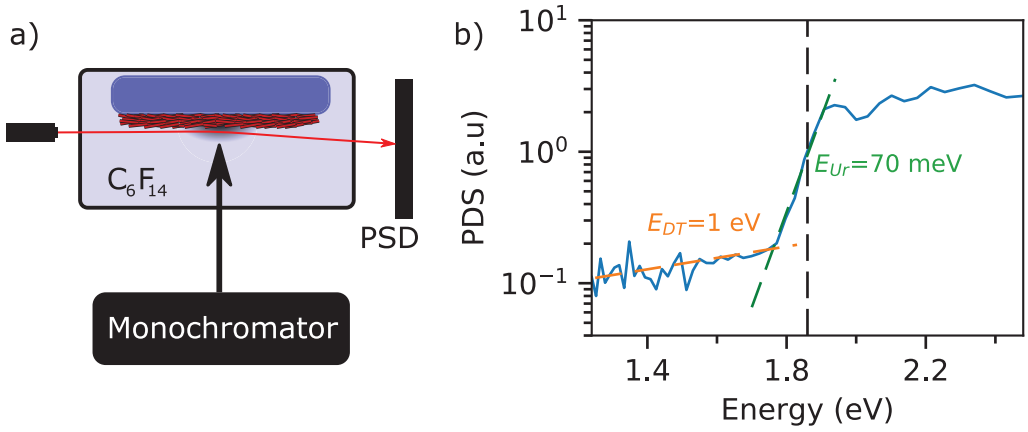

Fig. 7.10: Sub-gap absorption from photothermal-deflection spectroscopy. **a** Schematic layout of the PDS setup. Light from a monochromator is focused onto a SnIP thin film placed in C_6F_{14}, a liquid with a large gradient index with temperature. A glancing-angle He-Ne laser is deflected by a small angle, which is detected by a position sensitive detector (PSD). **b** PDS signal from a SnIP thin-film showing an exponential band-tail absorption with a width of 70 meV (orange line), a deep-level absorption tail with a width of 1 eV, and a saturation regime above the band edge (vertical dashed line).

is due to transitions from deep levels [194, 195].

7.3.3 X-Ray Diffraction

Powder X-Ray Diffraction (XRD) was used to probe the crystalline nature of the nanowire films in comparison to the bulk SnIP needles. The X-Ray diffractogram shown in Figure 7.11a shows excellent agreement between the powder XRD pattern calculated from the solved crystal structure and both the bulk and ultrasonicated samples. Figure 7.11b shows the same diffractogram with a reduced window size. In general, the linewidth of the ultrasonicated SnIP shows only a small broadening compared to the bulk SnIP, indicating that the ultrasonicated material remains crystalline. This is consistent with Raman spectroscopy (presented in the next section). However, the ultrasonicated SnIP contains several peaks not expected from the pure SnIP structure. These are an indication of a small amount of the clathrate compound $Sn_{24}P_{19.3}I_8$ [196].

A Rietveld-based phase analysis of the two existing phases after ultrasonication, SnIP and $Sn_{24}P_{19.8}I_4$, resulted in phase fractions of 0.909(6):0.091. For the Rietveld

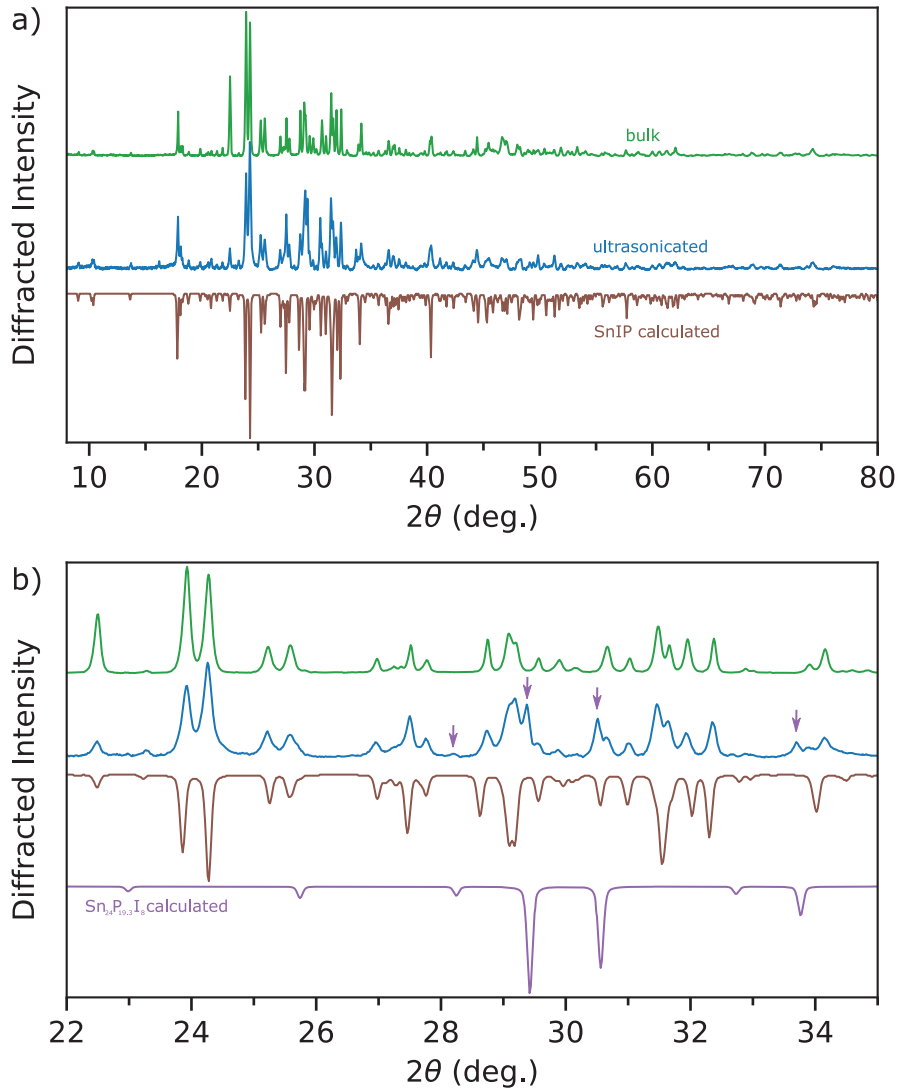

Fig. 7.11: X-Ray diffraction probe of crystallinity. a) Full range of 2θ for bulk needles SnIP (green), ultrasonicated nanowires (blue), and the calculated powder XRD pattern (maroon). b) Reduced range of 2θ with the impurity peaks attributed to $Sn_{24}P_{19.3}I_8$ (calculated spectrum in purple) indicated with purple arrows for the ultrasonicated SnIP.

analysis the two structure models were taken from literature [196, 179] using isotropic displacement parameters for each atom and keeping all crystallographic parameters fixed, except the lattice parameters and phase fraction. The final R values after refinements of the profile, lattice and phase fraction parameters are (in %): Profile R values: Rp 1.49, wRp 2.09; $Sn_{24}P_{19.8}I_4$: Robs(F) 3.37, wRall(F) 3.94; SnIP: Robs(F) 2.87, wRall(F) 3.62.

7.3.4 Raman Spectroscopy

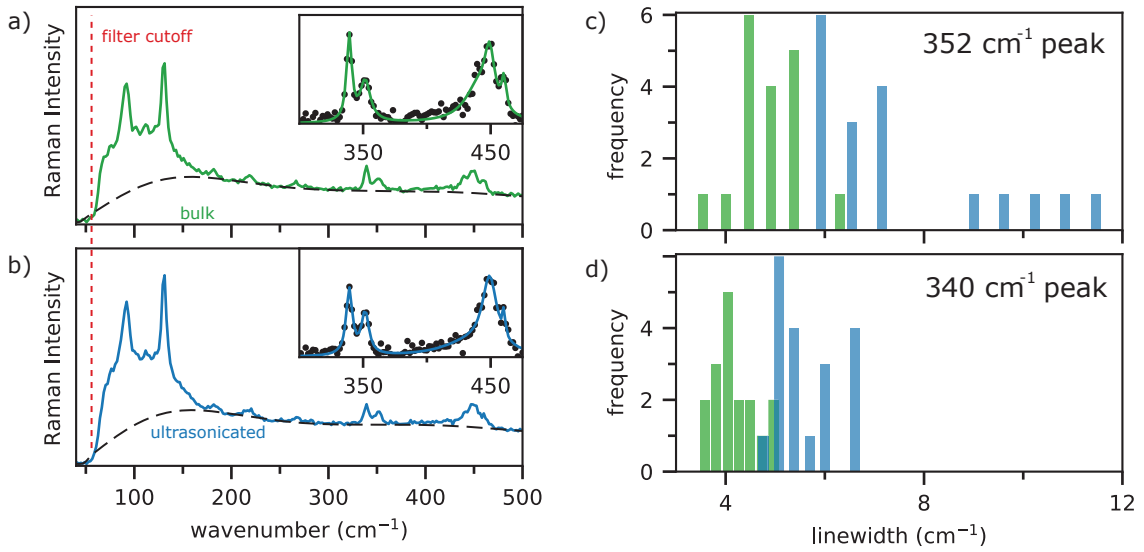

Fig. 7.12: Raman Spectroscopy: nanowires versus bulk needles. a) Micro-Raman spectrum of a single bulk SnIP needle and b) Raman spectrum of a single ultrasonicated SnIP nanowire. The insets show a magnified version of the high frequency peaks with the baseline subtracted. Histograms of the linewidth of the 340 and 352 cm^{-1} peaks are shown in c) and d), respectively.

Figure 7.12a, b contain a comparison of the Raman spectra for bulk SnIP needles and ultrasonicated SnIP nanowires. The spectra are qualitatively very similar, with all peaks in the bulk also present in the ultrasonicated SnIP. The filter cutoff near 70 cm^{-1} (2.1 THz), which is similar to the high-frequency edge of the THz spectrum in this work. However, in SnIP, which is centrosymmetric, all modes are either Raman or IR active, not both, so Raman and THz spectroscopy probe a different subset of modes.

To be more quantitative, we have plotted a histogram of the linewidth of the 352

cm^{-1} (Figure 7.12c) and 340 cm^{-1} peaks in bulk (green) and ultrasonicated (blue) peaks measured on a variety of individual needles and nanowires. These peaks were chosen for study as they are most easily distinguishable from the baseline and each other. Before fitting, the baseline was subtracted using a Python implementation of the ALS baseline subtraction routine. Even in the bulk material, the peak width fluctuates from needle to needle. In general, there is a slight increase in average peak width in the ultrasonicated materials. This indicates that the ultrasonication process may result in, at most, a small reduction in crystallinity, which is consistent with the XRD analysis. Alternatively, it is also possible that the peak-broadening is due to the increasing surface to volume ratio and the amount of disorder in the bulk could be unchanged.

7.4 Ab-Initio Electronic Structure

As a new material, very little is known from experiment about the electronic structure of SnIP. For example, the effective mass has not yet been measured, however, it is needed in order to extract the carrier mobility from THz spectroscopy. To date, there has been one reported calculation of the effective mass in SnIP by Li *et al.*, however, their calculation was for a 1D strand. Also, to date there has also been very little work done probing the anisotropy of the electronic structure. Intuitively, we can expect a large anisotropy between dispersion parallel versus perpendicular to the double-helix axis due to the dramatically different covalent versus van der Waals forces in each direction. In this section, we study the electronic structure in detail using DFT with a focus on several bands near the Fermi level. We explore the effective-mass approximation (EMA) using an expansion to third order in the wavevector near the conduction and valence band extreme and discover an unexpectedly large anisotropy in the plane perpendicular to the double-helix axis. Surprisingly, we will show that the conduction bands in SnIP show signatures of 2D-like behavior where transport in one of the dimensions perpendicular to the double-helix axis is suppressed.

7.4.1 Band Structure

Our calculations were performed using the Crystal17 DFT software package using the HSE06 functional [197] and Grimme's DFT-D3 dispersion correction [198].* This combination of functional and dispersion correction were previously shown to provide good agreement with both the SnIP structure, as extracted from single-crystal XRD, and band gap, as measured by optical spectroscopy [179]. Six Monkhorst-Pack-type k-points were used for sampling the reciprocal space and a double-density Gilat net of 12 points was used in the calculation of the Fermi energy.

Shown in Figure 7.13a is the SnIP band structure calculated on the path through k-space defined in Figure 7.13b. Also plotted is the density of states (DOS). The valence-band maximum (VBM) is located at the C point while the conduction-band minimum (CBM) is located near the Y point, so that the band gap is indirect. From this, we also see that neither of the extrema are located at the Γ point. For reference, the SnIP unit cell is shown in 7.13c with the correct orientation with respect to the Brillouin zone (BZ, Wigner-Seitz cell of the SnIP reciprocal lattice)in Figure 7.13b. Several bands near the Fermi level are colored amber, red, green, and magenta, which corresponds to bands that are studied in more detail in the following sections.

7.4.2 Effective Mass Approximation

To extract the effective mass, the band structure was calculated on a uniform grid around the conduction and valence band extrema. First, we can visualize the electronic structure by plotting the energy isosurfaces for the conduction (green) and valence (red) bands with a 5 meV offset from the extrema, as shown in Figure 7.14a. From this plot, we can confirm that the band gap is indirect with the valence band maximum centered at the C point and two conduction band minima slightly offset from the Y point in the direction of the valence band. We can also see that both the bands appear ellipsoidal as opposed to spherical due to the low symmetry of the

*The choice of functional dictates the approximation made in the calculation of the energy. The dispersion correction is a phenomenological addition to the functional that captures nonlocal corrections to the energy due to dispersion forces.

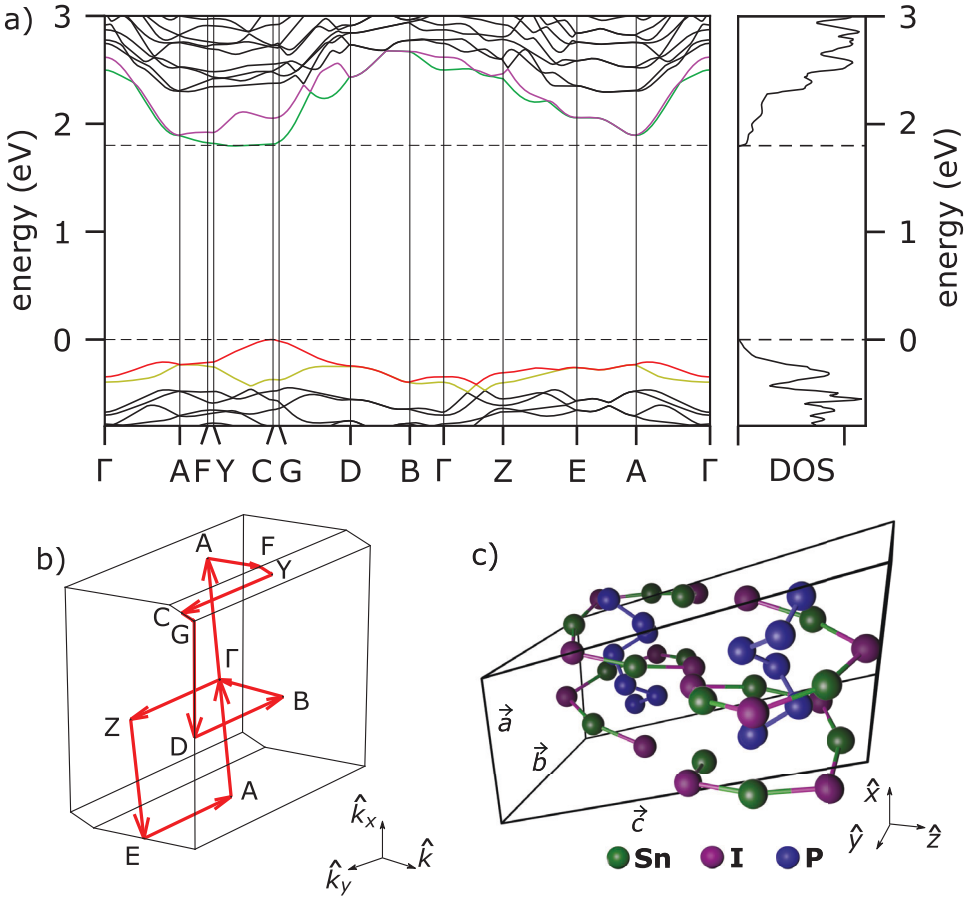

Fig. 7.13: SnIP electronic structure. **a** Band structure through the path in the BZ defined in **b**. **b** SnIP BZ, where the red arrows indicate the path traversed in k-space for the band structure calculation in **a**. The high-symmetry point labels were chosen as defined in the Crystal17 user manual. **c** SnIP unit cell oriented with respect to the BZ in **d**.

structure and anisotropy of the bonding.[†]

The energy can then be expanded about the extrema according to,

$$E^i_{\vec{k}} = E^i|_{\vec{k}_0} + \frac{1}{2!}H^i_{mn}|_{\vec{k}_0}(\vec{k}_m - \vec{k}_0)(\vec{k}_n - \vec{k}_0) + \frac{1}{3!}T^i_{mnl}|_{\vec{k}_0}(\vec{k}_m - \vec{k}_0)(\vec{k}_n - \vec{k}_0)(\vec{k}_l - \vec{k}_0) + \cdots , \tag{7.2}$$

where $H^i_{mn} = \partial_{km}\partial_{kn}E_{i\vec{k}}$ and $T^i_{mnl} = \partial_{km}\partial_{kn}\partial_{kl}E_{i\vec{k}}$ are the second (Hessian) and third rank partial derivative tensors, the subscripts m, n, and l are the Cartesian indices, and an implicit sum over like indices is assumed (Einstein notation) Including only the parabolic term yields the EMA and the effective-mass tensor, M^i_{mn}, can be calculated from the inverse of the Hessian as,[*]

$$M^i_{mn} = \left(\hbar^2 H^i_{mn}\right)^{-1}. \tag{7.3}$$

Finally, the eigenvalues and eigenvectors of the effective-mass tensor yield the principal axes and effective masses, respectively. The principle can be thought of as the axes along which the ellipsoidal isosurfaces are aligned in the EMA.

The Hessian matrix, its inverse (the effective mass tensor) were calculated from the Crystal17 output using Python and NumPy. The principal axes and effective masses were then extracted using the NumPy linear algebra package. We found that the calculated eigenvalues and eigenvectors of the effective mass matrix for one valley of the conduction band were given by,

$$m_1 = 0.28\, m_e,\ \hat{x}'_c = \begin{pmatrix} 0.982 \\ 0 \\ -0.191 \end{pmatrix}, \tag{7.4}$$

$$m_2 = 0.51\, m_e,\ \hat{y}'_c = \hat{y} = \begin{pmatrix} 0 \\ 1 \\ 0 \end{pmatrix}. \tag{7.5}$$

$$m_3 = 2.0\, m_e,\ \hat{z}'_c = \begin{pmatrix} 0.191 \\ 0 \\ -0.982 \end{pmatrix}. \tag{7.6}$$

[†]It is well known that the energy isosurfaces in, *e.g.*, silicon are also ellipsoidal despite the cubic symmetry and comparably simple bonding. However, in silicon there are multiple valleys with orthogonal orientation so that transport is isotropic.

[*]As a second rank tensor we can represent the Hessian as a matrix. It is not clear whether a similar inversion can be performed for the third rank tensor, which encapsulates the non-parabolicity.

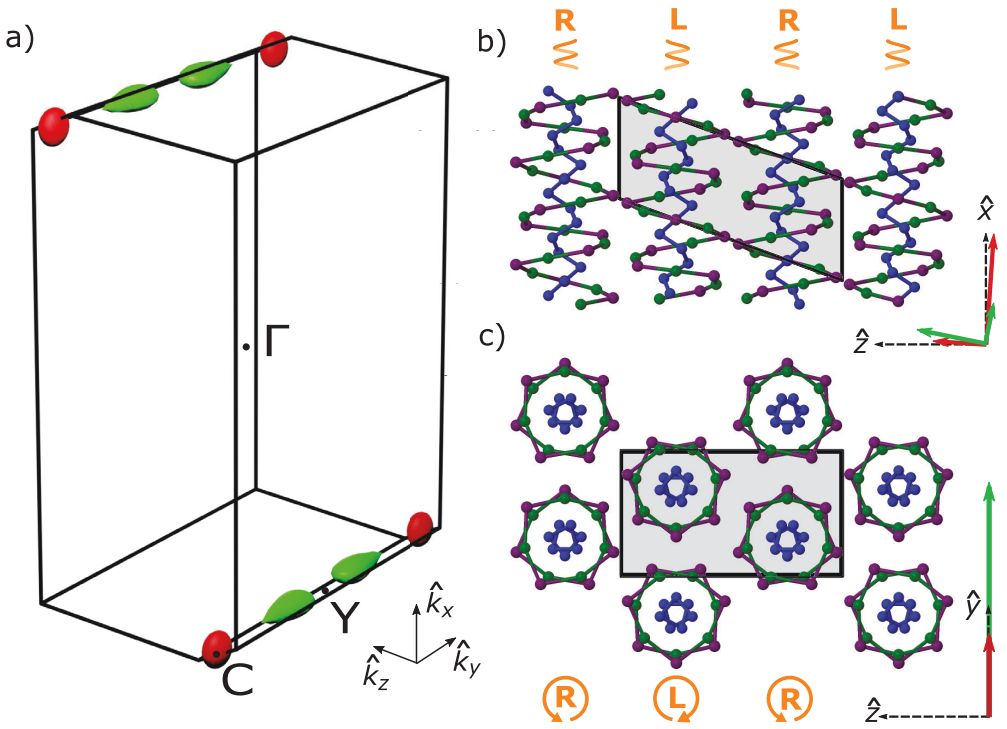

Fig. 7.14: Geometry of the low-energy excitations. a) Constant energy surfaces 5 meV below the valence band maximum (red) and above the conduction band minimum (green). Immediately apparent is the extreme anisotropy of the conduction band. The conduction (valence) band effective masses along the principal axes of the ellipsoidal constant energy surfaces were found to be 0.28 (0.71) m_e, 2.0 (0.66) m_e, and 0.51 (0.33) m_e in the $\hat{x}'$, $\hat{y}$, and $\hat{z}'$ directions, respectively. Projections of the crystal structure to the b) xz-plane and c) yz-plane with the vectors of the principal axes of the effective mass tensor for the conduction band (green) and valence band (red) shown in the bottom right corners. The directions of the colored vectors in b), which are rotated with respect to the Cartesian axes ($\hat{x}$, $\hat{y}$, $\hat{z}$), define the directions of $\hat{x}'$ and $\hat{z}'$ for the conduction band (green) and valence band (red). The preferred transport directions (directions of highest mobility) are indicated by the dashed green arrow for the conduction band (labeled $\mu_{e,max}$), which is almost parallel to the double-helix axis, and the dashed red arrow for the valence band (labeled $\mu_{h,max}$), which is almost perpendicular to the double-helix axis in the $\hat{z}$ direction. Additionally, the helicity of adjacent planes of double helices is indicated schematically.

And for the valence band, the eigenvalues and eigenvectors of the effective mass tensor are given by,

$$m_1 = -0.71\, m_e,\ \hat{x}'_v = \begin{pmatrix} 0.998 \\ 0 \\ 0.067 \end{pmatrix}, \tag{7.7}$$

$$m_2 = -0.66\, m_e,\ \hat{y}'_v = \hat{y} \begin{pmatrix} 0 \\ 1 \\ 0 \end{pmatrix}. \tag{7.8}$$

$$m_3 = -0.33\, m_e,\ \hat{z}'_v = \begin{pmatrix} 0.067 \\ 0 \\ 0.998 \end{pmatrix}. \tag{7.9}$$

Here, we have introduced the primed notation for the unit vectors of the principal axes. In the $\hat{y}'$, the principal axes are parallel to the Cartesian vector. While this is not the case in the monoclinic plane ($\hat{x}'$ and $\hat{z}'$ directions), we note that there is only a small rotation with respect to the Cartesian axes ($10.4°/3.8°$ for the conduction/valence bands), motivating the primed notation. In Figure 7.14b, c we plot the principal axis vectors along with projections of the SnIP structure over several periods.

As indicated previously, due to the low symmetry of the crystal and anisotropy of bonding, with strong covalent interactions parallel to the double helices ($\hat{x}$ direction) and weak vdW interactions perpendicular to the double helix ($\hat{y}$ and $\hat{z}$ directions), we expected anisotropy in the $\hat{x}$-direction effective mass in comparison to the $\hat{y}$ and $\hat{z}$ directions. Due to the strong covalent bonding, it is also natural to expect larger dispersion (lighter effective mass) in the $\hat{x}$-direction than either of the perpendicular directions, which is an intuition that holds for the conduction band. Here we see that $m_{cx'} = 0.28\, m_e$, where m_e is the free-space electron mass, is the preferred transport direction, while the $\hat{y}$ and $\hat{z}'$ masses are both significantly heavier. In contrast, we see that in the valence band transport is preferred in the $\hat{z}'$ direction, with mass $m_{vz'} = 0.33\, m_e$. In general, we see that the masses perpendicular to the double-helix axis are significantly lower in the valence band than the conduction band.

The breakdown of intuition relating transport and bond strength further illustrates the complexity of the SnIP system, however, it is possible to understand this behavior with a relatively simple picture based on the results of Li *et al.*, who showed that the

valence band states are more localized around the outer SnI helices [181], which could facilitate inter-helix hopping in comparison to the conduction band states that are more localized on the inner P helices. This behavior is analogous to the situation in organic semiconductor systems or vdW heterostructures, where orbital overlap (e.g. $\pi - \pi$ stacking) and conformational accuracy plays a role in determining transport properties [199]. This analogy then extends our understanding of how SnIP combines two worlds, with some features of both classical inorganic materials (element choice, covalent bonding) and organic semiconductor materials (vdW bonding, ultrasoft) [183].

The calculation also reveals large anisotropy in the effective masses in the plane perpendicular to the double-helix axis as $m_{z'} < m_y$ for both the conduction band and valence band. This anisotropy is more surprising, however, we highlight an additional asymmetry in the $\hat{y}$ and $\hat{z}$ directions that affects the inter-helix interaction strength. As seen in Figure 7.14b, c, which shows projections of the crystal structure onto the xz and yz planes, stacking in the $\hat{z}$ direction consists of alternating planes of right and left handed helices. Conversely, in the $\hat{y}$ direction, the stacking planes themselves are composed of alternating left and right handed helices with a buckled structure. This asymmetry, which results in anisotropic van der Waals interactions, has also been shown to directly affect the anisotropic mechanical properties of SnIP [183].

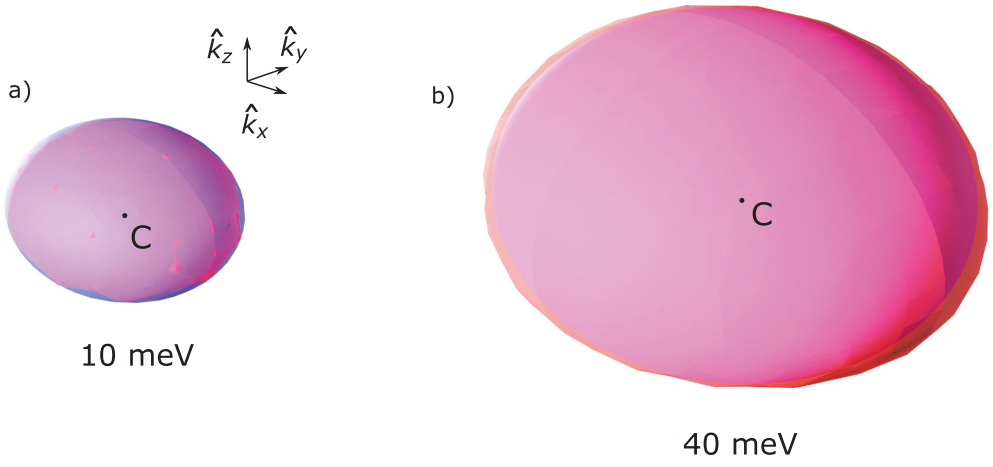

Fig. 7.15: Validity of the EMA in the valence band. Constant energy isosurfaces for the highest valence band as calculated from DFT (red) and the EMA (blue) at **a** 10 meV and **b** 40 meV below the VBM.

It is also worthwhile to study the range of validity of the EMA. To do this, we again rely on the tool of energy isosurfaces. The energy isosurfaces directly from the DFT calculation (red) and from the EMA (blue) are shown in Figure 7.15a, b for 10 meV and 40 meV below the VBM, respectively. At 10 meV, the isosurfaces are essentially identical, which, although expected for such a low energy, is a useful verification of the numerical accuracy of the calculation of the Hessian. Even at 40 meV, it can be seen that the EMA reproduces the energy surfaces calculated from DFT with reasonable accuracy.

Alternatively, if we make similar plots for the conduction band as seen in Figure 7.16a for the DFT calculation (green) and EMA (blue), we see for k vectors in the $\hat{x}$ and $\hat{z}$ directions away from the extrema the EFA provides good agreement with DFT. However, already at 5 meV above the CBM we see that the EMA breaks down. It is important to emphasize that this breakdown is not due to numerical error, as we see that the conduction band isosurfaces are highly asymmetric. Clearly it is not possible to reproduce this behavior with the EMA, which, as a quadratic approximation, is necessarily symmetric about the extrema. The failure of the EMA is even more dramatic if we look 10 meV above the band edge, as shown in Figure 7.16b, where the isosurface appears to be approximately cylindrical through a wide range of the BZ. We will return to this point in a following section.

As the EMA approximation breaks down at a very low energy, it is worth considering the validity of the expansion to third order in the wavevector, as shown in Figure 7.17. Shown in Figure 7.17a is the energy isosurface 5 meV above the CBM from DFT (green) and from the expansion including terms to third order in the wavevector (blue). We see that while the cubic approximation yields an asymmetric energy isosurface and extend the range of validity of the approximation a small amount, it still does not provide satisfactory agreement with the DFT calculation. This is even more clear if we look 10 meV above the band edge, as shown in Figure 7.17b.

7.4.3 Transport Mass

In the following chapter, we study carrier transport in our SnIP nanowire film using TRTS. As the film consists of a random ensemble nanowire orientations, it is

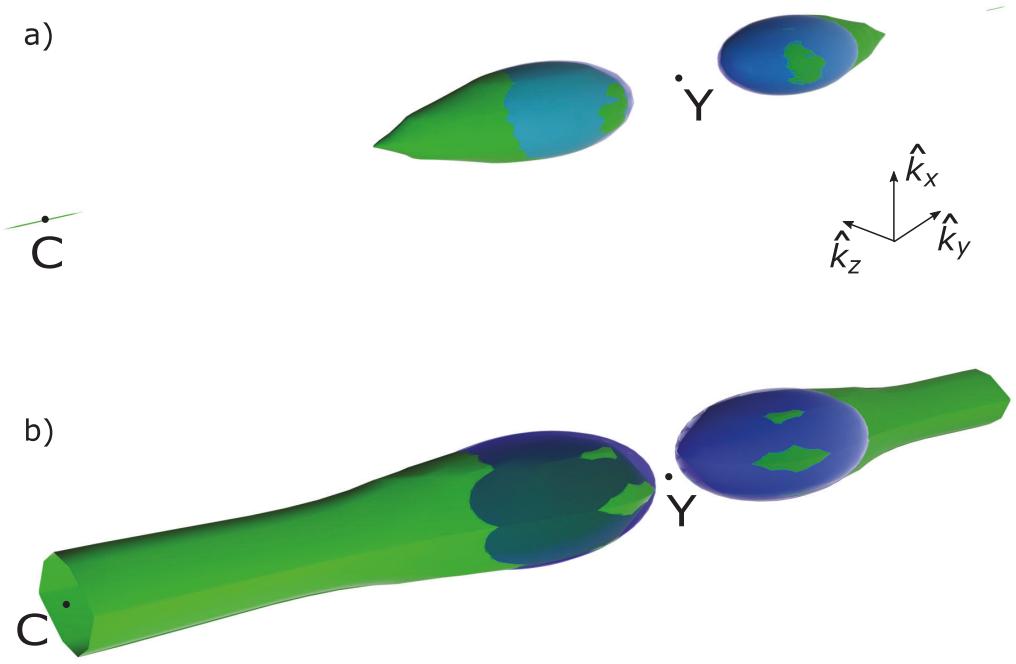

Fig. 7.16: Breakdown of the EMA in the conduction band. Constant energy isosurfaces for the lowest conduction band as calculated from DFT (green) and the EMA (blue) at **a** 5 meV and **b** 10 meV above the CBM.

therefore useful to derive a transport mass that is an appropriately weighted average of the directionally-dependent mass. This calculation is essentially a two-step procedure. We will find an expression for the effective mass as a function of angle in k-space, then we will define an appropriate weight as a function of angle and integrate over all solid angle. To find the angle-dependent effective mass we can work from the definition of the effective mass approximation where the energy is given by,

$$E_{\vec{k}} = \frac{1}{2}\hbar^2 M^{-1}_{mn} k_m k_n, \tag{7.10}$$

where H_{mn} is the Hessian matrix, or inverse of the effective mass tensor and $\vec{k}$ can be written as a function of angle as,

$$\vec{k} = (\cos(\theta)\hat{x} + \sin(\theta)\cos(\phi)\hat{y} + \sin(\theta)\sin(\phi)\hat{z})\,|\vec{k}|, \tag{7.11}$$

where θ is the azimuthal angle and ϕ is the polar angle with respect to the double-helix axis. Using the expressions for the eigenvalues and eigenvectors of the effective-mass

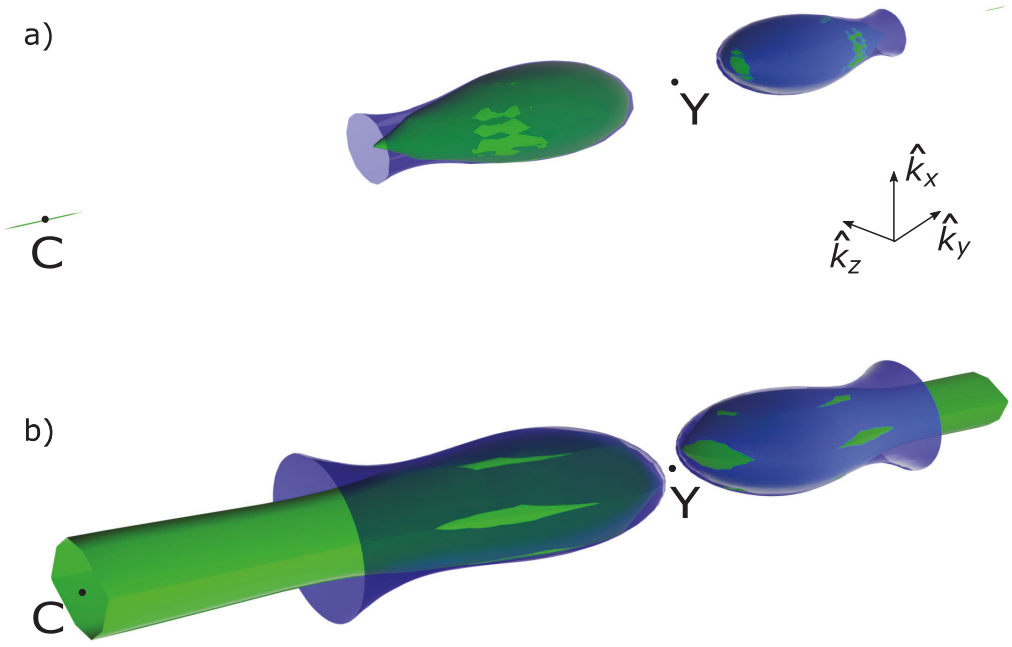

Fig. 7.17: Conduction band non-parabolicity to third order. Constant energy isosurfaces for the lowest conduction band as calculated from DFT (green) and with the third order expansion (blue) at **a** 10 meV and **b** 40 meV above the CBM.

tensor from section 7.4.2 we find,

$$E_{\vec{k}} = \frac{\hbar^2|\vec{k}|^2}{2}\left(\frac{\hat{x_x'}\sin^2(\theta)\cos^2(\phi)}{m_{x'}} + \frac{\hat{x_z'}\sin(\theta)\cos(\phi)\cos(\theta)}{m_{x'}} + \frac{\sin^2(\theta)\sin^2(\phi)}{m_y} + \frac{\hat{x_x'}\cos^2(\theta)}{m_{z'}} - \frac{\hat{x_z'}\sin(\theta)\cos(\phi)\cos(\theta)}{m_{z'}}\right), \tag{7.12}$$

where the quantity in brackets is the inverse angle-dependent inverse effective mass, $m_{eff}^{-1}(\theta,\phi)$. In the next step we integrate over all solid angles,

$$\bar{m}^{-1} = A(f(\theta,\phi))\int_0^{2\pi} d\theta \int_0^{\pi} d\phi\, m_{eff}^{-1}(\theta,\phi) f(\theta,\phi), \tag{7.13}$$

where A is a normalization constant that depends on the weighting factor $f(\theta,\phi)$. From Figure 7.5, we know that our thin films consist of randomly oriented nanowires with the nanowire axis in the plane of the substrate surface. The tendency of nanowires to lie flat on the surface implies that the weight as a function of the polar angle, θ, is constant. Furthermore, though we cannot obtain information about the

azimuthal angle from the HIM images, there is no reason to believe there is a preferred azimuthal angle so that the weight should be a constant function of ϕ and we can choose $f(\theta, \phi) = 1$. We then find $A = (2\pi^2)^{-1}$.* The result of the integration is,

$$\frac{1}{\bar{m}_i} = \frac{a}{m_{ix'}} + \frac{0.25}{m_{iy}} + \frac{b}{m_{iz'}}, \tag{7.14}$$

where a and b are constants that depend on the principal axes of the effective mass tensor and are equal to a=0.485 (0.499) and b=0.245 (0.250) for the conduction (valence) band. We find $\bar{m}_c$=0.42 m_e and $\bar{m}_v$=0.54 m_e.

7.4.4 2D-Like Behavior

As already noted, the conduction band isosurfaces become cylindrical over a wide range of the BZ for a range of energies. Shown in Figure 7.18 are the energy isosurfaces at 3 higher energies above the CBM. Notably, in Figure 7.18**c**, a second isosurface (magenta) appears as the energy is now above the minimum of the second conduction band. This band also appears to have cylindrical character, however, in a direction orthogonal to that of the lowest-lying conduction band. Notably, in each case the cylinder is oriented along one of the axes perpendicular to the double-helices, which once again highlights the surprisingly large anisotropy in the yz plane.

It is worth discussing some qualitative interpretations of the cylindrical geometry of the isosurfaces in order to appreciate the implications of this behavior. We note that the flatness of the bands in the y direction indicates zero curvature, or in other words, an infinite effective mass in this direction in a large region of the BZ. Another way think about this is in terms of propagation of a wavepacket distributed around one of these points. The lack of dispersion in the y direction implies that the group velocity in this direction goes to zero, *i.e.*, there is no transport in this direction, suggesting that electrons become localized to planes. This points to a reduction of dimensionality for carriers in some regions of the conduction band from 3D to 2D.*

We can also expect to see the 2D-like behavior in the DOS, as shown in Figure

*This weight is distinct from a uniform weight as a function of solid angle, where $f(\theta, \phi) = \sin(\theta)$, which would yield the more familiar normalization constant of $(4\pi)^{-1}$.

*This point could create confusion with our earlier claim that SnIP is a quasi-1D vdW material. Similarly to the way, *e.g.*, graphene exfoliates as 2D sheets, due to the nature of bonding in SnIP it exfoliates as 1D wires. The question of dimension in SnIP then depends on the context.

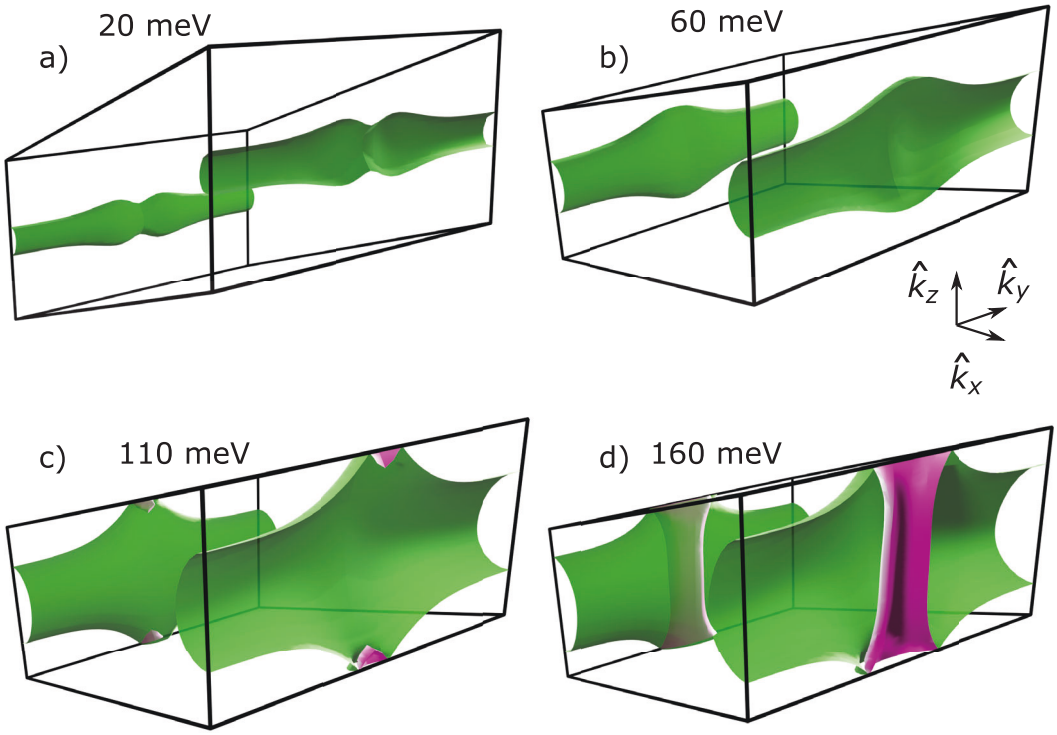

Fig. 7.18: 2D-like behavior of the conduction bands. Energy isosurfaces for **a** 20 meV, **a** 60 meV, **a** 110 meV, and **a** 160 meV above the conduction band minimum. The green and purple isosurfaces correspond to the first and second conduction bands, respectively.

7.19, where we calculated the energies on a uniform grid in k-space through the whole BZ and plotted a histogram of the energies. In the valence band, we know that the effective mass approximation holds to a reasonable degree of accuracy (see Figure 7.15) so the DOS should scale as the square root of the energy near the band edge, which holds to a reasonable degree of accuracy (red curve in Figure 7.19). Note, we also included the second valence band (amber) for completeness. Alternatively, based on our suggestion that the conduction bands show 2D-like behavior, we expect approximately step-edge behavior in the DOS. Especially the first conduction band clearly shows a step edge, confirming our conclusion. Over a narrow range near the minimum, the second conduction band shows roughly square-root like DOS, which in principle we should expect based on the geometry of the energy isosurface in Figure 7.18c. However, at higher energies (tens of meV above the band edge), there also appears to be a relatively constant DOS, again confirming the 2D-like behavior.

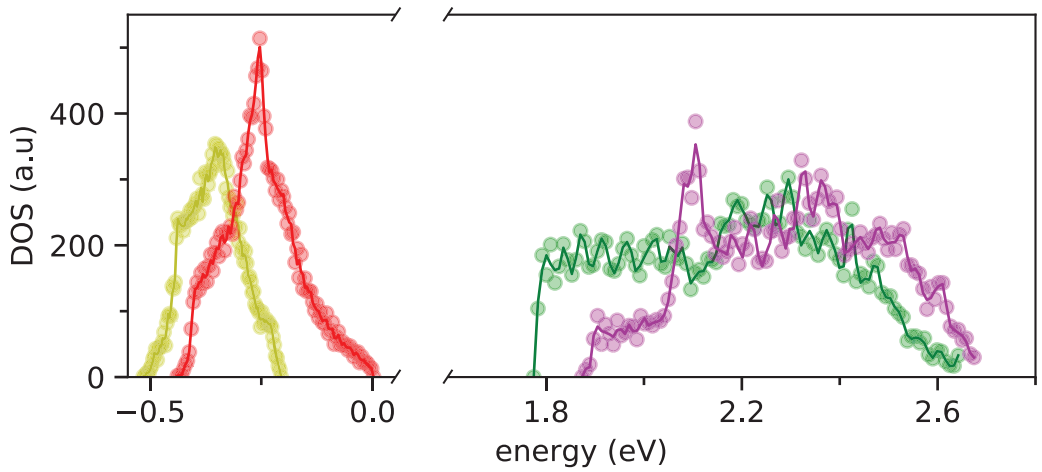

Fig. 7.19: 2D behavior in the DOS. Histogram of the energies calculated from DFT for several bands near the Fermi level. The number of energies in each bin is proportional to the DOS. The colors correspond to the colored bands in Figure 7.13. The circles correspond to the exact calculated values, which show large fluctuations due to the discretization of the BZ. The solid lines are smoothed curves using a Savitsky-Golay filter applied to the data.

7.5 Ab-Initio Vibrational Dynamics

In addition to the electronic structure, DFT can facilitate understanding of the vibrational spectrum. While the Raman spectrum has been calculated previously and shows reasonable agreement with experiment [183], the IR active modes have not yet been studied in as much detail. While Fourier-transform infrared (FTIR) spectroscopic studies were performed, no IR active vibrational modes were seen. This could be due to the relatively low frequencies of vibrations in SnIP so that the strongest modes are below the bandwidth of the FTIR spectrometer used. THz spectroscopy, on the other hand, is ideally suited for measurement of low-frequency IR modes and, as we will see, reveals 2 distinct IR modes in the 1-2 THz range. In this section we discuss the IR-active vibrational spectrum in SnIP as calculated by Crystal17 us-

ing the coupled-perturbed Kohn-Sham (CPKS) method using the PBE functional* and Grimme's D3 dispersion correction. The calculated dielectric function shows good agreement with experimental data, allowing us to identify twisting modes of the outer SnI helix as the source of the observed resonances.

7.5.1 IR-Active Intensities

In the framework of DFT, IR-active modes are characterized by their frequency, $f = \omega_0/2\pi$, and Born effective charge vector, $\vec{Z}_{p,i}$, where p is the mode index and i is the Cartesian direction [200, 201, 202]. The effective charge of each mode can be thought of as the change in macroscopic polarization for an infinitesimal displacement of all atoms in the basis of the mode itself. One way to quantify the strength of the p^{th} mode is using the intensity, which is defined as,

$$I_p = \frac{\pi N_A}{3c^2} \cdot d_p \cdot |\vec{Z}_p|^2, \tag{7.15}$$

where N_A is Avogadro's number and d_p is the degeneracy of the mode (in SnIP, $d_p = 1$ for all modes). The mode intensities as a function of frequency are shown in Figure 7.20a, b on a linear and log scale, respectively Clearly, the vibrational spectrum is quite complex. With N=42 atoms in the unit cell we expect 3N=132 vibrational modes (branches of phonons). Due to the lack of rotational symmetry there are no degenerate modes, and from the calculations, 60 of the 132 are IR active. The vibrational mode conformations for a number of the highest intensity modes are plotted in appendix A.9. In general, calculations suggest that the lower frequency modes correspond to oscillations predominantly of the outer helix while the higher frequency modes correspond to oscillations of the inner phosphorus helix. This can be expected when considering the relatively low mass of phosphorus with respect to tin and iodine.

*The HSE06 functional, which is used for the band structure calculation and showed the best agreement with the experimentally measured band gap, has not been implemented for use with the CPKS method in Crystal17. While the HSE06 functional performs significantly better in terms of calculating the band gap, the structure is less sensitive to the functional. A commonly iterated point is that if the choice of functional correctly predicts the structure, the vibrational spectrum should also be accurate, suggesting that use of the PBE functional should be sufficient for these calculations.

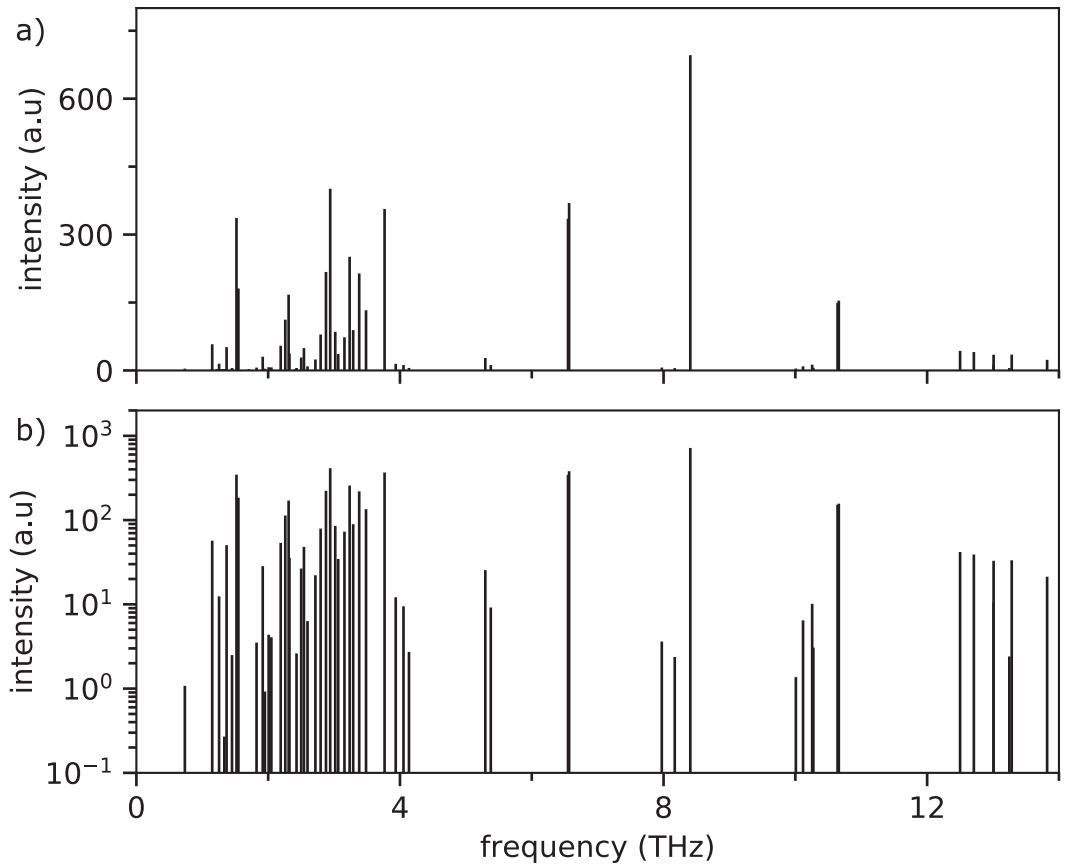

Fig. 7.20: Vibrational mode intensities in SnIP. Intensity of each normal mode as a function of its frequency, calculated using Crystal17, on **a** a linear and **b** a log scale.

7.5.2 Dielectric Function

Using the Born effective charges for each mode, we can also calculate the oscillator strength, which is a tensor quantity given by,

$$f_{p,ij} = \frac{4\pi}{\Omega} \frac{\vec{Z}_{p,i}\vec{Z}_{p,j}}{\omega_p^2}, \tag{7.16}$$

where Ω is the unit cell volume and ω_p is the mode angular frequency. Using the oscillator strength, we can then calculate the frequency dependent dielectric tensor by assuming each mode behaves as a Lorentz oscillator,

$$\epsilon_{ij}(\omega) = \epsilon_{\infty,ij} + \sum_{p=1}^{p_{max}} \frac{f_{p,ij}\omega_p^2}{\omega_p^2 - \omega^2 - i\gamma\omega}. \tag{7.17}$$

where ω is the angular frequency, and γ is a phenomenological damping constant, which we assume is the same for every mode although it can in principle vary. $\epsilon_{\infty,ij}$

is the high-frequency permittivity due to electronic transitions, which can also be calculated from DFT using the CPKS method. From our calculations we find,

$$\epsilon_{\infty,ij} = \begin{pmatrix} 7.7283 & 0 & 0.2167 \\ 0 & 6.8028 & 0 \\ 0.2167 & 0 & 7.2405 \end{pmatrix}, \tag{7.18}$$

which indicates similar electronic polarizability in each direction and a small off-diagonal coupling between $\hat{x}$ and $\hat{z}$ (recall that the $\hat{x}$ direction is parallel to the double-helix axis). Using the Born charges for each mode we can now use equation 7.17 to calculate the polarization-dependent dielectric function, as shown in Figure 7.21.

From these spectra, we see that the multitude of modes present in the intensity plot are not all individually visible due to their narrow spacing. The yy and zz components are qualitatively similar, with resonances in similar frequency bands, while the xx direction is significantly different. This reflects the obvious structural asymmetry parallel versus perpendicular to the double-helix axis. We also see that the polarizability is significantly larger along the double-helix axis with very high-amplitude resonances near 1.5 THz. As in the case of ϵ_∞, there is a small off-diagonal component, which is plotted in Figure 7.22. However, this component is significantly smaller than the on-diagonal components (note the difference in scale compared to Figure 7.21).

As it is not yet possible to produce SnIP samples with aligned needles or nanowires, it is also useful to define the average dielectric function,

$$\epsilon_{avg} = 0.5\,\epsilon_{xx} + 0.25\,\epsilon_{yy} + 0.25\,\epsilon_{zz}, \tag{7.19}$$

which assumes a linear superposition of the various directions and we have used a similar weighting as in the calculation of the average effective mass with the simplifying approximation that the principal axes of each mode are aligned with the Cartesian axes.

7.5.3 Comparison to Experiment

We performed THz-TDS on the SnIP nanowire thin film in the region circled in red shown in Figure 7.4. The conductivity of the thin-film was extracted using the

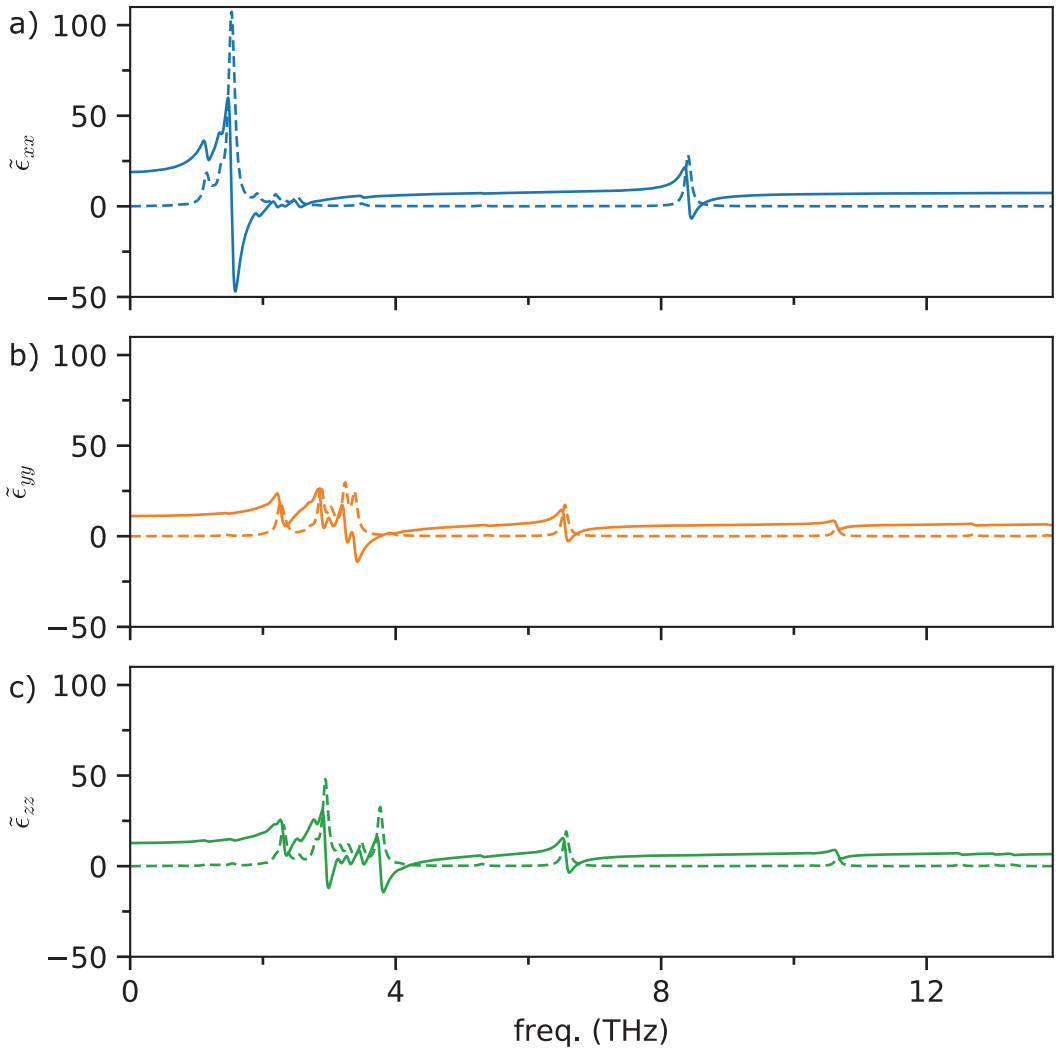

Fig. 7.21: Polarization-dependent dielectric function. Components of the complex dielectric function, a) ϵ_{zz}b) ϵ_{yy}. The dielectric function was calculated using the oscillator strength from DFT and a damping of 0.1 THz. In each plot the dashed line is the imaginary part of the susceptibility while the solid line is the real part.

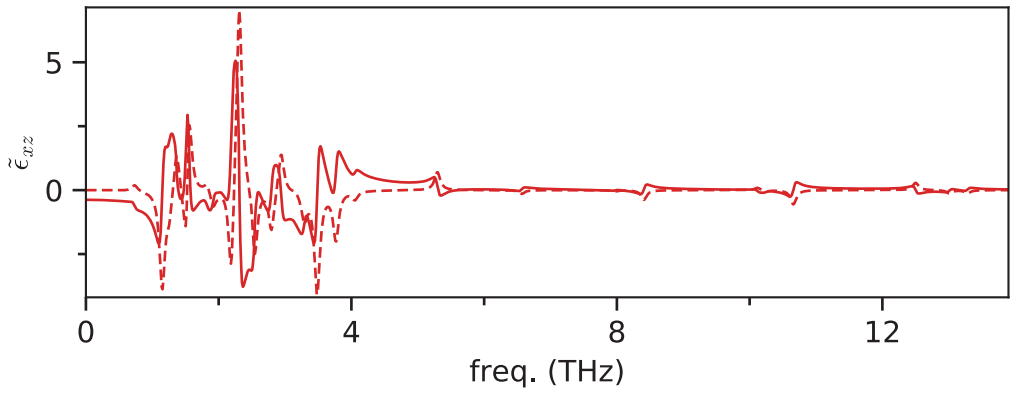

Fig. 7.22: Off diagonal component of the dielectric function. ϵ_{xz}, which indicates off-diagonal coupling of the electric field to the polarization. The xy and yz components are zero. The solid and dashed lines are the real and imaginary parts, respectively.

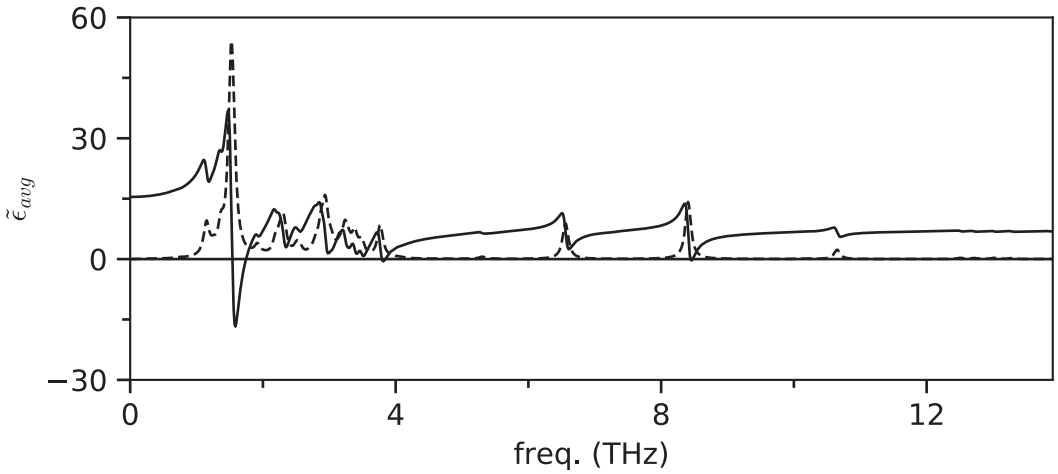

Fig. 7.23: Ensemble average dielectric function. Weighted linear combination of the calculated dielectric function according to equation 7.19 with a 0.1 THz damping.

Tinkham equation (equation A.17) and converted to the dielectric function using the relationship between the optical conductivity and dielectric function. The effective complex dielectric function,* $\tilde{\epsilon}_r = \epsilon_1 + i\epsilon_2$, of the SnIP nanowire film in the frequency range from 0.5 to 2.5 THz is shown in Figure 7.24a. A weak vibrational resonance at 1.13 THz and stronger resonance at 1.495 THz are observed (referred to in this thesis as mode 1 and mode 2, respectively). The blue and orange circles refer to ϵ_1 and ϵ_2, respectively, while the solid lines are a simultaneous fit to the real and imaginary components using two Lorentz oscillators,

$$\tilde{\epsilon}_r(\omega) = \epsilon_\infty + \sum_{i=1}^{2} \frac{A_{osc,i}}{\omega_{0,i}^2 - \omega^2 - i\omega\gamma_i}, \tag{7.20}$$

where ω is the angular frequency and $\omega_{0,i}$, $A_{osc,i}$, and γ_i, are the resonant angular frequency, amplitude, and damping of the i^{th} mode, respectively, and ϵ_∞ is the constant offset due to higher frequency vibrational modes and electronic transitions.

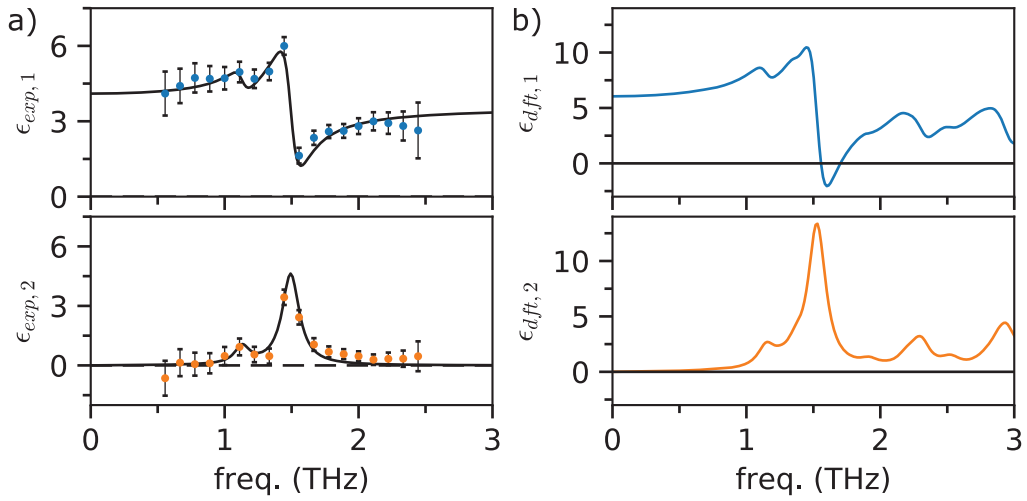

Fig. 7.24: THz IR spectrum: experiment versus quantum-chemical calculations. **a** Experimentally measured effective complex dielectric function, ϵ_1 (blue circles) and ϵ_2 (orange circles). The solid lines are a simultaneous fit using two Lorentz oscillators. **b** Calculated average dielectric function with a 0.15 THz broadening (from experiment) and weighted according to equation 7.19. A Linear combination of the air-gap dielectric function ($\epsilon_{air} = 1$) and the calculated average dielectric function was used assuming a 0.35 fill fraction.

*Here the terminology "effective" refers to the fact that the film is inhomogeneous on deeply sub-wavelength length scales so that it is an effective medium.

Taking into account the estimated filling fraction of the thin film (0.35, 7.3.1), we can scale the amplitude of the average dielectric function (Figure 7.23) to more directly compare to experiment, as seen in Figure 7.24b. While the random orientation of nanowires in our thin films obscures the underlying symmetry of the modes, making it more difficult to precisely assign peaks in the experimentally observed spectrum to individual modes [203], the calculated average dielectric function shows surprisingly good agreement with data.

As indicated previously, in general, the calculations suggest that motion in the 0.5-2.5 THz range is associated with oscillations of the $[SnI]^+$ (outer) helix. Two high intensity modes near mode 2 (1.495 THz) are revealed by DFT calculations at 1.52 THz and at 1.55 THz. Both peaks can be classified as primarily twisting modes of the outer $[SnI]^+$ helix. The Sn^{2+} and I^- atoms show the largest displacement with motion predominantly along the double-helix axis so that the mode is longitudinally polarized with respect to the nanowires. A smaller peak near mode 1 (1.13 THz) is revealed by the calculated spectra at 1.15 THz, corresponding to rocking motion of the outer $[SnI]^+$ helix. The oscillation vectors for the highest intensity mode, which is at 1.52 THz, are shown in Figure 7.25. Additionally, appendix A.9 contains plots of other high-intensity modes.

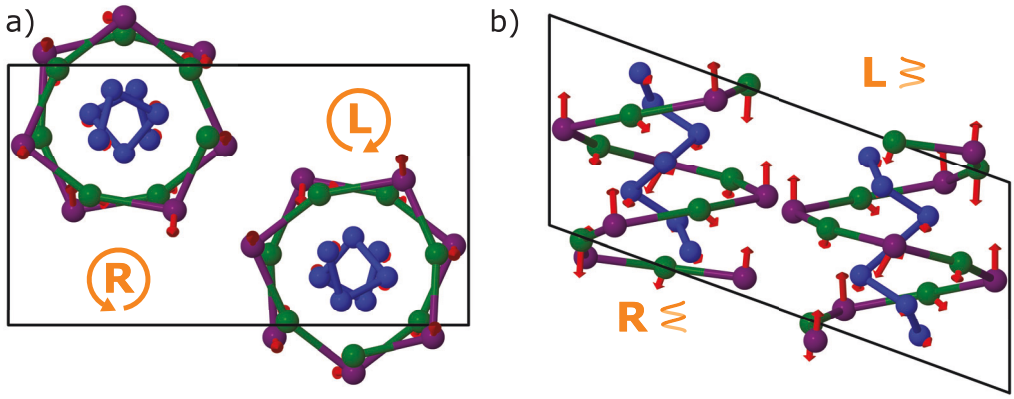

Fig. 7.25: Vibrational conformation of the calculated 1.52 THz mode. Vibrational mode vectors of the highest intensity mode in the 1-2 THz region projected along **a** the x-plane and y-plane, as defined in Figure 7.1.

7.5.4 Longitudinal Mode and Fröhlich Constant

In order to understand the nature of carrier transport, an important quantity that we can extract from the IR spectrum is the Fröhlich-polaron coupling constant, α. The anisotropic and highly non-parabolic electronic structure of SnIP as well as the polarization dependence of the dielectric function and large number of IR modes makes precise calculation of the Fröhlich constant more difficult [204, 205], however, using the standard theory that assumes in isotropic crystal can be a useful first approximation of the coupling strength. This also allows us to speculate to the regime of transport and the importance of polaronic effects. In this theory, the Fröhlich constant is given by,

$$\alpha = \frac{1}{137}\left(\frac{m^* c^2}{2hf_{LO}}\right)^{1/2}\left(\frac{1}{\epsilon_\infty} - \frac{1}{\epsilon_{st}}\right), \tag{7.21}$$

where m^* is the effective mass, c is the speed of light, f_{LO} is the longitudinal optical (LO) phonon frequency, and ϵ_{st} and ϵ_∞ are the static (low frequency) and infinite (high frequency) dielectric constants [206]. In general, $\alpha < 1$ implies the weak coupling regime where transport is expected to remain Drude-like [39].

From the fits to the experimental dielectric function we can only directly extract the transverse optical (TO) frequency. The Lyddane-Sachs-Teller (LST) relation is often used to calculate the LO phonon frequency from the TO phonon frequency if the static (zero frequency) and infinite (high frequency) dielectric constants are known,

$$\frac{f_{LO}^2}{f_{TO}^2} = \frac{\epsilon_{st}}{\epsilon_\infty}. \tag{7.22}$$

However, there are several important points to consider before applying this formula to calculate the LO frequency in SnIP. The LST relation strictly applies to the case of crystals with a single phonon mode, cubic symmetry, and zero damping [207], however, we can generalize it by considering its origin. Fundamentally, the relationship in equation 7.22 arises due to the apparent inconsistency between the macroscopic electric field produced by a polar LO mode and the Gauss law in a crystal with zero net charge density, where in 1D,

$$\epsilon \partial_x E_{LO} = \epsilon i k_{LO} |E|_{LO} = 0, \tag{7.23}$$

which can only be satisfied if ϵ=0, which is a necessary condition for the existence of a polar LO mode. From this condition and the equation for a single Lorentz oscillator, as in equation 7.20 but with only a single term with zero damping, we can extract the LST relation, equation 7.22.

Next, to generalize this relation to include the anisotropic dielectric tensor, we rewrite equation 7.23 as,

$$\nabla_a \epsilon_{ab} E_b = i k_{LO,a} \epsilon_{ab} |E_{LO,b}| = 0, \tag{7.24}$$

from which we can find the condition for a generalized LST relation: in order to satisfy equation 7.24 at the LO frequencies, where $|E_{LO}|$ is non-zero, the determinant of the matrix ϵ_{ab} must be zero. Conversely, the zeros of the determinant of the dielectric tensor yield the LO modes. In crystals where the dielectric tensor is diagonal, an LST-like relation can be applied to each polarization separately. In SnIP, while the off-diagonal components are non-zero our calculations suggest they are quite small compared to the on-diagonal terms. As a result, we will neglect them in our estimation of the experimental LO frequency.

Finally, before directly applying the LST relation to the experimental data we must account for the anisotropy and fill fraction of the thin film. Each of these steps introduces uncertainty into the calculation. Furthermore, the large uncertainty in film thickness should be considered. First, to account for the fill fraction and anisotropy we use,

$$f(0.5\epsilon_{\|} + 0.5\epsilon\perp) + (1-f)\epsilon_{vac} = \epsilon_{exp}, \tag{7.25}$$

where $\epsilon_{\|}$ is the dielectric function parallel to the double-helix axis and ϵ_{bot} is the dielectric function perpendicular to the double-helix axis.* We make the additional assumption that the parallel and perpendicular high-frequency dielectric constants are equal, *i.e.*, $\epsilon_{\infty\|} = \epsilon_{\infty\perp}$, which is shown to be approximately true based on the DFT calculations. From the experimentally measured values, $\epsilon_{st} = 4.1$ and $\epsilon_{\infty} = 3.5$, we then use equation 7.25 to find $\epsilon_{st\|} = 11.5$ and $\epsilon_{\infty\|} = \epsilon_{\infty\perp} = 8.17$. Finally, we find the contribution of mode 2 to the static dielectric constant, where $\Delta\epsilon_i$ is the

*Here, we are assuming that the two perpendicular directions have the same dielectric function, which is motivated by the calculations in Figure 7.21.

contribution of mode i, using the relation,

$$\epsilon_{st\|} = \Delta\epsilon_{1\|} + \Delta\epsilon_{2\|} + \epsilon_{\infty\|} = \frac{A_{1\|}}{\omega_{0,1}^2} + \frac{A_{2\|}}{\omega_{0,2}^2} + \epsilon_{\infty\|}, \tag{7.26}$$

where $A_{i\|}$ is the amplitude of the i^{th} oscillator parallel to the double-helix axis, and assuming the ratio $A_{1\|}/A_{2\|} = A_{osc,1}/A_{osc,2}$, we find an effective static permittivity for mode 2 of $\epsilon_{2st\|} = \Delta\epsilon_{2\|} + \epsilon_{\infty\|} = 10.9$. To calculate the LO frequency, we now use equation 7.22, with $\epsilon_\infty = \epsilon_{\infty\|}$ and $\epsilon_{st} = \epsilon_{2,st\|}$ and find $f_{LO} = 1.73$ THz.

To this point, we have still not considered the effect of damping and it is not yet clear that the LST relation used in this way is valid. Furthermore, we have not proved that the dispersion from mode 1 is insignificant near the LO frequency of mode 2. To do this, we note that in the zero damping limit, zeros in the dielectric function correspond to poles (zero-width peaks) in the inverse dielectric function [208]. Introducing damping broadens these peaks[†] so that rather than zeros in the dielectric function, LO resonances can be associated with peaks in the inverse dielectric function [209].

In Figure 7.26a, b we plot the estimated $\epsilon_\|$ as a function of frequency and its inverse, respectively. The green vertical lines are drawn to indicate the TO resonant frequencies extracted from fits to experimental data while the red vertical lines indicate the LO frequencies extracted from the LST relation, showing excellent agreement with the peaks in $\epsilon_\|^{-1}$. This validates our assumptions regarding the negligible dispersion of mode 1 and, moreover, is compelling indication of the applicability of the LST relation even in the case of non-zero damping.

Taking into account the uncertainties in each of the parameters involved in the calculation of the LO frequency (see Appendix A.1), the LO frequency is found to be $f_{LO} = 1.74 \pm 0.05$ THz. From this, along with equation 7.21, the Fröhlich constant is found to be $\alpha = 0.6 \pm 0.4$ and, using the relation $m_{rn}^*/m^* = 1 + \alpha/6$, the polaron mass is found to be $(0.31 \pm 0.02)\, m_e$ [206]. This indicates only a small renormalization with respect to the band mass. In chapter 8, due to the uncertainties and approximations involved in this calculation the band mass is used to extract the mobilities. As a result, the quoted mobilities are an upper bound, however, because α is small this is

[†]This is similar to the effect of damping on resonances in the dielectric function.

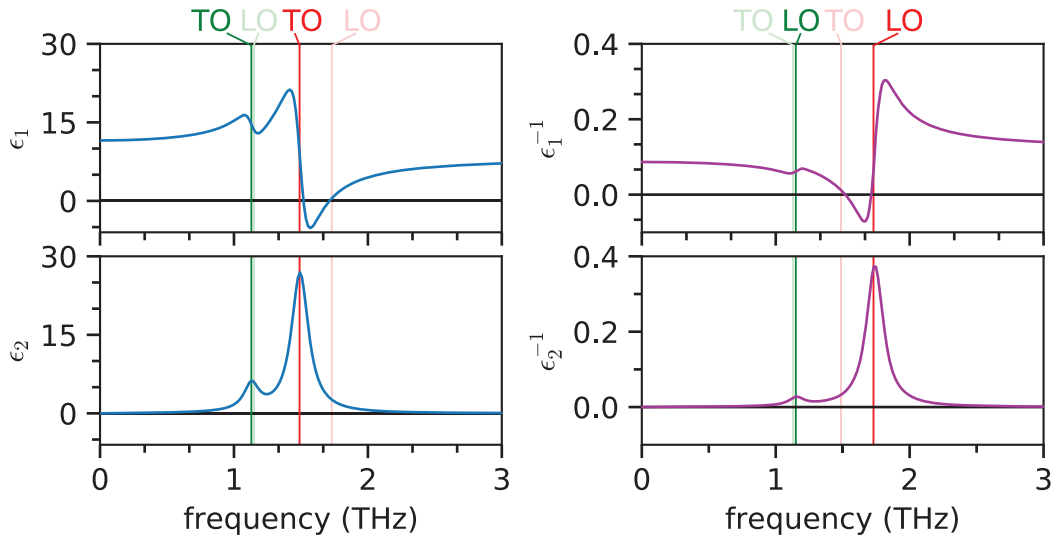

Fig. 7.26: LST relation and the inverse dielectric function. Estimated real (blue) and imaginary (orange) dielectric function along the double-helix axis. b) Real (blue) and imaginary (orange) part of the inverse of the dielectric function in a), showing peaks at the LO phonon frequencies. The vertical dashed lines indicate the TO phonon frequency extracted from THz spectroscopy and the LO phonon frequency calculated from the LST relationship.

a reasonable approximation.

Chapter 8

Time-Resolved THz Spectroscopy of SnIP Nanowire Films

8.1 Introduction

Time-resolved terahertz (THz) spectroscopy (TRTS) is a powerful ultrafast tool used in the study of picosecond charge-carrier dynamics in materials [210, 39]. The intermediate frequencies of THz pulses with respect to electronics and optical frequencies provide several important advantages. First, the time resolution of TRTS can be sub-picosecond, which is extremely valuable in the exploration of new materials where the carrier lifetime is often short. Second, the low frequencies of THz waves with respect to mid-infrared or optical pulses makes them much more sensitive to conductive processes, which for a Drude-like response are peaked at zero frequency.[†]

As far back as the 1980's, Auston used a variation of the TRTS technique to probe the mobility rise time in GaAs [211], providing the first direct evidence of the role of intervalley scattering in the relaxation of hot photoexcited carriers.[‡] Much of the early work was focused on the technologically relevant III-V semiconductors, and their alloys, heterostructures, and quantum wells. For an excellent review of this early work, see ref. [37]. It was noted early on that, as a non-contact probe

[†]Of course the conductivity is not always Drude-like, as we shall see in this chapter. Several conductivity models shift the spectral weight to higher frequencies, however, it is still true in general that lower frequencies are more sensitive to conductivity.

[‡]This study preceded the pivotal work by Jagdeep Shah probing intervalley scattering rates using time-resolved luminescence spectroscopy by nearly a year [212]. Both these studies came out of Bell Labs, which was an exciting place for ultrafast laser spectroscopists in the 1980's.

of transport, TRTS would play an important role in understanding carrier dynamics in nanostructures, which have since been studied extensively [213, 214, 215, 216]. TRTS has also been applied to many other classes of materials, such as liquids [217], organic semiconductors [218], strongly-correlated materials [219], phase-change materials [220], and more recently to exciting new material classes such as lead-halide perovskites [221, 222] and transition-metal dichalchogenides [223].

Here, we use TRTS to study picosecond charge carrier dynamics in SnIP nanowire films, introduced in Chapter 7. While it has been suggested as an excellent material for flexible electronics due to its mechanical properties, as-grown SnIP is highly resistive making it difficult to explore its transport properties. As such, TRTS is a uniquely suitable tool for exploration of transport in this interesting new material. From a detailed study of the photoconductivity spectra in terms of the three most common models for TRTS spectra, we conclude that Drude-Smith type transport is the most likely origin of our observations. Coupled with the insight into the electronic structure from DFT (Chapter 7), we find a maximum maximum electron mobility of 280 $\mathrm{cm^2\,V^{-1}s^{-1}}$ along the double-helix axis, an extraordinarily high mobility for a material as soft and flexible as SnIP. On the other hand, the hole mobility is largest perpendicular to the double-helix axis and is as high as 238 $\mathrm{cm^2\,V^{-1}s^{-1}}$, which is comparable to the hole mobility in silicon or gallium arsenide [224]. Interestingly, we also see a suppression of the photoconductivity near mode 2, the strong vibrational resonance at 1.495 THz studied in Chapter 7, which indicates a reduction in oscillator strength after photoexcitation due to a photoexcitation-induced charge redistribution [225, 39, 226, 227]. Using 2D scan of the differential conductivity after photoexcitation, we track the time evolution of both the transport (Drude-Smith) and oscillator parameters. We also performed a detailed study of the carrier relaxation dynamics as a function of excitation fluence and observe trap-filling dynamics that imply that the carrier mobility and lifetime are currently limited by a high density of trap states. This suggests that the carrier lifetime and mobility could be improved by optimized synthesis or passivation of traps, which would dramatically enhance photocatalytic activity [228, 229]. Furthermore, a study of the temperature-dependent photoconductivity spectrum shows that our SnIP nanowire films display band-like

transport, while the temperature-dependent relaxation dynamics reveal the presence of thermally-activated traps.

To provide context, in the final section we present a survey of the mobility and mechanical properties in a wide variety of materials. We find that SnIP displays an unparalleled combination of flexibility, high carrier mobility, and softness that makes it well suited for flexible electronics applications. While significant challenges must still be overcome, namely the synthesis of doped SnIP, our results demonstrate the exciting potential of this this material. This work therefore highlights the ability of TRTS to help accelerate scientific understanding of transport properties and mechanisms in new materials and, in principle, facilitate their transition to real-world applications.

8.2 Experimental Details

The principle of the TRTS system used in this experiment is summarized in Figure 8.1**a**. Briefly, a 400 nm or 800 nm photoexcitation laser pulse at a fixed time delay, Δt_1, with respect to the THz pulse modulates the THz transmission by generating free carriers in the SnIP thin film. The film consists of an ensemble of randomly oriented nanowires (see section 7.3.1), with their longitudinal axes parallel to the double-helix axis as indicated schematically in Figure 8.1**b**. The transmitted THz field is electro-optically sampled using a third optical pulse with time delay $\Delta t_2 = 0$ and monitored for changes induced by photoexcitation. A representative THz pulse waveform, proportional to the electric field of the THz pulse, is shown in Figure 8.1**c**, showing a few-cycle character. The fast-Fourier transform (FFT) of this pulse is shown in Figure 8.1**d**, with usable bandwidth from approximately 0.2 to 2.5 THz.*

Delaying the photoexcitation pulse with respect to both the THz and electro-optic (EO) gate pulses yields a measurement of the carrier lifetime.† Alternatively, to measure the conductivity spectrum, the change in THz field, ΔE_{THz}, the THz pulse is delayed with respect to the excitation and EO-gate pulses, with a representative

*In practice, we only use frequencies above 0.5 THz, which is roughly where the THz field starts to clip on the sample-holder aperture.

†This commonly-used approximation requires that the conductivity lineshape does not change as a function of time and that the pump-induced change in THz transmission is small, so that $\Delta E_{THz} \ll E_{THz}$. We will see that both of these assumptions hold in SnIP.

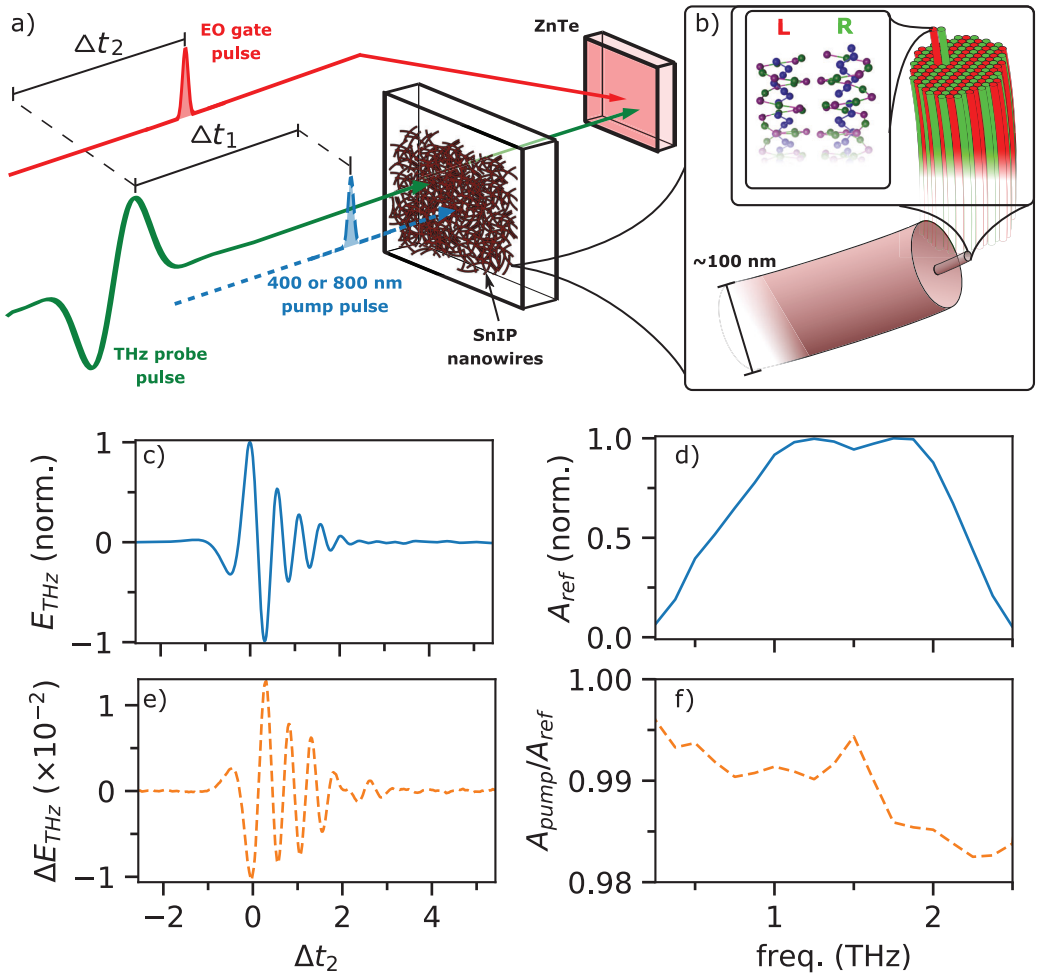

Fig. 8.1: Time-resolved THz spectroscopy of SnIP nanowires. a) Schematic of the TRTS experiment. A THz pulse is coincident on a drop-cast SnIP thin film along with a time-delayed (Δt_1) 400 or 800 nm photoexcitation (pump) pulse, which is modulated to enable simultaneous acquisition of reference and pumped waveforms. A third pulse is used as a gating beam at time delay Δt_2 for field-resolved electro-optic (EO) sampling of the transmitted THz pulse to monitor the pump-induced change in transmission. b) Schematic depiction of the nanowire morphology at various length scales. Representative THz **c** electric field and **d** amplitude spectrum. Pump-induced differential transmission with 10 mW pump power and 400 nm excitation wavelength in **e** the time domain and **f** the frequency domain.

ΔE_{THz} measurement shown in Figure 8.1e. The reference waveform (unexcited) and pumped wave are Fourier transformed to find the reference amplitude spectrum, A_{ref}, and pumped amplitude spectrum, A_{pump} and the modified thin-film formula (see section A.5) is used to extract the differential complex conductivity, $\Delta\tilde{\sigma} = \Delta\sigma_1 + i\Delta\sigma_2$, where the modified thin-film formula is given by,

$$d_\lambda \cdot \Delta\tilde{\sigma} = \frac{1 + \tilde{n}_{sub} + Z_0\tilde{\sigma}_0 d_{film}}{Z_0}\left(\frac{1}{\tilde{t}} - 1\right), \tag{8.1}$$

where d_λ is the optical penetration depth, d_{film} is the film thickness, $\tilde{n}_{sub}$ is the substrate refractive index, Z_0 is the impedance of free space, $\tilde{t} = \tilde{A}_{pump}/\tilde{A}_{ref}$, and $\tilde{\sigma}_0$ is the unexcited film conductivity (see Chapter 7). This modified Tinkham formula introduces small corrections to the extracted differential conductivity due to the dispersion of the thin film itself (see section A.5.3).

8.3 Carrier Lifetime

Shown in Figure 8.2a is the relative change in THz transmission, $-\Delta T/T_0$, where $-\Delta T$ is the pump-induced change in EO signal and T_0 is the EO signal with no pump, through a SnIP nanowire thin film on a quartz substrate induced by a 400 nm photoexcitation pulse with a fluence of 190 $\mu\mathrm{J\,cm^{-2}}$. As $-\Delta T$ is proportional to the conductivity, this measurement gives us an indication of the photocarrier lifetime. We explored the use of several alternative fit functions, including stretched exponential and power law functions as well as using various systems of rate equations, each of which can have the advantage of being associated with well-defined relaxation pathways. However, as our thin film consists of a complex distribution of nanowire diameters, lengths, and degrees of disorder (see section 7.3.1) it is likely that many factors contribute to the observed carrier lifetime (*e.g.*, the cylindrical geometry, distribution of sizes, and trapping dynamics). We therefore choose to use bi-exponential fits as they facilitate direct quantification of the lifetime and comparison of the relaxation dynamics with various excitation fluences and wavelengths. The solid line is therefore a fit with a bi-exponential function given by,

$$-\frac{\Delta T(t)}{T_0} = A_f e^{-t/\tau_f} + A_s e^{-t/\tau_s}, \tag{8.2}$$

where τ_s (τ_f) are the slow (fast) lifetimes and A_f (A_s) are their associated amplitudes. To account for the rise time of the system, the curves are convoluted with a Gaussian

response function with a 0.24 ps rise time. We find slow and fast lifetimes of 2.6 ps and 20 ps, respectively. Due to the high surface-to-volume ratio, it is likely that surface recombination contributes significantly to the relaxation, as seen in other semiconductor nanowire systems [230]. Also shown in Figure 8.2b is a semi-log scale version of the plot in Figure 8.2a. From this we see that the fit reproduces the curve reasonably well, however, there is some deviation at later times. This is not surprising due to the variety of contributions to the carrier lifetime discussed previously.

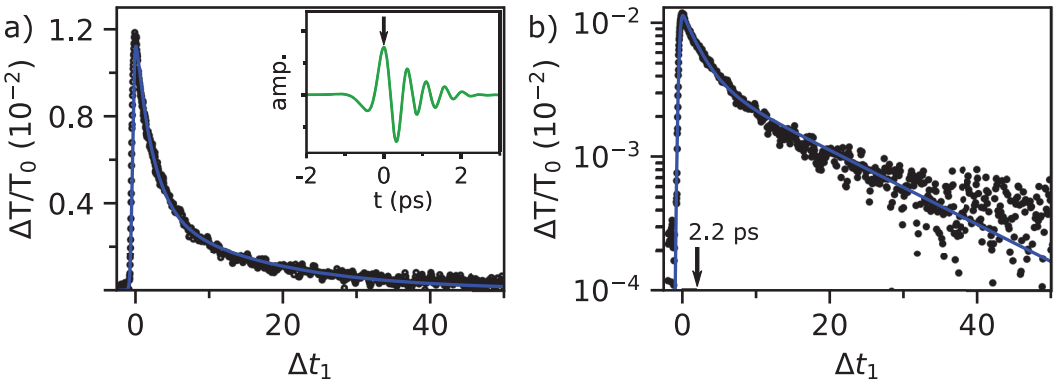

Fig. 8.2: Carrier lifetime in SnIP. a Relaxation of the differential THz transmission signal as a function Δt_1 fit with a bi-exponential decay. The signal was acquired with the probe pulse set to the peak of the THz field, as indicated in the inset. **b** The data from **a** on a semi-log scale. The time-delay of 2.2 ps indicates the time-delay chosen for photoconductivity measurements.

8.4 Photoconductivity Spectrum

The corresponding complex photoconductivity spectrum acquired 2.2 ps after the peak of the transient photoconductivity (see Figure 8.2**b**) is plotted in Figure 8.3a. Due to the geometry of the SnIP nanowires and needles, quantitative measurement of the optical penetration depth, d_λ, for a given excitation wavelength is difficult. As a result, we study the areal conductivity, $d_\lambda \cdot \Delta\tilde{\sigma}$, which is directly accessible in TRTS of thin films via the Tinkham formula.* We can learn a great deal about the nature of photoconductivity by studying the qualitative properties of the spectra. There are two main features in the observed spectrum. First, there is a broad increasing $\Delta\sigma_1$

*In TRTS, the distinction between areal and volume conductivity does not affect the measurement of carrier mobility, which is derived from the scattering time and is therefore a property of the dispersion rather than the amplitude of the conductivity

with frequency along with a corresponding negative $\Delta\sigma_2$, which is characteristic of free-carrier localization. Second, there is a negative peak in $\Delta\sigma_1$ with a corresponding kink in $\Delta\sigma_2$ near mode 2 (see Chapter 7.5.3), which indicates a photoexcitation-induced modification of the vibrational mode. To model the spectra, we treat these two contributions individually and use a fit function given by $\Delta\tilde{\sigma} = \tilde{\sigma}_{DS} + \tilde{\sigma}_{PS}$, where $\tilde{\sigma}_{DS}$ is the Drude-Smith model of optical conductivity and $\tilde{\sigma}_{PS}$ is the peak-shift model of the differential conductivity of a Lorentz oscillator [227]. The solid lines in Figure 8.3c show a simultaneous fit to the real and imaginary conductivity using this model, with fit parameters summarized in Table 8.2. Here we discuss each of these contributions in detail.

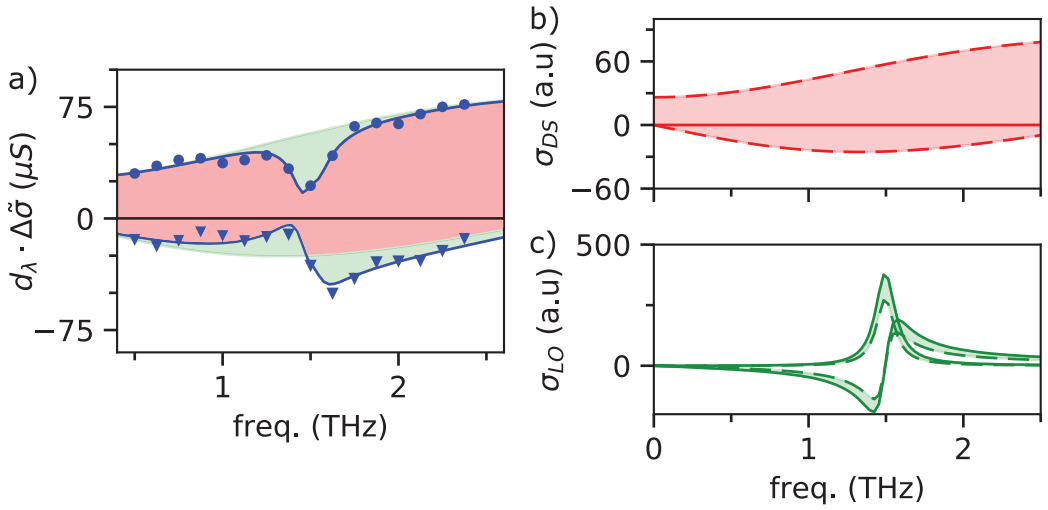

Fig. 8.3: Photoconductivity spectrum: carrier localization and vibrational mode suppression. **a** THz photoconductivity spectrum acquired 2.2 ps after the peak of the differential transmission. The solid blue line is a fit with a Drude-Smith plus peak-shift model. The dashed red line indicates the Drude-Smith contribution to the fit while the shaded green area indicates the peak-shift portion. **b** Drude-Smith fit, with a strong suppression of DC conductivity indicative of carrier localization. **c** Illustration of the change in the oscillator lineshape due to photoexcitation, where the solid line is the profile when the material is unexcited and the dashed line is the profile when the material is excited. The green shaded region corresponds to the green shaded region in **a**.

8.4.1 Drude-Smith Model and Carrier Mobility

We first consider the broad features. Several models are commonly applied to understand these features in the photoconductivity spectra, which are all used to

describe a free-carrier (*i.e.*, conductive) response [210, 39, 231, 232]. We note that the temperature dependence of the THz conductivity is consistent with band-like transport (see section 8.8). In the next section, we provide a detailed analysis of our data in terms of several different models (Bruggeman, Drude-Smith, and plasmon) and here summarize only the key criteria necessary to validate our eventual choice of the Drude-Smith model. Notably, the mobilities extracted from each model are similar, ranging from 150 to 280 $cm^2V^{-1}s^{-1}$. Bruggeman effective-medium theory has been used to describe the conductivity in inhomogeneous systems [214, 39, 231], however, we could only achieve reasonable fit quality to our data with this model by introducing an unphysical scaling of the fill fraction with fluence. A Drude-Lorentz model has been used to describe surface plasmon resonances in nanowires [228, 230, 231, 233] or to describe a mixed Drude response along with hydrogen-like transitions in excitonic systems [234, 235]. While the plasmon model provides excellent fit quality, it predicts a specific scaling of the resonant frequency with increasing excitation density, which we do not observe in our data. Moreover, in SnIP there are no excitonic signatures in either the absorbance or photoluminescence spectra [179, 183].

Alternatively, the Drude-Smith model (see section 5.6.3), a modified version of the Drude model [143, 236, 144, 237], is often applied to describe nanomaterial conductivity when carrier localization arises from nanoscale morphology [214, 238, 239, 240, 241, 242, 243, 244, 245, 235, 227, 246]. The Drude-Smith model has been shown to fit photoconductivity spectra over a broad frequency range [239], yield comparable conductivity to standard transport measurements [241], and provide qualitative information about carrier localization [238].* The functional form is given by,

$$\tilde{\sigma}_{DS}(\omega) = \frac{Ne^2\tau_{DS}/m}{1 - i\omega\tau_{DS}}\left(1 + \frac{c}{1 - i\omega\tau_{DS}}\right), \tag{8.3}$$

where m is the effective mass, τ_{DS} is the scattering time, e is the elementary charge, c is a phenomenological localization parameter that ranges from 0 to -1 for free and localized carriers, respectively, and N is the density of electron-hole pairs (see also equation 5.52). Due to the uncertainty in penetration depth discussed previously, we fit with the areal charge density, $d_\lambda N$. For the mass we use the weighted average

*As we shall see, it is also possible to extract, at least, semi-quantitative information about carrier localization.

of the direction-dependent reduced effective mass, $m = \bar{m}^* = 0.24\,m_e$ (see Section 7.4.2). Shown in Figure 8.3b is the Drude-Smith portion of the fit (red).

With knowledge of the effective mass, from fitting the conductivity spectrum we can now extract the areal charge density, localization parameter, and scattering time. The measured localization parameter of -0.82, which is a similar to that observed in 1D systems such as graphene nanoribbons and carbon nanotubes, indicates that carriers are highly localized [240]. We note that implicit in our model is the approximation that the Drude-Smith scattering time, measured to be τ_{DS} =45 fs, is isotropic and the same for electrons and holes.* While the weighted reduced mass is used to extract the density, the directionally-dependent effect mass can be used along with the scattering time to extract the carrier mobility. In the Drude-Smith model (equation 8.3), the mobility is given by $\mu = \frac{e\tau_{DS}}{m}$ (see section 5.6.3).

Along the $\hat{x}'$ direction (almost parallel to the double-helix axis, dashed green arrow in Figure 7.14b), with $m_{cx'} = 0.28\,m_e$, we find an electron mobility of $280\,\mathrm{cm^2\,V^{-1}s^{-1}}$ while along the $\hat{y}$ direction, with $m_{cy} = 2.0\,m_e$, we find a much smaller carrier mobility of $39\,\mathrm{cm^2\,V^{-1}s^{-1}}$ indicating a significant anisotropy in the carrier mobility. Alternatively, the hole mobility is largest in the $\hat{z}'$ direction (almost perpendicular to the double-helix axis, dashed red arrow in Figure 7.14b), and with $m_{vz'} = 0.33\,m_e$ we find a hole mobility of $238\,\mathrm{cm^2\,V^{-1}s^{-1}}$. Such a high mobility is similar to other vdW materials [247, 185] and many times higher than mobilities in organic semiconductors with comparable mechanical properties often used in flexible electronics [248]. The carrier mobility in these ultrasoft materials is strongly affected by both static and dynamic disorder, which can strongly perturb orbital overlap and inhibit transport [199, 249].

From the large negative c parameter, we can also see that long-range conductivity is reduced by localization due to the nanoscale morphology. This can be seen quantitatively with the long-range mobility, $\mu_{l-r} = \mu(1 + c)$, which is equal to $\mu_{lr,x'} = 45\,\mathrm{cm^2\,V^{-1}s^{-1}}$ in the $\hat{x}'$ direction. The directionally-dependent long-range and short range mobilities are summarized in Table 8.1. A detailed analysis (see sec-

*It is likely that this approximation holds to a reasonable degree of accuracy, however, in the future it will be important to verify this assumption with experiments on aligned SnIP samples.

tion 8.7.2) indicates that the characteristic length scale defining long-range transport in our samples is on the order of 20 nm. This highlights an advantage of THz spectroscopy, where the high frequency field naturally probes transport on small length scales and can therefore give an indication of the intrinsic mobility in nanostructured materials. Future work will focus on optimizing material synthesis and processing to mitigate the effects of localization and improve the long-range mobility.

Table 8.1: Anisotropic effective masses and mobilities for the highest-lying valence (lowest-lying conduction) bands, defined as m_v^* (m_c^*) and μ_v (μ_c), respectively. m_e is the free-space electron mass. Also shown is the directionally-dependent long-range mobility, $\mu_{l-r} = \mu(1+c)$. The directions are defined with respect to the axes in Figure 7.1. The scattering time used for the calculation was 45 fs as extracted from the Drude-Smith plus peak-shift model fits.

	m_c^* (m_e)	$\mu_{l-r,c}$ ($\mathrm{cm^2V^{-1}s^{-1}}$)	μ_c ($\mathrm{cm^2V^{-1}s^{-1}}$)	m_v^* (m_e)	$\mu_{l-r,v}$ ($\mathrm{cm^2V^{-1}s^{-1}}$)	μ_v ($\mathrm{cm^2V^{-1}s^{-1}}$)
$\hat{x}'$	0.28	45	281	0.71	18	111
$\hat{y}$	2.0	6	39	0.66	19	119
$\hat{z}'$	0.51	25	154	0.33	38	238

8.4.2 Peak-Shift Model and Vibrational Mode Suppression

We now shift focus to the narrow feature in the spectrum near 1.5 THz. The fingerprints of low-frequency vibrational dynamics on TRTS spectra has been the focus of several recent studies that have elaborated on a variety of interesting mechanisms [209, 250, 251, 225, 252, 244, 226, 253, 254, 206, 227, 255]. Narrow features in the conductivity spectrum are often attributed to resonant modulation of the conductivity due to polaronic effects from interactions with polar optical (LO) modes [244, 253, 254], however, here we estimate the LO mode to be at a significantly higher frequency of 1.73 THz (see section 7.5.4). The close proximity of the feature in the photoconductivity spectra to the transverse-optical (TO) mode at 1.495 THz, which does not couple strongly through the polar-optical mechanism responsible for strong electron-phonon coupling [256], instead suggests that the lineshape of mode 2 is modified by photoexcitation on a picosecond timescale [225, 252, 226, 227].

The simplest model we can use to fit this feature is a Lorentz oscillator, however, we note that we observe the differential conductivity and the difference between two Lorentz oscillators has a distinct lineshape from a Lorentzian. Ideally, we could therefore fit the spectra with the difference between two oscillators, however, due to the uncertainty in penetration depth we cannot perform the thickness-independent fitting in this way as with the Drude-Smith model. We therefore use the peak-shift model of Zhao *et al.* [227], a differential model with lineshape given by,

$$\tilde{\sigma}_{PS}(\omega) = \sum_{i=1}^{3} \frac{\partial \tilde{\sigma}_{osc,2}}{\partial x_i} \Delta x_i, \tag{8.4}$$

where the parameters x_i are the change in amplitude, $\Delta A_{osc,2}$, resonant frequency, $\Delta\omega_{0,2}$, and damping, $\Delta\gamma_2$ of mode 2. As this fit function is linear with respect to each of these parameters, we can now use the excited-film thickness independent form as with the Drude-Smith model using $d_\lambda \Delta\tilde{\sigma}_{PS}$ and using $d_\lambda \Delta A_{osc,2}$, $d_\lambda \Delta\omega_{0,2}$, and $d_\lambda \Delta\gamma_2$ as fit parameters. Illustrated in Figure 8.3c is the oscillator conductivity in the equilibrium (solid line) and photoexcited states.

The peak-shift portion of the fitting indicates a large photoexcitation-induced reduction in the amplitude along with a small reduction in linewidth and blue shift of the resonant frequency (for an estimation of the absolute change in lineshape, see appendix A.4.3). This behavior indicates that screening from the photoexcited carriers induces a charge redistribution that stiffens the potential-energy landscape of this mode and reduces its effective charge, *i.e.*, reduces its dipole moment [225, 39, 226, 227]. Interestingly, when the screening length is large compared to the interatomic spacing, as is the case in this work (see appendix A.6), such modulation of IR-active modes is not expected in prototypical covalent semiconductors [257, 209, 258]. However, in more complex systems changes to the vibrational spectrum have been linked to a photoinduced charge redistribution at the atomic scale [250, 225, 39, 226, 227]. This effect could be especially strong in SnIP due to the prevalence of long-range dispersion forces, which can be sensitive to free-carrier screening [259]. In addition to the amplitude reduction, from the fits we also see that the differential linewidth is negative, indicating a line narrowing. We speculate on two possible origins of this effect. First, the charge redistribution could lead to a lattice reorganization that

reduces strain inhomogeneity [260, 261], which would result in less inhomogeneous broadening [262]. Second, it could result from a reduction of lattice anharmonicity, which is sensitive to dispersion forces [263] that can in turn be modified by screening [259].

8.5 Model Dependent Spectroscopy

As suggested in the previous section, several models are commonly applied to understand the origin of conductivity spectra with negative σ_2 and increasing σ_1 with frequency. The most commonly used models are the Drude-Smith model, the plasmon model, and Bruggeman effective medium theory.* Although this topic has been debated extensively, there have been relatively few head-to-head comparisons of the various models. Here, we discuss our data in terms of all three and show that each predicts a similar microscopic carrier mobility, however, fluence-dependent results suggest that the Drude-Smith model is the most likely to apply to our data.

8.5.1 Drude-Smith model

Figure 8.4 shows the fluence dependence of the THz photoconductivity fit with a Drude-Smith model plus a peak-shift term. The conductivity was acquired 2.2 ps after the peak of the differential transmission with 400 nm excitation wavelength and 40 μJ cm^{-2}, 190 μJ cm^{-2}, and 470 μJ cm^{-2}. We see that the model provides excellent agreement with the data at all fluences. It is important to note that by itself the high fit quality is not a confirmation of the Drude-Smith model, however, it is encouraging.

Figure 8.4b-d shows the Drude-Smith fit scattering time, localization parameter, and areal charge density as a function of excitation fluence. We see that the scattering time decreases a small amount with fluence, which is typical for semiconductors at high excitation density [142, 92]. The increased scattering rate can be attributed to the onset of electron-hole scattering or to state filling, which leads to an increase in the phonon scattering rate [140]. The localization parameter is essentially independent

*While some authors consider Maxwell Garnett effective medium theory separately from the plasmon model, the two theories describe the same underlying physics. As a brief historical note on Maxwell Garnett theory, James Clerk Maxwell Garnett was named after his fathers close friend, the much more famous James Clerk Maxwell. As a result, many authors incorrectly assume that the latter contributed to Maxwell Garnett theory and use the hyphenated Maxwell-Garnett. This is, however, incorrect (see ref. [264]).

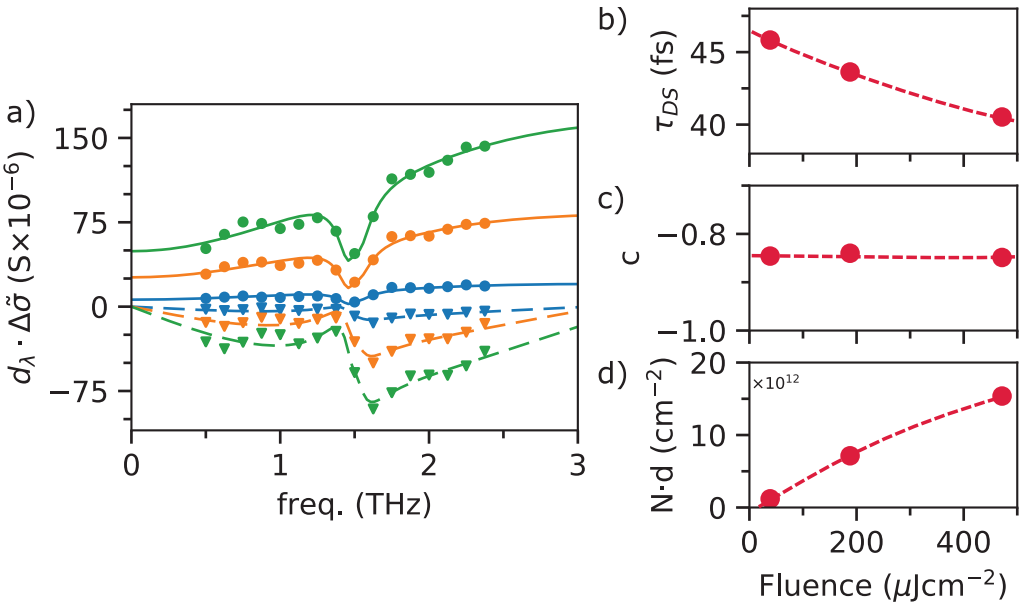

Fig. 8.4: Drude-Smith fluence dependence. a) THz photoconductivity spectrum with 40 μJ cm^{-2} (blue), 190 μJ cm^{-2} (orange), and 470 μJ cm^{-2} (green) photoexcitation fluence. The circles and triangles represent the measured σ_1 and σ_2, respectively, while the solid and dashed lines are the real and imaginary parts of the fits to the Drude-Smith plus Peak-Shift model. The Drude-Smith **b** scattering time, **c** localization parameter, and **d** carrier density extracted from fitting.

of fluence. The areal charge density, on the other hand, appears to show a threshold behavior as the dashed line, drawn as a guide to the eye, crosses the x-axis at a non-zero fluence. As we will see in section 8.7.3, the carrier lifetime in SnIP increases with fluence due to trap-filling dynamics. The threshold-like behavior in the fitted carrier density therefore occurs because we are acquiring the photoconductivity spectrum at 2.2 ps after the peak when, at low fluence, a larger fraction of carriers have already been trapped or recombined.

8.5.2 Plasmon model

As an alternative to the Drude-Smith conductivity, the plasmon model has been used to describe the THz conductivity of nanostructured systems [265, 215, 230, 266]. The plasmon model is characterized by a Drude-Lorentz conductivity,

$$\Delta\tilde{\sigma}(\omega) = \frac{A_D}{1 - i\omega\tau_{Plas}} + \frac{i\omega A_L}{\omega_0^2 - \omega^2 - i\omega/\tau_{Plas}}, \tag{8.5}$$

where A_D, A_L, τ_{Plas}, and ω_0 are the Drude amplitude, Lorentz amplitude, carrier scattering time, and resonant frequency, respectively. The Drude and Lorentz weights are proportional to carrier density contributing to the free carrier and plasmonic responses, respectively. In early studies of nanowires using TRTS, the presence of a free carrier (Drude) response in nanowire systems was attributed to transport along the longitudinal axis, where the resonant frequency is predicted to be quite low, while the plasmonic (Lorentzian) response was attributed from a transverse resonance [215]. More recently it has been suggested that the Drude component instead results from percolation pathways in the thin film [267]. Equation 8.5 is essentially equivalent to the generalized effective-medium theory of reference [267] with a Drude conductivity as the differential conductivity of the nanowire.

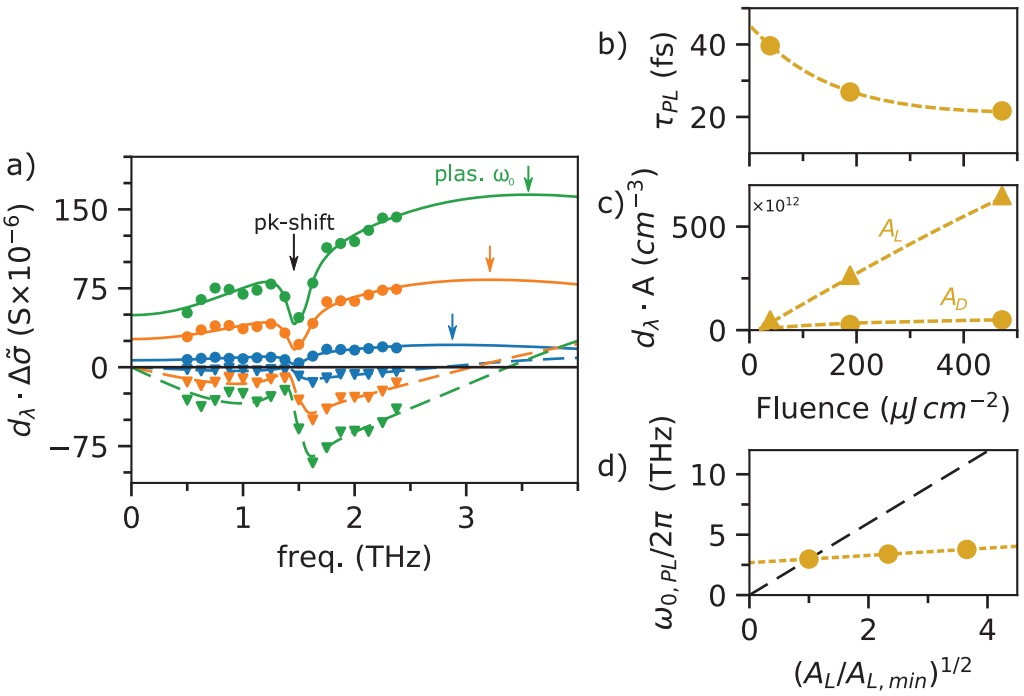

Fig. 8.5: Plasmon-model fluence dependence. a) THz photoconductivity spectrum with 40 μJ cm^{-2} (blue), 190 μJ cm^{-2} (orange), and 470 μJ cm^{-2} (green) photoexcitation fluence. The circles and triangles represent the measured σ_1 and σ_2, respectively, while the solid lines and dashed lines are the real and imaginary parts of the fits to the Drude-Lorentz plus peak-shift model. Fluence dependence of the **b** Drude-Lorentz scattering time, **c** Drude and Lorentz amplitudes (circles and triangles, respectively). **d** Scaling of the resonant frequency with the Lorentz amplitude.

In Figure 8.5a we show fits to the fluence-dependent spectra using the Drude-

Lorentz model. The Drude-Lorentz model also shows excellent agreement with data, similarly to the Drude-Smith model and, as a result, we are not able to rule out either model due to fit quality alone. This is somewhat expected as the two fit functions produce virtually identical spectra when the Drude-Smith localization parameter is close to -1. Shown in Figure 8.5b, c are the carrier scattering time and Drude/Lorentz amplitudes as a function of excitation fluence. We see a reduction in scattering time with fluence that is more dramatic than that of the Drude-Smith model. The Drude and Lorentz amplitudes also show a threshold like effect, which we can again attribute to the trap-filling dynamics. There also appears to be a slight sub-linearity to the scaling with fluence, although in this case it is less dramatic than that of the Drude-smith model.

While we cannot discount the plasmon model from the fit quality alone, we note that an important feature of this model is that the resonant frequency scales with the charge density according to,

$$\omega_0^2 = \frac{g\, N_f e^2}{\epsilon_r \epsilon_0 m^*}, \tag{8.6}$$

where ϵ_r is the dielectric function of the host medium, generally taken to be 1 in the low density limit, N_f is the free carrier density in the nanowire, m^* is the effective mass, and g is a geometric constant [268]. In our work, there is large uncertainty in the absolute density so we cannot directly verify equation 8.6. Instead, we note that the ratio of resonant frequency to square root of density should be a constant, *i.e.*,

$$\frac{\omega_0(N_1)}{\omega_0(N_2)} = \sqrt{\frac{N_1}{N_2}} = \sqrt{\frac{A_{L1}}{A_{L2}}}, \tag{8.7}$$

where ω_0 is that frequency at density N_i. A_i is the amplitude, which is proportional to the density in the Lorentz model.

Plotted in Figure 8.5d is the resonant frequency as a function of $(A_L/A_{L,1})^{1/2}$, where $A_{L,1}$ is the oscillator amplitude extracted from the 40 $\mu J\, cm^{-2}$ spectrum. Based on the analysis of equation 8.7, if the plasmon model applies to this system we expect a linear relationship with close to zero intercept, due to the low intrinsic carrier concentration, and a slope given by $\omega_0(A_{L,min})$. Moreover, while it is possible that background doping of the nanowires could lead to a resonant-frequency scaling similar to what is observed here, this would require a large background conductivity that

is inconsistent with conductance measurements [179] and not observed in our TDS measurements. We therefore conclude that the plasmon model does not apply to our data.*

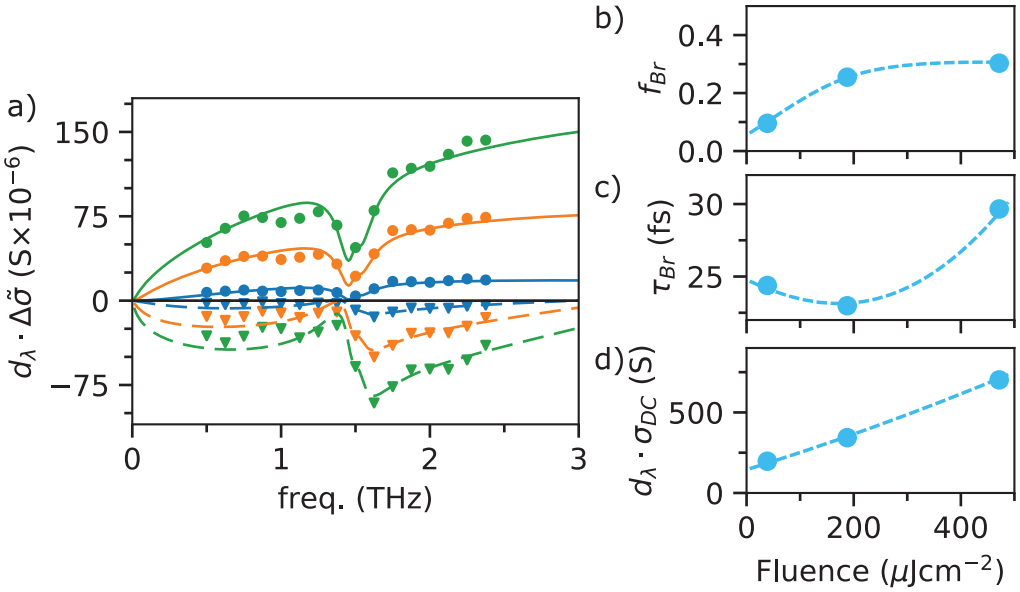

Fig. 8.6: Bruggeman model fluence dependence. a) THz photoconductivity spectrum with 40 μJ cm^{-2} (blue), 190 μJ cm^{-2} (orange), and 470 μJ cm^{-2} (green) photoexcitation fluence. The circles and triangles represent the measured σ_1 and σ_2, respectively, while the solid lines and dashed lines are the real and imaginary parts of the fits using a Drude dielectric function for the inclusions in the Bruggeman effective-medium theory plus a peak-shift term. Fluence dependence of the **b** Bruggeman fill fraction, **c** scattering time, and **d** Drude DC conductivity.

8.5.3 Bruggeman

An alternative effective medium theory that is often used in THz spectroscopy is the Bruggeman model. In Bruggeman theory the effective dielectric function, ϵ_{eff}, is related to the inclusion dielectric function, ϵ_{inc}, by the equation,

$$f\frac{\epsilon_{inc}-\epsilon_{BG}}{\epsilon_{inc}+2\epsilon_{BG}}+(1-f)\frac{1-\epsilon_{BG}}{1+2\epsilon_{BG}}=0, \tag{8.8}$$

where f is the filling fraction of the inclusion [269]. Shown in Figure 8.6 are fits to the fluence-dependent conductivity in our SnIP nanowire film using a Drude dielectric

*We note that the scaling of resonant frequency has been shown to hold to a high degree of accuracy in ref. [230], where the samples consisted of a low density of isolated nanowires. This suggesting that there is clearly a strong physical basis for its application in some conditions. Future experiments exploring the THz conductivity of nanowires or nanocrystals in variable-density films could therefore be quite interesting.

function for ϵ_{inc} in the Bruggeman model. Once again, we also include a peak-shift term to account for the changes to the vibrational mode. Note that the Drude conductivity is given by the first term in the right-hand side of equation 8.5 and we use the relationship between the optical conductivity and dielectric function,

$$\tilde{\epsilon}_r(\omega) = 1 + i\frac{\tilde{\sigma}(\omega)}{\omega\,\epsilon_0}, \tag{8.9}$$

to convert the conductivity to the dielectric function and vice-versa.*.

While the Bruggeman fit quality is reasonable, both the Drude-Lorentz+peak-shift or Drude-Smith+peak-shift fits are of higher quality, especially in the low frequency region of the imaginary conductivity. In addition to the poor fit quality, there are several features of the fitting that do not make sense physically. First, we note that the filling fraction, shown in Figure 8.6b, must be used as a free parameter in order to achieve reasonable fit quality at all fluences simultaneously, which is unphysical. Second, we see that the carrier scattering time, shown in Figure 8.6c, actually increases with fluence between 200 and 400 $\mu\mathrm{J\,cm^{-2}}$, which, although not unphysical, would be unusual. Finally, we see that the the Drude amplitude, shown in Figure 8.6c, does not extrapolate to zero in the low fluence regime. This is unusual as the Drude amplitude is proportional to the density of photoexcited electron-hole pairs, which should go to zero at zero fluence.

8.5.4 Comparison

To summarize, both the Drude-Smith and Drude-Lorentz models yield excellent fits to the data. The Bruggeman fits with a Drude dielectric function for ϵ_{inc} provide reasonable agreement across the spectrum, however, the fit quality in the low frequency regime is inferior to the Drude-Smith and Drude-Lorentz models. Furthermore, to achieve reasonable fit quality with the Bruggeman fits at all fluences, the filling fraction must be used as a free parameter, which is unphysical. The Drude amplitude and scattering time also showed unusual scaling with fluence in the Bruggeman fits, leading us to reject this model. We were also able to rule out the plasmon model due to the incorrect scaling of the plasmon frequency with amplitude (density).

*The Bruggeman equation, equation 8.8, can be solved by recasting it as a quadratic equation for ϵ_{BG}. The correct root (positive or negative) is not always obvious *a priori*, however, it can be chosen as based on the sign of the σ_1, which should be positive.

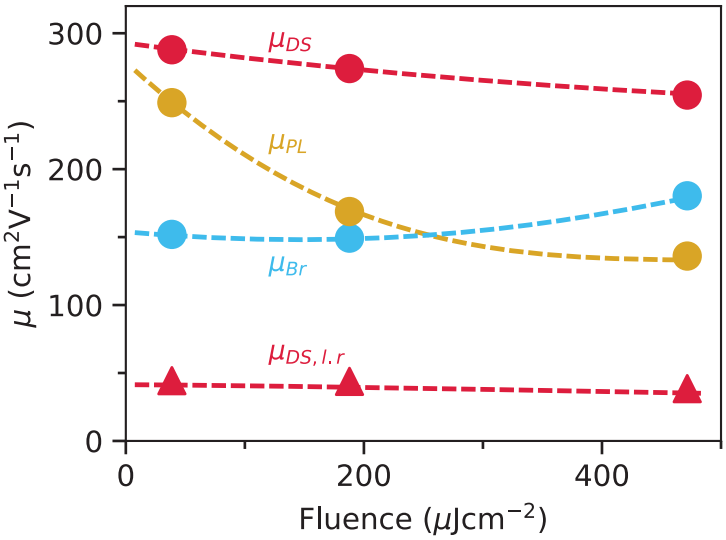

Fig. 8.7: Model-dependent carrier mobility. Comparison of mobilities for Drude-Lorentz and Drude-Smith fits. Orange curve: microscopic Drude-Smith mobility calculated using the scattering time without the $1+c$ factor. Blue: Drude-Lorentz mobility calculated from the scattering rate. Green: Drude-Smith mobility calculated from the scattering time and including the $1+c$ factor.

While in this case the Bruggeman model and plasmon model both have clear evidence to discount them, the inapplicability of these models is not necessarily confirmation that transport in our nanowire thin film is correctly described by the Drude-Smith model. Moreover, there are no analogous features of the data that can be used to rule out the Drude-Smith model. It is therefore useful to compare the mobility extracted from each of these models, as shown in Figure 8.7. The short-range Drude-smith mobility (μ_{DS}), plasmon mobility (μ_{PL}) and Bruggeman mobility (μ_{Br}) are all similar, ranging from 150 cm^{2}V^{-1}s^{-1}. Moreover, at low fluence the plasmon mobility approaches the short-range Drude-Smith mobility, which is encouraging. Interestingly, we also see that the Bruggeman and plasmon mobilities lie between the long-range and short-range Drude-Smith mobilities. This appears to be a common observation as a similar hierarchy was reported in tin oxide nanowires [270] and we have observed similar hierarchy in CdS nanowires (unpublished).

8.5.5 Peak-Shift Parameters

To this point, the peak-shift portion of the fitting with fluence has not been discussed. The differential oscillator parameters are plotted for each model in Figure 8.8a-c. We see that the peak-shift parameters extracted with the Drude-Smith and plasmon functions for the free-carrier response are nearly identical, which is expected as the two models produce nearly identical conductivity spectra. The parameters extracted with the Bruggeman fits, on the other hand, deviate from the other two models. This suggests that we should be cautious about interpreting the peak-shift parameters quantitatively. Nevertheless, the qualitative behavior of the scaling with fluence is similar between all three models. As seen in Figure 8.8a, the reduction in oscillator strength, $\Delta A_{osc.}$, decreases sublinearly with fluence. The change in damping, $\Delta\gamma$, behaves similarly, as seen in Figure 8.8b. Finally, as seen in Figure 8.8c, the change in resonant frequency shows the most deviation between the Bruggeman and Drude-Smith/plasmon fits, where in the latter for 470 μJ cm^{-2} the change in resonant frequency is smaller than at 190 μJ cm^{-2}.

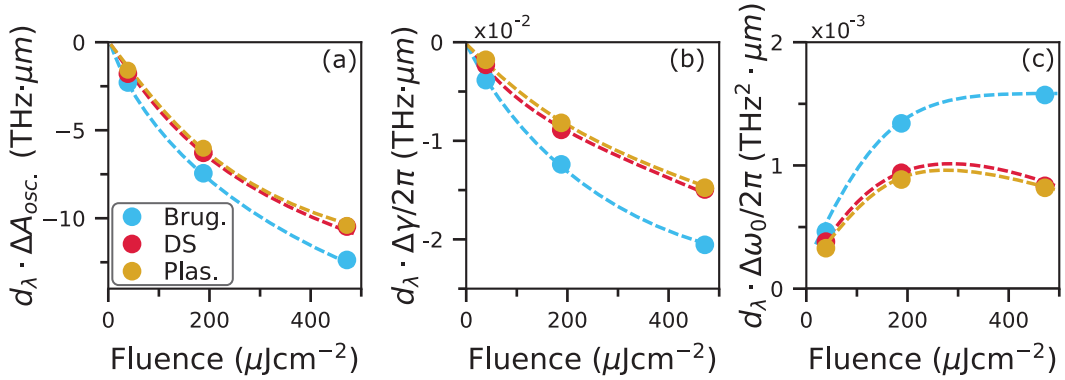

Fig. 8.8: Model-dependent peak-shift parameters. Peak-shift fit parameters using the Bruggeman (blue) Drude-Smith (crimson) and plasmon (gold) models for the free-carrier response. The differential oscillator **a** amplitude, **b** resonant frequency, and **c** damping.

While the fit parameters all show non-linear scaling with respect to the fluence, it is also important to study how they scale with respect to the carrier density extracted from the Drude-Smith fits, which itself scales sub-linearly with fluence. Plotted in Figure 8.9a-c is the differential oscillator amplitude, damping, and resonant frequency. Clearly, $\Delta A_{osc.}$ and $\Delta\gamma$ both scale nonlinearly with respect to the carrier density as

extracted from the Drude-Smith fitting. It is possible that the functional form of this scaling could be be linked to the non-linearity of the Debye screening length with respect to carrier density (see Appendix A.6). However, it will take significant progress from a theoretical perspective to develop a complete understanding of this behavior.

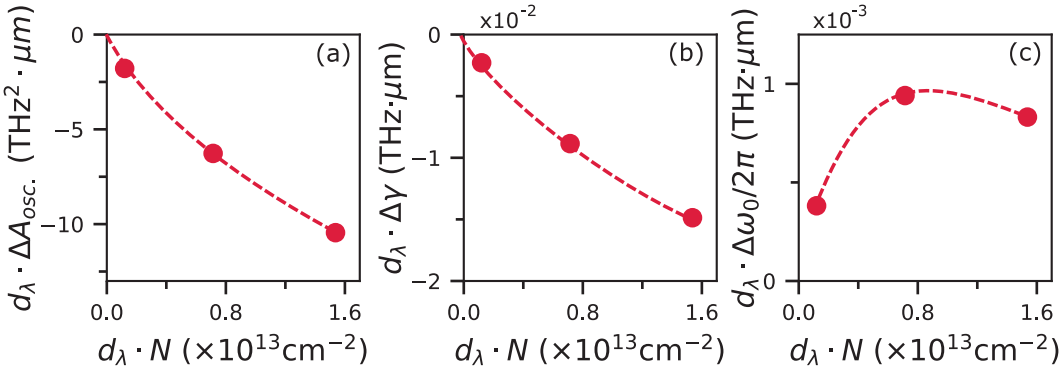

Fig. 8.9: Nonlinear scaling of the oscillator differential lineshape. Peak-shift fit parameters from fits as a function of the extracted Drude-Smith carrier density. The differential oscillator **a** amplitude, **b** resonant frequency, and **c** damping.

8.6 Two-Dimensional Conductivity Dynamics

We can also study the time dependence of the conductivity after photoexcitation using a 2D scan, which allows us to probe the picosecond evolution of the carrier mobility and charge redistribution. In Figure 8.10a,b we study the time evolution of the real and imaginary parts of the complex conductivity, respectively. The behavior of the vibrational mode is most striking in $\Delta\sigma_2$, suggesting some sort of transient behavior in the differential oscillator parameters at early times. It is, however, important to identify and rule out early-time artifacts that arise due to the system response [128, 52]. Our calculations (see Appendix A.7) suggest that for the low amplitude of modulation observed here the extracted conductivity accurately represents the material conductivity for delay times larger than 0.5 ps after the peak of the transient photoconductivity (chosen as $\Delta t_1 = 0\,\mathrm{ps}$), which itself is delayed from the arrival of the excitation pulse by approximately the system response (see the inward-facing ticks on the right axes of Figure 8.10a, b).

Shown in Figure 8.11a-c are the time-dependent Drude-Smith fit parameters ex-

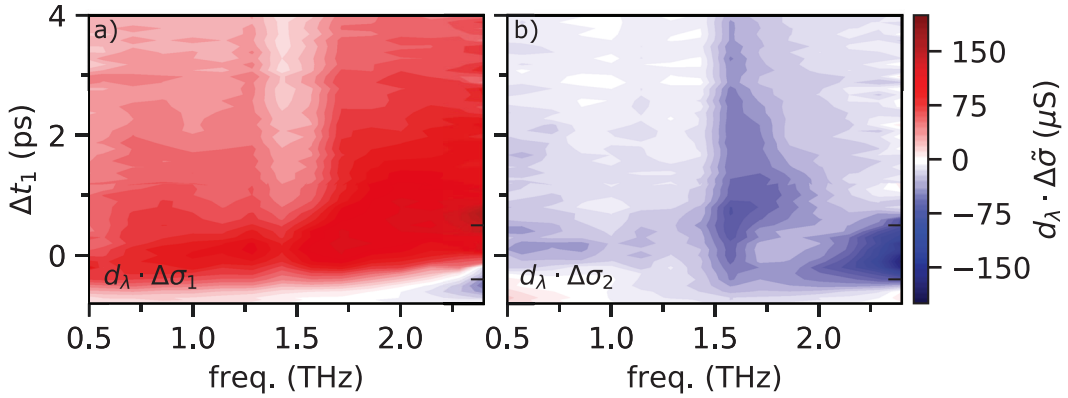

Fig. 8.10: Time-evolution of the photoconductivity. a) Real part and b) imaginary part of the time evolution of the photoconductivity for 400 nm excitation at a fluence of 190 μJ cm^{-2}. The inward facing ticks indicate time delays of -0.4 ps (the system response time) and 0.5 ps (estimated time where transient artifacts no longer affect the signal).

tracted from fitting the 2D conductivity at each time delay. The shaded regions of these shaded regions of these plots indicate the time when transient artifacts can effect the extracted conductivity. We see that the extrapolated DC conductivity, plotted in Figure 8.11a, decays on a similar timescale to the differential transmission (orange curve). In the region greater than 0.5 ps, the scattering time and localization parameter, shown in Figure 8.11b, c are stable, which means the mobility is essentially constant over this range of time delays. In combination with the similarity between the differential transmission this indicates that we can use 1D scans to probe the recombination and trapping of photocarriers, which we will make use of in the next section.

In contrast to the Drude-Smith parameters, the peak-shift fit parameters show more dynamic behavior. The reduction in oscillator amplitude, shown in Figure 8.12a, is largest at 1 ps after the peak of the differential transmission and recovers on a timescale comparable to the relaxation time of the extrapolated DC conductivity. The change in linewidth, shown in Figure 8.12, is also largest at approximately 1 ps, however, it shows a faster recovery than the differential amplitude. The change in resonant frequency in Figure 8.12b, $\Delta\omega_0/2\pi$, shows evidence of oscillatory behavior as a function of time after excitation. We also note the similarity between the 1 ps timescale where the differential parameters are largest and the oscillator lifetime,

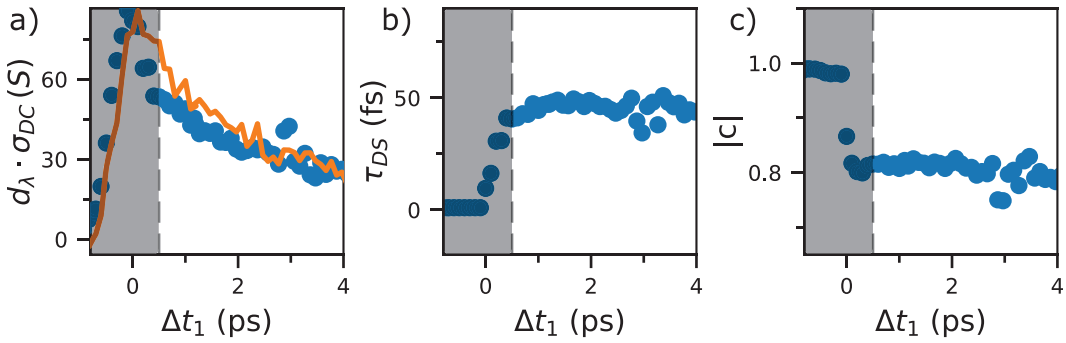

Fig. 8.11: Temporal evolution of the transport parameters. **a** The low frequency limit of the Drude-Smith fit, $\sigma_{DC} \cdot d$ (blue circles) with the time-domain differential transmission, $-\Delta T$, superimposed (orange line). **b** The scattering time τ_{DS}, and **c** localization parameter, c. The shaded areas for time-delays less than 0.5 ps indicate the region where early-time transient artifacts could potentially distort the extracted spectra.

$\gamma_2^{-1} \approx 1\,\text{ps}$. This connection could yield deeper insight into the dynamical process of charge redistribution.

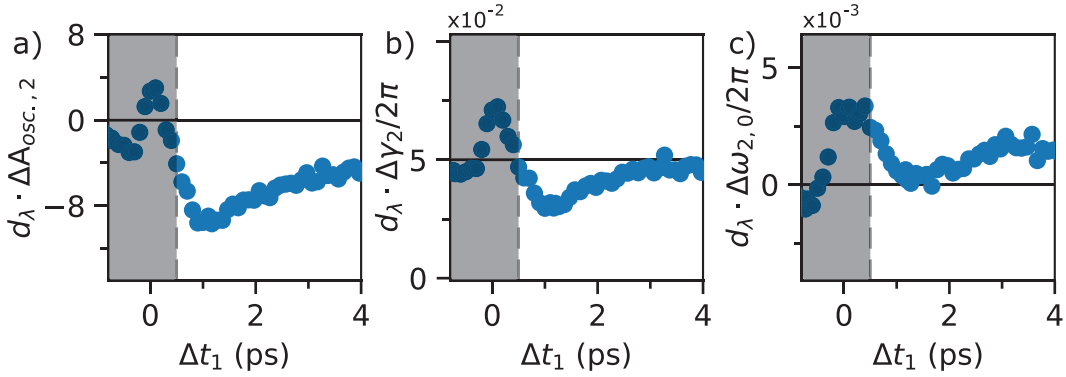

Fig. 8.12: Temporal evolution of the oscillator parameters. The change in **a** resonant frequency, **b** linewidth, and **c** amplitude as a function of time delay as extracted from the peak-shift portion of the fits to the 2D conductivity spectrum. The shaded areas for time-delays less than 0.5 ps indicate the region where early-time transient artifacts could potentially distort the extracted spectra.

With both the Drude-Smith and peak-shift parameters, it is tempting to look at the early time (<0.5 ps) dynamics. In the case of the Drude-Smith parameters, this would point to a slow rise to the carrier scattering time, and therefore mobility, that could in principle be linked to carrier-cooling dynamics. For the peak-shift parameters, this would point to more clearly oscillatory behavior, which would be

quite interesting. Future experiments probing these dynamics should focus on using sampling techniques that reduce transient artifacts, such as broader-bandwidth EO crystals [271, 272] or air-biased coherent detection [273, 274].

8.7 Excitation and Relaxation Channels

8.7.1 800 nm vs 400 nm Excitation

In this section we explore the excitation and relaxation channels in our SnIP nanowire film using 400 nm (3.1 eV) and 800 nm (1.55 eV) pump wavelengths, which are above and below the 1.86 eV band gap of SnIP, respectively (see section 7.3.2 and ref. [179]). In Figure 8.13a, b we plot the pump-induced differential THz transmission, $-\Delta T/T_0$, with 400 nm and 800 nm pump wavelengths and 190 μJ cm^{-2} and 850 μJ cm^{-2} excitation fluences, respectively. These fluences were chosen to yield approximately equal amplitude differential signals. To parameterize the relaxation, we fit the decay curves with a bi-exponential function. We find a slower initial decay for 400 nm than 800 nm excitation, with τ_f=2.6 ps and 1.4 ps, respectively. On the other hand, the long-lived component is shorter for 400 nm than 800 nm, with τ_s=20 ps and 35 ps, respectively.

The observation of photoconductivity with sub-gap excitation is interesting on its own, as it implies free carriers must be generated either by two-photon or band/defect-tail absorption [13]. The linearity of 800 nm transmission (see Appendix A.2) is inconsistent with two-photon absorption while the photon energy of 1.55 eV is too far below the 1.86 eV band gap for band-tail absorption, suggesting transitions from deep-level states are the dominant excitation channel, which is consistent with our observations with PDS (see section 7.3.2) [195]. The large amplitude of the signal, with similar photoconductivity at only 4.5 times the fluence (9 times the photon flux), is then somewhat surprising. This can be attributed in part to the increased thickness of the photoexcited layer due to the smaller absorption coefficient and partly to a high density of mid-gap states. It is also possible that weak light-trapping effects due to the nanowire-film morphology increase the effective interaction length of the 800 nm pulse [275].

The corresponding complex photoconductivity spectra for 400 nm and 800 nm ex-

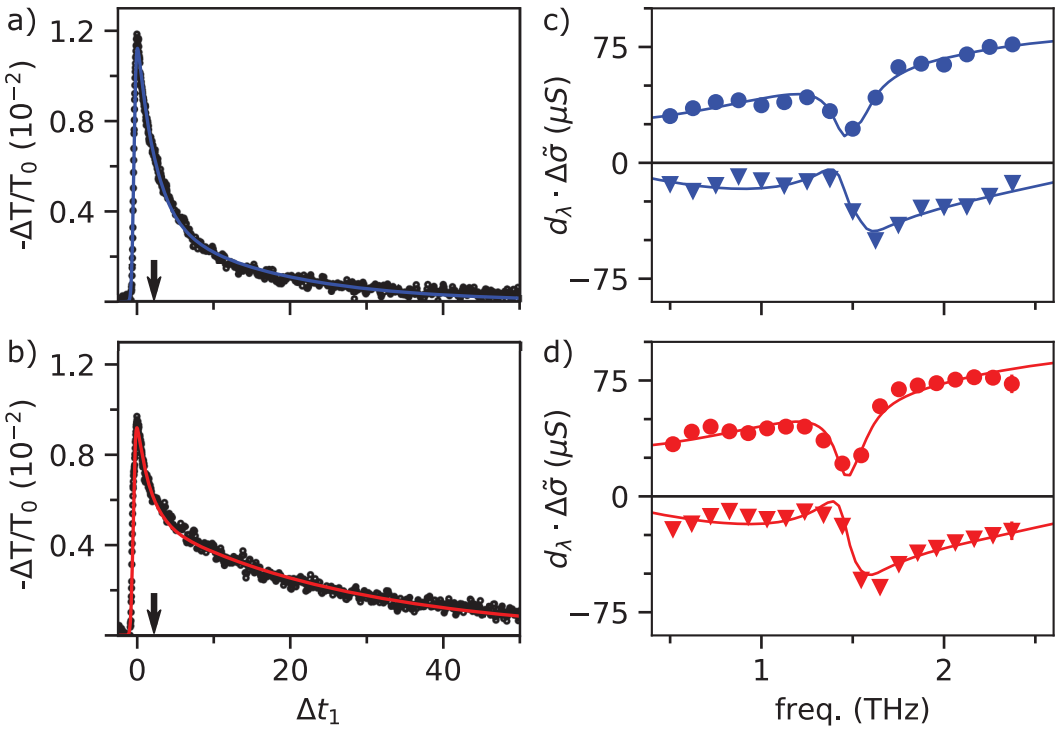

Fig. 8.13: Effect of excitation channels on photoconductivity. Differential THz transmission with **a** 400 nm excitation and **b** 800 nm excitation. The solid lines are fits with a bi-exponential function convoluted with a Gaussian response. The scans were performed with the THz/EO gate delay fixed to the maximum field. The black arrows indicate the time-delay chosen for measurement of the photoconductivity spectrum. THz photoconductivity spectrum with **c** 400 nm and **d** 800 nm excitation. The 400 nm (800 nm) fluence was 190 μJ cm^{-2} (850 μJ cm^{-2}).

citation, acquired 2.2 ps after the peak of the transient photoconductivity (indicated by the black arrows in Figure 8.13a,b)), are plotted in Figure 8.13c, d. The spectra are quite similar for 400 and 800 nm despite the difference in excitation channels. The solid lines in Figure 8.13c show a simultaneous fit to the real and imaginary conductivity using the Drude-Smith plus peak-shift model, with fit parameters summarized in Table 8.2. We see that the fit parameters are quantitatively very similar between the two, suggesting that the excitations formed through these different pathways are quite similar.

This leads us to propose the following picture of the excitation and initial relaxation pathways in SnIP, shown schematically in Figure 8.14a. Here, the 400 nm pump produces electron-hole pairs with large excess energy, exciting into high-lying

Table 8.2: Fit parameters obtained from the model described in the text for the differential conductivity, where N is the volume charge density, and τ_{DS} and c are the Drude-Smith scattering time and localization parameter, respectively. $\Delta\omega_{0,2}$, $\Delta\gamma_2$, and ΔA_2 are the photoexcitation-induced changes in oscillator resonant frequency, damping, and amplitude, respectively. d_λ is the photoexcited film thickness, so that $d_\lambda \cdot N$ is the areal charge density.

λ_{pump} (nm)	$d_\lambda \cdot N$ (cm^{-2})	τ_{DS} (fs)	c	$d_\lambda \cdot \Delta A_{osc,2}$ ($THz^2 \cdot \mu m$)	$d_\lambda \cdot \Delta\omega_{0,2}/2\pi$ ($THz \cdot \mu m$)	$d_\lambda \cdot \Delta\gamma_2/2\pi$ ($THz \cdot \mu m$)
400	3.5×10^{12}	45	-0.84	-6.7	0.9×10^{-3}	-9.1×10^{-3}
800	3.8×10^{12}	42	-0.84	-6.4	1.6×10^{-3}	-6.2×10^{-3}

conduction bands (blue vertical line). The excess energy must be dissipated before carrier trapping. Alternatively, the 800 nm excitation pulse excites carriers to/from mid-gap states into the band-like states similar to the 400 nm excitation. However, carriers are generated with less excess on average so that trapping can occur more rapidly, leading to the more rapid initial decay with 800 nm versus 400 nm excitation.

A complementary picture in real space, shown in Figure 8.14b, c, can help us understand the longer lived portion of the ΔT curves with 800 nm excitation. Here, because of the high absorption coefficient with 400 nm excitation, carriers are generated closer to the nanowire surface, as shown in 8.14b, so that the time for diffusion to the surface is short. Alternatively, with the low absorption coefficient of the 800 nm pulse, carriers are more uniformly distributed through the nanowire, seen in Figure 8.14c, so that diffusion to the surface is slower.*

8.7.2 Diffusive Timescale and Surface Recombination

In this section, we consider the timescales associated with carrier diffusion to help understand origin of carrier localization observed in THz spectroscopy and the carrier lifetime in the high fluence condition where bulk traps are saturated. The timescale for carriers to diffuse a distance x, for 1D diffusion, is given by $t = x^2/D$. The

*This first-order description of relaxation likely does not fully capture the dynamics. Due to the highly-anisotropic electronic structure (see section 7.4), the large excess energy of electrons likely also facilitates diffusion, which would be interesting to explore in detail with future studies.

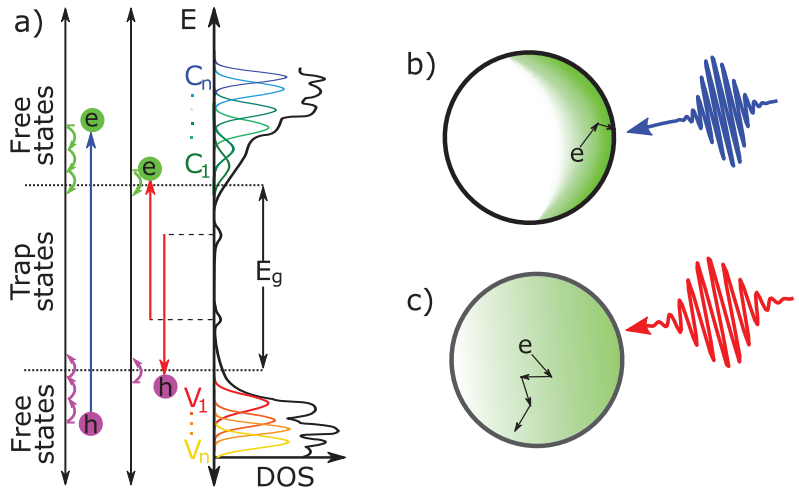

Fig. 8.14: Excitation and relaxation channels in SnIP nanowires. a Right: Schematic illustration of the density of states (DOS) (black curve) with contributing conduction (green/blue) and valence (red/orange) bands. The DOS below/above the conduction/valence bands can consist of traps due to band-tail states (exponentially decaying DOS near the band edge) and deep-level defects (mid-gap peaks in the DOS). Left: Illustration of the excitation pathways for 400 nm (blue) and 800 nm (red) pump wavelengths. The 400 nm pump produces electron-hole pairs with significant excess energy while the 800 nm pump, which has sub-gap photon energy, excites either holes or electrons out of mid-gap trap states. Cross-sectional view of the nanowire with **b** 400 nm excitation and **c** 800 nm excitation. The shaded green regions indicates the presence of photoexcited carriers and the arrows illustrate the path of the electron undergoing diffusive motion.

diffusion constant is given by,

$$D = \mu_{diff} k_B T / e, \tag{8.10}$$

where k_B is the Boltzmann constant. We find $D = 0.64\,\mathrm{cm^2\,s^{-1}}$ if we consider $\mu_{diff} = \mu_{l-r} = e\tau_{DS}(1+c)/m^*_{z'}$ for transport in the $\hat{z}'$-direction (approximately transverse to the double-helix/nanowire axis) and a temperature of 300 K. For nanowires on the small-diameter (80 nm) and large-diameter (300 nm) sides of the distribution, the timescale to drift one nanowire radius is 25 ps and 350 ps, respectively.

This implies, for the distribution of nanowires on average, a timescale of decay significantly longer than the photoconductive decays seen in Figure 8.13. If we instead consider $\mu_{diff} = \mu = e\tau_{DS}/m^*_{z'}$, we find $D = 4.3\,\mathrm{cm^2\,s^{-1}}$ and the diffusive timescale is reduced to 3.7 ps and 52 ps for 80 nm and 300 nm diameter nanowires, respectively,

which is closer to the experimentally observed timescales. We note that this is a simplified description of 2D diffusion in a cylindrical geometry, which would be a more precise description of the experiment (see supporting information in ref. [276]). Nevertheless, the discussion using the 1D approximation provides semi-quantitative validation of the relevant timescales and supports diffusion to the surface as the likely factor limiting recombination.

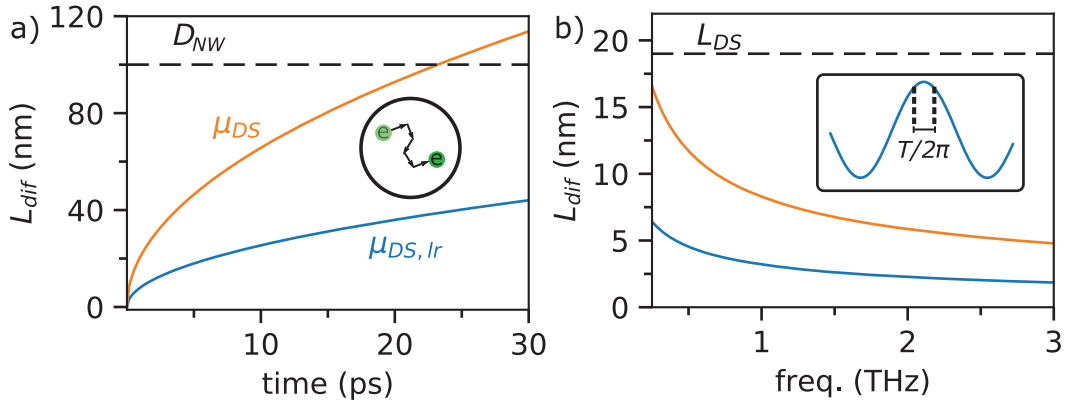

Fig. 8.15: Diffusive timescales and localization length. Diffusion length as a function of time for a carrier in SnIP using both the short range (orange) and long-range (blue) mobilities. The inset illustrates the principle of random motion due to scattering. **b** Length scale probed as a function of THz frequency assuming the short-range (orange) and long-range (blue) mobilities. The dashed black line indicates the localization length from the modified Drude-Smith model while the inset indicates the fraction of a cycle used for the calculation of the diffusion length as a function of frequency.

We can use similar length scale arguments to speculate on the origin of the large c parameter from the Drude-Smith fits. A commonly used estimate for the length scale probed by an AC field of frequency f is given by $x = \sqrt{D/(2\pi f)}$, which can be thought of as the diffusion length on a timescale of approximately $1/6^{th}$ of a cycle. Shown in Figure 8.15 is the length scale probed as a function of frequency using this estimate. Cocker *et al.*, found an analytic relationship between the length-scale of localization and the Drude-Smith scattering time using the modified Drude-Smith model (see section 5.6.3), where the conductivity is given by [144],

$$\sigma_{DS-mod} = \frac{Ne^2\tau_{DS}/m}{1 - i\omega\tau_{DS}}\left(1 + \frac{c}{1 - i\omega\tau_{diff}}\right), \tag{8.11}$$

where τ_{diff} is the characteristic timescale of a diffusive restoring force that gives rise

to the suppression of low frequency conductivity and the other parameters are defined similarly to the usual Drude-Smith model. Fitting our data to the modified Drude-Smith model, we find $\tau_{diff} \approx \tau_{DS}$, *i.e.*, the modified Drude-Smith model reduces to the usual Drude-Smith model (see section 5.6.3). For this special case, the length scale of localization is given by (see section V in ref. [144]),

$$L_{DS} = \frac{9\tau_{DS}}{2}\sqrt{\frac{k_B T}{m^*}}. \tag{8.12}$$

We find a value of $L_{DS} = 19\,\text{nm}$. For reference, a horizontal dashed line is plotted at L_{DS} in Figure 8.15, where we see that the length scale estimate from the relation $x = \sqrt{D/(2\pi f)}$ approaches the value of L_{DS} at low frequencies. This implies that our measurement is sensitive to transport on a comparable length scale to that of the carrier localization.

The approximately 20 nm length scale suggested by the modified Drude-Smith model is smaller than the most common nanowire size of 110 nm. It is possible that this length scale estimate, which assumes a rectangular box, does not hold for the cylindrical geometry. However, it seems unlikely that this explanation could account for such a large difference between estimated and observed length scale. Another explanation is the presence of morphological features on length scales smaller than those observable by helium-ion microscopy [241]. As our measurements indicate that our nanowire systems are crystalline and are not amorphous (see sections 7.3.3 and 7.3.4), it is likely that localization arises from, *e.g.*, grain boundaries such that transport should be well described by the Drude-Smith model [245, 144].

Another possibility is that spectral signatures of carrier localization are an intrinsic feature of transport in SnIP, as in potentially the case in highly-polar solids such as rubrene [277, 192]. Generally, theories that predict these spectral signatures require large electron-phonon coupling [278, 279], while in SnIP we estimate a Fröhlich constant of $\alpha = 0.7$ (see section 7.5.4), which is likely too small for such theories to apply. We therefore consider the presence of microscopic morphology to be the likely origin of the broad features in the conductivity spectra.

8.7.3 Trapping Dynamics

As indicated previously, because the differential transmission and extrapolated DC conductivity have similar time dependence and the mobility is essentially constant in time (see Figure 8.11), we can monitor the recombination and trapping of free carriers with 1D scans. Figure 8.16a and b show the fluence-dependent normalized differential transmission with 400 nm and 800 nm excitation, respectively, revealing an increasing lifetime with fluence in both cases.* This response is characteristic of trap-filling dynamics [280, 228]. Even at the highest fluence, the lifetime is still quite short, which implies that the surface states are non-saturable. We therefore propose that at low fluence ultrafast trapping in the bulk dominates relaxation, while at high fluence bulk traps are saturated and the lifetime is limited by surface recombination velocity.

We can also study how the peak photoconductivity changes as a function of pump fluence, as seen in Figure 8.17a, b for 400 nm and 800 nm excitation, respectively. Here we see dramatically different behavior for 800 nm versus 400 nm excitation: the peak differential transmission increases sublinearly with 400 nm and superlinearly with 800 nm excitation. First, we discuss the behavior of the 400 nm curve, which is fit with a phenomenological saturation model. We can rule out the introduction of new recombination channels as the lifetime does not decrease at high fluence [281]. We can also rule out optical nonlinearities as the ultrafast diffuse reflectance scales linearly (see Appendix A.2). While there is a slight reduction of mobility at high fluence, it is not enough to account for the sub-linearly scaling in Figure 8.17a. Instead, we note that at high fluences the carrier density is greater than 10^{18}cm^{-3} (see section 8.5.1), which is high enough that the quasi-Fermi level is pushed into the conduction band where the dispersion is highly non-parabolic. The electronic dispersion in these higher lying states becomes essentially flat in the y-direction and the system becomes effectively 2D in a large range of the Brillouin zone (see section 7.4.4. The sub-linearity at high fluence could therefore result from a combination of non-parabolicity in the $\hat{x}'$ and $\hat{z}'$ directions and a partial freeze out of transport in the $\hat{y}$-direction.

*The curves are also fit with bi-exponential functions, which provide reasonable agreement over the full range of fluences. The fluence dependent fit parameters are shown in Appendix A.3.

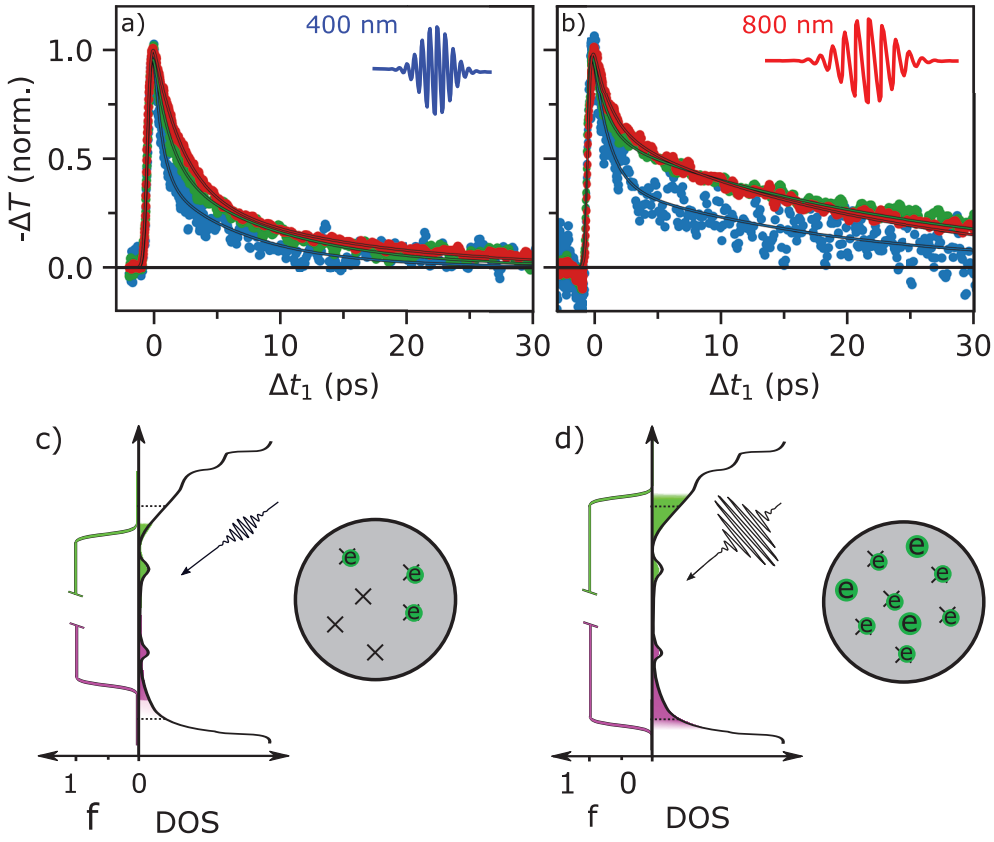

Fig. 8.16: Effect of trap-filling on relaxation dynamics. **a** Normalized differential THz transmission as a function of pump-probe time-delay for 20, 100, and 450 μJ cm^{-2} excitation fluences (blue, green, and red circles, respectively) at a pump wavelength of 400 nm. **b** Normalized differential THz transmission as a function of time-delay for 170, 570, and 860 μJ cm^{-2} excitation fluences (blue, green, and red circles, respectively) at a pump wavelength of 800 nm. **c** Illustration of the quasi-thermal occupancies of electrons (green) and holes (purple) in the low-fluence and case. At low fluence, the quasi-Fermi level is below the mobility edge and all carriers are rapidly captured. This is also illustrated in real space, where the X's indicate bulk traps with a higher density than the excited carriers. **d** Similar illustration as **c**, however, at high fluence where the quasi-Fermi level is above the mobility edge. In this case, all of the traps are full so that some carriers remain in mobile states longer.

In the case of the 800 nm excitation in Figure 8.17b, we can also rule out optical nonlinearities such as two-photon absorption (see Appendix A.2). We instead attribute the super-linear behavior at low fluence to trapping on timescales faster than the system response time [281], which is approximately 0.4 ps. To fit the curve in Figure 8.17b, a rate equation model with a saturable trap state is used in combination with a Gaussian system response function. The model is described in Appendix A.4.4. Interestingly, saturation fluence can be found by linearly extrapolating the high-fluence data back to the x-intercept (dashed line in Figure 8.17b). We find a saturation fluence of 150 μJ cm^{-2} (photon flux of 6×10^{14}cm^{-2}), with which we can estimate the bulk trap density to be 6×10^{18}cm^{-3} by assuming a penetration depth of 1 μm (similar to the film thickness).* Such a high trap density is also a likely source of scattering centers, which suggests that eliminating bulk defects by chemical passivation, optimized synthesis, or annealing would result in a significant enhancement in the carrier mobility.

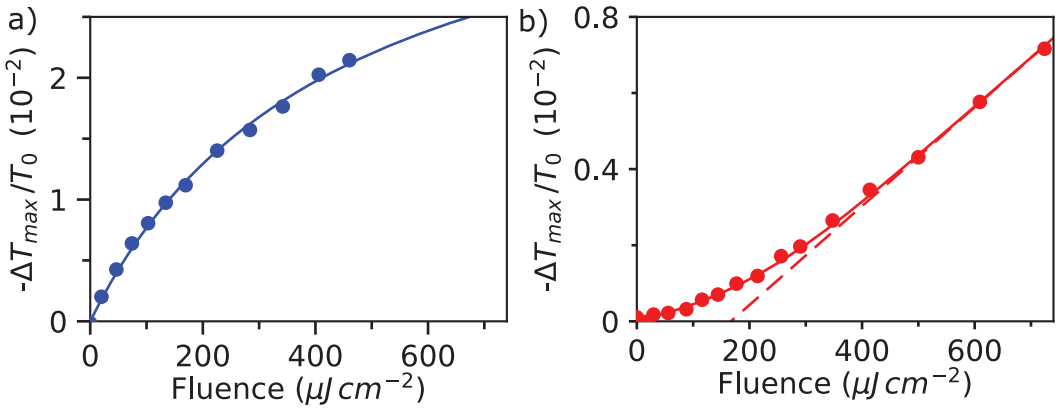

Fig. 8.17: Fluence dependence of the differential THz transmission. Peak differential THz transmission as a function of excitation fluence for **a** 400 nm excitation and **b** 800 nm excitation. The blue solid line in **a** is a fit to the data using a phenomenological saturation model. The red solid line in **b** 800 nm data is fit with a rate equation model with a saturable trap state while the dashed red line is a linear fit extrapolated from the 3 highest fluence data points.

*Furthermore, an estimate based on the fluence-dependent lifetime with 400 nm excitation yields a similar trap density.

8.8 Temperature Dependent TRTS

The normalized relaxation dynamics as a function of temperature is shown for high fluence and low fluence in Figure 8.18a, b, respectively. In general, the lifetime tends to decrease with decreasing temperature for both the high fluence and low fluence case. The largest change occurs between 295 and 230 K. Along with the decreasing lifetime, there is in general a small increase in the peak differential signal for a fixed excitation fluence as the temperature is reduced, as seen in Figure 8.18c. As the differential signal is proportional to conductivity, this points to an increasing conductivity as the temperature is lowered, which is consistent with band-like transport [218, 282] and inconsistent with hopping mechanisms [283, 284]. The fast and slow lifetimes from the bi-exponential fits are shown in Figure 8.18d.

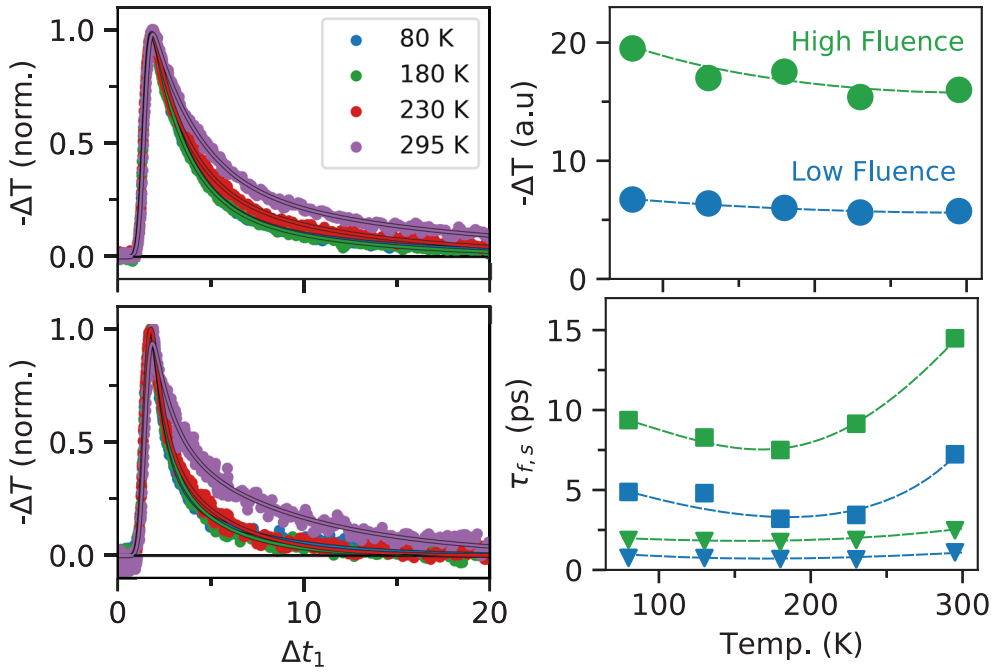

Fig. 8.18: Low-temperature relaxation dynamics. Temperature dependent relaxation dynamics with 400 nm photoexcitation for a) high fluence ($\sim$440 μJ cm^{-2}) and b) low fluence ($\sim$95 μJ cm^{-2}) at 4 temperatures varying from 295 K to 80 K. c) Amplitude of differential signal, $-\Delta T_{pk}$, in the low (blue) and high (green) fluence cases. The dashed line is drawn as a guide to the eye. d) Variation of the fast (circles) and slow (squares) lifetime for the low fluence (blue) and high fluence (green) cases. Again the dashed lines are drawn as a guide to the eye.

We suggest there are two different contributions to this behavior. For traps with

energies comparable to the thermal energy, increasing temperature could lower the trap occupancy due to increased thermal ionization, which would lower the rate of recombination. Alternatively, it is possible that an increased mobility with low temperature could lead to more rapid diffusion to the surface, which would result in a faster lifetime. Shown in Figure 8.19a is the mobility spectrum, defined as $\mu(\omega) = \sigma(\omega) \cdot d/N \cdot d_\lambda$, at 80 K and 295 K. The 80 K spectra shows the same features as at room temperature, namely, the negative imaginary conductivity, increasing real conductivity with frequency, and suppression of the 1.5 THz vibrational mode. The Drude-Smith mobility/scattering time and localization parameter are plotted in Figure 8.19b, c, respectively. The scattering time increases with decreasing temperature with the most dramatic difference between room temperature and 230 K. This initially seems to support the conclusion that increased mobility is the mechanism underlying the reduction in lifetime at low temperature, however, the diffusion constant is also inversely proportional to temperature. The increase in scattering time, with $\tau_{DS,80K} \approx 1.3\tau_{DS,295K}$, is small compared to the reduction 3.7 times reduction in temperature, which points to the ionization of traps as the dominant mechanism for increased lifetime at room temperature relative to low temperature.

The width of the feature at 1.5 THz also appears narrower at low temperature, which could suggest a slight reduction in line width. Shown in Figure 8.20 is the change in linewidth, $\Delta\gamma_2$, extracted from the Peak-shift fit as a function of temperature, which generally shows a more negative $\Delta\gamma_2$ at lower temperature. However, it appears that the fit quality is not as high at low temperature. We suspect that this is due in part to the changing oscillator parameters; the peak-shift model using the room-temperature parameters will no longer be able to accurately reproduce the differential lineshape if the unexcited lineshape changes with temperature. This could account for the qualitatively different behavior of $\Delta\gamma_2$ between 80 K and 130K. Future temperature-dependent studies will therefore need to perform both TRTS and TDS to obtain a more detailed picture of the dynamics.

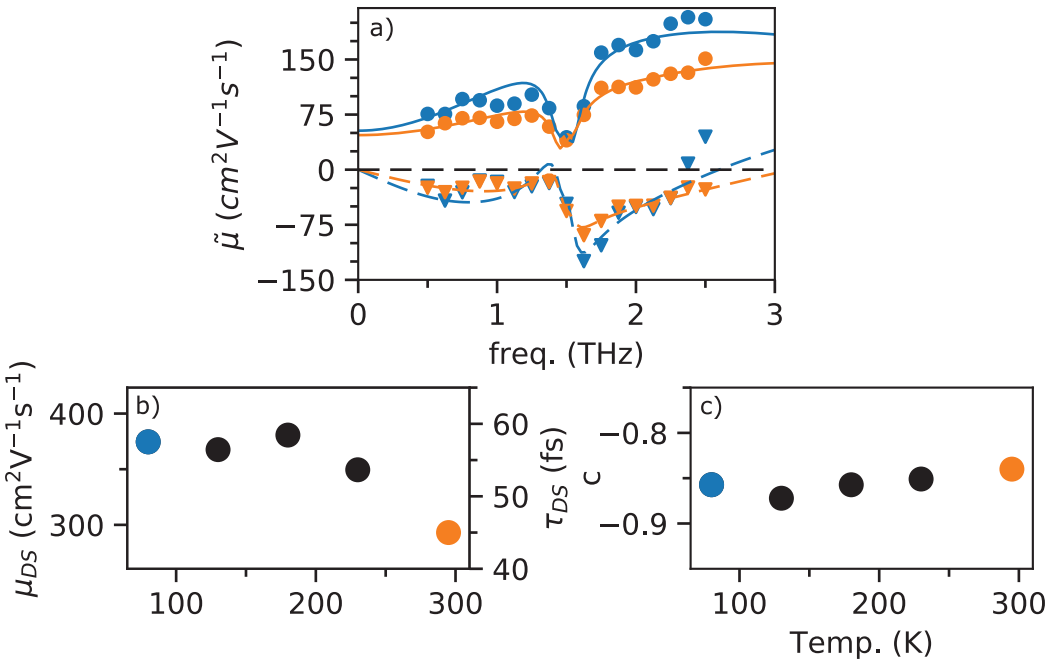

Fig. 8.19: Mobility enhancement at low temperature. **a** THz photoconductivity at room temperature (orange) and low temperature (blue) fit with a Drude-Smith model plus a peak-shift term. **b** Temperature dependence of the short-range mobility (left axis) and Drude-Smith scattering time (right axis). **c** Temperature dependence of the c parameter.

8.9 Prospects in Flexible Electronics

Shown seen in Figure 8.21a where we plot the carrier mobility versus bulk modulus for a wide variety of semiconductor materials.* The combination of high mobility and low bulk modulus seen in SnIP is quite rare and rivaled only by several soft, high-mobility, perovskites. However, these materials are brittle with a low fracture energy and therefore do not share the extreme elastic flexibility demonstrated by SnIP.

The high-mobility single-crystal organic semiconductors have a comparable or even lower bulk modulus than SnIP, however, these materials have a significantly lower mobility. They are extremely brittle with a low fracture energy and as a result do not share the extreme elastic flexibility demonstrated by SnIP. The high-mobility

*We chose 60 GPa as an upper limit o the bulk modulus to include several III-V and II-VI semiconductors that are relatively soft compared to their counterparts. The 60 GPa limit excludes several technologically-relevant high-mobility semiconductors such as GaAs and Si, which are more than 5 times harder than SnIP. We have also chosen to include only high mobility organic semiconductors, resulting in the omission of many that are significantly softer than SnIP.

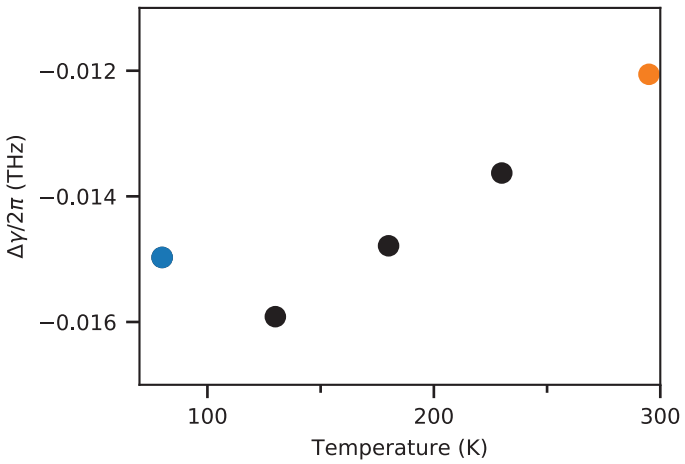

Fig. 8.20: Temperature dependence of $\Delta\gamma_2$. $\Delta\gamma_2$ extracted from the temperature dependent photoconductivity measurement.

elastomer i-TPU and the polymer PEDOT:PSS show similar flexibility to SnIP, however, the carrier mobilities in these materials are still less than $20\,\mathrm{cm^2\,V^{-1}s^{-1}}$, *i.e.*, more than 10 times lower than that of SnIP. One interesting material that is both flexible and has reasonably high mobility is α-AgS_2, which was recently reported as the first room-temperature ductile semiconductor [285]. We note, however, that it is significantly harder than SnIP and has mobility 2 times lower. Similarly, the transition metal dichalcogenides, which are quite flexible in their 2D form, all have a bulk modulus several times larger than SnIP.

The most comparable material to SnIP in this survey is tellurium, which, interestingly, is also (single) helical at the atomic scale. It has a high field effect mobility and, moreover, nanoscale tellurium chains are quite flexible. Recent work has led to a great deal of excitement towards applications in nanoelectronics [185]. Nevertheless, Te is a rare element in the earth's crust and is mildly toxic, in contrast to SnIP which is composed of non-toxic and abundant elements. Furthermore, the bulk modulus in Te is nearly double that of SnIP. In Figure 8.21b we qualitatively illustrate the unique combination of flexibility, softness, and high carrier mobility in SnIP. Furthermore, as discussed in section 7.1, there is reason to believe that SnIP could be just the first of many materials that share the nested double-helix structure. It is interesting to speculate that this new class of materials could share the unique combination of

mechanical and electronic properties of SnIP.

Several notable materials have been left off this survey due to their low-dimensional structure, namely, carbon nanotubes and graphene. Graphene has a high THz mobility (several hundred to several thousand $cm^2\,V^{-1}\,s^{-1}$ depending on the substrate [286]), however, as a semimetal, graphene-based transistors often show a low on/off ratio. On the other hand, semiconducting graphene nanoribbons show much lower field-effect mobilities on the order of 500 to 1000 $cm^2\,V^{-1}\,s^{-1}$ [287] and THz mobilities on the order of just 30 $cm^2\,V^{-1}\,s^{-1}$ [240]. On the other hand, carbon nanotubes, which can be either semiconducting or metallic depending on their structure and are quite flexible, also show THz mobilities on the order of several hundred $cm^2\,V^{-1}\,s^{-1}$ [288, 240], which is comparable to that of SnIP. We therefore suggest that SnIP has a favorable combination of mechanical and electronic properties that make it an attractive new material for applications in flexible electronics.

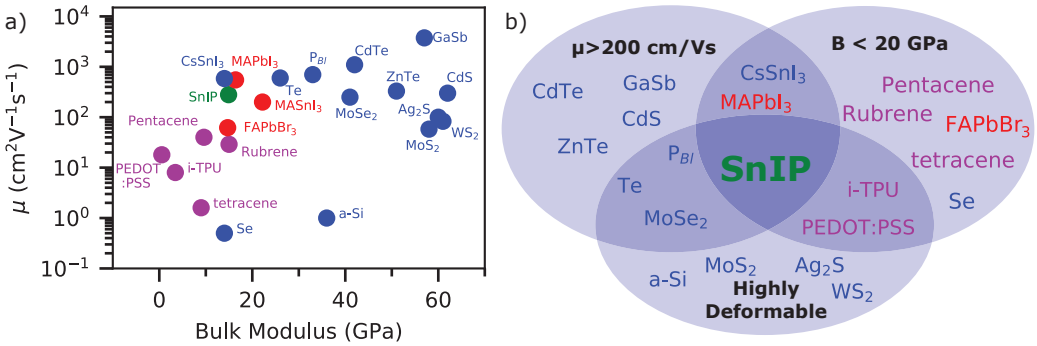

Fig. 8.21: SnIP in comparison to other soft/high-mobility materials. a) Carrier mobilities of several common organic, inorganic, and hybrid organic-inorganic semiconductors with bulk modulus, B, less than 60 GPa. Blue: inorganic, purple: organic, red: hybrid organic/inorganic, green: SnIP (also inorganic). b) Illustration of the unique combination of softness, high carrier mobility, and flexibility demonstrated by SnIP, in which individual needles can be bent beyond 90˙ reversibly. Data for these plots were obtained from the references provided in Appendix A.8.

8.10 Summary

In summary, we have performed the first ultrafast spectroscopy and made the first measurement of carrier mobility of SnIP, a fundamentally exciting new inorganic double-helix material with extreme flexibility and quasi-1D nature. THz spectroscopy, supplemented by quantum-chemical calculations that reveal a highly anisotropic elec-

tronic structure, indicates that SnIP has a carrier mobility as high as $280\,\mathrm{cm}^2\,\mathrm{V}^{-1}\mathrm{s}^{-1}$, which is remarkably high for a material as soft and flexible as SnIP. We also made the first observation of IR-active vibrational modes in SnIP and saw a photoexcitation-induced modification of a strong vibrational resonance indicating a redistribution of charge that occurs on a timescale comparable to the lifetime of the resonance. We also identified the dominant excitation and relaxation channels and suggested that reducing the bulk trap density could yield a considerable enhancement in carrier mobility and lifetime in SnIP. Our results yield valuable insight into the ultrafast photophysics in SnIP that will impact future exploration of SnIP as a photocatalytic material. Finally, we provide the first experimental evidence of high carrier mobility in SnIP, suggesting that it could be an excellent new material for flexible electronics.

Chapter 9

Conclusion and Future Directions

This thesis has focused on the ultrafast terahertz (THz) science and technology with applications to several problems in materials science. It has contributed to the fundamental understanding of tilted-pulse fronts and intense THz pulse sources, applications of intense THz pulses to control hot-carriers in semiconductors, and the study of photophysics in the new material SnIP. The important conclusions and future directions resulting from this work are detailed in the following.

9.1 Tilted-pulse front THz generation

Chapter 3 explored the concepts of pulse-front tilt and angular dispersion (AD) and explored their correspondence in detail. While this relationship is well understood to first-order in the literature, the importance of high-order AD for determining the full spatiotemporal dynamics of tilted-pulse fronts has not yet been appreciated. More explicitly, it was shown that to fully capture the propagation to order $[\phi(\lambda) - \phi(\lambda_0)]^n$ in the phase, the AD must be included to order $d^n\theta(\lambda)d\lambda^n$. From this detailed consideration, we proposed a simple new technique for control of higher order AD using a prism-grating pair that could find application in several areas of ultrafast science [73, 72, 74, 75, 76].

To study TPF-THz generation, a rigorous mapping of the 2D problem to 1D was performed, which revealed a correction term to the GVD-AD not taken into account in some studies. This mapping facilitated the study of TPF-THz generation in lithium niobate, for which calculations showed good agreement with experiment.

Furthermore, a novel TPF THz source was proposed based on a contact grating in GaN. Calculations suggest this device could provide an excellent source of intense THz generation in the 5-12 THz window that represents one of the current frontiers of nonlinear THz dynamics due to a lack of suitable tabletop emitters in this region [21].

Finally, we detailed the development of TPF sources in the Ultrafast Nanotools lab. We also discussed several aspects of these sources, including the use of Kapton tape as an AR coating, the effect of water absorption on the peak electric field, and the potential for studies of quasi-narrowband nonlinear dynamics using these sources. Most importantly, the peak fields obtained with the most recent source were as high as 640 kV/cm, which is quite competitive with the most powerful TPF sources reported in the literature. Nevertheless, there remains significant room for improvement in the repeatability of this source; it was not possible to achieve such high fields on a daily basis, which caused significant problems for application to the biological exposures that the system was designed for.

Future work in this area could proceed in several directions both theoretically and experimentally. Experimentally, with the standard TPF sources future work would be greatly facilitated the development of more rigorous beam diagnostics of the spatial mode, beam pointing, spectrum, and temporal envelope of the generation pulse. Moreover, as these sources show extreme sensitivity to changes in pointing, active beam stabilization could be beneficial. Alternatively, it would be quite interesting to explore imaging-less TPF THz generation based on the grating/prism combinations introduced in Chapter 3. Finally, we hope to see an experimental realization of the GaN based TPF THz source.

Theoretically, it would be interesting to study the effects of higher-order AD on TPF generation, which would require an extension of the THz generation code to 2D. While a similar analysis has been performed studying the spectrum and energy generation efficiency by Bodrov *et al.*, however, their work could be extended either by analyzing the focusing power of THz pulses generated with varying second-order AD, which could greatly affect the peak electric field. Moreover, it would be quite interesting to studying the effect of second-order AD on cascaded THz generation.

9.2 THz Control of Hot-Carriers

The second part of this work details the study of modulation of hot-carrier dynamics and the control of photoluminescence (PL) with intense THz pulses. Since the development of the TPF technique, which brought intense THz pulse generation to the tabletop, these sources have been used to control and drive luminescence in a variety of ways, revealing new insight into material dynamics and light emission. Previous work demonstrated the PL quenching in bulk semiconductors with intense THz pulses [160], and later PL enhancement in the high-energy luminescence tail [60].

However, the microscopic origin of these effects was unclear. The important contribution of this work was the development of a unified model of both the near-gap PL quenching and PL enhancement in the high-energy tail. We showed that a simple model based on THz-induced heating and 1D diffusion/bi-molecular recombination was able to qualitatively, and semi-quantitatively, capture the effect of THz heating on the PL spectrum. While the idea underlying the high-energy PL enhancement was simple; THz-driven heating increases the thermal occupancy of electrons and holes at high energies, the origin of PL quenching was more subtle. Two effects govern the quenching: hot-carrier diffusion into the substrate, which decreases the overall density of the system and therefore reduces the bi-molecular rate of recombination, and carrier heating results in an increased photon reabsorption, which reduces the external radiative efficiency.

Despite the successes of the model, there remain many unsolved problems, suggesting that there are new insights waiting to be found. In its present form the diffusive model does not capture the scaling of THz-ΔPL with optical fluence. It is possible that two straightforward extensions could solve this issue: First, a self-consistent treatment of the PL emission and reabsorption including the quasi-Fermi splitting and, therefore, enhanced transmission of near-gap PL in the high density regime would mitigate the photon reabsorption and reduce the low-energy PL quenching. Second, introducing a density-dependent carrier mobility would reduce the effect of THz-induced hot-carrier diffusion, which contributes to the reduction in radiative recombination rate, thereby mitigating the PL quenching.

Further exploration of these effects could provide useful information regarding hot-carrier cooling dynamics and radiative efficiency, which could be invaluable to the energy materials community. Indeed, recent work has begun to explore time-resolved PL quenching and enhancement in lead-halide perovskites, an important contemporary material for light harvesting [162]. Moreover, the control of hot-carrier temperature could prove useful in other areas of materials science such as hot-carrier solar cells [289] or photochemistry [290].

9.3 THz Spectroscopy of Double-Helix SnIP

The final portion of this thesis, chapters 7 and 8, focuses on the study of the exciting new double-helix semiconductor SnIP. This material has shown promise for photocatalysis and is extremely soft and flexible compared to other inorganic semiconductors. Moreover, its structure and chemistry and absolutely unique and the double-helix structure is somewhat of an inorganic analogue of the more familiar DNA. This alone adds a certain degree of fundamental curiosity to this material: Are there similar materials that share this unique structure? How does the double-helix structure affect the properties?

In chapter 7, the synthesis and characterization of SnIP nanowire films was elaborated. The properties of the nanowires were compared to the bulk needles in detail, showing that the nanowires retain a high crystal quality despite the rough treatment by grinding and ultrasonication. Quantum-chemical calculations were used to study the electronic structure-revealing a surprising 2D like behavior of the conduction bands-as well as to calculate the effective masses that are needed to extract the carrier mobility from TRTS. Moreover, the infrared active (IR) vibrational spectrum was calculated. Experimental results from time-domain THz spectroscopy (TDS) showed surprisingly good agreement with the averaged dielectric function, which took into account the distribution of nanowire orientations.

In chapter 8, the SnIP nanowire films were studied using TRTS. We made the first measurement of the carrier mobility, which was found to be remarkably high for such a soft and flexible material. This suggests that, if several challenges regarding synthesis can be overcome, SnIP could be an excellent new material for flexible electronics. We

also performed a comparison of several common models used in TRTS. In the field, some controversy exists regarding the correct choice of model, however, few studies provide such a direct comparison. In our case, we were able to show that the mobility extracted from each model is similar, which strengthens our claim about the high carrier mobility in this new material.

This chapter also provides an extensive study of the fluence and temperature dependent relaxation dynamics in SnIP. These results show that the as-prepared nanowires have a high trap density comparable to LT-GaAs, which significantly reduces the carrier lifetime. We propose that this high trap density is a limiting factor in the application of SnIP to photocatalysis and suggest that future work should focus on the passivation or removal of these trap states. Alternatively, future explorations of the ultrafast THz dynamics in SnIP could focus on 1D van der Waals (vdW) heterostructures such as self-assembled SnIP/transition metal dichalchogenide or graphene hybrids, which promises to be an important new area of materials science in the coming years [184, 185].

From a fundamental perspective, to better understanding the relationship between the unique structure and the properties in SnIP, future work should focus on further experimental verification of the quantum-chemical calculations. Synthesis of doped samples would facilitate application of standard probes to measure the effective mass, such as cyclotron resonance or angle-resolved photoemission (ARPES). This would also enable the application of more standard electronic probes of carrier mobility such as Hall resistivity and is also an important step towards applications in flexible electronics. Alternatively, it is possible that this emerging ultrafast probes such as THz cyclotron resonance [291], ultrafast ARPES [292], or high-harmonic generation [293] could provide more detailed information on the band structure in as-grown SnIP. Additional measurements should also focus on probing the symmetry of the vibrational resonances, which would provide powerful validation of the quantum-chemical calculations. This could proceed either via the development of aligned SnIP samples, which to date has proved challenging, or using near-field THz imaging techniques, which would enable studies of individual SnIP needles [294].

References

[1] T. E. Graedel, E. M. Harper, N. T. Nassar, and B. K. Reck, "On the materials basis of modern society," *Proceedings of the National Academy of Sciences*, vol. 112, pp. 6295–6300, May 2015.

[2] A. Greenfield and T. E. Graedel, "The omnivorous diet of modern technology," *Resources, Conservation, and Recycling*, vol. 74, pp. 1–7, 2013.

[3] D. Gielen, F. Boshell, and D. Saygin, "Climate and energy challenges for materials science," *Nature Materials*, vol. 15, pp. 117–120, Feb. 2016.

[4] N. P. de Leon, K. M. Itoh, D. Kim, K. K. Mehta, T. E. Northup, H. Paik, B. S. Palmer, N. Samarth, S. Sangtawesin, and D. W. Steuerman, "Materials challenges and opportunities for quantum computing hardware," *Science*, vol. 372, p. eabb2823, Apr. 2021.

[5] J. Cross, R. Opila, I. Boyd, and E. Kaufmann, "Materials characterization and the evolution of materials," *MRS Bulletin*, vol. 40, pp. 1019–1034, Dec. 2015.

[6] F. X. Kärtner, E. P. Ippen, and S. T. Cundiff, "Femtosecond Laser Development," in *Femtosecond Optical Frequency Comb: Principle, Operation, and Applications* (J. Ye and S. T. Cundiff, eds.), pp. 54–77, Boston, MA: Springer US, 2005.

[7] National Academies of Sciences, Engineering, and Medicine, *Opportunities in Intense Ultrafast Lasers: Reaching for the Brightest Light*. Washington, DC: The National Academies Press, 2018.

[8] M. Malinauskas, A. Žukauskas, S. Hasegawa, Y. Hayasaki, V. Mizeikis, R. Buividas, and S. Juodkazis, "Ultrafast laser processing of materials: from science to industry," *Light: Science & Applications*, vol. 5, pp. e16133–e16133, Aug. 2016.

[9] T. Fortier and E. Baumann, "20 years of developments in optical frequency comb technology and applications," *Communications Physics*, vol. 2, p. 153, Dec. 2019.

[10] C. B. Marblea and V. V. Yakovleva, "Biomedical optics applications of advanced lasers and nonlinear optics," *Journal of Biomedical Optics*, vol. 25, p. 1, Apr. 2020.

[11] R. Betti and O. A. Hurricane, "Inertial-confinement fusion with lasers," *Nature Physics*, vol. 12, pp. 435–448, May 2016.

[12] P. Hannaford, ed., *Femtosecond Laser Spectroscopy*. Springer US, 2005.

[13] A. Fox, *Optical Properties of Solids*. Oxford master series in condensed matter physics, Oxford University Press, 2001.

[14] J. A. Spies, J. Neu, U. T. Tayvah, M. D. Capobianco, B. Pattengale, S. Ostresh, and C. A. Schmuttenmaer, "Terahertz Spectroscopy of Emerging Materials," *The Journal of Physical Chemistry C*, vol. 124, pp. 22335–22346, Oct. 2020.

[15] F. Blanchard, L. Razzari, H. Bandulet, G. Sharma, R. Morandotti, J. C. Kieffer, T. Ozaki, M. Reid, H. F. Tiedje, H. K. Haugen, and F. A. Hegmann, "Generation of 1.5 µJ single-cycle terahertz pulses by optical rectification from a large aperture ZnTe crystal," *Optics Express*, vol. 15, no. 20, p. 13212, 2007.

[16] K.-L. Yeh, M. C. Hoffmann, J. Hebling, and K. A. Nelson, "Generation of 10 μJ ultrashort terahertz pulses by optical rectification," *Applied Physics Letters*, vol. 90, p. 171121, Apr. 2007.

[17] H. Hirori, A. Doi, F. Blanchard, and K. Tanaka, "Single-cycle terahertz pulses with amplitudes exceeding 1 MV/cm generated by optical rectification in $LiNbO_3$," *Applied Physics Letters*, vol. 98, p. 091106, Feb. 2011.

[18] T. Kampfrath, K. Tanaka, and K. A. Nelson, "Resonant and nonresonant control over matter and light by intense terahertz transients," *Nature Photonics*, vol. 7, pp. 680–690, Sept. 2013.

[19] H. A. Hafez, S. Kovalev, J.-C. Deinert, Z. Mics, B. Green, N. Awari, M. Chen, S. Germanskiy, U. Lehnert, J. Teichert, Z. Wang, K.-J. Tielrooij, Z. Liu, Z. Chen, A. Narita, K. Müllen, M. Bonn, M. Gensch, and D. Turchinovich, "Extremely efficient terahertz high-harmonic generation in graphene by hot Dirac fermions," *Nature*, vol. 561, pp. 507–511, Sept. 2018.

[20] E. J. Sie, C. M. Nyby, C. D. Pemmaraju, S. J. Park, X. Shen, J. Yang, M. C. Hoffmann, B. K. Ofori-Okai, R. Li, A. H. Reid, S. Weathersby, E. Mannebach, N. Finney, D. Rhodes, D. Chenet, A. Antony, L. Balicas, J. Hone, T. P. Devereaux, T. F. Heinz, X. Wang, and A. M. Lindenberg, "An ultrafast symmetry switch in a Weyl semimetal," *Nature*, vol. 565, pp. 61–66, Jan. 2019.

[21] S. S. Dhillon, M. S. Vitiello, E. H. Linfield, A. G. Davies, M. C. Hoffmann, J. Booske, C. Paoloni, M. Gensch, P. Weightman, G. P. Williams, E. Castro-Camus, D. R. S. Cumming, F. Simoens, I. Escorcia-Carranza, J. Grant, S. Lucyszyn, M. Kuwata-Gonokami, K. Konishi, M. Koch, C. A. Schmuttenmaer, T. L. Cocker, R. Huber, A. G. Markelz, Z. D. Taylor, V. P. Wallace, J. Axel Zeitler, J. Sibik, T. M. Korter, B. Ellison, S. Rea, P. Goldsmith, K. B. Cooper, R. Appleby, D. Pardo, P. G. Huggard, V. Krozer, H. Shams, M. Fice, C. Renaud, A. Seeds, A. Stöhr, M. Naftaly, N. Ridler, R. Clarke, J. E. Cunningham, and M. B. Johnston, "The 2017 terahertz science and technology roadmap," *Journal of Physics D: Applied Physics*, vol. 50, p. 043001, Feb. 2017.

[22] D. N. Purschke, M. Na, A. Longman, L. V. Titova, and F. A. Hegmann, "Enhancement of hot-carrier photoluminescence with intense terahertz pulses," *Applied Physics Letters*, vol. 112, p. 072105, Feb. 2018.

[23] D. N. Purschke, M. R. P. Pielmeier, E. Üzer, C. Ott, C. Jensen, A. Degg, A. Vogel, N. Amer, T. Nilges, and F. A. Hegmann, "Ultrafast Photoconductivity and Terahertz Vibrational Dynamics in Double-Helix SnIP Nanowires," *Advanced Materials*, vol. 33, p. 2100978, Aug. 2021.

[24] W. Kaiser and C. G. B. Garrett, "Two-Photon Excitation in Ca F 2 : Eu 2 +," *Physical Review Letters*, vol. 7, pp. 229–231, Sept. 1961.

[25] P. A. Franken, A. E. Hill, C. W. Peters, and G. Weinreich, "Generation of Optical Harmonics," *Physical Review Letters*, vol. 7, pp. 118–119, Aug. 1961.

[26] M. Bass, P. A. Franken, J. F. Ward, and G. Weinreich, "Optical Rectification," *Physical Review Letters*, vol. 9, pp. 446–448, Dec. 1962.

[27] T. H. Maiman, "Stimulated Optical Radiation in Ruby," *Nature*, vol. 187, pp. 493–494, Aug. 1960.

[28] J. Hecht, "Short history of laser development," *Optical Engineering*, vol. 49, p. 091002, Sept. 2010.

[29] F. Zernike and P. R. Berman, "Generation of Far Infrared as a Difference Frequency," *Physical Review Letters*, vol. 15, pp. 999–1001, Dec. 1965.

[30] K. H. Yang, P. L. Richards, and Y. R. Shen, "Generation of Far-Infrared Radiation by Picosecond Light Pulses in $LiNbO_3$," *Applied Physics Letters*, vol. 19, pp. 320–323, Nov. 1971.

[31] N. Matsumoto and T. Yajima, "Far-Infrared Generation by Self-Beating of Dye Laser Light," *Japanese Journal of Applied Physics*, vol. 12, pp. 90–97, Jan. 1973.

[32] D. H. Auston and A. M. Glass, "Optical Generation of Intense Picosecond Electrical Pulses," *Applied Physics Letters*, vol. 20, pp. 398–399, May 1972.

[33] D. H. Auston, "Picosecond optoelectronic switching and gating in silicon," *Applied Physics Letters*, vol. 26, pp. 101–103, Feb. 1975.

[34] A. Antonetti, A. Migus, M. M. Malley, and G. Mourou, "Optoelectronic sampling in the picosecond range," *Optics Communications*, vol. 21, pp. 211–214, May 1977.

[35] D. H. Auston, K. P. Cheung, J. A. Valdmanis, and D. A. Kleinman, "Cherenkov radiation from femtosecond optical pulses in electro-optic media," *Physical Review Letters*, vol. 53, no. 16, p. 1555, 1984.

[36] D. Grischkowsky, S. Keiding, M. van Exter, and C. Fattinger, "Far-infrared time-domain spectroscopy with terahertz beams of dielectrics and semiconductors," *Journal of the Optical Society of America B*, vol. 7, p. 2006, Oct. 1990.

[37] C. A. Schmuttenmaer, "Exploring Dynamics in the Far-Infrared with Terahertz Spectroscopy," *Chemical Reviews*, vol. 104, pp. 1759–1780, Apr. 2004.

[38] Q. Wu and X.-C. Zhang, "Free-space electro-optic sampling of terahertz beams," *Applied Physics Letters*, vol. 67, pp. 3523–3525, Dec. 1995.

[39] R. Ulbricht, E. Hendry, J. Shan, T. F. Heinz, and M. Bonn, "Carrier dynamics in semiconductors studied with time-resolved terahertz spectroscopy," *Reviews of Modern Physics*, vol. 83, pp. 543–586, June 2011.

[40] T. Kleine-Ostmann and T. Nagatsuma, "A Review on Terahertz Communications Research," *Journal of Infrared, Millimeter, and Terahertz Waves*, vol. 32, pp. 143–171, Feb. 2011.

[41] J.-H. Son, *Terahertz Biomedical Science and Technology (1st ed.)*. CRC Press, 2014.

[42] D. L. Woolard, J. O. Jensen, R. J. Hwu, and M. S. Shur, *Terahertz Science and Technology for Military and Security Applications*. WORLD SCIENTIFIC, 2007.

[43] Naftaly, Vieweg, and Deninger, "Industrial Applications of Terahertz Sensing: State of Play," *Sensors*, vol. 19, p. 4203, Sept. 2019.

[44] R. Boyd and D. Prato, *Nonlinear Optics*. Elsevier Science, 2008.

[45] J. Taylor, *Classical Mechanics*. University Science Books, 2005.

[46] J. B. Khurgin, A. Obeidat, S. J. Lee, and Y. J. Ding, "Cascaded optical nonlinearities: Microscopic understanding as a collective effect," *Journal of the Optical Society of America B*, vol. 14, p. 1977, Aug. 1997.

[47] M. Jewariya, M. Nagai, and K. Tanaka, "Enhancement of terahertz wave generation by cascaded $\chi^{(2)}$ processes in $LiNbO_3$," *Journal of the Optical Society of America B*, vol. 26, p. A101, Sept. 2009.

[48] G. Gallot and D. Grischkowsky, "Electro-optic detection of terahertz radiation," *Journal of the Optical Society of America B*, vol. 16, p. 1204, Aug. 1999.

[49] G. Agrawal, *Nonlinear Fiber Optics (Fifth Edition)*. Optics and Photonics, Boston: Academic Press, fifth edition ed., 2012.

[50] M. Hibberd, V. Frey, B. Spencer, P. Mitchell, P. Dawson, M. Kappers, R. Oliver, C. Humphreys, and D. Graham, "Dielectric response of wurtzite gallium nitride in the terahertz frequency range," *Solid State Communications*, vol. 247, pp. 68–71, Dec. 2016.

[51] C. M. Hough, *Biological Effects of Intense Terahertz Pulse*. PhD thesis, University of Alberta, 2021.

[52] C. Larsen, D. G. Cooke, and P. U. Jepsen, "Finite-difference time-domain analysis of time-resolved terahertz spectroscopy experiments," *Journal of the Optical Society of America B*, vol. 28, p. 1308, May 2011.

[53] D. E. Zelmon, D. L. Small, and D. Jundt, "Infrared corrected Sellmeier coefficients for congruently grown lithium niobate and 5 mol% magnesium oxide –doped lithium niobate," *Journal of the Optical Society of America B*, vol. 14, p. 3319, Dec. 1997.

[54] M. Schall, M. Walther, and P. Uhd Jepsen, "Fundamental and second-order phonon processes in CdTe and ZnTe," *Physical Review B*, vol. 64, p. 094301, Aug. 2001.

[55] F. D'Angelo, Z. Mics, M. Bonn, and D. Turchinovich, "Ultra-broadband THz time-domain spectroscopy of common polymers using THz air photonics," *Optics Express*, vol. 22, p. 12475, May 2014.

[56] C. Thierfelder, S. Sanna, A. Schindlmayr, and W. G. Schmidt, "Do we know the band gap of lithium niobate?," *physica status solidi (c)*, vol. 7, pp. 362–365, Feb. 2010.

[57] J. Hebling, G. Almasi, I. Kozma, and J. Kuhl, "Velocity matching by pulse front tilting for large area THz-pulse generation," *Optics Express*, vol. 10, p. 1161, Oct. 2002.

[58] A. G. Stepanov, J. Hebling, and J. Kuhl, "Efficient generation of subpicosecond terahertz radiation by phase-matched optical rectification using ultrashort laser pulses with tilted pulse fronts," *Applied Physics Letters*, vol. 83, pp. 3000–3002, Oct. 2003.

[59] A. K. Ayesheshim, *High-power Terahertz Pulse Generation and Nonlinear Terahertz Carrier Dynamics in Semiconductors*. PhD thesis, University of Alberta, 2015.

[60] D. N. Purschke, "Modulation of Semiconductor Photoluminescence with Intense Terahertz Pulses," Master's thesis, University of Alberta, 2016.

[61] C. E. Jensen, *Ultrafast imaging of nonlinear terahertz dynamics in semiconductors*. PhD, University of Alberta, 2017.

[62] M. A. B. Narreto, *Ultrafast Photoluminescence and Photoconductivity Dynamics of Semiconductors*. PhD thesis, University of Alberta, 2019.

[63] J. Hebling, "Derivation of the pulse front tilt caused by angular dispersion," *Optical and Quantum Electronics*, vol. 28, pp. 1759–1763, Dec. 1996.

[64] A. S. Barker and R. Loudon, "Dielectric Properties and Optical Phonons in $LiNbO_3$," *Physical Review*, vol. 158, pp. 433–445, June 1967.

[65] J. A. Fülöp, L. Pálfalvi, G. Almási, and J. Hebling, "Design of high-energy terahertz sources based on optical rectification," *Optics Express*, vol. 18, p. 12311, June 2010.

[66] K. Ravi, W. R. Huang, S. Carbajo, X. Wu, and F. Kärtner, "Limitations to THz generation by optical rectification using tilted pulse fronts," *Optics Express*, vol. 22, p. 20239, Aug. 2014.

[67] M. S. Piltch, R. Eckhardt, and R. Hinsley, "Determination of the nonlinear optical coefficient and SHG coherence length for crystal single zinc selenide," *Optics Communications*, vol. 22, pp. 239–242, Aug. 1977.

[68] D. Kreier and P. Baum, "Avoiding temporal distortions in tilted pulses," *Optics Letters*, vol. 37, p. 2373, June 2012.

[69] S. B. Bodrov, A. N. Stepanov, and M. I. Bakunov, "Generalized analysis of terahertz generation by tilted-pulse-front excitation in a $LiNbO_3$ prism," *Optics Express*, vol. 27, p. 2396, Feb. 2019.

[70] L. Pálfalvi, J. A. Fülöp, G. Almási, and J. Hebling, "Novel setups for extremely high power single-cycle terahertz pulse generation by optical rectification," *Applied Physics Letters*, vol. 92, p. 171107, Apr. 2008.

[71] M. I. Bakunov and S. B. Bodrov, "Terahertz generation with tilted-front laser pulses in a contact-grating scheme," *Journal of the Optical Society of America B*, vol. 31, p. 2549, Nov. 2014.

[72] O. Isaienko and E. Borguet, "Pulse-front matching of ultrabroadband near-infrared noncollinear optical parametric amplified pulses," *Journal of the Optical Society of America B*, vol. 26, p. 965, May 2009.

[73] P. Baum and A. H. Zewail, "Breaking resolution limits in ultrafast electron diffraction and microscopy," *Proceedings of the National Academy of Sciences*, vol. 103, no. 44, pp. 16105–16110, 2006.

[74] H. Vincenti and F. Quéré, "Attosecond Lighthouses: How To Use Spatiotemporally Coupled Light Fields To Generate Isolated Attosecond Pulses," *Physical Review Letters*, vol. 108, p. 113904, Mar. 2012.

[75] C. Chang, C. Tang, and J. Wu, "High-Gain Thompson-Scattering X-Ray Free-Electron Laser by Time-Synchronic Laterally Tilted Optical Wave," *Physical Review Letters*, vol. 110, p. 064802, Feb. 2013.

[76] A. W. Schiff-Kearn, L. Gingras, S. Bernier, N. Chamanara, K. Agarwal, J.-M. Ménard, and D. G. Cooke, "Front-induced transitions control THz waves," *arXiv:2102.02879 [physics]*, Feb. 2021. arXiv: 2102.02879.

[77] J. Hebling, A. G. Stepanov, G. Almási, B. Bartal, and J. Kuhl, "Tunable THz pulse generation by optical rectification of ultrashort laser pulses with tilted pulse fronts," *Applied Physics B*, vol. 78, pp. 593–599, Mar. 2004.

[78] L. Pálfalvi, J. Hebling, J. Kuhl, . Péter, and K. Polgár, "Temperature dependence of the absorption and refraction of Mg-doped congruent and stoichiometric $LiNbO_3$ in the THz range," *Journal of Applied Physics*, vol. 97, p. 123505, June 2005.

[79] O. M. Stafsudd, F. A. Haak, and K. Radisavljević, "Far-Infrared Spectrum of Cadmium Telluride," *Journal of the Optical Society of America*, vol. 57, p. 1475, Dec. 1967.

[80] T. O. Buchmann, E. J. Railton Kelleher, M. Jazbinsek, B. Zhou, J.-H. Seok, O.-P. Kwon, F. Rotermund, and P. U. Jepsen, "High-power few-cycle THz generation at MHz repetition rates in an organic crystal," *APL Photonics*, vol. 5, p. 106103, Oct. 2020.

[81] F. Blanchard, B. E. Schmidt, X. Ropagnol, N. Thiré, T. Ozaki, R. Morandotti, D. G. Cooke, and F. Légaré, "Terahertz pulse generation from bulk GaAs by a tilted-pulse-front excitation at 1.8 μm," *Applied Physics Letters*, vol. 105, p. 241106, Dec. 2014.

[82] A. Halpin, W. Cui, A. W. Schiff-Kearn, K. M. Awan, K. Dolgaleva, and J.-M. Ménard, "Enhanced Terahertz Detection Efficiency via Grating-Assisted Non-collinear Electro-Optic Sampling," *Physical Review Applied*, vol. 12, p. 031003, Sept. 2019.

[83] G. Gallot, J. Zhang, R. W. McGowan, T.-I. Jeon, and D. Grischkowsky, "Measurements of the THz absorption and dispersion of ZnTe and their relevance to the electro-optic detection of THz radiation," *Applied Physics Letters*, vol. 74, pp. 3450–3452, June 1999.

[84] X. Long, R. A. Myers, S. R. J. Brueck, R. Ramer, K. Zheng, and S. D. Hersee, "GaN linear electro-optic effect," *Applied Physics Letters*, vol. 67, pp. 1349–1351, Sept. 1995.

[85] S. R. Bowman, C. G. Brown, and B. Taczak, "Optical dispersion and phase matching in gallium nitride and aluminum nitride," *Optical Materials Express*, vol. 8, p. 1091, Apr. 2018.

[86] M. G. Moharam, T. K. Gaylord, D. A. Pommet, and E. B. Grann, "Stable implementation of the rigorous coupled-wave analysis for surface-relief gratings: enhanced transmittance matrix approach," *Journal of the Optical Society of America A*, vol. 12, p. 1077, May 1995.

[87] V. Liu and S. Fan, "S4 : A free electromagnetic solver for layered periodic structures," *Computer Physics Communications*, vol. 183, pp. 2233–2244, Oct. 2012.

[88] A. Sainte-Marie, O. Gobert, and F. Quéré, "Controlling the velocity of ultrashort light pulses in vacuum through spatio-temporal couplings," *Optica*, vol. 4, pp. 1298–1304, Oct. 2017. Publisher: OSA.

[89] D. H. Froula, D. Turnbull, A. S. Davies, T. J. Kessler, D. Haberberger, J. P. Palastro, S.-W. Bahk, I. A. Begishev, R. Boni, S. Bucht, J. Katz, and J. L. Shaw, "Spatiotemporal control of laser intensity," *Nature Photonics*, Mar. 2018.

[90] D. H. Froula, J. P. Palastro, D. Turnbull, A. Davies, L. Nguyen, A. Howard, D. Ramsey, P. Franke, W. Bahk, I. A. Begishev, R. Boni, J. Bromage, S. Bucht, R. K. Follett, D. Haberberger, G. W. Jenkins, J. Katz, J. L. Shaw, and J. Vieira, "Flying focus: Spatial and temporal control of intensity for laser-based applications," *Physics of Plasmas*, p. 10, 2019.

[91] M. Reid and R. Fedosejevs, "Quantitative comparison of terahertz emission from (100) InAs surfaces and a GaAs large-aperture photoconductive switch at high fluences," *Applied Optics*, vol. 44, p. 149, Jan. 2005.

[92] G. Sharma, I. Al-Naib, H. Hafez, R. Morandotti, D. G. Cooke, and T. Ozaki, "Carrier density dependence of the nonlinear absorption of intense THz radiation in GaAs," *Optics Express*, vol. 20, p. 18016, July 2012.

[93] I. Z. Kozma, G. Almási, and J. Hebling, "Geometrical optical modeling of femtosecond setups having angular dispersion," *Applied Physics B*, vol. 76, pp. 257–261, 2003.

[94] K. Murate and K. Kawase, "Perspective: Terahertz wave parametric generator and its applications," *Journal of Applied Physics*, vol. 124, p. 160901, Oct. 2018.

[95] F. Blanchard, X. Ropagnol, H. Hafez, H. Razavipour, M. Bolduc, R. Morandotti, T. Ozaki, and D. G. Cooke, "Effect of extreme pump pulse reshaping on intense terahertz emission in lithium niobate at multimilliJoule pump energies," *Optics Letters*, vol. 39, p. 4333, Aug. 2014.

[96] K. Ravi, W. R. Huang, S. Carbajo, E. A. Nanni, D. N. Schimpf, E. P. Ippen, and F. X. Kärtner, "Theory of terahertz generation by optical rectification using tilted-pulse-fronts," *Optics Express*, vol. 23, p. 5253, Feb. 2015.

[97] B. K. Ofori-Okai, P. Sivarajah, W. R. Huang, and K. A. Nelson, "THz generation using a reflective stair-step echelon," *arXiv preprint arXiv:1512.03941*, 2015.

[98] M. A. B. Narreto, C. Huang, D. N. Purschke, and F. A. Hegmann, "Modulated photoluminescence of germanium via intense terahertz pulse electric fields," in

Frontiers in Optics / Laser Science, p. JW3A.33, Optical Society of America, 2018.

[99] A. T. Tarekegne, H. Hirori, K. Tanaka, K. Iwaszczuk, and P. U. Jepsen, "Impact ionization dynamics in silicon by MV/cm THz fields," *New Journal of Physics*, vol. 19, p. 123018, Dec. 2017.

[100] A. Mousavian, B. Lee, A. D. Stickel, and Y.-S. Lee, "Ultrafast photocarrier dynamics in single-layer graphene driven by strong terahertz pulses," *Journal of the Optical Society of America B*, vol. 35, p. 1255, June 2018.

[101] Z. Liu, C. Vaswani, X. Yang, X. Zhao, Y. Yao, Z. Song, D. Cheng, Y. Shi, L. Luo, D.-H. Mudiyanselage, C. Huang, J.-M. Park, R. Kim, J. Zhao, Y. Yan, K.-M. Ho, and J. Wang, "Ultrafast Control of Excitonic Rashba Fine Structure by Phonon Coherence in the Metal Halide Perovskite $CH_3NH_3PbI_3$," *Physical Review Letters*, vol. 124, p. 157401, Apr. 2020.

[102] C. Lange, T. Maag, M. Hohenleutner, S. Baierl, O. Schubert, E. Edwards, D. Bougeard, G. Woltersdorf, and R. Huber, "Extremely Nonperturbative Nonlinearities in GaAs Driven by Atomically Strong Terahertz Fields in Gold Metamaterials," *Physical Review Letters*, vol. 113, Nov. 2014.

[103] M. Sajadi, M. Wolf, and T. Kampfrath, "Terahertz-field-induced optical birefringence in common window and substrate materials," *Optics Express*, vol. 23, p. 28985, Nov. 2015.

[104] B. Zhang, Z. Ma, J. Ma, X. Wu, C. Ouyang, D. Kong, T. Hong, X. Wang, P. Yang, L. Chen, Y. Li, and J. Zhang, "1.4-mJ High Energy Terahertz Radiation from Lithium Niobates," *Laser & Photonics Reviews*, vol. 15, p. 2000295, Mar. 2021.

[105] J. P. Palastro, J. L. Shaw, P. Franke, D. Ramsey, T. T. Simpson, and D. H. Froula, "Dephasingless Laser Wakefield Acceleration," *Physical Review Letters*, p. 6, 2020.

[106] X. Wu, C. Zhou, W. R. Huang, F. Ahr, and F. X. Kärtner, "Temperature dependent refractive index and absorption coefficient of congruent lithium niobate crystals in the terahertz range," *Optics Express*, vol. 23, p. 29729, Nov. 2015.

[107] P. D. Cunningham, N. N. Valdes, F. A. Vallejo, L. M. Hayden, B. Polishak, X.-H. Zhou, J. Luo, A. K.-Y. Jen, J. C. Williams, and R. J. Twieg, "Broadband terahertz characterization of the refractive index and absorption of some important polymeric and organic electro-optic materials," *Journal of Applied Physics*, vol. 109, pp. 043505–043505–5, Feb. 2011.

[108] K. Uchida, T. Otobe, T. Mochizuki, C. Kim, M. Yoshita, H. Akiyama, L. Pfeiffer, K. West, K. Tanaka, and H. Hirori, "Subcycle Optical Response Caused by a Terahertz Dressed State with Phase-Locked Wave Functions," *Physical Review Letters*, vol. 117, p. 277402, Dec. 2016.

[109] D. Zhang, M. Fakhari, H. Cankaya, A.-L. Calendron, N. H. Matlis, and F. X. Kärtner, "Cascaded Multicycle Terahertz-Driven Ultrafast Electron Acceleration and Manipulation," *Physical Review X*, vol. 10, p. 011067, Mar. 2020.

[110] R. Matsunaga, N. Tsuji, H. Fujita, A. Sugioka, K. Makise, Y. Uzawa, H. Terai, Z. Wang, H. Aoki, and R. Shimano, "Light-induced collective pseudospin precession resonating with Higgs mode in a superconductor," *Science*, vol. 345, pp. 1145–1149, Sept. 2014.

[111] X. Yang, C. Vaswani, C. Sundahl, M. Mootz, L. Luo, J. H. Kang, I. E. Perakis, C. B. Eom, and J. Wang, "Lightwave-driven gapless superconductivity and forbidden quantum beats by terahertz symmetry breaking," *Nature Photonics*, vol. 13, pp. 707–713, Oct. 2019.

[112] B. Cheng, N. Kanda, T. N. Ikeda, T. Matsuda, P. Xia, T. Schumann, S. Stemmer, J. Itatani, N. P. Armitage, and R. Matsunaga, "Efficient Terahertz Harmonic Generation with Coherent Acceleration of Electrons in the Dirac Semimetal Cd_3As_2," *Physical Review Letters*, vol. 124, p. 117402, Mar. 2020.

[113] S. Kovalev, R. M. A. Dantas, S. Germanskiy, J.-C. Deinert, B. Green, I. Ilyakov, N. Awari, M. Chen, M. Bawatna, J. Ling, F. Xiu, P. H. M. van Loosdrecht,

P. Surówka, T. Oka, and Z. Wang, "Non-perturbative terahertz high-harmonic generation in the three-dimensional Dirac semimetal Cd_3As_2," *Nature Communications*, vol. 11, p. 2451, Dec. 2020.

[114] O. Schubert, M. Hohenleutner, F. Langer, B. Urbanek, C. Lange, U. Huttner, D. Golde, T. Meier, M. Kira, S. W. Koch, and R. Huber, "Sub-cycle control of terahertz high-harmonic generation by dynamical Bloch oscillations," *Nature Photonics*, vol. 8, pp. 119–123, Feb. 2014.

[115] G. Vampa, T. J. Hammond, N. Thiré, B. E. Schmidt, F. Légaré, C. R. McDonald, T. Brabec, and P. B. Corkum, "Linking high harmonics from gases and solids," *Nature*, vol. 522, pp. 462–464, June 2015.

[116] F. H. Su, F. Blanchard, G. Sharma, L. Razzari, A. Ayesheshim, T. L. Cocker, L. V. Titova, T. Ozaki, J.-C. Kieffer, R. Morandotti, M. Reid, and F. A. Hegmann, "Terahertz pulse induced intervalley scattering in photoexcited GaAs," *Optics Express*, vol. 17, p. 9620, June 2009.

[117] P. Rasekh, A. Safari, M. Yildirim, R. Bhardwaj, J.-M. Ménard, K. Dolgaleva, and R. W. Boyd, "Terahertz nonlinear spectroscopy of water vapor," *ACS Photonics*, vol. 8, no. 6, pp. 1683–1688, 2021.

[118] L. S. Rothman, D. Jacquemart, A. Barbe, D. C. Benner, M. Birk, L. R. Brown, M. R. Carleer, C. Chackerian, K. Chance, L. H. Coudert, V. Dana, V. M. Devi, J.-M. Flaud, R. R. Gamache, A. Goldman, J.-M. Hartmann, K. W. Jucks, A. G. Maki, J.-Y. Mandin, S. T. Massie, J. Orphal, A. Perrin, C. P. Rinsland, M. A. H. Smith, J. Tennyson, R. N. Tolchenov, R. A. Toth, J. V. Auwera, P. Varanasi, and G. Wagner, "The HITRAN 2004 molecular spectroscopic database," *Journal of Quantitative Spectroscopy and Radiative Transfer*, vol. 96, pp. 139–204, 2005.

[119] M. Šimečková, D. Jacquemart, L. S. Rothman, R. R. Gamache, and A. Goldman, "Einstein A-coefficients and statistical weights for molecular absorption transitions in the HITRAN database," *Journal of Quantitative Spectroscopy and Radiative Transfer*, vol. 98, pp. 130–155, Mar. 2006.

[120] J. L. Oudar, D. Hulin, A. Migus, A. Antonetti, and F. Alexandre, "Subpicosecond Spectral Hole Burning Due to Nonthermalized Photoexcited Carriers in GaAs," *Physical Review Letters*, vol. 55, pp. 2074–2077, Nov. 1985.

[121] J. Kanasaki, H. Tanimura, and K. Tanimura, "Imaging Energy-, Momentum-, and Time-Resolved Distributions of Photoinjected Hot Electrons in GaAs," *Physical Review Letters*, vol. 113, p. 237401, Dec. 2014.

[122] J. Shah, *Ultrafast Spectroscopy of Semiconductors and Semiconductor Nanostructures*. Springer Science & Business Media, June 1999. Google-Books-ID: JvGThgPz6poC.

[123] A. Othonos, "Probing ultrafast carrier and phonon dynamics in semiconductors," *Journal of Applied Physics*, vol. 83, pp. 1789–1830, Feb. 1998.

[124] S. S. Prabhu, A. S. Vengurlekar, S. K. Roy, and J. Shah, "Nonequilibrium dynamics of hot carriers and hot phonons in CdSe and GaAs," *Physical Review B*, vol. 51, pp. 14233–14246, May 1995.

[125] R. Clady, M. J. Y. Tayebjee, P. Aliberti, D. König, N. J. Ekins-Daukes, G. J. Conibeer, T. W. Schmidt, and M. A. Green, "Interplay between the hot phonon effect and intervalley scattering on the cooling rate of hot carriers in GaAs and InP," *Progress in Photovoltaics: Research and Applications*, vol. 20, pp. 82–92, Jan. 2012.

[126] Y. Yang, D. P. Ostrowski, R. M. France, K. Zhu, J. van de Lagemaat, J. M. Luther, and M. C. Beard, "Observation of a hot-phonon bottleneck in lead-iodide perovskites," *Nature Photonics*, vol. 10, pp. 53–59, Jan. 2016.

[127] V. Abakumov, V. Perel, and I. Yassievich, *Nonradiative Recombination in Semiconductors*. Modern problems in condensed matter sciences, North-Holland, 1991.

[128] M. C. Beard, G. M. Turner, and C. A. Schmuttenmaer, "Transient photoconductivity in GaAs as measured by time-resolved terahertz spectroscopy," *Physical Review B*, vol. 62, pp. 15764–15777, Dec. 2000.

[129] R. Loudon, *The Quantum Theory of Light*. OUP Oxford, 2000.

[130] P. Würfel, "The chemical potential of radiation," *Journal of Physics C: Solid State Physics*, vol. 15, no. 18, p. 3967, 1982.

[131] G. Lasher and F. Stern, "Spontaneous and Stimulated Recombination Radiation in Semiconductors," *Physical Review*, vol. 133, pp. A553–A563, Jan. 1964.

[132] H. Ries and A. McEvoy, "Chemical potential and temperature of light," *Journal of Photochemistry and Photobiology A: Chemistry*, vol. 59, pp. 11–18, June 1991.

[133] J. K. Katahara and H. W. Hillhouse, "Quasi-Fermi level splitting and sub-bandgap absorptivity from semiconductor photoluminescence," *Journal of Applied Physics*, vol. 116, p. 173504, Nov. 2014.

[134] S. Hunsche, H. Heesel, A. Ewertz, H. Kurz, and J. H. Collet, "Spectral-hole burning and carrier thermalization in GaAs at room temperature," *Physical Review B*, vol. 48, no. 24, p. 17818, 1993.

[135] H. Haug and S. W. Koch, *Quantum Theory of the Optical and Electronic Properties of Semiconductors*. World Scientific, 5th ed., 2009.

[136] D. A. B. Miller, D. S. Chemla, D. J. Eilenberger, P. W. Smith, A. C. Gossard, and W. T. Tsang, "Large room-temperature optical nonlinearity in GaAs/$Ga_{1-x}Al_xAs$ multiple quantum well structures," *Applied Physics Letters*, vol. 41, pp. 679–681, Oct. 1982.

[137] Y. Rosenwaks, Y. Shapira, and D. Huppert, "Picosecond time-resolved luminescence studies of surface and bulk recombination processes in InP," *Physical Review B*, vol. 45, pp. 9108–9119, Apr. 1992.

[138] I. Pelant and J. Valenta, *Luminescence Spectroscopy of Semiconductors*. Luminescence Spectroscopy of Semiconductors, OUP Oxford, 2012.

[139] W. Shockley and W. T. Read, "Statistics of the Recombinations of Holes and Electrons," *Physical Review*, vol. 87, pp. 835–842, Sept. 1952.

[140] M. Lundstrom, *Fundamentals of Carrier Transport*. Cambridge University Press, July 2009.

[141] J. G. Champlain, "On the use of the term "ambipolar"," *Appl. Phys. Lett.*, p. 4, 2011.

[142] Z. Mics, A. D'Angio, S. A. Jensen, M. Bonn, and D. Turchinovich, "Density-dependent electron scattering in photoexcited GaAs in strongly diffusive regime," *Applied Physics Letters*, vol. 102, p. 231120, June 2013.

[143] N. Smith, "Classical generalization of the Drude formula for the optical conductivity," *Physical Review B*, vol. 64, p. 155106, Sept. 2001.

[144] T. L. Cocker, D. Baillie, M. Buruma, L. V. Titova, R. D. Sydora, F. Marsiglio, and F. A. Hegmann, "Microscopic origin of the Drude-Smith model," *Physical Review B*, vol. 96, p. 205439, Nov. 2017.

[145] I. Tsimperidis, T. Gregorkiewicz, H. H. P. T. Bekman, and C. J. G. M. Langerak, "Direct Observation of the Two-Stage Excitation Mechanism of Er in Si," *Physical Review Letters*, vol. 81, pp. 4748–4751, Nov. 1998.

[146] M. Forcales, M. Klik, N. Vinh, J. Phillips, J.-P. Wells, and T. Gregorkiewicz, "Two-color mid-infrared spectroscopy of optically doped semiconductors," *Journal of Luminescence*, vol. 102-103, pp. 85–90, May 2003.

[147] M. A. J. Klik, T. Gregorkiewicz, I. N. Yassievich, V. Y. Ivanov, and M. Godlewski, "Terahertz modulation of the blue photoluminescence in ZnSe," *Physical Review B*, vol. 72, p. 125205, Sept. 2005.

[148] J. Bhattacharyya, M. Wagner, M. Helm, M. Hopkinson, L. R. Wilson, and H. Schneider, "Terahertz activated luminescence of trapped carriers in InGaAs/GaAs quantum dots," *Applied Physics Letters*, vol. 97, p. 031101, July 2010.

[149] W. D. Rice, J. Kono, S. Zybell, S. Winnerl, J. Bhattacharyya, H. Schneider, M. Helm, B. Ewers, A. Chernikov, M. Koch, S. Chatterjee, G. Khitrova, H. M.

Gibbs, L. Schneebeli, B. Breddermann, M. Kira, and S. W. Koch, "Observation of Forbidden Exciton Transitions Mediated by Coulomb Interactions in Photoexcited Semiconductor Quantum Wells," *Physical Review Letters*, vol. 110, Mar. 2013.

[150] H. Hirori, K. Shinokita, M. Shirai, S. Tani, Y. Kadoya, and K. Tanaka, "Extraordinary carrier multiplication gated by a picosecond electric field pulse," *Nature Communications*, vol. 2, p. 594, Dec. 2011.

[151] B. C. Pein, W. Chang, H. Y. Hwang, J. Scherer, I. Coropceanu, X. Zhao, X. Zhang, V. Bulović, M. Bawendi, and K. A. Nelson, "Terahertz-Driven Luminescence and Colossal Stark Effect in CdSe–CdS Colloidal Quantum Dots," *Nano Letters*, vol. 17, pp. 5375–5380, Sept. 2017.

[152] M. B. Heindl, N. Kirkwood, T. Lauster, J. A. Lang, M. Retsch, P. Mulvaney, and G. Herink, "Quantum-probe field microscopy of ultrafast terahertz excitations," 2021.

[153] K. Iwaszczuk, M. Zalkovskij, A. C. Strikwerda, and P. U. Jepsen, "Nitrogen plasma formation through terahertz-induced ultrafast electron field emission," *Optica*, vol. 2, p. 116, Feb. 2015.

[154] J. Liu and X.-C. Zhang, "Plasma characterization using terahertz-wave-enhanced fluorescence," *Applied Physics Letters*, vol. 96, p. 041505, Jan. 2010.

[155] J. Liu and X.-C. Zhang, "Terahertz-Radiation-Enhanced Emission of Fluorescence from Gas Plasma," *Physical Review Letters*, vol. 103, p. 235002, Dec. 2009.

[156] J. Liu, J. Dai, S. L. Chin, and X.-C. Zhang, "Broadband terahertz wave remote sensing using coherent manipulation of fluorescence from asymmetrically ionized gases," *Nature Photonics*, vol. 4, pp. 627–631, Sept. 2010.

[157] L. A. Downes, A. R. MacKellar, D. J. Whiting, C. Bourgenot, C. S. Adams, and K. J. Weatherill, "Full-Field Terahertz Imaging at Kilohertz Frame Rates Using Atomic Vapor," *Physical Review X*, vol. 10, p. 011027, Feb. 2020.

[158] K. Kimura, Y. Morinaga, H. Imada, I. Katayama, K. Asakawa, K. Yoshioka, Y. Kim, and J. Takeda, "Terahertz-Field-Driven Scanning Tunneling Luminescence Spectroscopy," *ACS Photonics*, vol. 8, pp. 982–987, Apr. 2021.

[159] Y. Luo, G. Chen, Y. Zhang, L. Zhang, Y. Yu, F. Kong, X. Tian, Y. Zhang, C. Shan, Y. Luo, J. Yang, V. Sandoghdar, Z. Dong, and J. Hou, "Electrically Driven Single-Photon Superradiance from Molecular Chains in a Plasmonic Nanocavity," *Physical Review Letters*, vol. 122, p. 233901, June 2019.

[160] J. Liu, G. Kaur, and X.-C. Zhang, "Photoluminescence quenching dynamics in cadmium telluride and gallium arsenide induced by ultrashort terahertz pulse," *Applied Physics Letters*, vol. 97, p. 111103, Sept. 2010.

[161] Z. Chu, J. Liu, and J. Liu, "Study of THz-wave-induced photoluminescence quenching in GaAs and CdTe," *Applied Physics B*, vol. 109, pp. 113–119, Oct. 2012.

[162] F. Sekiguchi, H. Hirori, G. Yumoto, A. Shimazaki, T. Nakamura, A. Wakamiya, and Y. Kanemitsu, "Enhancing the Hot-Phonon Bottleneck Effect in a Metal Halide Perovskite by Terahertz Phonon Excitation," *Physical Review Letters*, vol. 126, p. 077401, Feb. 2021.

[163] L. Razzari, F. H. Su, G. Sharma, F. Blanchard, A. Ayesheshim, H.-C. Bandulet, R. Morandotti, J.-C. Kieffer, T. Ozaki, M. Reid, and F. A. Hegmann, "Nonlinear ultrafast modulation of the optical absorption of intense few-cycle terahertz pulses in n -doped semiconductors," *Physical Review B*, vol. 79, May 2009.

[164] M. C. Hoffmann, J. Hebling, H. Y. Hwang, K.-L. Yeh, and K. A. Nelson, "THz-pump/THz-probe spectroscopy of semiconductors at high field strengths [Invited]," *JOSA B*, vol. 26, no. 9, pp. A29–A34, 2009.

[165] J. Hebling, M. C. Hoffmann, H. Y. Hwang, K.-L. Yeh, and K. A. Nelson, "Observation of nonequilibrium carrier distribution in Ge, Si, and GaAs by terahertz pump–terahertz probe measurements," *Physical Review B*, vol. 81, p. 035201, Jan. 2010.

[166] M. C. Hoffmann and D. Turchinovich, "Semiconductor saturable absorbers for ultrafast terahertz signals," *Applied Physics Letters*, vol. 96, p. 151110, Apr. 2010.

[167] I.-C. Ho and X.-C. Zhang, "Driving intervalley scattering and impact ionization in InAs with intense terahertz pulses," *Applied Physics Letters*, vol. 98, p. 241908, June 2011.

[168] C. J. Hwang, "Quantum efficiency and radiative lifetime of the band-to-band recombination in heavily doped n-type GaAs," *Physical Review B*, vol. 6, no. 4, p. 1355, 1972.

[169] S. R. Johnson, D. Ding, J.-B. Wang, S.-Q. Yu, and Y.-H. Zhang, "Excitation dependent photoluminescence measurements of the nonradiative lifetime and quantum efficiency in GaAs," *Journal of Vacuum Science & Technology B: Microelectronics and Nanometer Structures*, vol. 25, no. 3, p. 1077, 2007.

[170] J. Crank and P. Nicolson, "A practical method for numerical evaluation of solutions of partial differential equations of the heat-conduction type," *Mathematical Proceedings of the Cambridge Philosophical Society*, vol. 43, pp. 50–67, Jan. 1947.

[171] T. Markvart and L. Castañer, "Semiconductor Materials and Modelling," in *Practical Handbook of Photovoltaics*, pp. 33–62, Elsevier, 2012.

[172] I. Tsimberova, Y. Rosenwaks, and M. Molotskii, "Minority carriers recombination in n -InP single crystals," *Journal of Applied Physics*, vol. 93, pp. 9797–9802, June 2003.

[173] M. C. Hoffmann, K.-L. Yeh, J. Hebling, and K. A. Nelson, "Efficient terahertz generation by optical rectification at 1035 nm," *Optics Express*, vol. 15, no. 18, p. 11706, 2007.

[174] V. Soghomonian, Q. Chen, R. C. Haushalter, J. Zubieta, and C. J. O'Connor, "An Inorganic Double Helix: Hydrothermal Synthesis, Structure, and Mag-

netism of Chiral $[(CH_3)_2NH_2]K_4[V_{10}O_{10}(H_2O)_2(OH)_4(PO_4)_7]\cdot 4H_2O$," *Science*, vol. 259, pp. 1596–1599, Mar. 1993.

[175] D. S. Su, "Inorganic Materials with Double-Helix Structures," *Angewandte Chemie International Edition*, vol. 50, pp. 4747–4750, May 2011.

[176] A. S. Ivanov, A. J. Morris, K. V. Bozhenko, C. J. Pickard, and A. I. Boldyrev, "Inorganic Double-Helix Structures of Unusually Simple Lithium-Phosphorus Species," *Angewandte Chemie International Edition*, vol. 51, pp. 8330–8333, Aug. 2012.

[177] M.-Q. Zhao, Q. Zhang, G.-L. Tian, and F. Wei, "Emerging double helical nanostructures," *Nanoscale*, vol. 6, no. 16, pp. 9339–9354, 2014.

[178] D. Haldar and C. Schmuck, "Metal-free double helices from abiotic backbones," *Chem. Soc. Rev.*, vol. 38, no. 2, pp. 363–371, 2009.

[179] D. Pfister, K. Schäfer, C. Ott, B. Gerke, R. Pöttgen, O. Janka, M. Baumgartner, A. Efimova, A. Hohmann, P. Schmidt, S. Venkatachalam, L. van Wüllen, U. Schürmann, L. Kienle, V. Duppel, E. Parzinger, B. Miller, J. Becker, A. Holleitner, R. Weihrich, and T. Nilges, "Inorganic Double Helices in Semiconducting SnIP," *Advanced Materials*, vol. 28, pp. 9783–9791, Nov. 2016.

[180] M. Baumgartner, R. Weihrich, and T. Nilges, "Inorganic SnIP-Type Double Helices in Main-Group Chemistry," *Chemistry - A European Journal*, vol. 23, pp. 6452–6457, May 2017.

[181] X. Li, Y. Dai, Y. Ma, M. Li, L. Yu, and B. Huang, "Landscape of DNA-like inorganic metal free double helical semiconductors and potential applications in photocatalytic water splitting," *Journal of Materials Chemistry A*, vol. 5, no. 18, pp. 8484–8492, 2017.

[182] T. K. Bijoy, P. Murugan, and V. Kumar, "Atomic and electronic structure of solids of Ge_2Br_2PN, Ge_2I_2PN, Sn_2Cl_2PN, Sn_2Br_2PN and Sn_2I_2PN inorganic double helices: a first principles study," *RSC Advances*, vol. 10, no. 25, pp. 14714–14719, 2020.

[183] C. Ott, F. Reiter, M. Baumgartner, M. Pielmeier, A. Vogel, P. Walke, S. Burger, M. Ehrenreich, G. Kieslich, D. Daisenberger, J. Armstrong, U. K. Thakur, P. Kumar, S. Chen, D. Donadio, L. S. Walter, R. T. Weitz, K. Shankar, and T. Nilges, "Flexible and Ultrasoft Inorganic 1d Semiconductor and Heterostructure Systems Based on SnIP," *Advanced Functional Materials*, vol. 29, p. 1900233, May 2019.

[184] R. Xiang, T. Inoue, Y. Zheng, A. Kumamoto, Y. Qian, Y. Sato, M. Liu, D. Tang, D. Gokhale, J. Guo, K. Hisama, S. Yotsumoto, T. Ogamoto, H. Arai, Y. Kobayashi, H. Zhang, B. Hou, A. Anisimov, M. Maruyama, Y. Miyata, S. Okada, S. Chiashi, Y. Li, J. Kong, E. I. Kauppinen, Y. Ikuhara, K. Suenaga, and S. Maruyama, "One-dimensional van der Waals heterostructures," *Science*, vol. 367, pp. 537–542, Jan. 2020.

[185] J.-K. Qin, P.-Y. Liao, M. Si, S. Gao, G. Qiu, J. Jian, Q. Wang, S.-Q. Zhang, S. Huang, A. Charnas, Y. Wang, M. J. Kim, W. Wu, X. Xu, H.-Y. Wang, L. Yang, Y. Khin Yap, and P. D. Ye, "Raman response and transport properties of tellurium atomic chains encapsulated in nanotubes," *Nature Electronics*, vol. 3, pp. 141–147, Mar. 2020.

[186] M. G. Burdanova, R. J. Kashtiban, Y. Zheng, R. Xiang, S. Chiashi, J. M. Woolley, M. Staniforth, E. Sakamoto-Rablah, X. Xie, M. Broome, J. Sloan, A. Anisimov, E. I. Kauppinen, S. Maruyama, and J. Lloyd-Hughes, "Ultrafast Optoelectronic Processes in 1D Radial van der Waals Heterostructures: Carbon, Boron Nitride, and MoS_2 Nanotubes with Coexisting Excitons and Highly Mobile Charges," *Nano Letters*, vol. 20, pp. 3560–3567, May 2020.

[187] M. R. P. Pielmeier and T. Nilges, "Formation Mechanisms for Phosphorene and SnIP," *Angewandte Chemie International Edition*, vol. 60, pp. 6816–6823, Mar. 2021.

[188] E. Üzer, P. Kumar, R. Kisslinger, P. Kar, U. K. Thakur, K. Shankar, and T. Nilges, "Vapor growth of binary and ternary phosphorus-based semiconductors into TiO_2 nanotube arrays and application in visible light driven water splitting," *Nanoscale Advances*, vol. 1, no. 8, pp. 2881–2890, 2019.

[189] M. R. P. Pielmeier, A. J. Karttunen, and T. Nilges, "Toward Atomic-Scale Inorganic Double Helices via Carbon Nanotube Matrices—Induction of Chirality to Carbon Nanotubes," *The Journal of Physical Chemistry C*, vol. 124, pp. 13338–13347, June 2020.

[190] H. Lim, H. S. Kim, R. Qazi, Y. Kwon, J. Jeong, and W. Yeo, "Advanced Soft Materials, Sensor Integrations, and Applications of Wearable Flexible Hybrid Electronics in Healthcare, Energy, and Environment," *Advanced Materials*, vol. 32, p. 1901924, Apr. 2020.

[191] P. J. Yunker, T. Still, M. A. Lohr, and A. G. Yodh, "Suppression of the coffee-ring effect by shape-dependent capillary interactions," *Nature*, vol. 476, pp. 308–311, Aug. 2011.

[192] W. Zhang, *Experimental and Computational Analysis of Random Cylinder Packings with Applications*. PhD thesis, Louisiana State University, 2006. AAI3245014.

[193] G. D. Gesesse, A. Gomis-Berenguer, M.-F. Barthe, and C. O. Ania, "On the analysis of diffuse reflectance measurements to estimate the optical properties of amorphous porous carbons and semiconductor/carbon catalysts," *Journal of Photochemistry and Photobiology A: Chemistry*, vol. 398, p. 112622, July 2020.

[194] O. Ambacher, W. Rieger, P. Ansmann, H. Angerer, T. Moustakas, and M. Stutzmann, "Sub-bandgap absorption of gallium nitride determined by Photothermal Deflection Spectroscopy," *Solid State Communications*, vol. 97, pp. 365–370, Feb. 1996.

[195] S. Hao, M. Hetzl, V. F. Kunzelmann, S. Matich, Q. Sai, C. Xia, I. D. Sharp, and M. Stutzmann, "Sub-bandgap optical spectroscopy of epitaxial β-Ga_2O_3 thin films," *Applied Physics Letters*, vol. 116, p. 092102, Mar. 2020.

[196] M. M. Shatruk, K. A. Kovnir, A. V. Shevelkov, I. A. Presniakov, and B. A. Popovkin, "First Tin Pnictide Halides $Sn_{24}P_{19.3}I_8$ and $Sn_{24}As_{19.3}I_8$: Synthesis and the Clathrate-I Type of the Crystal Structure," *Inorganic Chemistry*, vol. 38, pp. 3455–3457, July 1999.

[197] J. Heyd, G. E. Scuseria, and M. Ernzerhof, "Hybrid functionals based on a screened Coulomb potential," *The Journal of Chemical Physics*, vol. 118, pp. 8207–8215, May 2003.

[198] L. Goerigk, "A Comprehensive Overview of the DFT-D3 London-Dispersion Correction," in *Non-Covalent Interactions in Quantum Chemistry and Physics*, pp. 195–219, Elsevier, 2017.

[199] D. L. Cheung and A. Troisi, "Modelling charge transport in organic semiconductors: from quantum dynamics to soft matter," *Physical Chemistry Chemical Physics*, vol. 10, no. 39, p. 5941, 2008.

[200] C. M. Zicovich-Wilson, F. Pascale, C. Roetti, V. R. Saunders, R. Orlando, and R. Dovesi, "Calculation of the vibration frequencies of α-quartz: The effect of Hamiltonian and basis set," *Journal of Computational Chemistry*, vol. 25, pp. 1873–1881, Nov. 2004.

[201] M. Ferrero, M. Rérat, R. Orlando, and R. Dovesi, "Coupled perturbed Hartree-Fock for periodic systems: The role of symmetry and related computational aspects," *The Journal of Chemical Physics*, vol. 128, p. 014110, Jan. 2008.

[202] A. Erba, M. Ferrabone, R. Orlando, and R. Dovesi, "Accurate dynamical structure factors from *ab initio* lattice dynamics: The case of crystalline silicon," *Journal of Computational Chemistry*, vol. 34, pp. 346–354, Feb. 2013.

[203] M. Schubert, A. Mock, R. Korlacki, and V. Darakchieva, "Phonon order and reststrahlen bands of polar vibrations in crystals with monoclinic symmetry," *Physical Review B*, vol. 99, p. 041201, Jan. 2019.

[204] H. Fock, B. Kramer, and H. Büttner, "Polarons and effective electron-hole interaction in anisotropic polar crystals," *physica status solidi (b)*, vol. 67, pp. 199–206, Jan. 1975.

[205] R. W. Hellwarth and I. Biaggio, "Mobility of an electron in a multimode polar lattice," *Physical Review B*, vol. 60, pp. 299–307, July 1999.

[206] Y. Lan, B. J. Dringoli, D. A. Valverde-Chávez, C. S. Ponseca, M. Sutton, Y. He, M. G. Kanatzidis, and D. G. Cooke, "Ultrafast correlated charge and lattice motion in a hybrid metal halide perovskite," *Science Advances*, vol. 5, p. eaaw5558, May 2019.

[207] R. H. Lyddane, R. G. Sachs, and E. Teller, "On the Polar Vibrations of Alkali Halides," *Physical Review*, vol. 59, pp. 673–676, Apr. 1941.

[208] M. Born and K. Huang, *Dynamical Theory of Crystal Lattices*. International series of monographs on physics, Clarendon Press, 1988.

[209] R. Huber, C. Kübler, S. Tübel, A. Leitenstorfer, Q. T. Vu, H. Haug, F. Köhler, and M.-C. Amann, "Femtosecond Formation of Coupled Phonon-Plasmon Modes in InP: Ultrabroadband THz Experiment and Quantum Kinetic Theory," *Physical Review Letters*, vol. 94, p. 027401, Jan. 2005.

[210] P. Jepsen, D. Cooke, and M. Koch, "Terahertz spectroscopy and imaging – Modern techniques and applications," *Laser & Photonics Reviews*, vol. 5, pp. 124–166, Jan. 2011.

[211] M. C. Nuss, D. H. Auston, and F. Capasso, "Direct Subpicosecond Measurement of Carrier Mobility of Photoexcited Electrons in Gallium Arsenide," *Physical Review Letters*, vol. 58, pp. 2355–2358, June 1987.

[212] J. Shah, B. Deveaud, T. C. Damen, W. T. Tsang, A. C. Gossard, and P. Lugli, "Determination of intervalley scattering rates in GaAs by subpicosecond luminescence spectroscopy," *Physical review letters*, vol. 59, no. 19, p. 2222, 1987.

[213] D. G. Cooke, F. A. Hegmann, Y. I. Mazur, W. Q. Ma, X. Wang, Z. M. Wang, G. J. Salamo, M. Xiao, T. D. Mishima, and M. B. Johnson, "Anisotropic photoconductivity of InGaAs quantum dot chains measured by terahertz pulse spectroscopy," *Applied Physics Letters*, vol. 85, pp. 3839–3841, Oct. 2004.

[214] J. B. Baxter and C. A. Schmuttenmaer, "Conductivity of ZnO Nanowires, Nanoparticles, and Thin Films Using Time-Resolved Terahertz Spectroscopy †," *The Journal of Physical Chemistry B*, vol. 110, pp. 25229–25239, Dec. 2006.

[215] P. Parkinson, J. Lloyd-Hughes, Q. Gao, H. H. Tan, C. Jagadish, M. B. Johnston, and L. M. Herz, "Transient Terahertz Conductivity of GaAs Nanowires," *Nano Letters*, vol. 7, pp. 2162–2165, July 2007.

[216] L. V. Titova, T. L. Cocker, D. G. Cooke, X. Wang, A. Meldrum, and F. A. Hegmann, "Ultrafast percolative transport dynamics in silicon nanocrystal films," *Physical Review B*, vol. 83, p. 085403, Feb. 2011.

[217] E. Knoesel, M. Bonn, J. Shan, and T. F. Heinz, "Charge Transport and Carrier Dynamics in Liquids Probed by THz Time-Domain Spectroscopy," *Physical Review Letters*, vol. 86, pp. 340–343, Jan. 2001.

[218] O. Ostroverkhova, D. G. Cooke, S. Shcherbyna, R. F. Egerton, F. A. Hegmann, R. R. Tykwinski, and J. E. Anthony, "Bandlike transport in pentacene and functionalized pentacene thin films revealed by subpicosecond transient photoconductivity measurements," *Physical Review B*, vol. 71, p. 035204, Jan. 2005.

[219] R. D. Averitt, G. Rodriguez, A. I. Lobad, J. L. W. Siders, S. A. Trugman, and A. J. Taylor, "Nonequilibrium superconductivity and quasiparticle dynamics in $YBa_2Cu_3O_{7-\delta}$," *Physical Review B*, vol. 63, p. 140502, Mar. 2001.

[220] T. L. Cocker, L. V. Titova, S. Fourmaux, H. C. Bandulet, D. Brassard, J. C. Kieffer, M. A. El Khakani, and F. A. Hegmann, "Terahertz conductivity of the metal-insulator transition in a nanogranular VO_2 film," *Applied Physics Letters*, vol. 97, p. 221905, Nov. 2010.

[221] R. L. Milot, G. E. Eperon, H. J. Snaith, M. B. Johnston, and L. M. Herz, "Temperature-Dependent Charge-Carrier Dynamics in $CH_3NH_3PbI_3$ Perovskite Thin Films," *Advanced Functional Materials*, vol. 25, pp. 6218–6227, Oct. 2015.

[222] D. A. Valverde-Chávez, C. S. Ponseca, C. C. Stoumpos, A. Yartsev, M. G. Kanatzidis, V. Sundström, and D. G. Cooke, "Intrinsic femtosecond charge generation dynamics in single crystal $CH_3NH_3PbI_3$," *Energy & Environmental Science*, vol. 8, no. 12, pp. 3700–3707, 2015.

[223] C. J. Docherty, P. Parkinson, H. J. Joyce, M.-H. Chiu, C.-H. Chen, M.-Y. Lee, L.-J. Li, L. M. Herz, and M. B. , "Ultrafast Transient Terahertz Conductivity of Monolayer MoS_2 and WSe_2 Grown by Chemical Vapor Deposition," *ACS Nano*, vol. 8, pp. 11147–11153, Nov. 2014.

[224] S. M. Sze and K. K. Ng, *Physics of semiconductor devices*. Hoboken, N.J: Wiley-Interscience, 3rd ed ed., 2007.

[225] M. Koeberg, E. Hendry, J. M. Schins, H. A. van Laarhoven, C. F. J. Flipse, K. Reimann, M. Woerner, T. Elsaesser, and M. Bonn, "Simultaneous ultrafast probing of intramolecular vibrations and photoinduced charge carriers in rubrene using broadband time-domain THz spectroscopy," *Physical Review B*, vol. 75, p. 195216, May 2007.

[226] K. T. Butler, B. J. Dringoli, L. Zhou, P. M. Rao, A. Walsh, and L. V. Titova, "Ultrafast carrier dynamics in $BiVO_4$ thin film photoanode material: interplay between free carriers, trapped carriers and low-frequency lattice vibrations," *Journal of Materials Chemistry A*, vol. 4, no. 47, pp. 18516–18523, 2016.

[227] D. Zhao, H. Hu, R. Haselsberger, R. A. Marcus, M.-E. Michel-Beyerle, Y. M. Lam, J.-X. Zhu, C. La-o vorakiat, M. C. Beard, and E. E. M. Chia, "Monitoring Electron–Phonon Interactions in Lead Halide Perovskites Using Time-Resolved THz Spectroscopy," *ACS Nano*, vol. 13, pp. 8826–8835, Aug. 2019.

[228] P. Parkinson, H. J. Joyce, Q. Gao, H. H. Tan, X. Zhang, J. Zou, C. Jagadish, L. M. Herz, and M. B. Johnston, "Carrier Lifetime and Mobility Enhancement in Nearly Defect-Free Core-Shell Nanowires Measured Using Time-Resolved Terahertz Spectroscopy," *Nano Letters*, vol. 9, pp. 3349–3353, Sept. 2009.

[229] K. Ozawa, S. Yamamoto, R. Yukawa, R.-Y. Liu, N. Terashima, Y. Natsui, H. Kato, K. Mase, and I. Matsuda, "Correlation between Photocatalytic Activity and Carrier Lifetime: Acetic Acid on Single-Crystal Surfaces of Anatase and Rutile TiO_2," *The Journal of Physical Chemistry C*, vol. 122, pp. 9562–9569, May 2018.

[230] H. J. Joyce, C. J. Docherty, Q. Gao, H. H. Tan, C. Jagadish, J. Lloyd-Hughes, L. M. Herz, and M. B. Johnston, "Electronic properties of GaAs, InAs and InP nanowires studied by terahertz spectroscopy," *Nanotechnology*, vol. 24, p. 214006, May 2013.

[231] H. J. Joyce, J. L. Boland, C. L. Davies, S. A. Baig, and M. B. Johnston, "A review of the electrical properties of semiconductor nanowires: insights gained from terahertz conductivity spectroscopy," *Semiconductor Science and Technology*, vol. 31, p. 103003, Oct. 2016.

[232] P. Kužel and H. Němec, "Terahertz Spectroscopy of Nanomaterials: a Close Look at Charge-Carrier Transport," *Advanced Optical Materials*, vol. 8, p. 1900623, Feb. 2020.

[233] J. L. Boland, F. Amaduzzi, S. Sterzl, H. Potts, L. M. Herz, A. Fontcuberta i Morral, and M. B. Johnston, "High Electron Mobility and Insights into Temperature-Dependent Scattering Mechanisms in InAsSb Nanowires," *Nano Letters*, vol. 18, pp. 3703–3710, June 2018.

[234] C. Poellmann, P. Steinleitner, U. Leierseder, P. Nagler, G. Plechinger, M. Porer, R. Bratschitsch, C. Schüller, T. Korn, and R. Huber, "Resonant internal quantum transitions and femtosecond radiative decay of excitons in monolayer WSe_2," *Nature Materials*, vol. 14, pp. 889–893, Sept. 2015.

[235] L. Luo, L. Men, Z. Liu, Y. Mudryk, X. Zhao, Y. Yao, J. M. Park, R. Shinar, J. Shinar, K.-M. Ho, I. E. Perakis, J. Vela, and J. Wang, "Ultrafast terahertz snapshots of excitonic Rydberg states and electronic coherence in an organometal halide perovskite," *Nature Communications*, vol. 8, p. 15565, Aug. 2017.

[236] H. Němec, P. Kužel, and V. Sundström, "Far-infrared response of free charge carriers localized in semiconductor nanoparticles," *Physical Review B*, vol. 79, p. 115309, Mar. 2009.

[237] J. Kuchařík, H. Němec, and T. Ostatnický, "Terahertz conductivity and coupling between geometrical and plasmonic resonances in nanostructures," *Physical Review B*, vol. 99, p. 035407, Jan. 2019.

[238] M. Walther, D. G. Cooke, C. Sherstan, M. Hajar, M. R. Freeman, and F. A. Hegmann, "Terahertz conductivity of thin gold films at the metal-insulator percolation transition," *Physical Review B*, vol. 76, p. 125408, Sept. 2007.

[239] D. G. Cooke, A. Meldrum, and P. Uhd Jepsen, "Ultrabroadband terahertz conductivity of Si nanocrystal films," *Applied Physics Letters*, vol. 101, p. 211107, Nov. 2012.

[240] S. A. Jensen, R. Ulbricht, A. Narita, X. Feng, K. Müllen, T. Hertel, D. Turchinovich, and M. Bonn, "Ultrafast Photoconductivity of Graphene Nanoribbons and Carbon Nanotubes," *Nano Letters*, vol. 13, pp. 5925–5930, Dec. 2013.

[241] J. M. LaForge, T. L. Cocker, A. L. Beaudry, K. Cui, R. T. Tucker, M. T. Taschuk, F. A. Hegmann, and M. J. Brett, "Conductivity control of as-grown branched indium tin oxide nanowire networks," *Nanotechnology*, vol. 25, p. 035701, Jan. 2014.

[242] W. H. Evers, J. M. Schins, M. Aerts, A. Kulkarni, P. Capiod, M. Berthe, B. Grandidier, C. Delerue, H. S. J. van der Zant, C. van Overbeek, J. L. Peters, D. Vanmaekelbergh, and L. D. A. Siebbeles, "High charge mobility in two-dimensional percolative networks of PbSe quantum dots connected by atomic bonds," *Nature Communications*, vol. 6, p. 8195, Nov. 2015.

[243] H. Liu, J. Lu, Z. Yang, J. Teng, L. Ke, X. Zhang, L. Tong, and C. H. Sow, "Ultrahigh photoconductivity of bandgap-graded CdS_xSe_{1-x} nanowires probed by terahertz spectroscopy," *Scientific Reports*, vol. 6, p. 27387, July 2016.

[244] M. Ziwritsch, S. Müller, H. Hempel, T. Unold, F. F. Abdi, R. van de Krol, D. Friedrich, and R. Eichberger, "Direct Time-Resolved Observation of Carrier Trapping and Polaron Conductivity in $BiVO_4$," *ACS Energy Letters*, vol. 1, pp. 888–894, Nov. 2016.

[245] L. V. Titova, T. L. Cocker, S. Xu, J.-M. Baribeau, X. Wu, D. J. Lockwood, and F. A. Hegmann, "Ultrafast carrier dynamics and the role of grain boundaries in polycrystalline silicon thin films grown by molecular beam epitaxy," *Semiconductor Science and Technology*, vol. 31, p. 105017, Oct. 2016.

[246] G. Li, N. Amer, H. A. Hafez, S. Huang, D. Turchinovich, V. N. Mochalin, F. A. Hegmann, and L. V. Titova, "Dynamical Control over Terahertz Electromagnetic Interference Shielding with 2D $Ti_3C_2T_y$ MXene by Ultrafast Optical Pulses," *Nano Letters*, vol. 20, pp. 636–643, Jan. 2020.

[247] Z. Yu, Z.-Y. Ong, S. Li, J.-B. Xu, G. Zhang, Y.-W. Zhang, Y. Shi, and X. Wang, "Analyzing the Carrier Mobility in Transition-Metal Dichalcogenide MoS_2 Field-Effect Transistors," *Advanced Functional Materials*, vol. 27, p. 1604093, May 2017.

[248] X. Gao and Z. Zhao, "High mobility organic semiconductors for field-effect transistors," *Science China Chemistry*, vol. 58, pp. 947–968, June 2015.

[249] G. Schweicher, G. D'Avino, M. T. Ruggiero, D. J. Harkin, K. Broch, D. Venkateshvaran, G. Liu, A. Richard, C. Ruzié, J. Armstrong, A. R. Kennedy, K. Shankland, K. Takimiya, Y. H. Geerts, J. A. Zeitler, S. Fratini, and H. Sirringhaus, "Chasing the "Killer" Phonon Mode for the Rational Design of Low-Disorder, High-Mobility Molecular Semiconductors," *Advanced Materials*, vol. 31, p. 1902407, Oct. 2019.

[250] C. Kübler, H. Ehrke, R. Huber, R. Lopez, A. Halabica, R. F. Haglund, and A. Leitenstorfer, "Coherent Structural Dynamics and Electronic Correlations during an Ultrafast Insulator-to-Metal Phase Transition in VO_2," *Physical Review Letters*, vol. 99, p. 116401, Sept. 2007.

[251] P. Gaal, W. Kuehn, K. Reimann, M. Woerner, T. Elsaesser, and R. Hey, "Internal motions of a quasiparticle governing its ultrafast nonlinear response," *Nature*, vol. 450, pp. 1210–1213, Dec. 2007.

[252] S. Sim, M. Brahlek, N. Koirala, S. Cha, S. Oh, and H. Choi, "Ultrafast terahertz dynamics of hot Dirac-electron surface scattering in the topological insulator Bi_2Se_3," *Physical Review B*, vol. 89, p. 165137, Apr. 2014.

[253] W. Yang, S. Lee, H.-C. Kwon, J. Tan, H. Lee, J. Park, Y. Oh, H. Choi, and J. Moon, "Time-Resolved Observations of Photo-Generated Charge-Carrier Dynamics in Sb_2Se_3 Photocathodes for Photoelectrochemical Water Splitting," *ACS Nano*, vol. 12, pp. 11088–11097, Nov. 2018.

[254] E. Cinquanta, D. Meggiolaro, S. G. Motti, M. Gandini, M. J. Alcocer, Q. A. Akkerman, C. Vozzi, L. Manna, F. De Angelis, A. Petrozza, and S. Stagira, "Ultrafast THz Probe of Photoinduced Polarons in Lead-Halide Perovskites," *Physical Review Letters*, vol. 122, p. 166601, Apr. 2019.

[255] Y. Lan, X. Tao, X. Kong, Y. He, X. Zheng, M. Sutton, M. G. Kanatzidis, H. Guo, and D. G. Cooke, "Coherent charge-phonon correlations and exciton dynamics in orthorhombic $CH_3NH_3PbI_3$ measured by ultrafast multi-THz spectroscopy," *The Journal of Chemical Physics*, vol. 151, p. 214201, Dec. 2019.

[256] P. Yu and M. Cardona, *Fundamentals of Semiconductors: Physics and Materials Properties*. Graduate Texts in Physics, Springer Berlin Heidelberg, 2010.

[257] B. B. Varga, "Coupling of Plasmons to Polar Phonons in Degenerate Semiconductors," *Physical Review*, vol. 137, pp. A1896–A1902, Mar. 1965.

[258] D. Turchinovich, F. D'Angelo, and M. Bonn, "Femtosecond-timescale buildup of electron mobility in GaAs observed via ultrabroadband transient terahertz spectroscopy," *Applied Physics Letters*, vol. 110, p. 121102, Mar. 2017.

[259] M. Li, J. R. Reimers, J. F. Dobson, and T. Gould, "Faraday cage screening reveals intrinsic aspects of the van der Waals attraction," *Proceedings of the National Academy of Sciences*, vol. 115, pp. E10295–E10302, Oct. 2018.

[260] Y. Zhou, L. You, S. Wang, Z. Ku, H. Fan, D. Schmidt, A. Rusydi, L. Chang, L. Wang, P. Ren, L. Chen, G. Yuan, L. Chen, and J. Wang, "Giant photo-

striction in organic–inorganic lead halide perovskites," *Nature Communications*, vol. 7, p. 11193, Sept. 2016.

[261] D. Zheng, C. Zhu, Z. Li, Z. Li, J. Li, S. Sun, Y. Zhang, F. Wang, H. Tian, H. Yang, and J. Li, "Ultrafast lattice and electronic dynamics in single-walled carbon nanotubes," *Nanoscale Advances*, vol. 2, no. 7, pp. 2808–2813, 2020.

[262] C. Neumann, S. Reichardt, P. Venezuela, M. Drögeler, L. Banszerus, M. Schmitz, K. Watanabe, T. Taniguchi, F. Mauri, B. Beschoten, S. V. Rotkin, and C. Stampfer, "Raman spectroscopy as probe of nanometre-scale strain variations in graphene," *Nature Communications*, vol. 6, p. 8429, Dec. 2015.

[263] M. L. Marcondes, R. M. Wentzcovitch, and L. V. Assali, "Importance of van der Waals interaction on structural, vibrational, and thermodynamic properties of NaCl," *Solid State Communications*, vol. 273, pp. 11–16, May 2018.

[264] J. C. M. Garnett and J. Larmor, "Xii. colours in metal glasses and in metallic films," *Philosophical Transactions of the Royal Society of London. Series A, Containing Papers of a Mathematical or Physical Character*, vol. 203, no. 359-371, pp. 385–420, 1904.

[265] H.-K. Nienhuys and V. Sundström, "Influence of plasmons on terahertz conductivity measurements," *Applied Physics Letters*, vol. 87, p. 012101, July 2005.

[266] S. A. Jensen, K.-J. Tielrooij, E. Hendry, M. Bonn, I. Rychetský, and H. Němec, "Terahertz Depolarization Effects in Colloidal TiO_2 Films Reveal Particle Morphology," *The Journal of Physical Chemistry C*, vol. 118, pp. 1191–1197, Jan. 2014.

[267] P. Kužel and H. Němec, "Terahertz conductivity in nanoscaled systems: effective medium theory aspects," *Journal of Physics D: Applied Physics*, vol. 47, p. 374005, Sept. 2014.

[268] V. Myroshnychenko, J. Rodríguez-Fernández, I. Pastoriza-Santos, A. M. Funston, C. Novo, P. Mulvaney, L. M. Liz-Marzán, and F. J. García de Abajo,

"Modelling the optical response of gold nanoparticles," *Chemical Society Reviews*, vol. 37, no. 9, p. 1792, 2008.

[269] V. A. Markel, "Introduction to the Maxwell Garnett approximation: tutorial," *Journal of the Optical Society of America A*, vol. 33, p. 1244, July 2016.

[270] X. Zou, J. Luo, D. Lee, C. Cheng, D. Springer, S. K. Nair, S. A. Cheong, H. J. Fan, and E. E. M. Chia, "Temperature-dependent terahertz conductivity of tin oxide nanowire films," *Journal of Physics D: Applied Physics*, vol. 45, p. 465101, Nov. 2012.

[271] A. Leitenstorfer, S. Hunsche, J. Shah, M. C. Nuss, and W. H. Knox, "Detectors and sources for ultrabroadband electro-optic sampling: Experiment and theory," *Applied Physics Letters*, vol. 74, pp. 1516–1518, Mar. 1999.

[272] X. Zheng, A. Sinyukov, and L. M. Hayden, "Broadband and gap-free response of a terahertz system based on a poled polymer emitter-sensor pair," *Applied Physics Letters*, vol. 87, p. 081115, Aug. 2005.

[273] N. Karpowicz, J. Dai, X. Lu, Y. Chen, M. Yamaguchi, H. Zhao, X.-C. Zhang, L. Zhang, C. Zhang, M. Price-Gallagher, C. Fletcher, O. Mamer, A. Lesimple, and K. Johnson, "Coherent heterodyne time-domain spectrometry covering the entire "terahertz gap"," *Applied Physics Letters*, vol. 92, no. 1, p. 011131, 2008.

[274] X. Lu and X.-C. Zhang, "Balanced terahertz wave air-biased-coherent-detection," *Applied Physics Letters*, vol. 98, p. 151111, Apr. 2011.

[275] M. Pathirane, B. Iheanacho, A. Tamang, C.-H. Lee, R. Lujan, D. Knipp, and W. S. Wong, "Hybrid ZnO nanowire/a-Si:H thin-film radial junction solar cells using nanoparticle front contacts," *Applied Physics Letters*, vol. 107, p. 143903, Oct. 2015.

[276] M. R. Bergren, C. E. Kendrick, N. R. Neale, J. M. Redwing, R. T. Collins, T. E. Furtak, and M. C. Beard, "Ultrafast Electrical Measurements of Isolated Silicon Nanowires and Nanocrystals," *The Journal of Physical Chemistry Letters*, vol. 5, pp. 2050–2057, June 2014.

[277] O. Ostroverkhova, D. G. Cooke, F. A. Hegmann, J. E. Anthony, V. Podzorov, M. E. Gershenson, O. D. Jurchescu, and T. T. M. Palstra, "Ultrafast carrier dynamics in pentacene, functionalized pentacene, tetracene, and rubrene single crystals," *Applied Physics Letters*, vol. 88, p. 162101, Apr. 2006.

[278] G. De Filippis, V. Cataudella, A. Mishchenko, N. Nagaosa, A. Fierro, and A. de Candia, "Crossover from Super- to Subdiffusive Motion and Memory Effects in Crystalline Organic Semiconductors," *Physical Review Letters*, vol. 114, p. 086601, Feb. 2015.

[279] S. Fratini, D. Mayou, and S. Ciuchi, "The Transient Localization Scenario for Charge Transport in Crystalline Organic Materials," *Advanced Functional Materials*, vol. 26, pp. 2292–2315, Apr. 2016.

[280] P. Uhd Jepsen, W. Schairer, I. H. Libon, U. Lemmer, N. E. Hecker, M. Birkholz, K. Lips, and M. Schall, "Ultrafast carrier trapping in microcrystalline silicon observed in optical pump–terahertz probe measurements," *Applied Physics Letters*, vol. 79, pp. 1291–1293, Aug. 2001.

[281] D. G. Sahota, R. Liang, M. Dion, P. Fournier, H. A. Dąbkowska, G. M. Luke, and J. S. Dodge, "Many-body recombination in photoexcited insulating cuprates," *Physical Review Research*, vol. 1, p. 033214, Dec. 2019.

[282] J.-H. Choi, A. T. Fafarman, S. J. Oh, D.-K. Ko, D. K. Kim, B. T. Diroll, S. Muramoto, J. G. Gillen, C. B. Murray, and C. R. Kagan, "Bandlike Transport in Strongly Coupled and Doped Quantum Dot Solids: A Route to High-Performance Thin-Film Electronics," *Nano Letters*, vol. 12, pp. 2631–2638, May 2012.

[283] L. S. Kadyrov, E. S. Zhukova, V. I. Torgashev, B. P. Gorshunov, A. S. Prokhorov, E. A. Motovilova, F. Fischgrabe, V. Moshnyaga, T. Zhang, R. Kremer, U. Pracht, S. Zapf, J. Pokorný, G. Untereiner, S. Kamba, and M. Dressel, "Terahertz-infrared spectroscopy of overdoped manganites $La_{1-x}Ca_xMnO_3$," *Physica B: Condensed Matter*, vol. 460, pp. 199–201, Mar. 2015.

[284] B. T. Benton, B. L. Greenberg, E. Aydil, U. R. Kortshagen, and S. A. Campbell, "Variable range hopping conduction in ZnO nanocrystal thin films," *Nanotechnology*, vol. 29, p. 415202, Oct. 2018.

[285] X. Shi, H. Chen, F. Hao, R. Liu, T. Wang, P. Qiu, U. Burkhardt, Y. Grin, and L. Chen, "Room-temperature ductile inorganic semiconductor," *Nature Materials*, vol. 17, pp. 421–426, May 2018.

[286] S. Scarfe, W. Cui, A. Luican-Mayer, and J.-M. Ménard, "Systematic THz study of the substrate effect in limiting the mobility of graphene," *Scientific Reports*, vol. 11, p. 8729, Dec. 2021.

[287] W. S. Hwang, P. Zhao, K. Tahy, L. O. Nyakiti, V. D. Wheeler, R. L. Myers-Ward, C. R. Eddy, D. K. Gaskill, J. A. Robinson, W. Haensch, H. G. Xing, A. Seabaugh, and D. Jena, "Graphene nanoribbon field-effect transistors on wafer-scale epitaxial graphene on SiC substrates," *APL Materials*, vol. 3, p. 011101, Jan. 2015.

[288] M. C. Beard, J. L. Blackburn, and M. J. Heben, "Photogenerated Free Carrier Dynamics in Metal and Semiconductor Single-Walled Carbon Nanotube Films," *Nano Letters*, vol. 8, pp. 4238–4242, Dec. 2008.

[289] D. König, K. Casalenuovo, Y. Takeda, G. Conibeer, J. Guillemoles, R. Patterson, L. Huang, and M. Green, "Hot carrier solar cells: Principles, materials and design," *Physica E: Low-dimensional Systems and Nanostructures*, vol. 42, pp. 2862–2866, Sept. 2010.

[290] M. Kim, M. Lin, J. Son, H. Xu, and J.-M. Nam, "Hot-Electron-Mediated Photochemical Reactions: Principles, Recent Advances, and Challenges," *Advanced Optical Materials*, vol. 5, p. 1700004, Aug. 2017.

[291] C. Q. Xia, M. Monti, J. L. Boland, L. M. Herz, J. Lloyd-Hughes, M. R. Filip, and M. B. Johnston, "Hot electron cooling in InSb probed by ultrafast time-resolved terahertz cyclotron resonance," *Physical Review B*, vol. 103, p. 245205, June 2021.

[292] M. X. Na, A. K. Mills, F. Boschini, M. Michiardi, B. Nosarzewski, R. P. Day, E. Razzoli, A. Sheyerman, M. Schneider, G. Levy, S. Zhdanovich, T. P. Devereaux, A. F. Kemper, D. J. Jones, and A. Damascelli, "Direct determination of mode-projected electron-phonon coupling in the time domain," *Science*, vol. 366, pp. 1231–1236, Dec. 2019.

[293] G. Vampa, T. Hammond, N. Thiré, B. Schmidt, F. Légaré, C. McDonald, T. Brabec, D. Klug, and P. Corkum, "All-Optical Reconstruction of Crystal Band Structure," *Physical Review Letters*, vol. 115, p. 193603, Nov. 2015.

[294] F. Blanchard and K. Tanaka, "Improving time and space resolution in electro-optic sampling for near-field terahertz imaging," *Optics Letters*, vol. 41, p. 4645, Oct. 2016.

[295] C. La-o vorakiat, L. Cheng, T. Salim, R. A. Marcus, M.-E. Michel-Beyerle, Y. M. Lam, and E. E. M. Chia, "Phonon features in terahertz photoconductivity spectra due to data analysis artifact: A case study on organometallic halide perovskites," *Applied Physics Letters*, vol. 110, p. 123901, Mar. 2017.

[296] R. C. Rumpf, "Improved formulation of scattering matrices for semi-analytical methods that is consistent with convention," *Progress In Electromagnetics Research B*, vol. 35, pp. 241–261, 2011.

[297] R. Aksoy, E. Selvi, and Y. Ma, "X-ray diffraction study of molybdenum diselenide to 35.9 GPa," *Journal of Physics and Chemistry of Solids*, vol. 69, pp. 2138–2140, Sept. 2008.

[298] J. Dong and G. Ouyang, "Thickness-Dependent Semiconductor-to-Metal Transition in Molybdenum Tungsten Disulfide Alloy under Hydrostatic Pressure," *ACS Omega*, vol. 4, pp. 8641–8649, May 2019.

[299] V. Kumar, J. K. Singh, and G. M. Prasad, "Elastic properties of elemental, binary and ternary semiconductor materials," *Indian Journal of Pure & Applied Physics*, vol. 53, p. 7, 2015.

[300] J. Feng, "Mechanical properties of hybrid organic-inorganic $CH_3NH_3BX_3$ (B=Sn,Pb;X=Br,I) perovskites for solar cell absorbers," *APL Materials*, vol. 2, p. 081801, Aug. 2014.

[301] A. Ferreira, A. Létoublon, S. Paofai, S. Raymond, C. Ecolivet, B. Rufflé, S. Cordier, C. Katan, M. Saidaminov, A. Zhumekenov, O. Bakr, J. Even, and P. Bourges, "Elastic Softness of Hybrid Lead Halide Perovskites," *Physical Review Letters*, vol. 121, p. 085502, Aug. 2018.

[302] R. Keller, W. B. Holzapfel, and H. Schulz, "Effect of pressure on the atom positions in Se and Te," *Physical Review B*, vol. 16, pp. 4404–4412, Nov. 1977.

[303] A. K. Bandyopadhyay and D. B. Singh, "Pressure induced phase transformations and band structure of different high pressure phases in tellurium," *Pramana*, vol. 52, pp. 303–319, Mar. 1999.

[304] M. Oehzelt, A. Aichholzer, R. Resel, G. Heimel, E. Venuti, and R. G. Della Valle, "Crystal structure of oligoacenes under high pressure," *Physical Review B*, vol. 74, p. 104103, Sept. 2006.

[305] Y. Wu, A. R. Chew, G. A. Rojas, G. Sini, G. Haugstad, A. Belianinov, S. V. Kalinin, H. Li, C. Risko, J.-L. Brédas, A. Salleo, and C. D. Frisbie, "Strain effects on the work function of an organic semiconductor," *Nature Communications*, vol. 7, p. 10270, Apr. 2016.

[306] P. Wang, R. Zhao, L. Wu, and M. Zhang, "Effect of Y doping on high-pressure behavior of Ag_2S nanocrystals," *RSC Advances*, vol. 7, no. 56, pp. 35105–35110, 2017.

[307] L. Cartz, S. R. Srinivasa, R. J. Riedner, J. D. Jorgensen, and T. G. Worlton, "Effect of pressure on bonding in black phosphorus," *The Journal of Chemical Physics*, vol. 71, pp. 1718–1721, Aug. 1979.

[308] B. Liu, Y. Li, Y. Yue, Y. Tao, Z. Qin, and C. Cheng, "Mechanically Strengthened Amorphous Silicon by Phosphorus: A Molecular Dynamics Simulation

and Experimental Study," *DEStech Transactions on Engineering and Technology Research*, Jan. 2019.

[309] U. Lang, N. Naujoks, and J. Dual, "Mechanical characterization of PEDOT:PSS thin films," *Synthetic Metals*, vol. 159, pp. 473–479, Mar. 2009.

[310] M. S. Uddin and J. Ju, "Enhanced Coarse-Graining of Thermoplastic Polyurethane Elastomer for Multiscale Modeling," *Journal of Engineering Materials and Technology*, vol. 139, p. 011001, Jan. 2017.

[311] N. R. Pradhan, D. Rhodes, Y. Xin, S. Memaran, L. Bhaskaran, M. Siddiq, S. Hill, P. M. Ajayan, and L. Balicas, "Ambipolar Molybdenum Diselenide Field-Effect Transistors: Field-Effect and Hall Mobilities," *ACS Nano*, vol. 8, pp. 7923–7929, Aug. 2014.

[312] H. Schmidt, S. Wang, L. Chu, M. Toh, R. Kumar, W. Zhao, A. H. Castro Neto, J. Martin, S. Adam, B. Özyilmaz, and G. Eda, "Transport Properties of Monolayer MoS_2 Grown by Chemical Vapor Deposition," *Nano Letters*, vol. 14, pp. 1909–1913, Apr. 2014.

[313] Y. Cui, R. Xin, Z. Yu, Y. Pan, Z.-Y. Ong, X. Wei, J. Wang, H. Nan, Z. Ni, Y. Wu, T. Chen, Y. Shi, B. Wang, G. Zhang, Y.-W. Zhang, and X. Wang, "High-Performance Monolayer WS_2 Field-Effect Transistors on High-κ Dielectrics," *Advanced Materials*, vol. 27, pp. 5230–5234, Sept. 2015.

[314] O. Madelung, ed., *Semiconductors — Basic Data*. Berlin, Heidelberg: Springer Berlin Heidelberg, 1996.

[315] J. Gutowski, K. Sebald, and T. Voss, "CdTe: mobility," in *New Data and Updates for II-VI Compounds* (U. Roessler, ed.), vol. 44B, pp. 142–147, Berlin, Heidelberg: Springer Berlin Heidelberg, 2009. ISSN: 1616-9549 Series Title: Landolt-Börnstein - Group III Condensed Matter.

[316] L. M. Herz, "Charge-Carrier Mobilities in Metal Halide Perovskites: Fundamental Mechanisms and Limits," *ACS Energy Letters*, vol. 2, pp. 1539–1548, July 2017.

[317] P. Bhaskar, A. W. Achtstein, S. L. Diedenhofen, and L. D. A. Siebbeles, "Mobility and Decay Dynamics of Charge Carriers in One-Dimensional Selenium van der Waals Solid," *The Journal of Physical Chemistry C*, vol. 121, pp. 18917–18921, Aug. 2017.

[318] O. Jurchescu, M. Popinciuc, B. van Wees, and T. Palstra, "Interface-controlled, high-mobility organic transistors," *Advanced Materials*, vol. 19, no. 5, pp. 688–692, 2007.

[319] M. Yamagishi, J. Takeya, Y. Tominari, Y. Nakazawa, T. Kuroda, S. Ikehata, M. Uno, T. Nishikawa, and T. Kawase, "High-mobility double-gate organic single-crystal transistors with organic crystal gate insulators," *Applied Physics Letters*, vol. 90, p. 182117, Apr. 2007.

[320] C. Reese, W.-J. Chung, M.-m. Ling, M. Roberts, and Z. Bao, "High-performance microscale single-crystal transistors by lithography on an elastomer dielectric," *Applied Physics Letters*, vol. 89, p. 202108, Nov. 2006.

[321] A. Rudenko, S. Brener, and M. Katsnelson, "Intrinsic Charge Carrier Mobility in Single-Layer Black Phosphorus," *Physical Review Letters*, vol. 116, p. 246401, June 2016.

[322] X. Wang, X. Zhang, L. Sun, D. Lee, S. Lee, M. Wang, J. Zhao, Y. Shao-Horn, M. Dincă, T. Palacios, and K. K. Gleason, "High electrical conductivity and carrier mobility in oCVD PEDOT thin films by engineered crystallization and acid treatment," *Science Advances*, vol. 4, p. eaat5780, Sept. 2018.

[323] D. H. Park, H. W. Park, J. W. Chung, K. Nam, S. Choi, Y. S. Chung, H. Hwang, B. Kim, and D. H. Kim, "Highly Stretchable, High-Mobility, Free-Standing All-Organic Transistors Modulated by Solid-State Elastomer Electrolytes," *Advanced Functional Materials*, vol. 29, p. 1808909, May 2019.

[324] V. Jelic, *Imaging Ultrafast Dynamics on the Atomic Scale with a Terahertz Scanning Tunneling Microscope*. PhD thesis, University of Alberta, 2018.

[325] G. De Los Reyes, *Ultrafast Photoluminescence Spectroscopy of Silicon Nanocrystals*. PhD, University of Alberta, 2015.

[326] D. E. Spence, P. N. Kean, and W. Sibbett, "60-fsec pulse generation from a self-mode-locked Ti:sapphire laser," *Optics Letters*, vol. 16, no. 1, pp. 42–44, 1991.

[327] T. Brabec, C. Spielmann, P. F. Curley, and F. Krausz, "Kerr lens mode locking," *Optics Letters*, vol. 17, no. 18, pp. 1292–1294, 1992.

[328] G. Herink, "Resolving the build-up of femtosecond mode-locking with single-shot spectroscopy at 90 MHz frame rate," *Nature Photonics*, vol. 10, p. 7, 2016.

[329] D. Strickland and G. Mourou, "Compression of amplified chirped optical pulses," *Optics Communications*, vol. 56, no. 3, pp. 219–221, 1985.

[330] B. N. Carnio and A. Y. Elezzabi, "Investigation of ultra-broadband terahertz generation from sub-wavelength lithium niobate waveguides excited by few-cycle femtosecond laser pulses," *Optics Express*, vol. 25, p. 20573, Aug. 2017.

[331] L. Xu, X.-C. Zhang, and D. H. Auston, "Terahertz beam generation by femtosecond optical pulses in electro-optic materials," *Applied Physics Letters*, vol. 61, pp. 1784–1786, Oct. 1992.

[332] Z. Wang, F. Su, and F. A. Hegmann, "Ultrafast imaging of terahertz Cherenkov waves and transition-like radiation in $LiNbO_3$," *Optics Express*, vol. 23, p. 8073, Mar. 2015.

[333] T. Seifert, S. Jaiswal, U. Martens, J. Hannegan, L. Braun, P. Maldonado, F. Freimuth, A. Kronenberg, J. Henrizi, I. Radu, E. Beaurepaire, Y. Mokrousov, P. M. Oppeneer, M. Jourdan, G. Jakob, D. Turchinovich, L. M. Hayden, M. Wolf, M. Münzenberg, M. Kläui, and T. Kampfrath, "Efficient metallic spintronic emitters of ultrabroadband terahertz radiation," *Nature Photonics*, vol. 10, pp. 483–488, July 2016.

[334] A. Rehn, D. Jahn, J. C. Balzer, and M. Koch, "Periodic sampling errors in terahertz time-domain measurements," *Optics Express*, vol. 25, p. 6712, Mar. 2017.

Appendix A

Appendices for SnIP Chapters

A.1 Estimate of the uncertainty f_{LO} and α

In the calculation of f_{LO} using the Lyddane-Sachs-Teller relation (see section 7.5.4), there is uncertainty in: 1) the film thickness, 2) the fill fraction, 3) the difference between $\epsilon_{\parallel}$ and $\epsilon_{\perp}$, 4) experimental uncertainty in the amplitude of the dielectric function due to fluctuations in the THz pulse amplitude during acquisition, and 5) the TO frequency from experiment, and 6) the size of the off-diagonal components. We found that the uncertainty in fit parameters (4 and 5) is small compared to the other uncertainties so they will not be considered in what follows. Moreover, the calculation of the polarization-dependent dielectric function (see 7.22) suggests that the y and z components are small in the region of interest so that the off-diagonal component in the vicinity of f_{LO} is likely dominated by the x-polarized mode. Since the polarizability of this mode is zero near the LO resonance, this implies that the off-diagonal component should be zero.

A Monte Carlo sampling of the possible values of 1), 2) and 3) was used to estimate f_{LO}. A Gaussian distribution of each parameter was assumed, as shown in Figure A.1a-c. For the filling fraction, we use a mean of 0.4 with a standard deviation of 0.2, for the film thickness we use a mean of 1.5 μm with a standard deviation of 0.5 μm (from section 7.3.1), and we parameterize the ratio $\epsilon_{\perp}/\epsilon_{\parallel}$ to be between 0.9 and 1.5. This is motivated by the calculations in Figure 7.21, that suggest a ratio of $\epsilon_{\perp}/\epsilon_{\parallel} = 1.2$. The bounds of ± 0.3 were chosen based on sampling the calculated ratio in several frequency ranges away from resonances. Figure A.1d shows the distribution

of LO frequencies calculated by sampling from the distributions in Figure A.1a-c. The red arrow, labeled f_{opt}, indicates the calculated result from the simple calculation using the optimum parameters, which is close to the average of the distribution. The distribution is also asymmetric, biased towards higher frequencies of the LO phonon. From this distribution we estimate a value of $f_{LO} = 1.74 \pm 0.05$ THz.

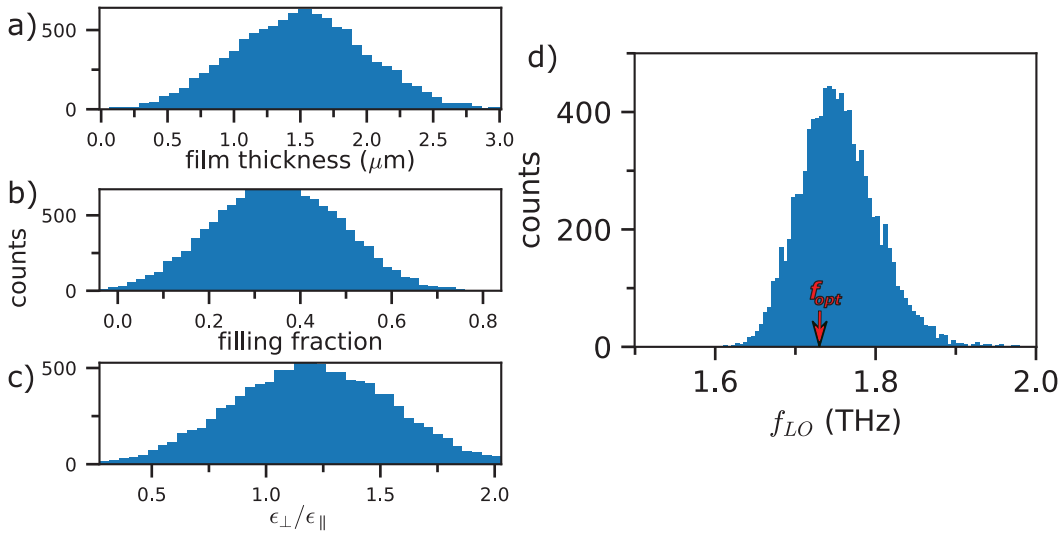

Fig. A.1: Monte Carlo estimate of LO frequency. Distribution of **a** film thicknesses, **b** filling fraction, and **c** ratio of the parallel/perpendicular dielectric function used to estimate the range of possible LO frequencies. **d** Distribution of possible LO frequencies, peaked at 1.74 THz with possible values as low as 1.63 THz and as high as 1.9 THz.

Equation 7.21 can also be used to calculate the range of possible values of α, the Fröhlich coupling constant. In Figure A.2a, we show the distribution of values of α extracted from the Monte Carlo sampling of the LO frequency. As with the LO frequency, we see that the distribution is asymmetric, with a tail of possible values beyond $\alpha = 2$ and below $\alpha = 0.1$. From this distribution, we estimate a Fröhlich constant of $\alpha = 0.6 \pm 0.4$, which suggests that we are likely in the weak-coupling regime where transport should be Drude-like. Nevertheless, it is clear from the width of the distribution the possibility of, at least, intermediate coupling with $\alpha \approx 2$. Future experiments with more controlled systems and more sensitive THz spectrometers are therefore necessary to fully understand the electron-phonon coupling in SnIP.

Finally, the renormalization of the effective mass can be estimated using $m^*_{rn}/m^* =$

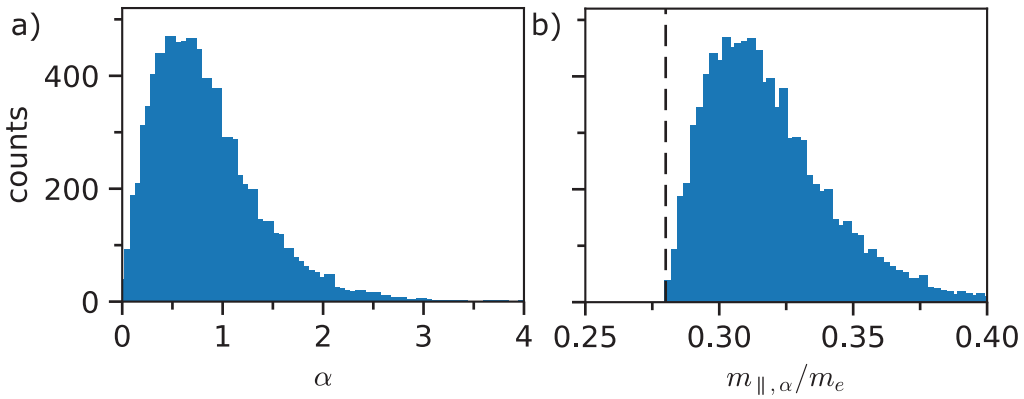

Fig. A.2: Monte Carlo estimate of Fröhlich cconstant and renormalized electron mass. Distribution of values of **a** α and **b** $m_{\parallel}/m_e$ resulting from the range of estimates in A.1a-c.

$1 + \alpha/6$ along with the Monte Carlo sampling, as shown in Figure A.2. Here, the vertical dashed line indicates the calculated effective mass extracted directly from DFT, which provides a lower bound for the polaron mass. The Fröhlich coupling results in only a small renormalization and results in a polaron mass of 0.31 m_e versus the calculated band mass of 0.28 m_e.

A.2 Linearity of Reflectance and Transmittance

To rule out optical nonlinearity as the source of nonlinear scaling in Figure 8.17, we studied the ultrafast diffuse reflectance at 400 nm and ultrafast transmission at 800 nm. To mimic the excitation conditions of the TRTS experiment, a partially closed iris was imaged onto the sample location. The pulse was first projected onto a thin Teflon screen and imaged with a CMOS camera. The beam profile was a super Gaussian rather than flat top due to the imperfect imaging conditions, which was acceptable for this experiment that aims to study only the scaling with fluence. The iris size was adjusted until the spot size was approximately 1 mm, similar to the aperture size in the TRTS measurements. The incident beam power was adjusted and measured after the iris and uniform illumination was assumed to calculated the fluence.

Shown in Figure A.3a is the diffusely reflected power for 400 nm excitation. Diffuse reflection was chosen for 400 nm the only transmission through the film was leakage

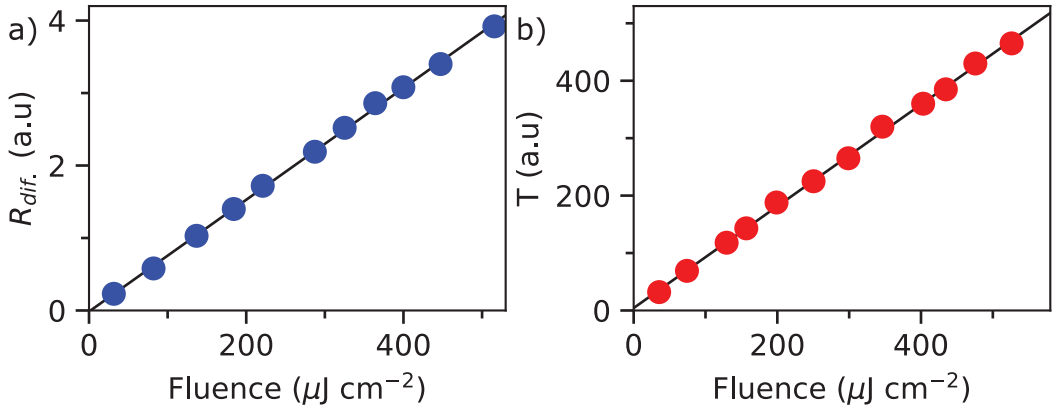

Fig. A.3: Linearity of ultrafast optical excitation. a) Diffusely reflected power with 400 nm excitation. b) Transmitted power with 800 nm excitation.

through gaps in nanowire coverage. Care was taken to avoid the specularly reflected portion of the beam as it was composed partly of the front-surface reflection from the quartz substrate due to micron-scale gaps in the film. The diffuse reflectance should be proportional to the absorption via the Kubelka-Munk transformation, as in section 7.3.2. Deviations from linearity in the reflected beam power should therefore be an indication of optical nonlinearity, however, in Figure A.3a the signal is linear within the sensitivity of the measurement. This shows that absorption saturation is not the dominant mechanism of the saturation behavior in the photoconductivity with 400 nm excitation shown in Figure 8.17a.

Shown in Figure A.3b is the transmitted power with 800 nm excitation. Here, the transmitted power is significantly larger than can be accounted for by the micron-scale gaps in the film. Transmission was therefore chosen as opposed to diffuse reflection due to the relative ease of the measurement. Again, the signal is linear with incident power through the whole range of fluence. The decrease in transmission expected if 2-photon absorption was occurring is not seen and rules it out as the origin of the super-linear scaling observed in 8.17b.

A.3 Fluence-Dependent Bi-Exponential Fit Parameters

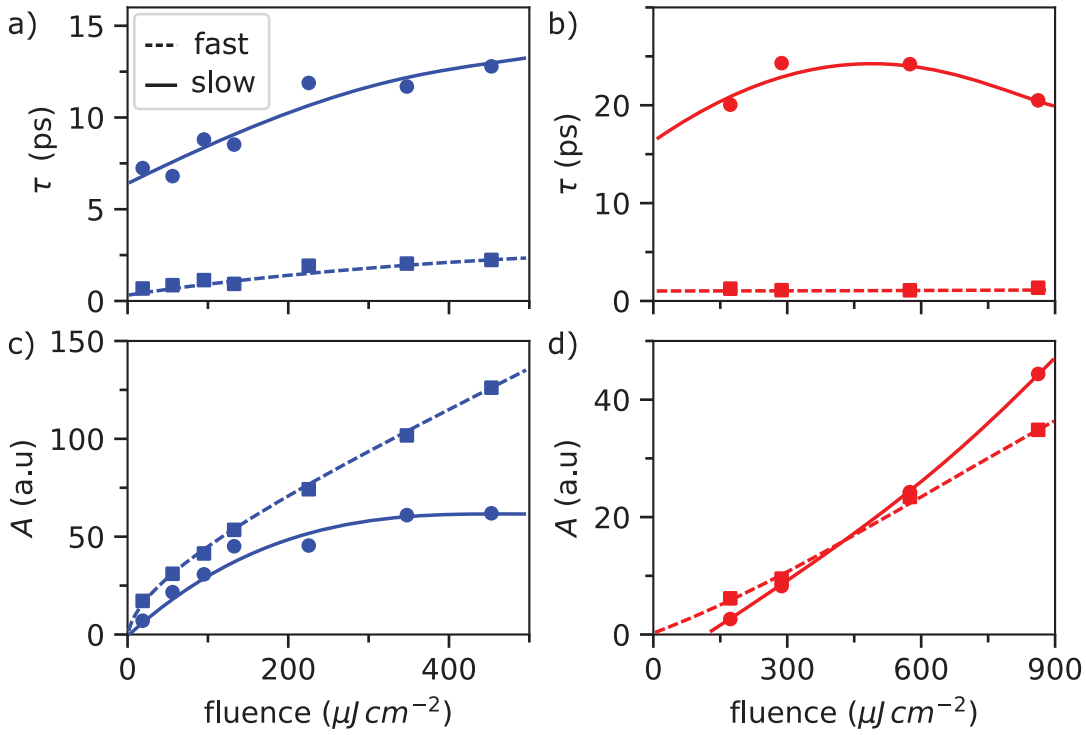

Fig. A.4: Excitation-fluence dependent bi-exponential fit parameters. a) Fast and slow lifetime, τ_f (squares) and τ_s (circles), respectively, and b) amplitude of the fast (squares) and slow (circles) lifetime for 400 nm excitation. c) and d) The corresponding lifetimes and amplitudes for 800 nm excitation. The solid lines are drawn as guides to the eye.

A.4 Peak-Shift Model

A.4.1 Mathematical Formulation

A term proportional to the difference in the oscillator lineshape between the photoexcited state, $\tilde{\sigma}'_{osc,2}$, and the static state, $\tilde{\sigma}_{osc,2}$, must be included to fit the photoconductivity spectrum for SnIP, which can be expressed as,

$$\Delta\tilde{\sigma}_{osc,2}(\omega) = \tilde{\sigma}'_{osc,2} - \tilde{\sigma}_{osc,2}. \tag{A.1}$$

Using equation 7.20 from section 7.5.3, this can be written as,

$$\frac{i\Delta\tilde{\sigma}_{osc,2}(\omega)}{\omega\epsilon_0} = \frac{A'_{osc,2}}{\omega'^2_{0,2} - \omega^2 + i\omega\gamma'_2} - \frac{A_{osc,2}}{\omega^2_{0,2} - \omega^2 + i\omega\gamma_2}, \tag{A.2}$$

where the prime superscript indicates the value of each parameter in the photoexcited state. A photoexcitation induced change in the center frequency or damping therefore results in a non-Lorentzian differential lineshape. With this lineshape, knowledge of the photoexcited film thickness is required, however, as discussed in section 8.4 this is not known precisely in SnIP. To overcome this issue, we employ the peak-shift (PS) model of Zhao *et al.*[227], where the differential lineshape is given by,

$$\tilde{\sigma}_{PS}(\omega) = \sum_{i=1}^{3} \frac{\partial\tilde{\sigma}_{osc,2}}{\partial x_i}\Delta x_i \tag{A.3}$$

where the parameters, Δx_i, are the change in center frequency, $\omega_{0,2}$, amplitude, $A_{osc,2}$, and damping, γ_2, of mode 2 and the oscillator conductivity, $\tilde{\sigma}_{LO,2}$ is given by,

$$\tilde{\sigma}_{LO,2}(\omega) = -i\omega\epsilon_0 \cdot \left(\frac{A_{osc,2}}{\omega^2_{0,2} - \omega^2 + i\omega\gamma_2} + \epsilon_\infty - 1\right). \tag{A.4}$$

The differential lineshape is then given explicitly by,

$$\begin{aligned}\Delta\tilde{\sigma}_{PS} = \frac{i\omega\epsilon_0}{\omega^2_{0,2} - \omega^2 - i\gamma_2\omega} \cdot \Bigg(-\Delta A_{osc,2} + \frac{2\omega_{0,2}A_{osc,2}}{\omega^2_{0,2} - \omega^2 - i\gamma_2\omega} \cdot \Delta\omega_{0,2} - \\ \frac{i\omega A_{osc,2}}{\omega^2_{0,2} - \omega^2 - i\gamma_2\omega} \cdot \Delta\gamma_2\Bigg),\end{aligned} \tag{A.5}$$

so that the differential parameters show up in the numerator and can be grouped with the film thickness for fitting.

A.4.2 Accuracy of the differential formulation

In the following, we confirm that the differential form of the peak-shift model is valid for our data. Due to the linearity of the conductivity with respect to the oscillator amplitude, the differential form is exact with respect to $\Delta A_{osc,2}$. However, the situation is more complicated for the damping and center frequency. To examine the range of validity we plot the differential lineshape, equation A.5, and the exact difference function, equation A.2. Shown in Figure A.5 is a study of the accuracy of the peak-shift model with respect to a change in center frequency. The linewidth was chosen to represent the relative linewidth in SnIP with respect to the center frequency.

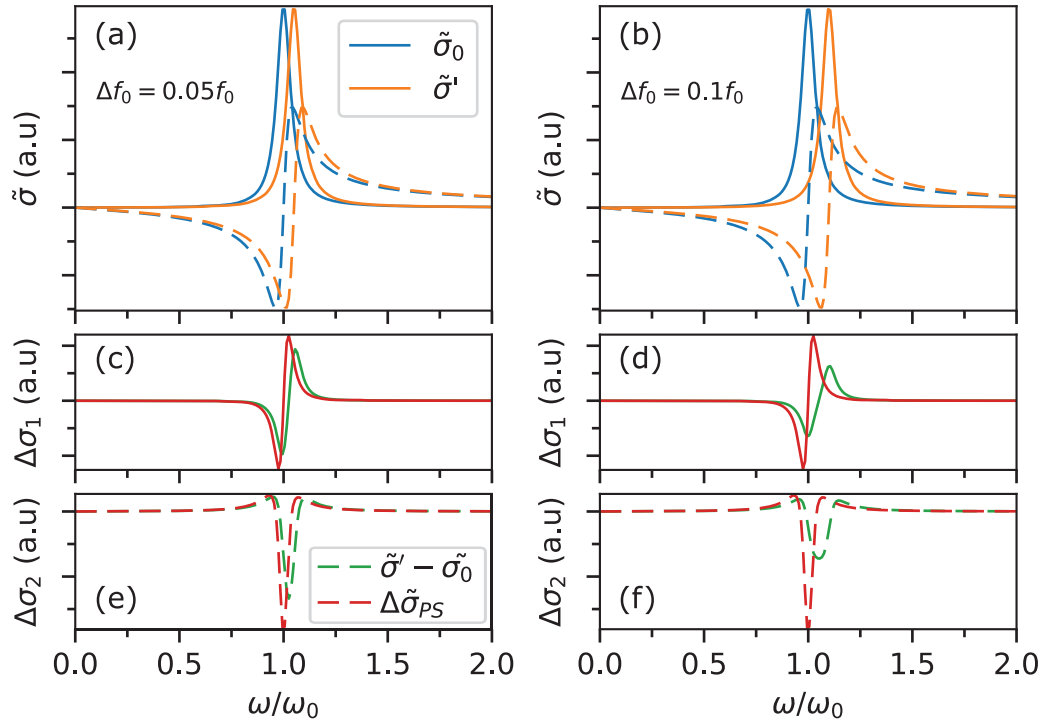

Fig. A.5: Accuracy of peak-shift model with $\Delta\omega_0$. Complex conductivity of an oscillator with (orange) and without (blue) a perturbation to the resonant frequency, ω_0, of **a** $0.05\omega_0$, and **b** $0.1\omega_0$. **c**,**d** the real part and **e**,**f** the imaginary part of the corresponding the corresponding difference in oscillator conductivity (blue) and differential lineshape from the peak-shift model (orange).

For a 1% change in ω_0, the peak-shift model accurately reproduces the difference in conductivity, however, at 5% modulation the peak-shift model already fails to reproduce the correct differential lineshape quantitatively. By 10% difference, the

peak-shift model does not work at all. Somewhat counter intuitively, it is actually the percent change in resonant frequency with respect to the linewidth that is the determining factor for the range of validity rather than with respect to the center frequency itself. For larger values of damping, the range of validity is larger.

Alternatively, we can examine the accuracy of the peak-shift model with respect to change in damping, as shown in Figure A.6. In this case, the range of validity is significantly larger and the differential lineshape shows reasonable quantitative agreement all the way to 20% change in γ. Even at 40% change in γ, the peak-shift model correctly reproduces the lineshape qualitatively.

It is also interesting to note the similarity between the lineshape of the $\Delta\gamma$ term and the ΔA_{osc}, which are qualitatively similar. However, we find that the lineshape is significantly narrower than that of the ΔA_{osc} term and it contains peaks to either side of the center frequency with opposite sign to the main peak, which makes it possible for fitting algorithms to distinguish between the two terms. Furthermore, we note the similarity between the real and imaginary parts of the $\Delta\gamma$ and $\Delta\omega_0$ terms as they are nearly complex conjugates. This coincidence is due to the functional form of the Lorentzian denominator, $\omega_0^2 - \omega^2 - i\omega\gamma$, where ω_0^2 and γ are nearly complex conjugates other than a factor of ω, which does not vary significantly in a narrow spectral range.

A.4.3 Estimate of the absolute oscillator change

Finally, we estimate the absolute change in oscillator parameters. From the fits to experimental data using the Drude-Smith plus peak-shift model in the section 8.4.2 we measured the products $\Delta\omega_{0,2}/2\pi \cdot d = 9 \times 10^{-4}\,\mathrm{THz}\cdot\mu\mathrm{m}$, $\Delta\gamma_2/2\pi \cdot d = -9.1 \times 10^{-3}\,\mathrm{THz}\cdot\mu$ m, and $\Delta A_{osc,2} \cdot d = -6.7\,\mathrm{THz}^2 \cdot \mu\mathrm{m}$, where d is the photoexcited film thickness. Using an estimate of $d = 100\,nm$ for the penetration depth of 400 nm light, a direct calculation of $\Delta A_{osc,2}$ from $\Delta A_{osc,2} \cdot d$ yields a negative oscillator amplitude after photoexcitation.

This inconsistency could result from several possible origins: An overestimate of the film thickness for TDS, an underestimate of the 400 nm penetration depth, or complications due to the inhomogeneous film morphology. While it is easy to see how

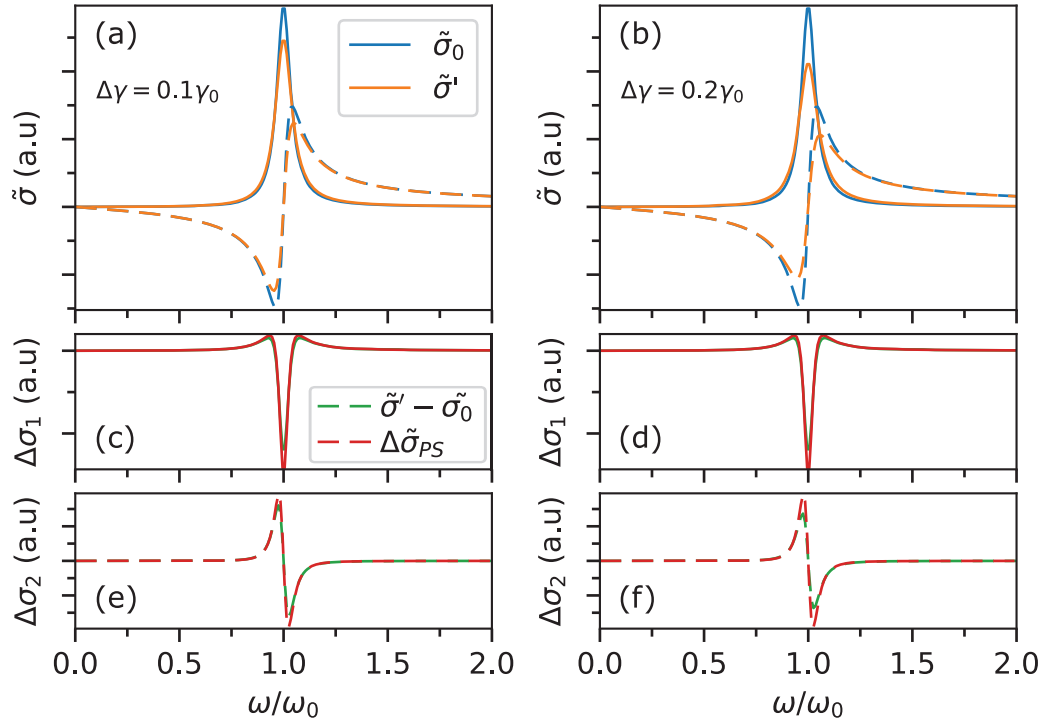

Fig. A.6: Accuracy of peak-shift model with $\Delta\gamma$. Complex conductivity of an oscillator with (orange) and without (blue) a perturbation to the damping, γ, of **a** 0.2γ and **b** 0.4γ. **c**,**d** the real part and **e**,**f** the imaginary part of the corresponding the corresponding difference in oscillator conductivity (blue) and differential lineshape from the peak-shift model (orange).

the film and penetration depth thickness could result in an underestimate of $A_{osc,2}$ and overestimate of $\Delta A_{osc,2}$, respectively, however, it is not as easy to see how the inhomogeneous morphology would affect the result. To understand this, we note that the the feature sizes are of comparable size to the excitation wavelength. As a result, the excitation pulse does not see an effective medium in the same way as the THz and can excite a film with a larger areal filling fraction for an infinitesimal slice of the film. To be more specific, the photoexcitation pulse can penetrate the air gaps present in the first several layers of the film to excite nanowires deeper in the film.

To take this into account, we suggest that as a first approximation when calculating the absolute change in oscillator amplitude the effective film thickness should be taken as the penetration depth divided by the filling fraction. With 0.35 as an estimate of the volume filling fraction of our films (section 7.3.1) and with a 100 nm penetration depth we find an absolute change in oscillator amplitude of $\Delta A_{osc,2} = -6.7\,\mathrm{THz}^2\mu\mathrm{m}/(100\,\mathrm{nm}/0.35)$=-23 THz^2, or approximately 50% of the absolute oscillator amplitude. Additionally, we find $\Delta\gamma_2/2\pi = 3.2 \times 10^{-2}\,\mathrm{THz}$ and $\Delta\omega_{0,2}/2\pi = 3 \times 10^{-3}\,\mathrm{THz}$ or a modulation of 20% and 0.2%, respectively. To visualize this change, in Figure A.7a, b we plot the oscillator conductivity before and after photoexcitation. In Figure A.7b we also include the Drude-Smith conductivity to see the relative scale. The absolute Drude-Smith conductivity was also calculated using a 100 nm film thickness and 0.35 filling fraction.

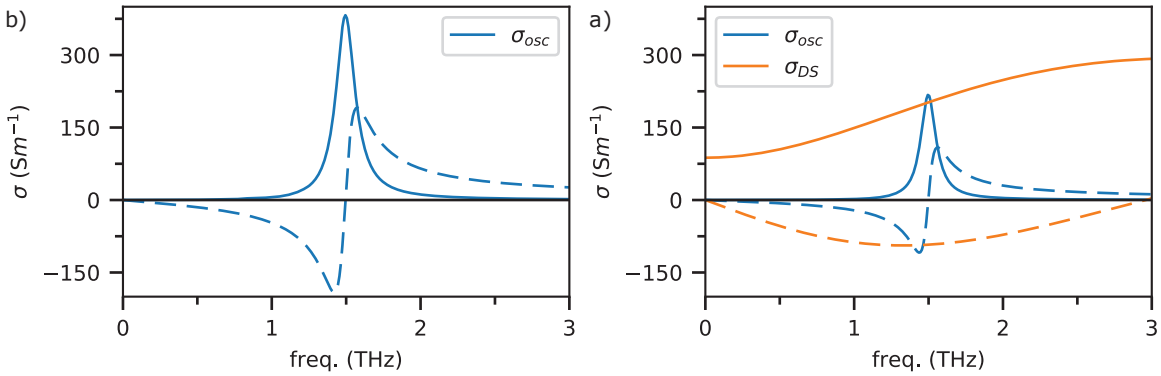

Fig. A.7: Estimated absolute oscillator change. Real (solid) and imaginary (dashed) oscillator conductivity of mode 2 using the parameters extracted by THz-TDS. b) Real (solid) and imaginary (dashed) conductivity of the oscillator (blue) after photoexcitation, using the parameters estimated in this section, along with the Drude-Smith conductivity for reference.

A.4.4 Three-Level Trapping Model

This section expands on the rate equation model to help understand the role of trapping dynamics in recombination in SnIP. A simple model that can capture the trap-filling dynamics consists of a three-level system with a ground state, N_0, a conductive state, N_1, and a saturable trap state (non-conducting), N_2, as pictured in Figure A.8a. Excitation consists of a delta function source at $t = 0$ while rates of coupling between each level are parameterized by k_{ij}. We note that this formulation is insufficient to reproduce the relaxation dynamics and fit the photoconductivity decay curves quantitatively. This is unsurprising, as we know that diffusion in the cylindrical geometry and surface recombination are important, making the full relaxation dynamics more complex. Nevertheless, by parameterizing the observed fast lifetime with k_{10} and the sub-response time trapping with k_{12} we can gain insight into the early time behavior.

The system of equations governing the relaxation is given by,

$$\frac{dN_1}{dt} = N_{1,0}\delta(0) - (k_{eff,12} + k_{10})N_1, \tag{A.6}$$

$$\frac{dN_2}{dt} = k_{eff,12}N_1 - k_{21}N_2, \tag{A.7}$$

$$\tag{A.8}$$

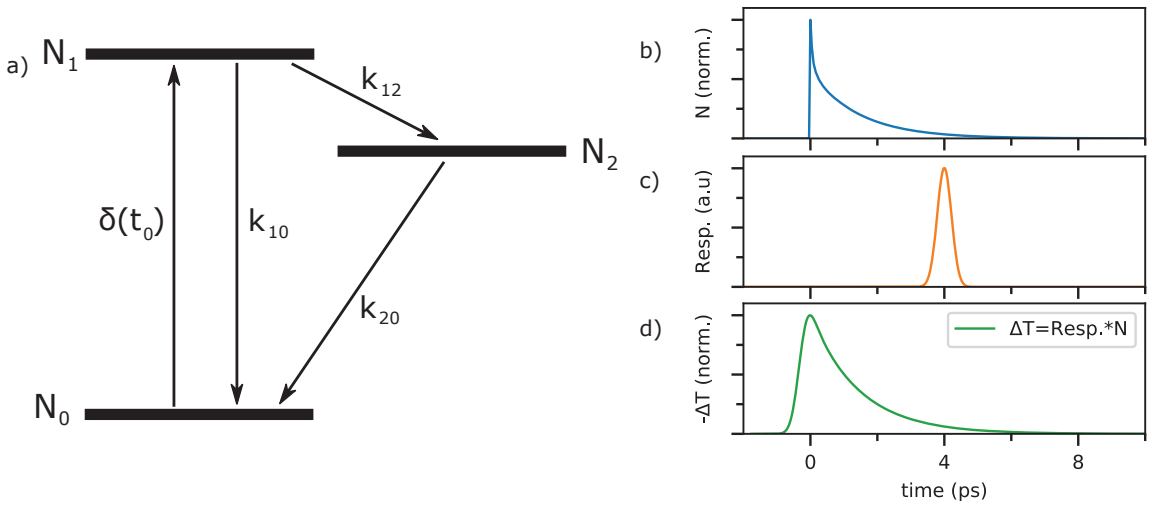

Fig. A.8: Three-level model of trap-filling dynamics. a) Level diagram showing the conducting state (N_1) and non-conducting states (ground state N_0 and saturable trap state N_2). b) Numerical calculation of the system in a) with a delta function input. c) Gaussian system response function. d) Convolution of the system response and numerically calculated relaxation dynamics.

where $N_{1,0}$ is the initial density and we have defined the effective coupling rate,

$$k_{eff,12} = \left(1 - \frac{N_2}{N_{2,sat}}\right) k_{12}, \tag{A.9}$$

where $N_{2,sat}$ is the density at which all traps are filled [280].

Figure A.8b shows the density as a function of time with $k_{21} = 0$, $k_{12} = 8\,\mathrm{ps}^{-1}$, $k_{10} = 0.7\,\mathrm{ps}^{-1}$ and $N_{2,sat} = 0.2$ in units where $N = 1$ is the density normalized to the maximum fluence with 800 nm excitation (850 $\mu\mathrm{J\,cm}^{-2}$). We note that the linearity of the system of equations allows us to work in normalized units in this way without redefining rate constants (lifetimes). The rate k_{10} was taken to match the experimentally observed time-constant at early times, k_{12} and $N_{2,sat}$ were found by fitting the fluence-dependent ΔT signal in Figure 8.17b, and $k_{20} = 0$ was chosen for simplicity.

To go from the time-dependent density to the differential transmission, the system response, R, must be taken into account. Here R, approximated as a Gaussian (Figure A.8c). A weighting factor, η, between the simulation density and differential

transmission is also required for fitting data so that,

$$\Delta T = \eta N_1 * R, \tag{A.10}$$

where $*$ indicates a convolution and η is a linear weighting factor. Deviations from linearity could occur due to a time- or fluence-dependent scattering rate or localization parameter, however, the assumption of linearity is reasonable as a first approximation because the lineshape does not change significantly with time or excitation density (see Figures 8.11 and 8.4). The convoluted signal is shown in Figure A.8d, where we see that the sub-response time trapping is smeared out by the system response. This model was used to fit the data in Figure 8.17b, showing excellent agreement with experiment.

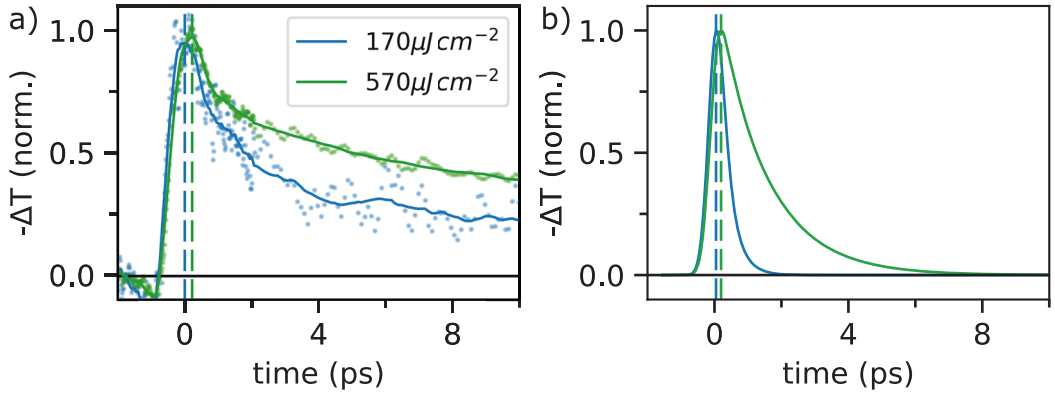

Fig. A.9: Rise-time dynamics in the three-level model model. a Experimentally measured $-\Delta$T at low and high fluence, showing a small increase in rise time at high fluence. The solid lines are results from a smoothing algorithm applied to the data. **b** Numerically calculated density as a function of time convoluted with the Gaussian response of the system, which also shows a slight increase in rise time at high fluence. The vertical dashed lines indicate the time delay of the peak signal. The rate k_{10} is chosen to fit the fast lifetime of the 800 nm photoconductivity decay.

To further study the behavior of this system of equations, we look at the time dependence of the calculated $-\Delta$T in comparison to experimental observation, shown in Figure A.9a, b. As stated previously, we are not able to reproduce the time-dependence of the photoconductive decay quantitatively with this model. This is clear from the longer-lived component of the experimental curve in Figure A.9a at both low and high fluence, which is not present in the calculated curves in Figure A.9b. However, as expected the rate equation description is able to reproduce the

lifetime enhancement at high fluence. Furthermore, we see that both the experimental curve and calculated curves show a small increase in rise time at high fluence*

A.5 Modified Tinkham Equation

As discussed in Chapter 8 and ref. [295], the dispersion of the unexcited film leads to corrections in the Tinkham equation for the differential conductivity. This appendix outlines the derivation of the modified Tinkham equation in equation 8.1. For the case where the photoexcited region covers the entire thin film, the expression derived here is similar to that of La-o-vorakiat *et al.* [295], however, it is also valid in the more general case where only a narrow region near the surface of the thin film is excited.

A.5.1 Derivation

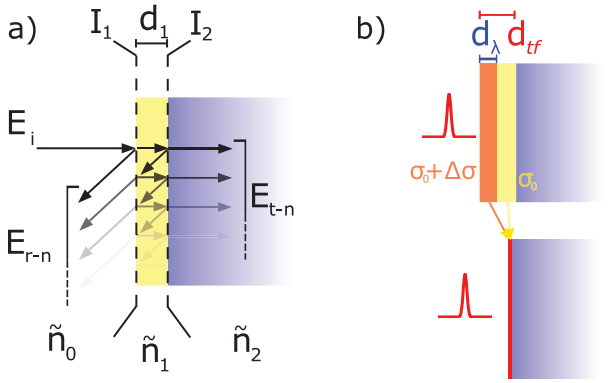

Fig. A.10: Thin-film transmission. a Multiple-beam interference through a thin film into a substrate. The transmitted field is composed of the sum of all the reflected fields as the beam traverses the film. **b** Illustration of the collapse of the thin film down to an infinitesimally thin layer with the same total conductivity as the entire film.

The situation considered here is illustrated in Figure A.10a, where an optical field is incident on a thin film of thickness d_1 and refractive index $\tilde{n}_1$ placed on a substrate with refractive index $\tilde{n}_2$. For generality, the refractive index of the initial region is assumed to be $\tilde{n}_0$, though it is typically air or vacuum with $n = 1$ in experiment. The

*In the low fluence case, it was necessary to use a smoothing algorithm (Savitsky-Golay filter in SciPy) as the data was quite noisy. The extremely small ΔT signals in SnIP with 800 nm excitation at low fluence make it difficult to study this regime.

reflection and transmission at interface 1 and 2 is given by the Fresnel coefficients,

$$\tilde{r}_{ab} = \frac{\tilde{n}_b - \tilde{n}_a}{\tilde{n}_b \tilde{n}_a}, \tag{A.11}$$

$$\tilde{t}_{ab} = \frac{2\tilde{n}_a}{\tilde{n}_b + \tilde{n}_a}, \tag{A.12}$$

where the subscript a refers to the incident region. The propagation in each layer is given by,

$$\tilde{p}_a = e^{i\tilde{n}_a k d_a}, \tag{A.13}$$

where k is the wavevector of the field. The field transmitted into the substrate is given by a sum over the multiple reflections, which can be summed using the geometric series so that,

$$\tilde{t}_{012} = \frac{\tilde{t}_{01}\tilde{t}_{12}}{\tilde{p}_1^{-1} - \tilde{r}_{12}\tilde{r}_{10}\tilde{p}_1}, \tag{A.14}$$

which, inserting the expressions for reflection, transmission, and propagation and rearranging can be rewritten as,

$$\tilde{t}_{012} = \frac{2\tilde{n}_0\tilde{n}_1}{(\tilde{n}_0 - \tilde{n}_1)(\tilde{n_1} - \tilde{n_2})e^{i\tilde{n}_1 k d} - (\tilde{n}_0 + \tilde{n}_1)(\tilde{n}_1 + \tilde{n}_2)e^{-i\tilde{n}_1 k d}}, \tag{A.15}$$

and expanding the exponentials, rearranging, and using the relationship between the optical conductivity and the refractive index, $\tilde{n}^2 = 1 + \frac{i\tilde{\sigma}}{\omega\epsilon_0}$, and the relationship $Z_0 = \frac{1}{c\epsilon_0}$, this becomes,

$$\tilde{t}_{012} = \frac{2n_0}{n_0 + n_2 + Z_0\tilde{\sigma}d - i(n_0 n_2 + 1)kd}. \tag{A.16}$$

Assuming the term $i(n_0 n_2 + 1)kd$ is small, which is reasonable in the thin-film approximation where $kd << 1$, the expression for the transmission becomes,

$$\tilde{t}_{012} = \frac{2n_0}{n_0 + n_2 + Z_0\tilde{\sigma}d}. \tag{A.17}$$

Defining the ratio $\Delta\tilde{t} = \tilde{t}_{012}/\tilde{t}_{02}$, which is similar to the differential transmission in TRTS, solving for the conductivity yields the Tinkham formula,

$$\sigma = \frac{1 + \tilde{n}_2}{Z_0 d}\left(\frac{1}{\Delta\tilde{t}} - 1\right). \tag{A.18}$$

If, instead, we had defined the ratio $\Delta\tilde{t} = \tilde{t}_{01'2}/\tilde{t}_{012}$, where the 1' subscript indicates the photoexcited film with conductivity $\sigma' = \sigma_0 + \Delta\sigma$, we could instead solve for the differential conductivity,

$$\Delta\sigma = \frac{1 + \tilde{n}_2 + Z_0\sigma_0 d}{Z_0 d}\left(\frac{1}{\Delta\tilde{t}} - 1\right), \tag{A.19}$$

which is similar to the expression of La-o-vorakiat *et al.*. To deal with the situation where only a thin portion of the thin film is photoexcited, we make the phenomenological substitution $\sigma_d \rightarrow \int_0^d \sigma(x)dx$. If only a region with thickness equal to the penetration depth, d_λ, is excited this can be written as $\int_0^{d_{tf}} \sigma dx = \sigma_0 d_{tf} + \Delta\sigma d_\lambda$, where d_{tf} is the full film thickness. This procedure can be thought of as "collapsing" the volume conductivity of the full thin film into an infinitesimally thin sheet, as illustrated in Figure A.10b*. With this substitution, equation A.19 becomes,

$$\Delta\sigma = \frac{1 + \tilde{n}_2 + Z_0\sigma_0 d_{tf}}{Z_0 d_\lambda}\left(\frac{1}{\Delta\tilde{t}} - 1\right), \tag{A.20}$$

which is the thin-film formula used in Chapter 8

A.5.2 Validation

To show that the modified Tinkham formula in equation A.20 correctly removes phonon artifacts from THz conductivity spectra, the accuracy of the two equations was compared numerically. As illustrated in Figure A.11a, the transmission of a THz pulse through a single thin film and a thin film with and without a narrow excited region near the surface was calculated using a multilayer-film transmission code†[296]. The static dielectric function, calculated from the fit parameters extracted from the SnIP, is shown in Figure A.11b. The conductivity in the photoexcited region also has a Drude-Smith contribution as shown by the black line in Figure A.11c.

Equations A.19 and A.20 were used to extract the Drude-Smith conductivity from the ratio of transmission with and without the excited region. The results are also plotted in Figure A.11c in red and green for equations A.19 and A.20, respectively, which shows that the second version of the modified Tinkham equation, with the phenomenological substitution of the integral over the film thickness, correctly removes the phonon artifacts. To highlight this, in Figure A.11d,e a magnified version of σ_1 and σ_2 in the region with the strong vibrational mode are plotted, respectively. It is clear that the phonon artifacts are not present in the green curve, calculated from equation A.20.

*This procedure is clearly not formally sound and would likely make a more mathematically inclined physicist cringe. The validity of this approach is justified in the next section with comparison to exact calculations of the transmission in a 2-film case.

†The author of ref. [296] has also released a series of freely available high-quality lectures on computational electromagnetics that was useful for developing the multilayer-transmission code.

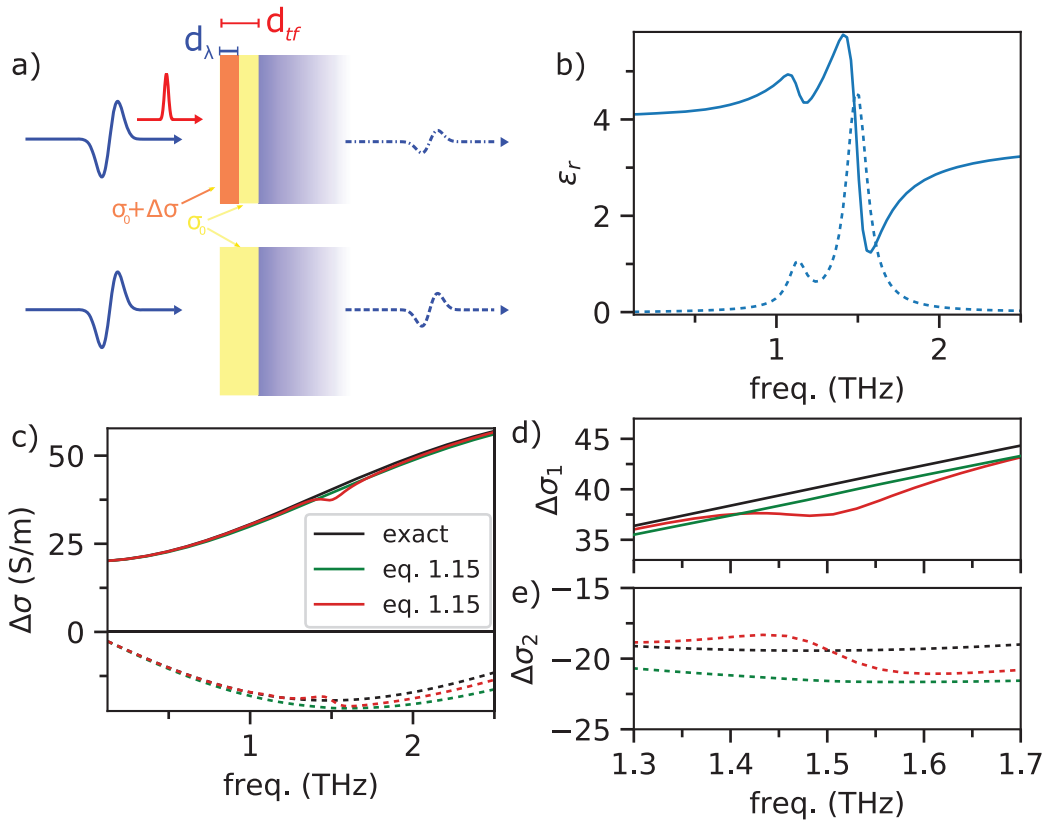

Fig. A.11: Accuracy of the modified thin-film formula. **a** Top: both a THz and optical pulse are incident on a thin-film. The conductivity is $\sigma_0 + \Delta\sigma$ in the red (excited) region and σ_0 in the yellow region. Bottom: no photoexcitation pulse is present so the conductivity of the whole film is σ_0. **b** Dielectric function of the unexcited film. **c** Input differential conductivity ($\Delta\sigma$, black line), conductivity extracted with equation A.19 (red) and with equation A.20. **d** Real and **e** imaginary part of conductivities from **c** highlighting the region with the large-amplitude oscillator in the static conductivity. The Green curve, extracted using equation A.20 correctly removes the phonon artifact from the extracted conductivity.

A.5.3 Application to SnIP

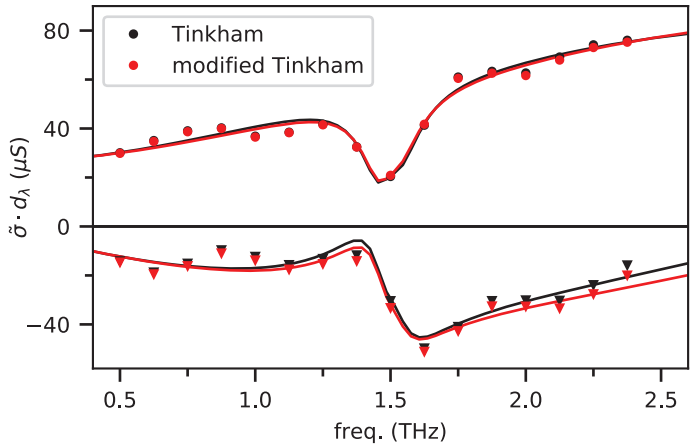

Fig. A.12: Effect of the oscillator on $\Delta\tilde{\sigma}$ in SnIP. Comparison of the conductivity extracted using the standard Tinkham formula (black) and the modified Tinkham formula (red).

To see the effect of the modified thin-film formula on the extracted conductivity, the differential conductivity calculated from the standard Tinkham formula and that calculated from equation A.20 are plotted in Figure A.12. As can be seen, the modified Tinkham formula yields only a small correction to the differential conductivity, as shown in appendix A.5.

A.6 Debye-Length Estimate

In order to estimate the screening length, we need to know photoexcited volume charge density instead of the areal charge density that we extract from the THz spectra, so we must estimate the penetration depth, δ. In typical semiconductors, with excitation well above the band gap the penetration depth is typically less than 100 nm. With $N \cdot d_\lambda = 7 \times 10^{12}\,\mathrm{cm}^{-2}$ and an estimate of 100 nm for the penetration depth with 400 nm excitation (similar to silicon), we find a carrier density of $N = 7 \times 10^{17}\mathrm{cm}^{-3}$.

In the low-density high-temperature limit, we can use the Debye length as a simple estimate of the screening length,

$$\lambda_D = \left(\frac{\epsilon_{st} k_B T}{N e^2} \right)^{1/2}, \tag{A.21}$$

where $\epsilon_{st} = 11.5$ is the static permittivity, and k_B, and T are the Boltzmann constant and carrier temperature, respectively. For a temperature of 300 K and density of $7 \times 10^{17}\,\mathrm{cm}^{-3}$ we find a screening length of 5 nm, which is several times larger than the dimensions of the unit cell and significantly larger than the bond lengths. Clearly the assumption of 100 nm penetration depth makes this an order of magnitude estimate only. If we instead use a penetration depth of 20 nm (similar to GaAs), the screening length, which scales proportionally to $N^{-0.5}$ ($\delta^{0.5}$), we find a screening length of 2 nm, which is still significantly larger than the bond length.

A.7 Detector Response in 2D Conductivity Spectra

In THz-TDS, the optical constants are extracted from a ratio of two spectra so that the detector response function cancels, however, in TRTS this cancellation does not always hold. In general, the conductivity can be thought of as a two-time response function, $\sigma(t, t')$. When the system is time invariant it can be rewritten as $\sigma(t - t')$, which facilitates a Fourier transform to yield $\sigma(\omega)$. Obviously, photoexcitation breaks this time invariance. It is still possible to consider the instantaneous frequency dependence of the conductivity, $\sigma(t, \omega)$, where the Fourier transformed dimension is the time after photoexcitation so that it is desirable to measure $\sigma(t, t - t')$. In TRTS this amounts to Fourier transforming along a dimension with a fixed optical pump and probe delay with a variable THz delay. However, the smearing of the THz pulse due to phase mismatch, which is discussed in section 2.5, occurs in the t' dimension.

Measurement of the full 2D conductivity spectrum can facilitate deconvolution of this detector response, as discussed by Beard *et al.* [128]. However, this process is sensitive to the precise details of the THz pulse spectrum and THz/optical refractive indexes. Rather than attempt to deconvolute the detector response to extract the actual time-dependent conductivity, another approach is to convolute calculated spectra with the detector response to try to fit the experimental spectra, as discussed by Larsen *et al.* [52]. However, we find that it is difficult to fit 2D spectra in this manner. Instead, we use the convolution approach to estimate the time delay at which the transient artifacts no longer affect the TRTS spectra. and choose not to speculate on the nature of the earlier-time dynamics.

The convolution procedure is outlined in Figure A.13: First, the time-dependent transmission is calculated in the projected* frequency domain using the thin-film transmission formula. While finite-difference time-domain (FDTD) calculation are often used for this step. Because the optical penetration depth in our case is small, the effect of the co-propagation of the THz and optical pulses is unlikely to significantly affect the transmission of the THz pulse in comparison to what is expected from the thin-film formula. Notably, for calculations in GaAs, our method produces similar

*Here, "projected" refers to the direction along which the optical pump/probe pulse delay is fixed, *i.e.*, the $t - t'$ dimension.

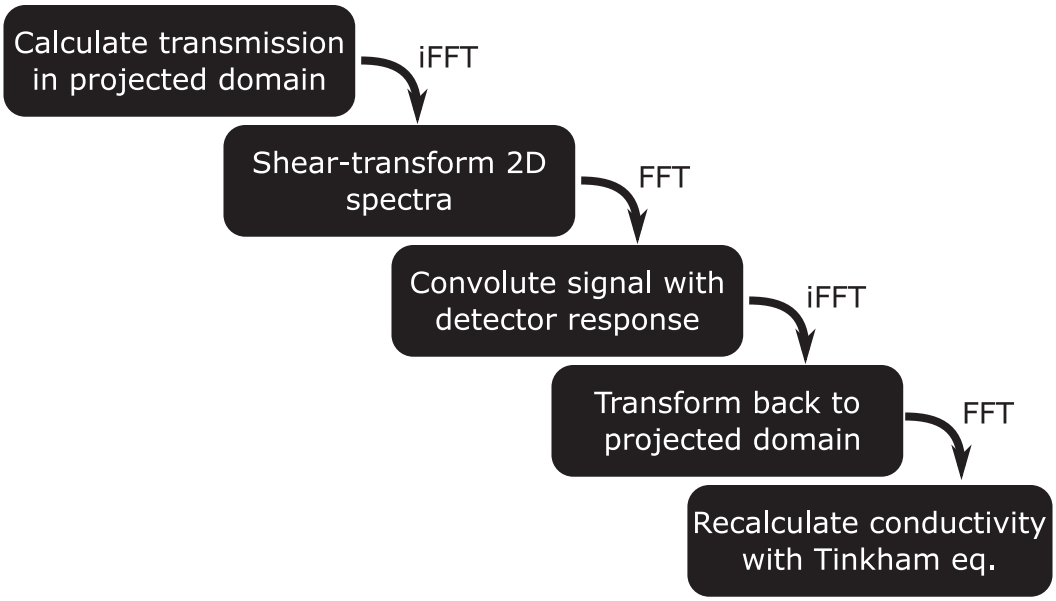

Fig. A.13: Procedure for detector convolution study. Flow chart of the calculation of the effect of detector response on 2D TRTS spectra.

features to Larsen *et al.* [52]. An inverse Fourier transform is applied to the data and the 2D time-dependent spectra are sheared to transform to the t, t' coordinate system and then Fourier transformed. The detector response is then applied to the data, which is then inverse Fourier transformed and sheared back to the projected domain. Finally, the data is again Fourier transformed and the conductivity is extracted from the spectra using the Tinkham formula.

This procedure was performed for a SnIP-like material using a Drude-Smith conductivity with a scattering time of 50 fs, a c-parameter of -0.9, and a DC conductivity of 1000 $\mathrm{S\,cm^{-1}}$. Shown in Figure A.14a is the time-dependent DC conductivity input into the calculation (blue line) and experimentally measured differential transmission, $-\Delta\mathrm{T}/\mathrm{T}_0$ (orange) as a function of time delay ($t - t'$ in the convention used here). The peak of the differential transmission lags behind that of σ_{DC} by approximately 0.5 ps due to the detector response.

As suggested, the purpose of this calculation is to determine at which point the experimentally measured spectra accurately represent the real conductivity. Shown in Figure A.14b-d are the input conductivity (blue) and extracted conductivity (orange) for three different time delays after the peak of the differential transmission. The

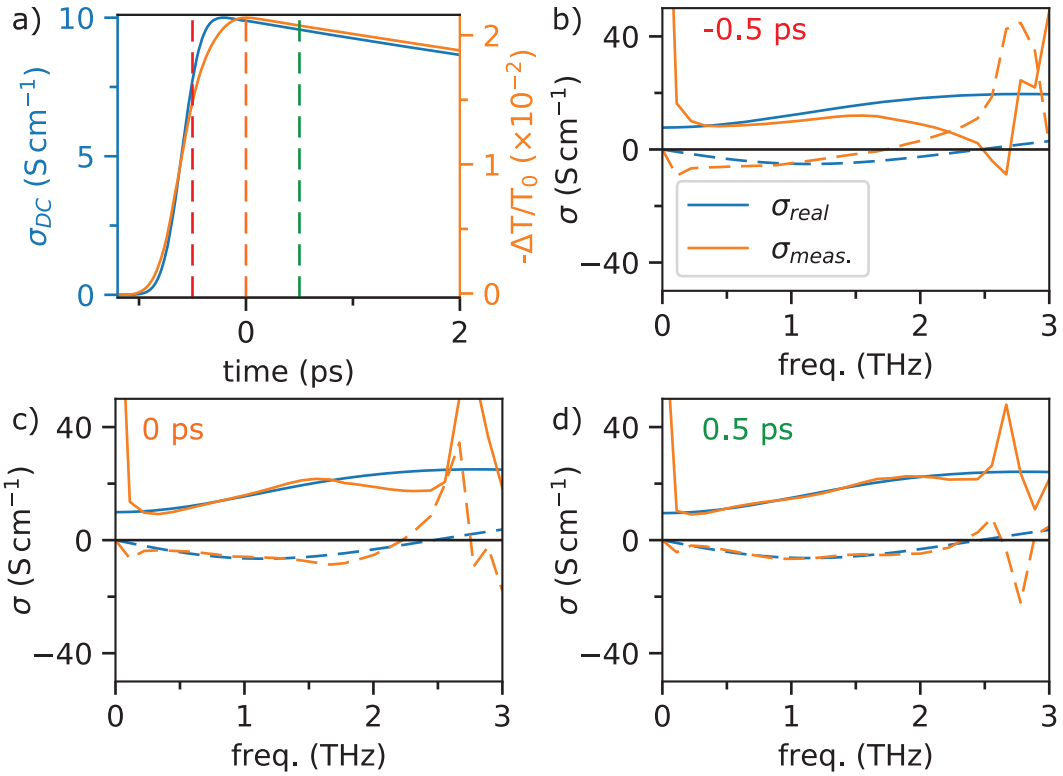

Fig. A.14: Artifacts in conductivity spectra. **a** Time-dependent DC conductivity input into the calculation (blue) and differential transmission after convolution (orange). Input conductivity spectrum (blue) and extracted conductivity spectrum (orange) at a time delay of **b** 0 ps, **c** 0.5 ps, and **d** 1 ps with respect to the peak of the differential transmission. The solid lines represent σ_1 and dashed lines σ_2. The vertical dashed lines in **a** indicate the time delays for figures **c**-**d**. The calculation was performed with an excited film thickness of 100 nm and the Drude-Smith conductivity was chosen with a similar c-parameter, scattering time, and carrier density to that of SnIP.

differential transmission was chosen as the reference point because it is most readily extracted from experiment. As seen in Figure A.14b, the conductivity at the peak of the differential transmission fails to reproduce the real conductivity, especially in the region above 1.5 THz. By 0.5 ps after the peak of the differential transmission, the extracted conductivity reasonably reproduces the input conductivity over most of the spectrum. By 1 ps after the peak of the differential transmission the extracted spectrum is accurately over the entire region with usable bandwidth.

A.8 References for Materials Summary

The references for the material properties plotted in Figure 8.21 are given as follows. Bulk modulus: $MoSe_2$[297], WS_2 and MoS_2 [298], CdTe, GaSb, CdS, ZnTe, and $CsSnI_3$ [299], $MAPbI_3$ and $MASnI_3$[300], $FAPbBr_3$[301], Se[302], for Te[303], pentacene[304], rubrene[305], tetracene[304], α-Ag_2S[306], black phosphorus[307], amorphous silicon[308] and SnIP[183]. It was more difficult to find reliable values for the bulk modulus of PEDOT:PSS[309] and i-TPU[310], which were estimated from the Young's modulus and Poisson ratio. Room-temperature carrier mobility: $MoSe_2$[311], MoS_2[312], WS_2[313], GaSb, CdS, and ZnTe [314], CdTe [315], $CsSnI_3$, $MAPbI_3$, $MASnI_3$, and $FAPbI_3$ [316], Se[317], Te[185], pentacene[318], rubrene[319], tetracene[320], α-Ag_2S[285], black phosphorus[321], amorphous silicon[248], PEDOT:PSS[322], i-TPU[323], and SnIP (this work).

A.9 Vibrational Mode Conformations

To give a broader perspective of the types of infrared (IR) active modes in SnIP, this appendix shows the vibrational mode conformation for several of the highest intensity modes throughout the spectrum. For reference, the intensities are shown in Figure A.15. The modes highlighted in red are plotted in what follows.

Additionally attached are animations of the following mode 9, 23, 24, 43, 63, 92, and 99, which are highlighted in Figure A.15 with projections of their normal mode vectors to the a and b axes shown in Figures SA.16-SA.22. Modes 9, 23, and 24 were chosen as they are the most likely to correspond to the modes observed in our THz spectra, while modes 43, 63, 92, and 99 were chosen due to their high intensities and representative of the types of motion in each frequency range. The mode numbers are indexed according to the number in the attachment Vibration_table.xlsx.

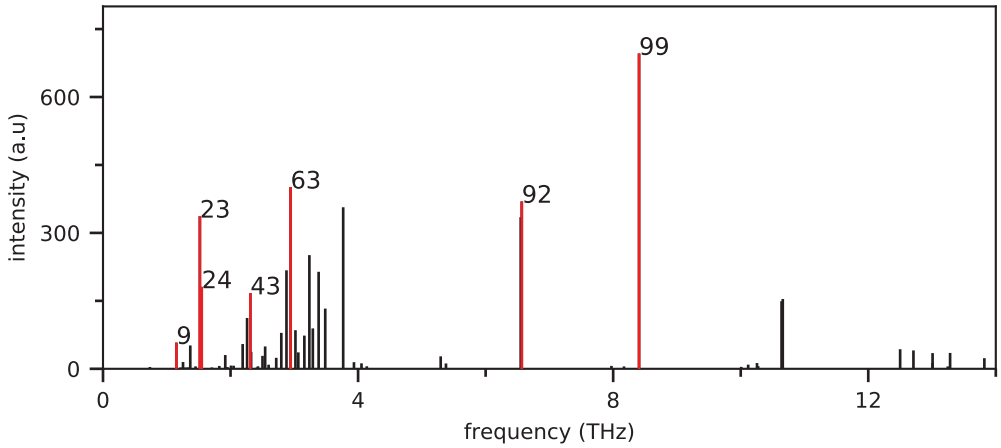

Fig. A.15: Normal mode infrared intensities. IR Intensity of each normal mode as a function of its frequency, calculated using Crystal17. The lines colored red and numbered indicate the modes that we have provided animations and displacement vectors for.

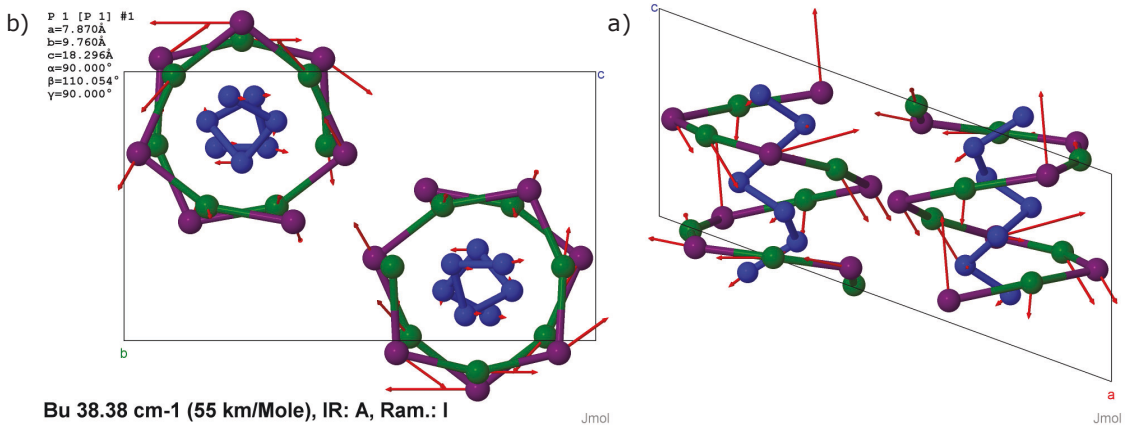

Fig. A.16: Mode 9. a) vectors projected along the a-axis and b) projected along the b-axis.

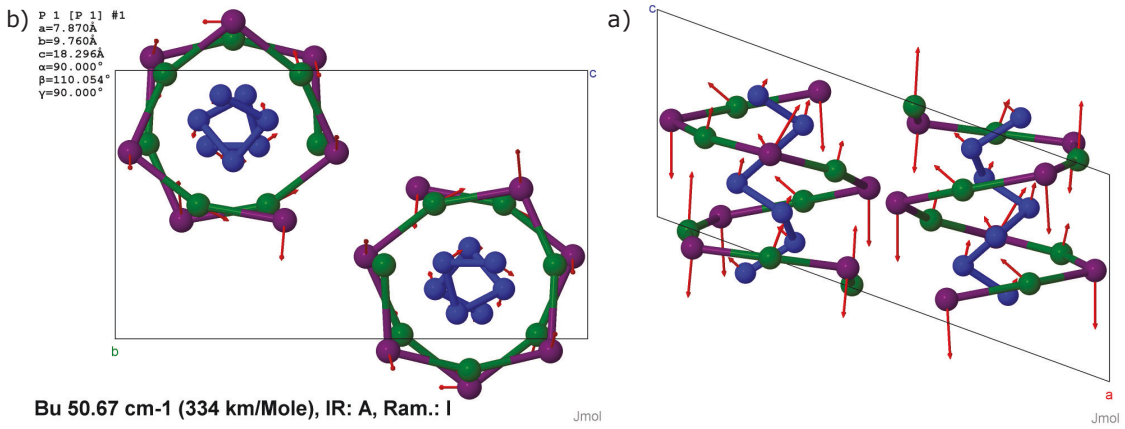

Fig. A.17: Mode 23. a) vectors projected along the a-axis and b) projected along the b-axis.

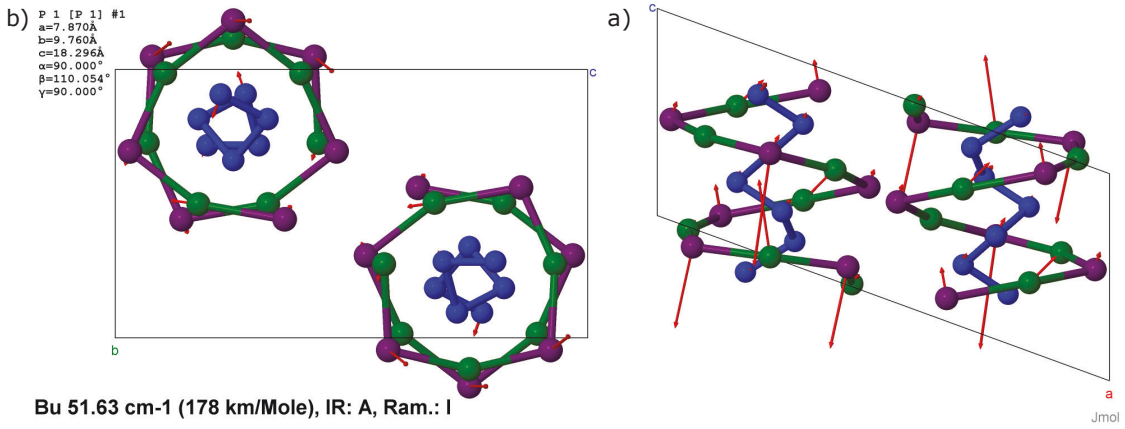

Fig. A.18: Mode 24. a) vectors projected along the a-axis and b) projected along the b-axis.

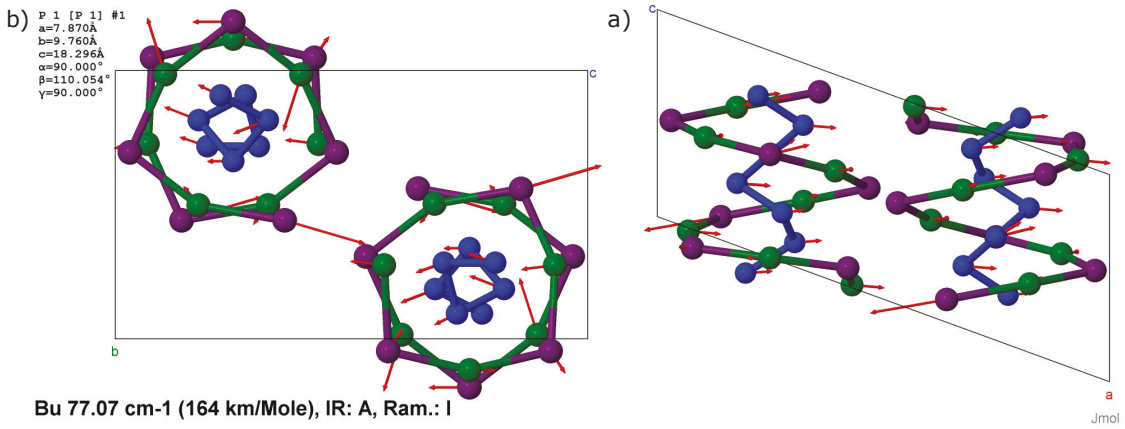

Fig. A.19: Mode 43. a) vectors projected along the a-axis and b) projected along the b-axis.

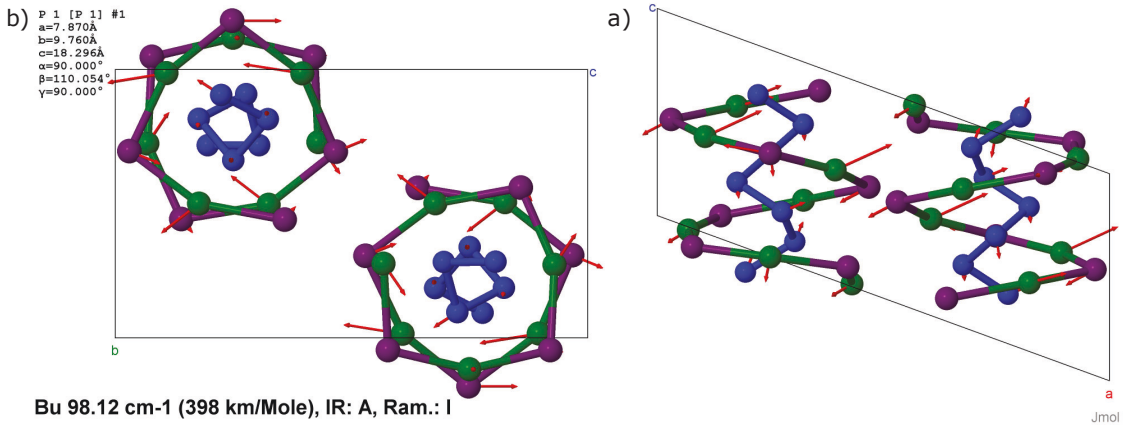

Fig. A.20: Mode 63. a) vectors projected along the a-axis and b) projected along the b-axis.

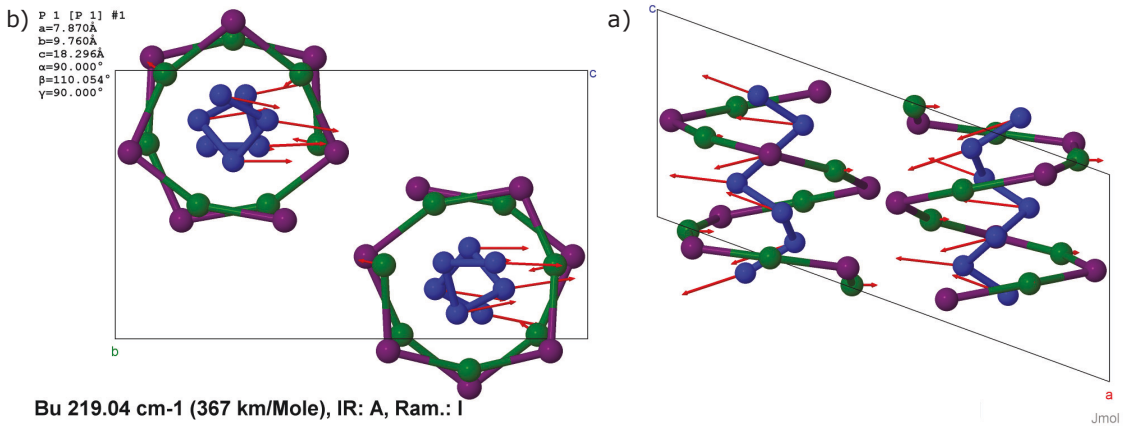

Fig. A.21: Mode 92. a) vectors projected along the a-axis and b) projected along the b-axis.

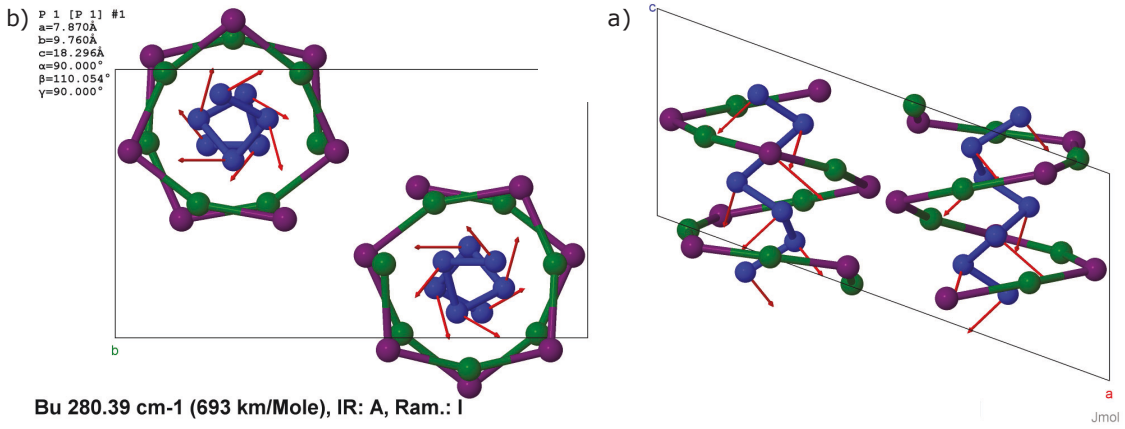

Fig. A.22: Mode 99. a) vectors projected along the a-axis and b) projected along the b-axis.

Appendix B

UNL Laser System

B.1 Overview

The laser system in UNL, shown schematically in Figure B.1, consists of a Ti:sapphire oscillator (Coherent Micra) that seeds both a 250 kHz amplifier (Coherent Rega) and 1 kHz amplifier (Coherent Legend USP), which can be run in parallel. This work will focus primarily on the Micra and Legend systems, however, briefly the Rega system is a chirped-pulse amplifier with an external stretcher/compressor. It is a Q-switched/cavity dumped system with acousto-optic modulators to achieve the 250 kHz repetition rate. The Rega system is used mainly for THz-coupled scanning tunneling microscopy (THz-STM)[324] and time-correlated single-photon counting (TCSPC)[325, 62]. It is also coupled to an OPA tunable through the visible range. The Micra and Legend will be described in more detail in the following.

B.2 Oscillator

The layout of the Micra is shown in Figure B.2. The Ti:sapphire rod is pumped with 5 W continuous wave (CW) 532 nm laser (Coherent Verdi-5). The system operates on the principle of Kerr-lens modelocking, where the gradient-index lens formed by the intensity-dependent refractive index in the laser rod enables higher gain for pulsed versus CW operation, as shown schematically in the inset of Figure B.2 [326, 327]. A mirror coupled to a piezo-electric shaker provides the fluctuations in the laser intensity to drive the system into the modelocked state [328]. An intracavity prism compressor is used to compensate the GDD of the cavity. A wedged window

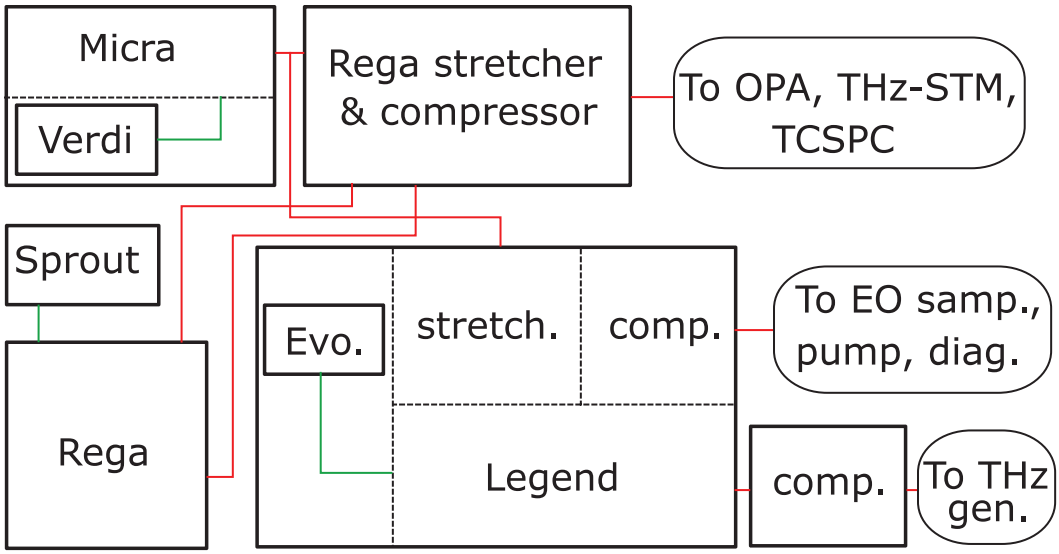

Fig. B.1: Laser System in the Ultrafast Nanotools Lab. An ultrafast Ti:Sapphire oscillator (Coherent Micra) seeds a 250 kHz (Coherent Rega) and a 1 kHz amplifier (Coherent Legend) in parallel. The 1 kHz amplifier is used for intense THz pulse generation to study nonlinear dynamics.

placed after the output coupler diverts a small fraction of the beam to two photodiodes located within the Micra box, which are monitored by the Micra controller for two applications. The first is a fast photodiode that is used to determine if the laser is modelocked, which is used in a feedback loop coupled to the piezoelectric shaker. The second is a large photodiode used to monitor the power of the modelocked pulse and is coupled to a feedback loop controlling the pointing of the Verdi pump beam in order to stabilize the beam power. Although the area of this photodiode is larger than the beam diameter, its reading is sensitive to the pointing of the laser, which can change if the cavity end mirrors are adjusted. The photodiode also has a non-uniform responsivity across the spectrum of the pulse. During optimization, it is therefore advantageous to use an external power meter with a large aperture and flat spectral responsivity during optimization of the laser.

B.3 Kilohertz Amplifier

The Legend USP operates on the principle of chirped-pulse amplification (CPA) [329], where an ultrafast pulse is chirped to a duration of hundreds of picoseconds in order to reduce the peak intensity by several orders of magnitude and avoid self focus-

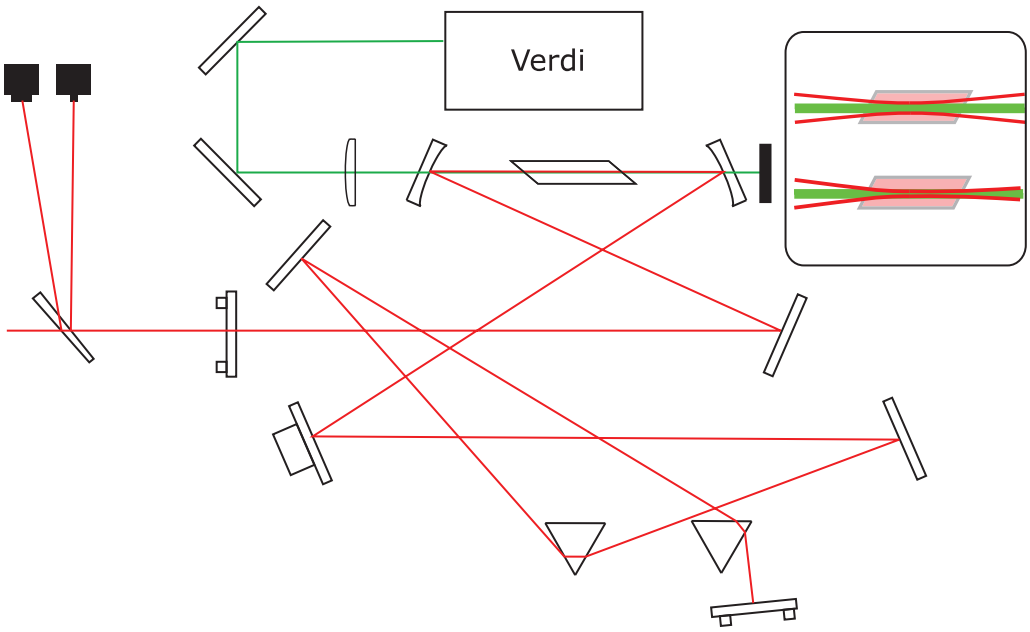

Fig. B.2: Oscillator layout. Schematic diagram of the Micra laser oscillator layout. Inset: Principle of Kerr-lens modelocking.

ing of the amplified pulse in the laser rod. The layout of the Legend system is shown in Figure B.3. The Micra pulse train is passed through a beam-reducing/collimating telescope system followed by an optical isolator before passing in to the pulse stretcher. Two spatially-separated photodiodes pick up a higher-order diffracted mode from the stretcher grating and are used for the interlock*. After the stretcher, the pulse train is coupled into the cavity with vertical polarization via reflection at the Brewster window of the laser rod. The pulse train passes through a quarter-wave Pockel's cell followed by a quarter waveplate. The cell is initially off, so the polarization of each pulse in the oscillator pulse train is rotated by 90° and is therefore transmitted through the Brewster window. On the second pass, the polarization is again rotated by 90° and is therefore coupled out of the cavity.

After triggering, the injection Pockel's cell turns on over a timescale of 2-3 ns so that the round-trip polarization change is 0°. The timing of this Pockel's cell with respect to the seed pulse is critical for two reasons. First, the Pockel's cell must turn

*With highly chirped pulses, reducing the bandwidth counter-intuitively reduces the pulse duration, which leads to a higher intensity pulse during amplification that can damage the laser rod due to filamentation.

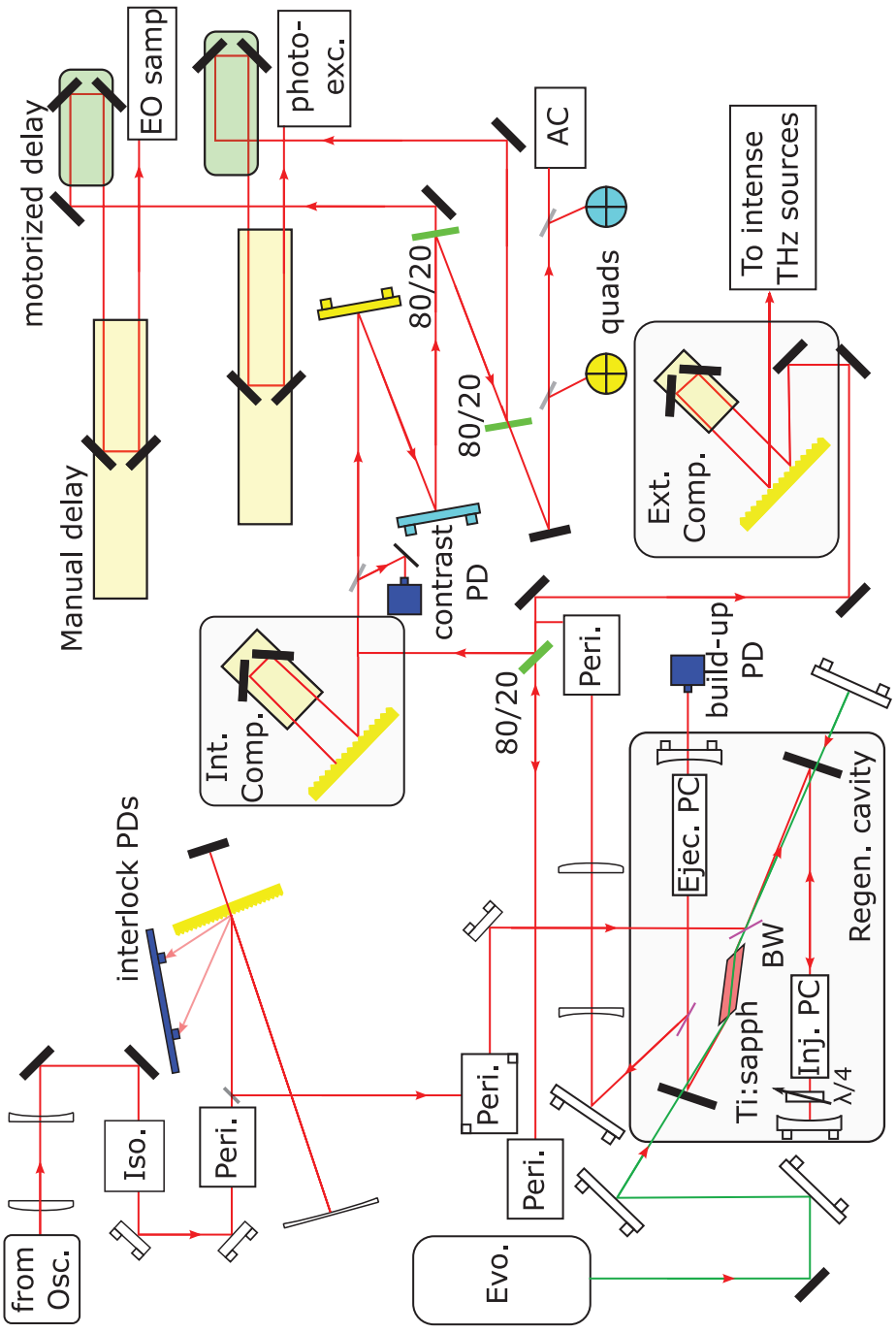

Fig. B.3: Legend regenerative amplifier. Layout of the 1 kHz stretcher, regenerative amplifier, compressors, and delay stages. Abbreviations: photodiode (PD) periscope (peri.) Evolution pump laser (Evo.) oscillator (osc.) optical isolator (Iso.) internal compressor (int. comp.) external compressor (ext. comp.) quadrant detectors (quads) photoexcitation (photo-exc.) autocorrelation (AC) Brewster window (BW) titanium sapphire laser rod (Ti:sapph) injection/ejection Pockel's cell (Inj./Ejec. PC) 80/20 beam-splitter (80/20).

on after the chosen seed pulse has passed through on its first return trip in order to rotate the polarization by 90° and transmit through the Brewster window of the laser rod. Second, it must turned on before the next pulse from the oscillator pulse train arrives in order to prevent a second pulse from coupling into the regen cavity. The injected pulse then completes several round trips through the cavity*. When the gain has saturated, the second Pockel's cell is turned on, rotating the polarization of the amplified pulse, which is then coupled out through a reflective polarizer. The Legend is pumped by a Q-switched pump laser with a 40 ns rise time and 150 ns ring down time (Coherent Evolution). The Evolution consists of a diode-pumped Nd:YLF laser with an intracavity LBO crystal. Two beam-steering mirrors are used to direct the pump laser into the Ti:sapphire crystal at Brewster's angle and a retroreflector is used to redirect the transmitted portion of the beam back into the crystal to maximize population inversion.

The manufacturer specifications suggest that the Legend amplifier is capable of producing pulses with duration less than 35 fs. In ref. [60], we were only able to obtain an autocorrelation width as small as 79 fs, which, assuming a Gaussian envelope, translates to a 56 fs pulse duration. Subsequently, we replaced the thermoelectric cooler for the laser rod, which significantly reduced the autocorrelation width to 56.6 fs, as shown in Figure B.4, corresponding to a Gaussian pulse duration of 40.0 fs. This suggests that thermal lens resulted in spatiotemporal aberrations that negatively affected the pulse duration. Furthermore, we found that by matching the center wavelength of the Micra seed pulse to the design wavelength of 800 nm for the Legend amplifier we were able to achieve an autocorrelation trace as short as 50.8 fs, as shown in Figure B.5, corresponding to a Gaussian pulse duration of 35.9 fs.

Based on the 30 nm bandwidth (Figure B.5b) and assuming a Gaussian pulse duration, the transform-limit pulse duration is as low as 30 fs. This suggests that some higher order phase is present in our pulses, which could be due to cubic phase accumulated from the optical elements between the Legend output and autocorrelator, mismatched cubic phase between the stretcher and compressor, or residual higher-

*The Legend manual suggests this number is 8-10, however, the timing of the SDG suggests this number is 14-16. This could be because the seed-pulse energy is lower than specifications due to the parallel-amplifier scheme, which would lower the gain over the first several passes.

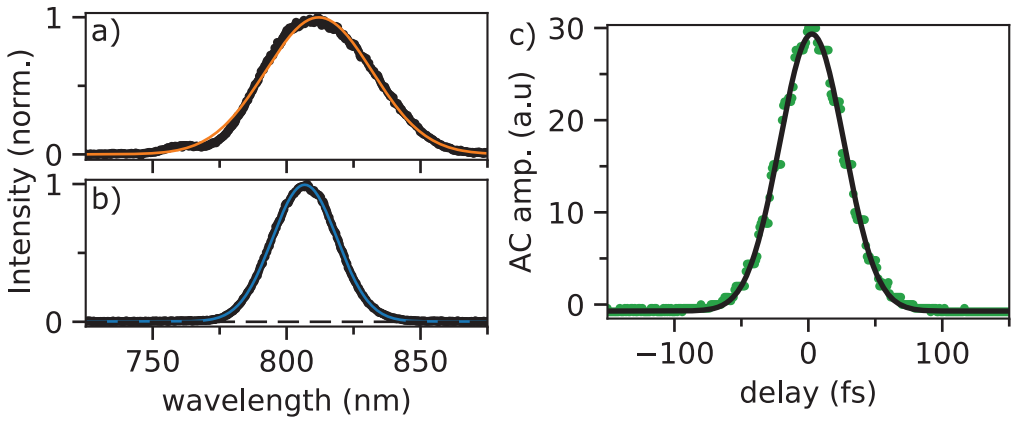

Fig. B.4: Legend spectrum and autocorrelation after TEC replacement. a Seed pulse spectrum before realignment. **b** Amplifier spectrum after compressor. **c** Corresponding autocorrelation with a FWHM of 56.7 fs.

order phase from the self-phase modulation process in the oscillator*.

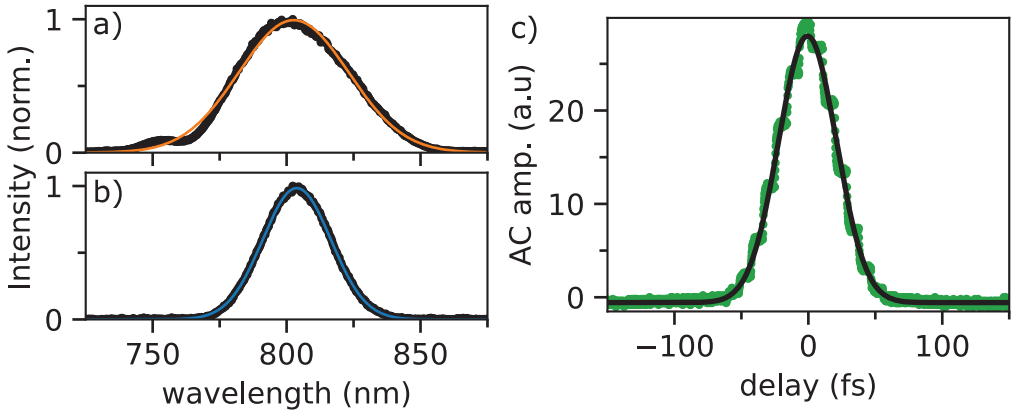

Fig. B.5: Legend spectrum and autocorrelation after seed realignment. a Seed pulse spectrum after realignment to match the 803 nm output wavelength of the amplifier. **b** Amplifier spectrum after compressor. **c** Corresponding autocorrelation with a FWHM of 50.8 fs.

Another figure of merit for the Legend amplifier is the pre-pulse and post-pulse contrast ratios, for which the manufacturer specifications are 500:1 and 1000:1, respectively. Shown in Figure B.6a is the oscilloscope trace of the output of a fast photodiode placed after the legend stretcher, with a peak of 602 mV. To avoid pickup of the radio-frequency (RF) from the high voltage pulse of the Pockel's cells, it is

*We note that the difference in pulse characteristics between even the 40 fs pulse and the 30 fs transform limit pulse is small and is unlikely to manifest in most experiments performed in the UNL.

necessary to carefully perform a background subtraction of the trace with the laser pulse blocked. At the scale of the main peak of the pulse, the dynamic range of the oscilloscope is not sufficient to resolve the prepulses and the range of the ADC must be adjusted and a new background subtraction performed, as shown in Figure B.6b. Here, at negative time we see several pre-pulses with a maximum amplitude of 1.3 mV, suggesting a contrast ratio of 463:1, which is close to the specifications. At positive time, the most obvious feature is located near 20 ps, with a negative peak followed by a postive spike and another negative peak. This is due to an electronic reflection in the BNC cable and is not a post pulse*. Considering the 9.5 ns round-trip time of the cavity the expected location of the post pulse is marked with an arrow. Indeed, there appears to be a peak, however, on this voltage scale the impulse response of the photodiode overwhelms the post-pulse signal. It is not possible to measure the contrast ratio accurately, however, we estimate that it is at least larger than the pre-pulse contrast ratio.

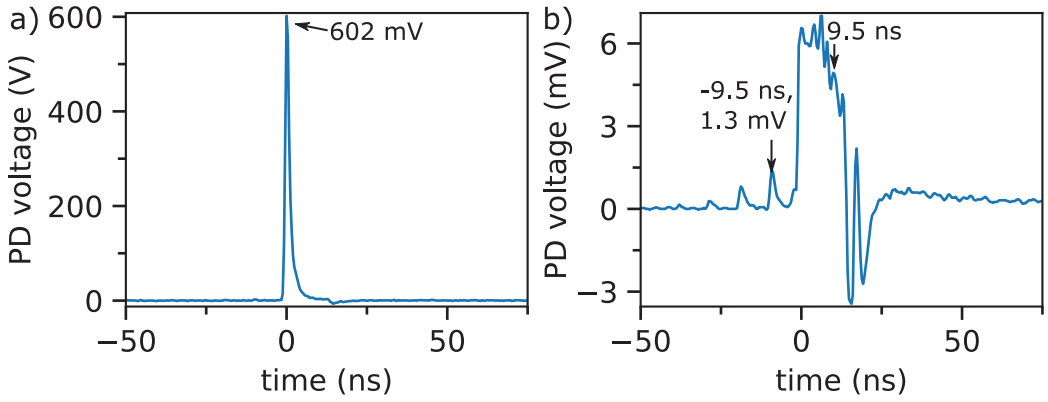

Fig. B.6: Legend Pre- and Post-pulses. **a** Full fast-photodiode trace from the output of the Legend amplifier. **b** Zoomed and background subtracted fast-photodiode trace from the output of the Legend amplifier. The closest pre-pulse to the main peak is highlighted along with the first post-pulse. The large pulse near 20 ns is due to an electronic reflection in the BNC cable.

Finally, we document an interesting problem that arose due to the dual-amplifer system. Shown in Figure B.7 is the Micra photodiode trace (yellow) synchronized to the Legend electronic trigger (blue). Here we see that despite the optical isolator, the amplified pulse of the Legend couples back into the Micra and disrupts the pulse

*This was confirmed by using a longer BNC and noting the time-shift of the feature.

train* While this did not affect the stability of the seed for the Legend, as the recovery time of the Micra was tens of nanoseconds, due to the asynchronous pulse picking of the Rega it resulted in a highly unstable output in this amplifier. This problem arose after the replacement of the Legend thermoelectric cooler and was solved by adjusting the tilt of the injection and ejection Pockel's cells†

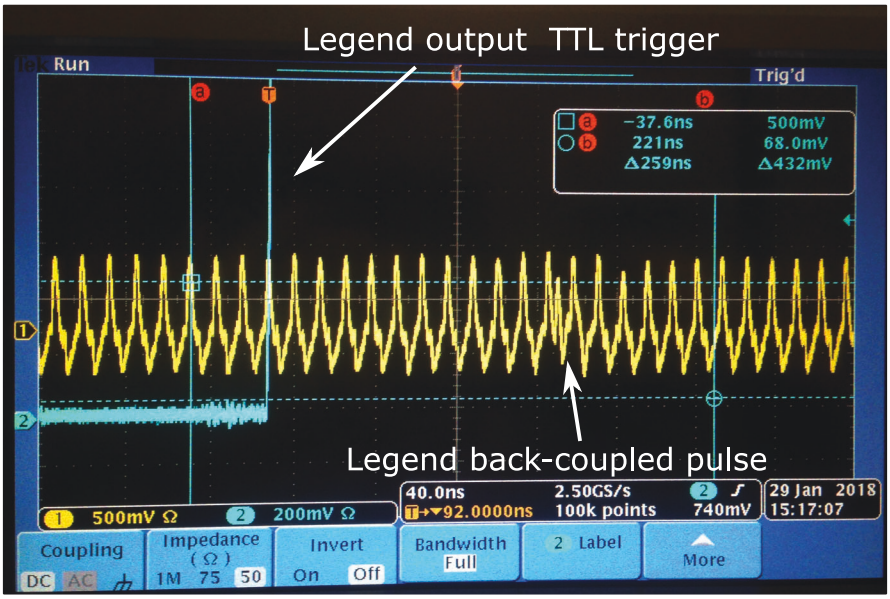

Fig. B.7: Legend backcoupling to Micra. Example oscilloscope trace highlighting the back coupling of the amplified pulse to the seed laser cavity.

*This problem could not be solved by adjusting the set screw of the isolator, which tunes the magnetic field of the Faraday rotator.

†Here, the term solved is used rather loosely: the back coupling is still present in the Micra trace, however, it was reduced enough that the Rega stability appears to be unaffected by the Legend amplifier.

Appendix C

Evidence of emission above 10 THz from LN

In general, the THz spectra in this thesis are windowed to the low frequency regime as the spectrum is dominated by the strongly polar phonon resonance at 7.7 THz [64, 106]. With the 35 fs pulse duration of the Legend, it should also be possible to generate THz in the region above this resonance [330], however, the coherence length at these frequencies is very small (see Chapter 2). Nevertheless, in the TPF geometry part of the beam propagates through only a small portion of the crystal, as illustrated in Figure C.1. Furthermore, we expect a small amount of THz generation from the interface region (see ref. 4.10a or refs. [331, 332]).

Shown in Figure C.1b is the amplitude spectrum up to 20 THz measured in a nitrogen purged environment with the Gen. 2 source. The corresponding waveform is in the inset. The main lobe of the spectrum shows spectral content up to 5 THz while secondary and tertiary lobes appear at higher frequencies between approximately 7 and 10 THz followed by 11 and 13 THz. Finally, there appears to be another lobe near 18 THz, which is close to the second strongest resonance in the spectrum at 18.8 THz [64]. Notably, the gap between the second and third lobes is located in the range of the reststrahlen band of GaP, where the detector response should fall of dramatically [271].

Notably, high-frequency emission above the phonon has already been observed from ZnTe [333, 50]. However, the reality of the high-frequency emission from LN

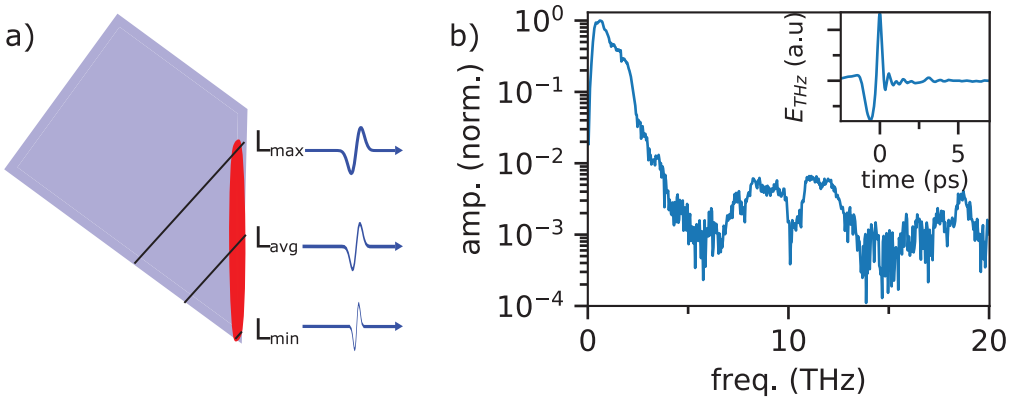

Fig. C.1: Evidence of high-frequency THz generation from LN. a Geometry of the TPF THz source showing the propagation length in the crystal as a function of lateral position along the exit face of the crystal. **b** Amplitude spectrum from the Fourier transform of the waveform in the inset up to 20 THz, showing frequency content between 8 and 12 THz and up to almost 20 THz.

remains unconfirmed and it could be simply an artifact of the time-domain acquisition *et al.* [334]. Notably, numerical simulations suggest that the period sampling error discussed by Renh *et al.* in ref. [334] cannot account for the behavior observed here, however, it is possible that there remains unconsidered artifacts that could explain our data. Future experiments could help confirm this emission by resolving known water-absorption lines in this range, which has proved challenging so far with this source, or using high-contrast filters or grating spectrometers along with energy meters such as bolometers.